

Rochester Institute of Technology

RIT Digital Institutional Repository

Theses

7-12-2019

**Methodology for the Integration of Optomechanical System
Software Models with a Radiative Transfer Image Simulation
Model**

Keegan S. McCoy
ksm8470@rit.edu

Follow this and additional works at: <https://repository.rit.edu/theses>

Recommended Citation

McCoy, Keegan S., "Methodology for the Integration of Optomechanical System Software Models with a Radiative Transfer Image Simulation Model" (2019). Thesis. Rochester Institute of Technology. Accessed from

This Dissertation is brought to you for free and open access by the RIT Libraries. For more information, please contact repository@rit.edu.

Methodology for the Integration of Optomechanical System Software
Models with a Radiative Transfer Image Simulation Model

by

Keegan S. McCoy

B.S. in Electrical Engineering, The Pennsylvania State University, 2012

B.S. in Astronomy and Astrophysics, The Pennsylvania State University, 2012

M.S. in Electrical Engineering, The Pennsylvania State University, 2012

A dissertation submitted in partial fulfillment of the
requirements for the degree of Doctor of Philosophy
in the Chester F. Carlson Center for Imaging Science
College of Science

Rochester Institute of Technology

July 12, 2019

Signature of the Author _____

Accepted by _____
Coordinator, Ph.D. Degree Program Date

CHESTER F. CARLSON CENTER FOR IMAGING SCIENCE
COLLEGE OF SCIENCE
ROCHESTER INSTITUTE OF TECHNOLOGY
ROCHESTER, NEW YORK

CERTIFICATE OF APPROVAL

Ph.D. DEGREE DISSERTATION

The Ph.D. Degree Dissertation of Keegan S. McCoy
has been examined and approved by the
dissertation committee as satisfactory for the
dissertation required for the
Ph.D. degree in Imaging Science

Dr. John Kerekes, Dissertation Advisor

Dr. Alan Raisanen, External Chair

Dr. Michael Gartley

Dr. Scott Rohrbach

Date

Methodology for the Integration of Optomechanical System Software Models with a Radiative Transfer Image Simulation Model

by

Keegan S. McCoy

Submitted to the

Chester F. Carlson Center for Imaging Science

in partial fulfillment of the requirements

for the Doctor of Philosophy Degree

at the Rochester Institute of Technology

Abstract

Stray light, any unwanted radiation that reaches the focal plane of an optical system, reduces image contrast, creates false signals or obscures faint ones, and ultimately degrades radiometric accuracy. These detrimental effects can have a profound impact on the usability of collected Earth-observing remote sensing data, which must be radiometrically calibrated to be useful for scientific applications. Understanding the full impact of stray light on data scientific utility is of particular concern for lower cost, more compact imaging systems, which inherently provide fewer opportunities for stray light control. To address these concerns, this research presents a general methodology for integrating point spread function (PSF) and stray light performance data from optomechanical system models in optical engineering software with a radiative transfer image simulation model. This integration method effectively emulates the PSF and stray light performance of a detailed system model within a high-fidelity scene, thus producing realistic simulated imagery. This novel capability enables system trade studies and sensitivity analyses to be conducted on parameters of interest, particularly those that influence stray light, by analyzing their quantitative impact on user applications when imaging realistic operational scenes. For Earth

science applications, this method is useful in assessing the impact of stray light performance on retrieving surface temperature, ocean color products such as chlorophyll concentration or dissolved organic matter, etc. The knowledge gained from this model integration also provides insight into how specific stray light requirements translate to user application impact, which can be leveraged in writing more informed stray light requirements.

In addition to detailing the methodology’s radiometric framework, we describe the collection of necessary raytrace data from an optomechanical system model (in this case, using FRED Optical Engineering Software), and present PSF and stray light component validation tests through imaging Digital Imaging and Remote Sensing Image Generation (DIRSIG) model test scenes. We then demonstrate the integration method’s ability to produce quantitative metrics to assess the impact of stray light-focused system trade studies on user applications using a Cassegrain telescope model and a stray light-stressing coastal scene under various system and scene conditions. This case study showcases the stray light images and other detailed performance data produced by the integration method that take into account both a system’s stray light susceptibility and a scene’s at-aperture radiance profile to determine the stray light contribution of specific system components or stray light paths. The innovative contributions provided by this work represent substantial improvements over current stray light modeling and simulation techniques, where the scene image formation is decoupled from the physical system stray light modeling, and can aid in the design of future Earth-observing imaging systems. This work ultimately establishes an integrated-systems approach that combines the effects of scene content and the optomechanical components, resulting in a more realistic and higher fidelity system performance prediction.

DISCLAIMER

The views expressed in this work are those of the author and do not reflect the official policy or position of the United States Air Force, Department of Defense, or the United States Government.

*The light shines in the darkness,
and the darkness has not overcome it.*

John 1:5 (NIV)

Acknowledgements

First and foremost, I would like to thank God for standing by me not just during my time in this rigorous Ph.D. program, but throughout my entire life. You provide me with the strength to meet all of life's challenges and I pray that I can continue to use the talents that you have provided me for your glory. Though a doctorate degree is the pinnacle of academic achievement, the more I learn about you and the world you have created, the more humble I become.

I would like to thank my wife for her incredible amount of love and support. Though my Ph.D. diploma has my name on it, you have been just as integral a part of the effort. Being a military spouse is not easy in general, but this is especially true during a time-intensive Ph.D. program in which we experienced life-altering changes, both joyful and tragic. You have been a steady presence throughout it all and I look forward to sharing more of life's many adventures with you as we move on from our time in Rochester. I also apologize for teaching you more about stray light and optical system modeling and simulation than you probably ever care to know.

I would like to thank my parents, grandparents, and the rest of my family for their love and encouragement not only during this Ph.D. program, but from the moment I was born. I have been truly blessed to have all of you in my life. I thank you for fostering a love of learning in me from a young age and believing in me every step of the way along my academic journey. I would also like to thank my mother-in-law for her faith in me and I hope that I have made you proud.

I would like to thank the U.S. Air Force and RIT for the opportunity to pursue a doctorate degree. I am truly appreciative and have learned a great deal through the experience, only a portion of which you see here in this dissertation. I am also thankful for those Air Force officers who provided valuable mentorship regarding their times at RIT and helped

make this experience a reality.

I would like to thank Dr. John Kerekes, my Ph.D. advisor, for all of his guidance and support over the past few years. I appreciate your trust in me and for helping me to learn the ropes as a Ph.D. student researcher. Thank you to my dissertation committee members, Dr. Alan Raisanen, Dr. Mike Gartley, and Dr. Scott Rohrbach, for agreeing to serve on my committee and for providing knowledgeable feedback along the way. A special thanks goes out to Dr. Gartley for his creation of the “LA” DIRSIG scene used in the work presented here.

I would like to thank my fellow Air Force students and all of my friends here in Rochester. You have provided a community of support during these challenging times and I look forward to staying in touch.

I would like to thank the DIRSIG team of Dr. Scott Brown, Dr. Adam Goodenough, Dr. Rolando Raqueño, and Jared Van Cor for their knowledge and support with using the DIRSIG model. This has been an exciting project to work on and I am glad that my contributions have helped expand DIRSIG’s impressive capabilities.

I would like to thank Ryan Irvin of Photon Engineering for his amazing level of support in helping me to learn how to use FRED Optical Engineering Software and in developing the integration method presented here. You have been an absolutely essential team member and this work would not have been possible without you. However, I may or may not be finished with my somewhat regular 2 a.m. e-mails to you.

I would like to thank Dr. Ray Ohl of the NASA Goddard Space Flight Center for his mentorship, both during my internship at Goddard in the summer of 2009 and ever since. You have played a key role in guiding my career through the Air Force and this Ph.D. program. I also thank you for recommending the use of FRED in this research project, which prompted the entire software model integration concept for modeling stray light-focused system trade

studies.

Finally, I would like to thank Rich Pfisterer, Dr. Jim Fienup and his graduate students, and the many others who have contributed to this research.

To my wife and daughters.

Contents

List of Figures	xvii
List of Tables	xxxi
1 Introduction	1
1.1 CONTEXT	1
1.2 OBJECTIVES	11
1.3 DISSERTATION LAYOUT	11
1.3.1 Chapter 2: Background	11
1.3.2 Chapter 3: Integration Methodology (Objective 1)	12
1.3.3 Chapter 4: Point Spread Function Component Validation (Objectives 1 & 2)	12
1.3.4 Chapter 5: Stray Light Component Validation (Objectives 1 & 3)	13
1.3.5 Chapter 6: System Trade Study Demonstration (Objectives 1, 4, & 5)	13
1.3.6 Chapter 7: Summary and Conclusions	13
1.4 NOVEL CONTRIBUTIONS	13

2	Background	15
2.1	RADIOMETRIC TERMS	15
2.1.1	Radiant Energy	16
2.1.2	Radiant Flux	16
2.1.3	Irradiance	17
2.1.4	Radiant Intensity	17
2.1.5	Radiance	18
2.2	STRAY LIGHT	19
2.2.1	Stray Light Paths	21
2.2.2	Critical and Illuminated Surfaces	22
2.2.3	In-Field and Out-of-Field Stray Light	24
2.2.4	Stray Light Mechanisms	24
2.2.5	Bidirectional Scattering Distribution Function (BSDF)	26
2.2.6	Stray Light Radiative Transfer Equation	28
2.2.7	Stray Light as Noise	31
2.2.8	Causes of Stray Light	31
2.2.9	Stray Light Metrics	39
2.2.10	Stray Light Requirements	43
2.2.11	Critical Step in Design Process	48
2.2.12	Stray Light Analysis	48
2.2.13	Optical Engineering Software Programs	52
2.3	LINEAR SYSTEMS THEORY	54
2.3.1	Linearity	54
2.3.2	Point Spread Function (PSF)	56

2.3.3	Shift-Invariance	57
2.3.4	Linear Shift-Invariant and Linear Shift-Variant Systems	57
2.3.5	Modulation Transfer Function (MTF)	58
2.4	MODELING AND SIMULATION OF OPTOMECHANICAL SYSTEMS	59
2.4.1	Overview of PSF and Stray Light Modeling Efforts	62
2.4.2	Digital Imaging and Remote Sensing Image Generation (DIRSIG) Model	72
2.5	CONCLUSIONS	78
3	Integration Methodology	81
3.1	INTRODUCTION	81
3.2	INTEGRATION METHODOLOGY FRAMEWORK	84
3.2.1	PSF Component Radiance to Irradiance Conversion	85
3.2.2	Integration Method Component Radiometry	87
3.3	STRAY LIGHT ANGULAR SUSCEPTIBILITY MAP (ASM)	92
3.3.1	Capture a Stray Light ASM	93
3.3.2	Stray Light ASM Analysis	99
3.3.3	Shift-Variant Stray Light ASMs	104
3.4	INTEGRATION METHOD VALIDATION TESTS	107
3.5	CONCLUSIONS	110
4	Point Spread Function Component Validation	113
4.1	INTRODUCTION	113
4.2	CAPTURE SYSTEM PSF	115
4.3	METHODOLOGY	118

4.3.1	2-D RECT Function PSF Validation Test	119
4.3.2	Cassegrain PSF Validation Test	122
4.3.3	Evaluation Metrics	123
4.4	RESULTS	126
4.4.1	2-D RECT Function PSF Validation Test Results	126
4.4.2	Cassegrain PSF Validation Test Results	133
4.4.3	PSF Importance Sampling and the Law of Large Numbers	142
4.5	SUMMARY AND CONCLUSIONS	144
5	Stray Light Component Validation	147
5.1	INTRODUCTION	147
5.2	METHODOLOGY	149
5.3	RESULTS	159
5.4	SUMMARY AND CONCLUSIONS	169
6	System Trade Study Demonstration	171
6.1	METHODOLOGY	173
6.1.1	System Stray Light Performance Conditions	173
6.1.2	DIRSIG Scene and Conditions	176
6.1.3	Nominal Irradiance Images	182
6.1.4	Cassegrain Shift-Variant Stray Light ASMs	183
6.1.5	DIRSIG ERM	186
6.1.6	Stray Light Radiant Flux Contribution Maps	186
6.1.7	Stray Light Irradiance Images	188
6.1.8	Combination of Nominal and Stray Light Irradiance Images	188

6.1.9	Percent Stray Light Images	189
6.1.10	Contrast Reduction	190
6.2	RESULTS	191
6.2.1	Nominal Irradiance Images	191
6.2.2	Cassegrain Shift-Variant Stray Light ASMs	192
6.2.3	DIRSIG ERMs	201
6.2.4	Stray Light Irradiance Images	202
6.2.5	Stray Light Radiant Flux Contribution Maps	211
6.2.6	Combined Nominal and Stray Light Irradiance Images	214
6.2.7	Percent Stray Light Images	216
6.2.8	System Trade Study Analysis	222
6.2.9	Contrast Reduction	226
6.3	CONCLUSIONS	229
7	Summary and Conclusions	235
7.1	CONCLUSIONS	238
7.2	FUTURE WORK	241
	Bibliography	243

List of Figures

1.1	Landsat program timeline with the operational on-orbit duration of each mission [7].	3
1.2	Integrating an optomechanical system model from optical engineering software with a radiative transfer image simulation model combines the unique benefits of each type of model in creating the complete imaging chain. . . .	10
2.1	Example of a second-order stray light path [17].	22
2.2	Optical system with critical and illuminated surfaces labeled [17].	23
2.3	Off-axis source scatters off a critical baffle surface and to the detector (left). With vanes included, the light can now only reach the detector via multiple scattering, which greatly attenuates the stray light power (right) [67]. . . .	23
2.4	Specular reflection and refraction at an interface between two media [17]. . .	25
2.5	Incident and reflected angles used in describing a surface's bidirectional scattering distribution function (BSDF) [17].	27
2.6	Geometry for scattering from a source area to a collector area [67].	28

2.7	Mircroscope image of surface roughness on a fused silica surface due to grinding and polishing. The image is approximately 10 μm across, with an RMS surface roughness of 5 \AA [76].	32
2.8	Vectors used in the Harvey-Shack scatter model [80].	33
2.9	Example Harvey-Shack scatter model curve with $L = 0.01$, $b_0 = 0.1$, and $S = -1.5$. Assuming $\lambda = 0.55 \mu\text{m}$, these parameters correspond to an approximate surface roughness of $\sigma_{RMS} = 14.7 \text{\AA}$ [81].	35
2.10	Number of particles of diameter $\geq D$ v. D according to IEST-STD-CC1246D for CLs 200, 400, and 600 [17].	37
2.11	Example of how dendrites can be used to trap light. The angles of incidence are defined according to the macroscopic surface normal and not the variable dendrite profile. [17].	39
2.12	Setup used for a veiling glare test [17].	42
2.13	Stray light systems engineering flowchart illustrating the necessary steps from stray light requirements definition to final system build and model validation [17].	44
2.14	Strengths and weakness of the build-and-test v. model-and-predict methods for stray light analysis [68].	52
2.15	Image of a bar target (a) without stray light and (b) with stray light. Stray light acts to reduce the contrast of the bar target. [17].	59
2.16	DIRSIG simulation of the Port of Tacoma, WA imaged with a 2-D framing array on a commercial small satellite [149].	74

2.17	The 2-step PSF importance sampling process combines a single random pixel location with a single random PSF offset: (a) One initial and final ray sampling location. (b) Numerous initial and final ray sampling locations.	77
2.18	DIRSIG image of a resolution test target and a helicopter with rotating rotor blades: (a) No Gaussian PSF or time integration. (b) With a Gaussian PSF and time integration.	78
3.1	Integrating optical engineering software programs with a radiative transfer image simulation model combines the unique benefits of each type of software.	83
3.2	Integration method flowchart illustrating how system PSF and stray light performance data collected from an optomechanical system model in optical engineering software (blue steps) can be used to image a scene using a radiative transfer image simulation model (orange steps) to produce simulated output imagery.	83
3.3	As detailed by the integration method's underlying radiometry, the stray light contributions reaching the focal plane of an optical system are inherently a product of the system's stray light susceptibility and the scene's at-aperture radiance profile.	90
3.4	(a) TIRS band 11 (11.50–12.51 μm) image of the Red Sea with image intensity ranging from 8.5 to 11.5 $\text{W}/\text{m}^2/\text{sr}/\mu\text{m}$. Far-field stray light leads to a banding effect that is evident in the across-track direction between the three FPAs. (b) Map from USGS Earth Explorer showing the extent of the scene. Reproduced with permission, courtesy of Montanaro et al. (2014) [57].	92

3.5	Cassegrain telescope FRED model with a flat black paint scatter model (TIS = 2% at normal incidence) assigned to the mechanical surfaces (labeled in black). A Harvey-Shack scatter model ($b_0 = 0.1$, $L = 0.01$, and $S = -1.5$) and Mie scatter model representing particulate contamination (CL400) have been assigned to the optical surfaces (labeled in blue).	94
3.6	Reverse raytrace using the Cassegrain telescope model along with the stray light ASM coordinate system. The system's stray light susceptibility data is captured at the entrance aperture as a radiant intensity profile by the DAE. These data are then converted to stray light radiant flux per grid element by multiplying by each DAE grid element's solid angle.	96
3.7	Scatter model importance sampling demonstration. (a) Scatter rays into the full hemisphere. (b) Scatter rays towards a detector. The latter case produces greatly improved radiometric results due to the increased numbers of rays scattered to the surface of interest [17].	98
3.8	(a) Cassegrain system stray light ASM at $1^\circ \times 1^\circ$ resolution (log of radiant flux). (b) Visualization of the Cassegrain stray light ASM on the entrance aperture DAE grid in FRED (log of radiant intensity). Azimuthal angle $\phi = 0^\circ$ points in the positive x-axis direction, while $\phi = +90^\circ$ points towards the positive y-axis. Polar angle $\theta = 0^\circ$ points directly out of the page from the center of the entrance aperture, while polar angle $\theta = 90^\circ$ points along the entrance aperture edge.	101

3.9	Visualization of the Cassegrain telescope’s highest susceptibility stray light path. In the forward direction, these rays enter the Cassegrain telescope’s entrance aperture and scatter off of the primary mirror baffle’s inner wall directly to the detector. In our reverse raytrace, this stray light path is solely responsible for 46.9% of the total stray light radiant flux captured by the detector’s stray light ASM.	102
3.10	Validation levels for end-to-end system modeling and simulation. Work supporting the 2nd level of validation is presented in this dissertation, whereas the 1st and 3rd levels have system and scene dependencies and are therefore left to the users of this integration method.	108
4.1	Cassegrain telescope FRED model. The optical surfaces are labeled in blue and the mechanical surfaces are labeled in black [60].	116
4.2	Forward raytrace to capture the Cassegrain telescope’s on-axis PSF [60]. . .	117
4.3	Irradiance plot of the Cassegrain system on-axis PSF at $\lambda = 0.55 \mu\text{m}$ (log scale). The black box denotes the spatial extent of a $9\text{-}\mu\text{m}$ FPA pixel [60]. .	117
4.4	System setup for the PSF validation tests.	119
4.5	Ideal result and DIRSIG output images for the 2-D RECT function PSF validation test: (a) Ideal result. (b) 250 sampling rays per FPA pixel. (c) 500 sampling rays per FPA pixel. (d) 1,000 sampling rays per FPA pixel. (e) 10,000 sampling rays per FPA pixel. (f) 100,000 sampling rays per FPA pixel.	128
4.6	Difference image between the ideal result and the DIRSIG image with 10,000 sampling rays per FPA pixel for the 2-D RECT function PSF validation test.	129

4.7	2-D correlation coefficient between the ideal result and the DIRSIG images for each test case of the 2-D RECT function PSF validation test. The data points indicate the mean value of the ten simulations conducted for each test case, with the error bars extending plus or minus one standard deviation.	130
4.8	RMSE in 2-D correlation coefficient v. number of DIRSIG sampling rays for the 2-D RECT function PSF validation test.	131
4.9	Irradiance ratio for each test case of the 2-D RECT function PSF validation test. The data points indicate the mean value of the ten simulations conducted for each test case, with the error bars extending plus or minus one standard deviation.	132
4.10	RMSE of the irradiance ratio v. number of DIRSIG sampling rays for the 2-D RECT function PSF validation test.	133
4.11	Ideal result and DIRSIG output images for the Cassegrain PSF validation test (log scales): (a) FRED Cassegrain PSF. (b) 500 sampling rays per FPA pixel. (c) 2,500 sampling rays per FPA pixel. (d) 10,000 sampling rays per FPA pixel. (e) 25,000 sampling rays per FPA pixel. (f) 100,000 sampling rays per FPA pixel.	135
4.12	2-D correlation coefficient between the FRED Cassegrain PSF and the DIRSIG images for the Cassegrain PSF validation test. The data points indicate the mean value of the ten simulations conducted for each test case, with the error bars extending one standard deviation in each direction.	137
4.13	2-D correlation coefficient RMSE v. number of DIRSIG sampling rays for the Cassegrain PSF validation test.	138

4.14	Irradiance ratio for each test case of the Cassegrain PSF validation test. The data points indicate the mean value of the ten simulations conducted for each test case, with the error bars extending plus or minus one standard deviation.	140
4.15	RMSE of the irradiance ratio v. number of DIRSIG sampling rays for the Cassegrain PSF validation test.	141
5.1	Simple FRED setup of two parallel aligned square surfaces for use in the first stray light validation test. A source placed directly above the source area illuminates the Lambertian source surface, scattering rays towards the collector. The scatter radiant flux captured by the collector during a series of FRED raytraces can then be compared to the analytically calculated value.	150
5.2	Integration method stray light radiant flux contribution equation in graphical form: (top) Cassegrain stray light ASM converted to radiant flux. (middle) 0.10° circle target source ERM from DIRSIG integrated over the detector’s spectral bandpass. (bottom) Stray light radiant flux contribution map. The summation of the stray light radiant flux contribution map provides the detector’s total stray light radiant flux.	167
6.1	Different scatter models applied to the Cassegrain telescope’s optical and mechanical surfaces to represent various stray light performance conditions.	174
6.2	DIRSIG “LA scene” covering 450 × 375 km of central and southern California.	177
6.3	Wide-area view of the DIRSIG LA scene with lower-resolution Earth background and inset outlining the LA scene location.	178
6.4	DIRSIG LA scene with Santa Barbara scene location within the Cassegrain telescope’s FOV.	180

6.5 LA scene with Earth background for the different combinations of DIRSIG scene conditions (common log scales of spectral radiance at $\lambda = 0.55 \mu\text{m}$). The very small black box near the center of each scene marks the Cassegrain telescope’s nominal FOV over Santa Barbara, CA. (a) 1 Aug 2019 at 1:15 p.m. PDT with wind speed = 2.5 m/s W to E. (b) 1 Aug 2019 at 1:15 p.m. PDT with wind speed = 7.5 m/s W to E. (c) 1 Aug 2019 at 11:30 a.m. PDT with wind speed = 7.5 m/s W to E. (d) 1 Apr 2019 at 1:15 p.m. PDT with wind speed = 7.5 m/s W to E. 182

6.6 Face-on view of the Cassegrain FPA detailing the pixel numbering scheme used in FRED for capturing the shift-variant stray light ASMs. This is necessary to keep track of which stray light ASM was collected for each FPA pixel. 185

6.7 Block diagram of the integration method’s stray light radiant flux contribution equation. The ERM of a scene is multiplied solid angle grid element-by-solid angle grid element with a detector element’s stray light ASM for a given set of system stray light susceptibility conditions to produce the detector element’s stray light radiant flux contribution map. The summation of the stray light radiant flux contributions for each solid angle grid element across the contribution map provides the detector element’s total stray light radiant flux. 187

6.8 Nominal irradiance images for Harvey-Shack mirror surface roughness ($\sigma_{RMS} = 14.7 \text{ \AA}$) and CL400 particulate contamination (common irradiance scale). (a) 1 Aug 2019 at 1:15 p.m. PDT with wind speed = 2.5 m/s. (b) 1 Aug 2019 at 1:15 p.m. PDT with wind speed = 7.5 m/s. (c) 1 Aug 2019 at 11:30 a.m. PDT with wind speed = 7.5 m/s. (d) 1 Apr 2019 at 1:15 p.m. with wind speed = 7.5 m/s. 192

6.9 Cassegrain telescope stray light ASMs for a pixel near the center of the FPA (x356 y356) with system stray light susceptibility conditions including Harvey-Shack mirror surface roughness ($\sigma_{RMS} = 14.7 \text{ \AA}$), CL400 particulate contamination, and flat black paint TIS = 2% (common log of radiant flux scale). (a) 10 million initial rays. (b) 100 million initial rays. The greater number of rays traced in the latter case has reduced the statistical noise of the system stray light susceptibility data. 194

6.10 Cassegrain telescope stray light ASMs for a pixel in the center of the FPA (x356 y356) with varying system stray light susceptibility conditions: (common log of radiant flux scale). All of the system conditions have Harvey-Shack mirror surface roughness ($\sigma_{RMS} = 14.7 \text{ \AA}$) included. (a) CL400 particulate contamination and flat black paint TIS = 2%. (b) CL400 particulate contamination and flat black paint TIS = 1%. (c) CL600 particulate contamination and flat black paint TIS = 1%. 196

- 6.11 Cassegrain telescope shift-variant stray light ASMs for various pixels across the FPA (common log of radiant flux scale). The system stray light susceptibility conditions include Harvey-Shack mirror surface roughness ($\sigma_{RMS} = 14.7 \text{ \AA}$), CL400 particulate contamination, and flat black paint TIS = 2%. All FPA pixel locations are based on viewing the FPA face on in the FRED model (y-axis pointing up, x-axis pointing to the left). (a) top left corner (pixel x5 y5). (b) top right (pixel x716 y5). (c) center (pixel x356 y356). (d) bottom left (pixel x5 y716). (e) bottom right (pixel x716 y716). 200
- 6.12 DIRSIG ERMs for the different scene conditions (common log of spectral radiance scale). The black circles at the top center of each plot marks the Santa Barbara scene location for reference. (a) 1 Aug 2019 at 1:15 p.m. PDT with wind speed = 2.5 m/s. (b) 1 Aug 2019 at 1:15 p.m. PDT with wind speed = 7.5 m/s. (c) 1 Aug 2019 at 11:30 a.m. PDT with wind speed = 7.5 m/s. (d) 1 Apr 2019 at 1:15 p.m. with wind speed = 7.5 m/s. 202

6.13 Illustration of how the azimuthal angles where different FPA pixels have their highest stray light susceptibility map to the scene. The scene shown is 1 Aug 2019 at 1:15 p.m. with wind speed = 2.5 m/s plotted on a linear spectral radiance scale. (a) The orange arrows mark the azimuthal angle of highest susceptibility for the labeled FPA corner pixels. The red arrows map the Cassegrain telescope’s stray light ASM azimuthal angles to the scene (polar angle $\theta = 0^\circ$ points directly into the page). The very small black box in the center of the scene outlines the Cassegrain telescope’s nominal FOV over Santa Barbara, CA. (b) Face-on view of the Cassegrain FPA within the FRED model with the corner pixel locations labeled and scene cardinal directions mapped to the FPA. 204

6.14 Orientation of the Cassegrain FPA within the FRED model to the DIRSIG FPA used to produce the nominal, stray light, and combined final output images. The Cassegrain FPA must be flipped vertically to match the DIRSIG FPA. As detailed by the cardinal directions, this specific orientation of the DIRSIG FPA was chosen so that north in the Santa Barbara scene points up, east points to the right, etc. for improved visualization of the output images. 205

- 6.15 Stray light irradiance images for the 1 Aug 2019 at 1:15 p.m. PDT, wind speed = 2.5 m/s scene with different system stray light susceptibility conditions. Note that every image has a different irradiance scaling to best highlight its unique distribution. All system stray light susceptibility conditions include Harvey-Shack mirror surface roughness ($\sigma_{RMS} = 14.7 \text{ \AA}$). (a) Large-area view of the scene for 1 Aug 2019 at 1:15 p.m. PDT with wind speed = 2.5 m/s for reference. The small black box in the center of the scene outlines the Cassegrain telescope's FOV. (b) No particulate contamination, flat black paint TIS = 2%. (c) CL400, flat black paint TIS = 1%. (d) CL400, flat black paint TIS = 2%. (e) CL600, flat black paint TIS = 1%. (f) CL600, flat black paint TIS = 2%. 207
- 6.16 Stray light irradiance images for the stray light susceptibility conditions with Harvey-Shack mirror surface roughness ($\sigma_{RMS} = 14.7 \text{ \AA}$), CL400 particulate contamination, and flat black paint TIS = 2% for each of the different scene conditions. Note that every image has a different irradiance scaling to best highlight its unique distribution. (a) 1 Aug 2019 at 1:15 p.m. PDT, wind speed = 2.5 m/s. (b) 1 Aug 2019 at 1:15 p.m. PDT, wind speed = 7.5 m/s. (c) 1 Aug 2019 at 11:30 a.m. PDT, wind speed = 7.5 m/s. (d) 1 Apr 2019 at 1:15 p.m. PDT, wind speed = 7.5 m/s 210

6.17 Stray light radiant flux contribution maps for the 1 Aug 2019 at 1:15 p.m. PDT, wind speed = 2.5 m/s scene and system stray light susceptibility conditions with Harvey-Shack mirror surface roughness ($\sigma_{RMS} = 14.7 \text{ \AA}$), CL400 particulate contamination, and flat black paint TIS = 2% (common log of radiant flux scales). The summation of these stray light radiant flux contribution maps provides the total stray light radiant flux for the given FPA pixel. (a) Pixel x5 y5 (bottom left of DIRSIG Cassegrain FPA) (b) Pixel x716 y716 (top right of DIRSIG Cassegrain FPA). 212

6.18 The nominal (top left) and stray light (top right) images for a given set of system stray light susceptibility and scene conditions are added together to form the final output image (bottom center). This example is for the 1 Aug 2019 at 1:15 p.m. PDT, wind speed = 2.5 m/s scene and system stray light susceptibility conditions with Harvey-Shack mirror surface roughness ($\sigma_{RMS} = 14.7 \text{ \AA}$), CL400 particulate contamination, and flat black paint TIS = 2%. Note that the nominal and final output images are plotted on the same irradiance scale. 216

6.19 Percent stray light images for the 1 Aug 2019 at 1:15 p.m. PDT, wind speed = 2.5 m/s scene with different system stray light susceptibility conditions (common percent stray light scaling). All system stray light susceptibility conditions include Harvey-Shack mirror surface roughness ($\sigma_{RMS} = 14.7 \text{ \AA}$). (a) No particulate contamination, flat black paint TIS = 2%. (b) CL400, flat black paint TIS = 1%. (c) CL400, flat black paint TIS = 2%. (d) CL600, flat black paint TIS = 1%. (e) CL600, flat black paint TIS = 2%. 220

- 6.20 Percent stray light images for the system stray light susceptibility conditions with Harvey-Shack mirror surface roughness ($\sigma_{RMS} = 14.7 \text{ \AA}$), CL400 particulate contamination, and flat black paint TIS = 1% across the different scene conditions. Note that every image has a different irradiance scaling to best highlight its unique distribution. (a) 1 Aug 2019 at 1:15 p.m. PDT, wind speed = 2.5 m/s. (b) 1 Aug 2019 at 1:15 p.m. PDT, wind speed = 7.5 m/s. (c) 1 Aug 2019 at 11:30 a.m. PDT, wind speed = 7.5 m/s. (d) 1 Apr 2019 at 1:15 p.m. PDT, wind speed = 7.5 m/s. 222
- 6.21 Ideal Cassegrain telescope final output image and the final output images (nominal + stray light image) of 1 Aug 2019 at 1:15 p.m. PDT, wind speed = 2.5 m/s scene under different stray light susceptibility conditions (common irradiance scale). All system stray light susceptibility conditions include Harvey-Shack mirror surface roughness ($\sigma = 14.7 \text{ \AA}$). Note that every image has the same irradiance scaling to best highlight the contrast reduction compared to the ideal image. (a) Ideal Cassegrain system. (b) No particulates, BP TIS = 2%. (c) CL400, BP TIS = 1%. (d) CL400, BP TIS = 2%. (e) CL600, BP TIS = 1%. (f) CL600, BP TIS = 2%. 228

List of Tables

3.1	Cassegrain telescope designed optical path in the forward direction (object space to focal plane).	95
3.2	Percentage of the total stray light radiant flux on the detector's stray light ASM from first-order stray light paths including significant scattering surfaces. The surfaces listed are where the single scattering event took place in each case. Since many unique first-order stray light paths can share the same scatter surface, these percentages are the summation of all first-order stray light paths for each scatter surface.	102
4.1	Number of DIRSIG sampling rays per FPA pixel tested for the PSF validation tests.	124

5.1	Comparison between the collector scatter radiant flux analytical calculation and the FRED raytrace results for the source-collector test setup. The FRED raytrace results display the mean and standard deviation of the collector scatter radiant flux across the twenty raytraces conducted. The difference from analytical indicates the percentage difference between the mean raytrace collector scatter radiant flux and the analytically calculated value.	160
5.2	Comparison between the detector scatter radiant flux for the original analytical calculation, FRED forward raytraces, and FRED reverse raytraces. The FRED raytrace results display the mean and standard deviation of the detector scatter radiant flux across the twenty raytraces conducted in each case.	162
5.3	Comparison of the mirror GCFs in the original Peterson analytical equation and the corrected GCFs from FRED for the detector as seen by each mirror.	163
5.4	Comparison of the system transmittances at each mirror used in the original Peterson analytical equation and the corrected system transmittances from FRED taking into account projection effects from the target source and mechanical components.	163
5.5	Comparison between the detector scatter radiant flux for the original and corrected analytical calculations and the FRED forward raytrace. The FRED raytrace results display the mean and standard deviation of the detector scatter radiant flux across the twenty raytraces conducted in each case. . .	164

5.6	Comparison between the FRED forward and reverse raytrace results and the integration method applied to the simplified Cassegrain telescope and circular target source imaging scenario. Each set of results display the mean and standard deviation of the detector scatter radiant flux across the twenty raytraces conducted in each case.	168
6.1	Different combinations of stray light performance conditions. All cases include the same Harvey-Shack scatter model ($b_0 = 0.1$, $L = 0.01$, and $S = -1.5$; $\sigma_{RMS} = 14.7 \text{ \AA}$) for optical surface roughness. The flat black paint TIS percentages refer to the value at normal incidence.	175
6.2	Different combinations of DIRSIG scene conditions. All times of day are listed in Pacific Daylight Time (PDT).	181
6.3	The Cassegrain telescope G#'s for different optical surface conditions. Note that these G#'s are all calculated for the center of the focal plane. The Harvey-Shack scatter model includes $b_0 = 0.1$, $L = 0.01$, and $S = -1.5$, which corresponds to $\sigma_{RMS} = 14.7 \text{ \AA}$ at $\lambda = 0.55 \mu\text{m}$	191
6.4	Total stray light (SL) radiant flux and pixel percent stray light for a pixel (x356 y356) near the center of the Cassegrain telescope's FPA under different system stray light susceptibility conditions. "BP" refers to the flat black paint scatter model assigned to the mechanical components and the TIS values are for normal incidence. All of the system conditions include Harvey-Shack mirror surface roughness ($\sigma_{RMS} = 14.7 \text{ \AA}$).	198

6.5	Mean irradiance values for the stray light images of the 1 Aug 2019 at 1:15 p.m. PDT, wind speed = 2.5 m/s scene with different system stray light susceptibility conditions.	208
6.6	Mean of the irradiance values for the stray light images with Harvey-Shack mirror surface roughness ($\sigma_{RMS} = 14.7 \text{ \AA}$), CL400 particulate contamination, and flat black paint TIS = 2% for each of the different scene conditions. . .	211
6.7	Percentage of the total stray light irradiance for pixel x5 y5 that originates from sources within the given polar angle ranges in object space. These data are for the 1 Aug 2019 at 1:15 p.m. PDT, wind speed = 2.5 m/s scene and system stray light susceptibility conditions with Harvey-Shack mirror surface roughness ($\sigma_{RMS} = 14.7 \text{ \AA}$), CL400 particulate contamination, and flat black paint TIS = 2%. The components causing scatter are the major scatter contributors for each polar angle range.	214
6.8	Percentage of the total stray light irradiance for pixel x716 y716 that originates from sources within the given polar angle ranges in object space. These data are for the 1 Aug 2019 at 1:15 p.m. PDT, wind speed = 2.5 m/s scene and system stray light susceptibility conditions with Harvey-Shack mirror surface roughness ($\sigma_{RMS} = 14.7 \text{ \AA}$), CL400 particulate contamination, and flat black paint TIS = 2%. The components causing scatter are the major scatter contributors for each polar angle range.	214
6.9	Mean percent stray light values for the land and water pixels across all combinations of system stray light susceptibility and scene conditions.	218

- 6.10 Contrast values and reductions from the ideal images to final output images (nominal + stray light images) across every combination of system stray light susceptibility and scene conditions. All of the system stray light susceptibility conditions include Harvey-Shack mirror surface roughness ($\sigma_{RMS} = 14.7 \text{ \AA}$). 227

Chapter 1

Introduction

1.1 CONTEXT

Since its very formation, the Earth has been a dynamic world of change. Natural forces have dramatically altered the landscape, with rivers and glaciers slowly etching away valleys and canyons, tectonic plates colliding to form towering mountain ranges and triggering jarring earthquakes, volcanoes spewing forth lava to create new land, and both wind and precipitation eroding and weathering the surface. Biological forces have also played a role, as animals and plants combine to form complex and diverse ecosystems that evolve over time. We as humans have altered the Earth in dramatic ways by building sprawling cities, planting fields of crops, cutting down forests, diverting water resources to barren lands, and polluting the environment.

Collecting data to monitor and analyze these global changes has been an arduous manual task for much of human history. As transportation and communication evolved, more information could be gathered and shared about our ever-changing world. The dawn of

flight greatly improved our ability to capture global change information via remote sensing, the acquisition of information about objects or phenomena without coming into physical contact with the target. Medium-to-high resolution Earth imagery from low-flying aircraft could be collected and pieced together to produce aerial views that no human had ever seen before. However, it was the advent of satellites that truly revolutionized our capability to collect detailed information about the entire Earth. Satellites present many advantages for remote sensing, including synoptic views (“big-picture” views of large areas), periodic revisits of specific ground locations, and the ability to collect data quickly, over inaccessible areas, and simultaneously at different wavelengths and modalities using a single platform.

Although much of the nascent United States space program focused on manned missions, the concept of an Earth-orbiting satellite to monitor natural resources was first advocated by the Department of the Interior and the U.S. Geological Survey (USGS) in the early 1960s [1]. On July 23, 1972, the National Aeronautics and Space Administration (NASA) launched the Earth Resources Technology Satellite (ERTS), the first satellite with the expressed intent to study and monitor the Earth’s landmasses [2]. Once a duplicate ERTS was launched in 1975, the two satellites were renamed Landsat 1 and Landsat 2. A total of seven successful Landsat missions have collected some six million multispectral images of the Earth over the past forty-seven years, establishing Landsat as the longest running, space-based Earth observation program [3]. Figure 1.1 shows the operational lifetime for each mission, clearly detailing the fact that at least one Landsat satellite has been active at any given time since the program’s first launch. Although instrument advancements have led to better radiometry, improved spatial resolution, and the addition of new spectral bands over the course of the Landsat program’s lifetime, its core visible and near-infrared (NIR) spectral coverage date back to the program’s beginning [1]. It is this multispectral, continuous

temporal record of the Earth that has made Landsat so essential for conducting global change research; maintaining and extending this historical record into the future remains a key priority of the program. Although only a brief overview of the Landsat program’s history is provided here, more extensive historical details and the characteristics of specific missions have been chronicled elsewhere [1, 4–6].

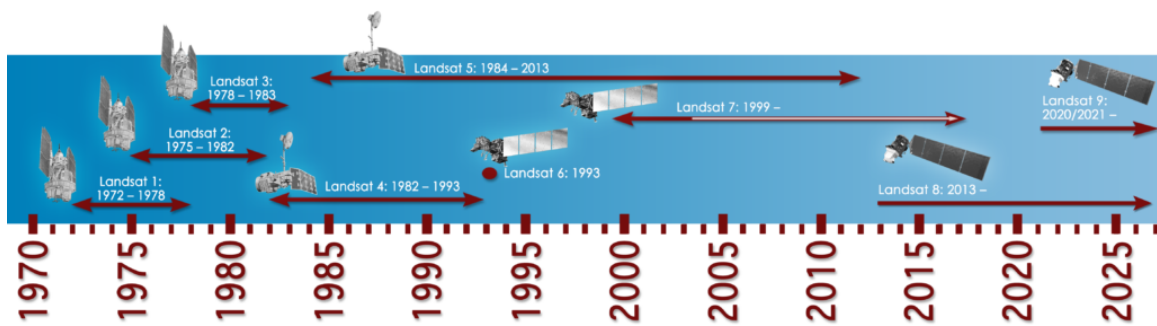


Figure 1.1: Landsat program timeline with the operational on-orbit duration of each mission [7].

The world has undergone significant change over the Landsat program’s roughly half-century lifetime, particularly from the growth of the world population and economy. There are numerous scientific, economic, and humanitarian applications that benefit from Landsat’s imagery documenting these global changes, including agriculture, forestry, geology, regional planning, disaster relief, natural resource monitoring, climate research, and land use and cover analysis [8–10]. Although there are increasing numbers of international and commercial moderate-resolution Earth-orbiting satellites, Landsat remains the so-called “gold standard” of land remote sensing for its unique ability to meet the following five criteria [1]:

1. Landsat’s spatial resolution is fine enough to monitor human and environmental

change, yet sufficiently coarse to allow for seasonal coverage of the globe.

2. Landsat provides spectral coverage in the visible and NIR, with additional bands in the short-wave infrared (SWIR) and thermal-infrared regions.
3. Landsat data is calibrated to science-quality at-sensor radiance and reflectance, so long-term changes in the land can be separated from varying trends in instrument performance.
4. Landsat collects data from all over the globe, providing seasonal coverage of all land masses.
5. Landsat data is freely available and open to distribution.

Landsat 8, the most recent addition to the program, launched in February 2013; Landsat 9, a successor satellite, is currently under development and slated for a tentative launch date in December 2020 [11]. In an effort to maintain the almost half-century record of data continuity, NASA and the USGS have already initiated technology and requirement studies for a future Landsat 10 to launch later in the 2020s [12]. Whereas Landsat 9 will largely replicate its Landsat 8 predecessor, NASA and the USGS are investigating long-term mission architectures and technological innovations that will enhance the imaging capabilities of Landsat 10 and beyond [12].

Some of the Landsat 10 mission architecture options include launching constellations of satellites with more compact, lower cost designs, which could provide improved temporal coverage of the Earth, a priority for future Landsat systems [12]. Throughout the Landsat program's history, advancements in focal plane array (FPA) technology have led to an increased density of detector elements and size of imaging arrays, improving image quality

and enabling overall system miniaturization and reduced cost [13]. In recent years, the emergence of freeform optical components, which contain optical surfaces that have no rotational symmetry about any axis, has vastly expanded the toolbox of optical designers. Freeform optics allow for improved image quality and reduced aberrations while using fewer overall optical components that are reduced in size, thus offering the potential for cost savings [14–16]. Despite the mission benefits, compact instrument designs also increase the number of overlapping optical paths and reduce opportunities for controlling stray light, such as inserting baffles.

In a simplistic sense, stray light is defined as any unwanted radiation that reaches the focal plane of an optical system. Stray light occurs because it is not possible to perfectly control every ray of light that enters a system and direct it to the proper location on the focal plane [17]. Stray light can be created by a number of mechanisms, including surface roughness due to material properties or as a result of manufacturing techniques, ghost reflections from light rays that reflect off of lens surfaces, diffraction from apertures, self-emission of optical components in thermal systems, or atmospheric scattering. Control of this unwanted stray light is important in scenarios where one is observing faint objects near bright sources, when high radiometric precision or contrast is required, when imaging with infrared camera systems susceptible to thermal self-emission, or when making multispectral or hyperspectral measurements that can result in spectral crosstalk [17]. Stray light is a particular concern for the Landsat program and its myriad scientific applications, which rely upon radiometrically calibrated data [18]. Stray light acts as a form of optical noise that obscures the desired signal, degrading scientific accuracy and potentially preventing meaningful analysis altogether [19].

The elevated stray light concern of compact instruments in smaller satellites is not

unique to the Landsat program. The U.S. Department of Defense (DoD) has conducted studies on the resiliency benefits of satellite disaggregation, distributing the capabilities of larger satellites into multiple smaller spacecraft, to preserve the United States' operational advantage in space [20,21]. The past decade has also witnessed the proliferation of cubesats and nanosats, as space agencies, militaries, universities, and commercial companies across the world are interested in small satellites for a wide range of applications. The design constraints inherent in these compact systems lead to tighter systems engineering trade-offs, underscoring the need to better understand the quantitative linkage between stray light performance and impact to user applications.

Current stray light research is largely deficient in clearly relating system stray light requirements and performance to user application impact. Much of the stray light literature analyzes the pre-mission stray light performance of a specific optomechanical system [18, 22–28], provides an assessment of how well a system's operational stray light performance matches its predicted performance [29–31], or introduces post-processing methods to correct for stray light in imagery [30,32–37]. The pre-mission and operational assessments generally focus on stray light requirement verification rather than validating that a system's stray light performance is acceptable for user applications. This indicates an implicit trust that a system's stray light requirements have been properly defined, i.e. that the system will satisfy user expectations if its stray light performance meets the requirements.

However, stray light performance depends on many different optomechanical design parameters, thus complicating the task of drafting suitable stray light requirements for a specific system and its range of user applications. As a result, stray light requirements are often based on historical requirements from similar previous missions rather than explicitly traced to current mission user needs. At best, setting stray light requirements in this

manner runs the risk of overestimating the level of stray light performance truly needed for a system, leading to additional costs and delays building in the performance margin. At worst, the new system's design or user applications may be inherently more susceptible to stray light and the heritage-derived requirements will not be sufficient, resulting in possible redesign of the entire system or risking a dissatisfied user community. In fact, in the worst case scenario, it may not even be possible for the new system to meet more strict heritage-derived stray light requirements while meeting all other system requirements. The practice of simply using more stringent heritage-derived stray light requirements and over engineering a system's stray light performance with sufficient margin is less feasible in the future as systems push theoretical and manufacturing limits (e.g. compact systems using freeform optics) [38]. It is evident that a method is needed to set stray light requirements based upon a clear quantitative linkage to the acceptable levels of stray light for user applications.

Beyond the challenge of stray light requirement definition and justification, a significant amount of stray light-related research focuses on characterizing a system's point spread function (PSF) through direct measurement [39–41], image analysis [1, 42–47], or mathematical modeling [36, 46, 48–52]. The characterization of a system's stray light performance through PSFs is intrinsically limited to near-field stray light, which originates from sources in or near a detector element's instantaneous field of view (IFOV), while ignoring far-field stray light originating from sources farther beyond the IFOV. Focusing on near-field stray light therefore almost entirely excludes stray light from sources outside of a system's field of view (FOV), which can scatter off mechanical components or optical component surface roughness and particulate contamination or undergo ghost reflections, thus resulting in significant stray light contributions at the focal plane. Several modeling techniques have been

presented that include out-of-FOV stray light sources for astronomical applications [53–56], but these have been applied to more restricted operational scenarios and scenes of interest. Other methods have used out-of-FOV stray light source mapping in conjunction with empirical weightings for post-processing stray light correction [57, 58].

The need remains to incorporate a system’s comprehensive susceptibility to stray light (i.e. near-field and far-field) in a predictive assessment of its Earth-observing performance imaging a scene of interest under a range of operational scenarios. With a sufficient solution, system trade studies and sensitivity analyses could then be conducted to quantitatively link detailed design parameters influencing an Earth-observing system’s stray light performance to their impact on user applications. This problem is not only limited to stray light, as there is a general systems engineering need to analyze the impact of specific optomechanical design parameters on user applications and to draft informed system requirements that minimize negative impact while optimizing cost.

In summary, the current state of stray light analysis for imaging systems is deficient in the following respects:

- Existing stray light analyses focus more on stray light requirement verification rather than validating that stray light levels meet user application needs.
- Existing stray light requirements lack sufficient quantitative justification traceable to user applications.
- Existing modeling and simulation techniques are inadequate to conduct end-to-end stray light-focused system trade studies or sensitivity analyses that quantitatively link system design parameters or decisions to user application impact when imaging realistic operational scenes.

From these deficiencies, it is apparent that an end-to-end stray light modeling and simulation capability is needed, where optomechanical design trade studies can be explored using system software models and the resulting user application impact of each system condition assessed on realistic operational scenes. This capability would lead to more informed system design decisions and the writing of stray light and system requirements with a direct understanding of user impact. Additionally, this capability would aid in testing stray light correction algorithms pre-mission, so that decisions could be made to either change the system design for improved stray light performance or to correct for the observed levels of stray light via post-processing.

The Digital Imaging and Remote Sensing (DIRS) Laboratory at the Rochester Institute of Technology (RIT) has a decades-long history of partnering with NASA and the USGS in researching technical areas of interest for the Landsat program. To address the needs presented here, we have developed a novel modeling and simulation-based methodology to integrate optomechanical system software models with a radiative transfer image simulation model that incorporates the rest of the imaging chain [59]. This capability enables users to assess the PSF and stray light performance of optomechanical system software models on high-fidelity simulations imitating realistic operational scenes [60]. The methodology first characterizes a system's PSF and stray light susceptibility through the collection of raytrace data from a 3-D computer-aided design (CAD) optomechanical system model using optical engineering software. This process is greatly enhanced by using optical engineering software's new graphical processing unit (GPU) raytracing capabilities. These raytrace data are then integrated with a radiative transfer image simulation model to simulate the imaging of a complex, highly-realistic scene description and evaluate the system's operational performance. Figure 1.2 highlights the role that each model plays in enabling this unique

software integration.

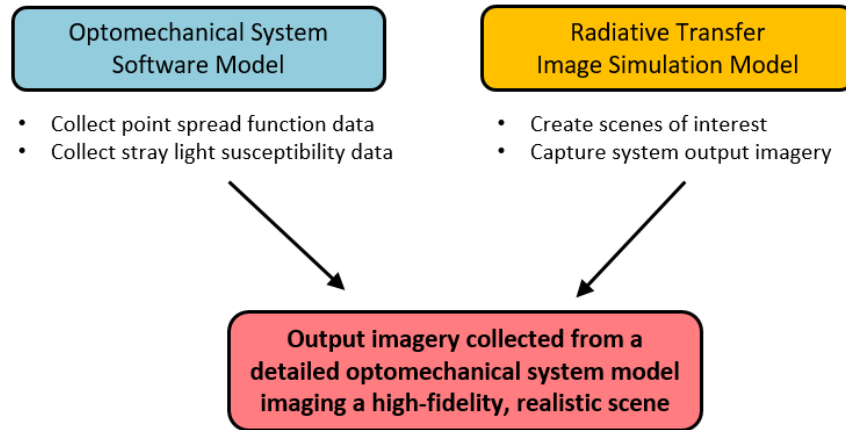


Figure 1.2: Integrating an optomechanical system model from optical engineering software with a radiative transfer image simulation model combines the unique benefits of each type of model in creating the complete imaging chain.

In the work presented here, we use FRED Optical Engineering Software [61] by Photon Engineering and the Digital Imaging and Remote Sensing Image Generation (DIRSIG) model [62], a physics-based scene creation and image and data simulation model developed at RIT, to validate and demonstrate the software integration method. However, our integration method generalizes *to any optical engineering software program* capable of collecting the necessary PSF and stray light raytrace data and *to any radiative transfer image simulation model* that can create physics-based scenes and incorporate the captured PSF and stray light performance data. Although stray light is the impetus for this research, the integration methodology is versatile and can be used to investigate other parameters of interest, including image quality, the effects of aberrations and distortions, tolerancing and alignment of optical and mechanical components, or degradation expected during a system’s operational lifecycle.

1.2 OBJECTIVES

We have defined a set of research objectives to address the needs and shortcomings of current stray light analysis, modeling and simulation capabilities, and requirement definition.

- Objective 1: Demonstrate a general methodology for integrating optomechanical system software models with a radiative transfer image simulation model.
- Objective 2: Validate the integration method's capability to accurately incorporate point spread function (PSF) performance data from an optomechanical system software model.
- Objective 3: Validate the integration method's capability to accurately incorporate stray light performance data from an optomechanical system software model.
- Objective 4: Demonstrate the integration method's system trade study capability using various system stray light susceptibility and scene conditions.
- Objective 5: Demonstrate how the integration method can be used to produce quantitative metrics that are useful in determining the impact of stray light on user applications.

1.3 DISSERTATION LAYOUT

1.3.1 Chapter 2: Background

This chapter provides an introduction to stray light, including its fundamental mechanisms, causes, and metrics, as well as the primary methods to analyze system stray light performance via building and testing or modeling and simulation. The importance of stray light

analysis within the system design process is emphasized and the capabilities of modern optical engineering software programs are reviewed. An overview of linear systems theory is provided to introduce necessary details regarding system imaging performance. Finally, previous efforts to model and simulate imaging system performance are discussed, focusing on those modeling stray light or using DIRSIG.

1.3.2 Chapter 3: Integration Methodology (Objective 1)

This chapter provides an overview of the integration method's basic radiometric framework, including a mathematical explanation of the PSF and stray light components. These two components are then discussed in terms of the specific data that must be collected from an optomechanical system software model to incorporate their contributions into the integration method. The collection and analysis of stray light performance data from an optomechanical system software model is demonstrated in order to better illustrate this key component of the integration method.

1.3.3 Chapter 4: Point Spread Function Component Validation (Objectives 1 & 2)

This chapter covers the details of the integration method's PSF component, including how PSF data can be collected from an optomechanical system software model. Two tests are presented to validate a method for using PSF data to image a scene within a radiative transfer image simulation model and to validate the successful incorporation of PSF data from an optomechanical system software model with a radiative transfer image simulation model.

1.3.4 Chapter 5: Stray Light Component Validation (Objectives 1 & 3)

This chapter includes several tests to validate the stray light radiometry of an optical engineering software program and the integration method itself. This provides confidence to users of the integration method that the stray light component can produce accurate stray light radiometry for an arbitrary system and scene.

1.3.5 Chapter 6: System Trade Study Demonstration (Objectives 1, 4, & 5)

This chapter presents an in-depth demonstration of the integration method's capability to perform a stray light-focused system trade study. This case study is performed using a Cassegrain telescope model and a coastal scene of southern California. Quantitative stray light metrics are presented and discussed in detail to provide insights into the application of the integration method for an arbitrary system and scene.

1.3.6 Chapter 7: Summary and Conclusions

This chapter summarizes the research motivation and objectives, the work that has been performed and its innovative contributions, presents final conclusions, and recommends future work.

1.4 NOVEL CONTRIBUTIONS

The novel contributions of this research include the following items:

- Development and validation of a general methodology for the integration of optomechanical system software models with a radiative transfer image simulation model.

- Validation of an importance sampling-based approach for emulating PSF convolution in-the-loop of a simulation performed using a radiative transfer image simulation model.
- Development and validation of a method to estimate the stray light irradiance of each detector element across the focal plane given an optomechanical imaging system's shift-variant stray light susceptibility and a scene's at-aperture radiance profile.
- Demonstration of optical engineering software's GPU raytracing capability to collect detailed shift-variant system stray light susceptibility data for use in conducting system trade studies.
- Introduction of simulated stray light irradiance images that include stray light contributions from all of object space for any combination of system stray light susceptibility and scene conditions.
- Introduction of detailed performance data that take into account both a system's stray light susceptibility and a scene's at-aperture radiance profile to determine the stray light contribution of specific components, ray paths, or scene elements.
- Demonstration of the integration method's capability to perform stray light-focused system trade studies using stray light-stressing remote sensing scenes in order to evaluate the impact of stray light on user applications.

Chapter 2

Background

This chapter is provided as a more in-depth examination of the fundamentals of stray light, linear systems theory, and the modeling and simulation of imaging systems.

2.1 RADIOMETRIC TERMS

It is important to define a few radiometric terms before delving into the discussion on stray light. The definitions presented here are consistent with internationally recognized standards [63], and these terms will be used throughout the background discussion and subsequent chapters. International System of Units (SI) measurements are listed in brackets [] for these quantities.

2.1.1 Radiant Energy

The energy of a single photon of light, q , is given by

$$q = h\nu = \frac{hc}{\lambda} \quad [\text{joules, J}], \quad (2.1)$$

where $h \approx 6.626 \times 10^{-34}$ J · s is Planck's constant, ν is the photon's frequency, $c \approx 2.998 \times 10^8$ m/s is the speed of light, and λ is the photon's wavelength [m]. It is apparent from Eq. 2.1 that shorter wavelength photons carry more energy than lower wavelength photons.

The total energy, Q , of a beam of light is a summation of the number of photons at each wavelength, calculated according to

$$Q = \sum q_i = \sum_i n_i h\nu = \sum_i \frac{n_i hc}{\lambda_i} \quad [\text{J}], \quad (2.2)$$

where n_i is the number of photons at each wavelength, λ_i .

2.1.2 Radiant Flux

It is often more useful to consider the rate at which energy impinges on a surface rather than the total energy deposited. The radiant flux, or power (Φ), is the energy flow to or from a surface and is the first derivative of the radiant energy with respect to time (t), i.e.,

$$\Phi = \frac{dQ}{dt} \quad [\text{watts, W}]. \quad (2.3)$$

2.1.3 Irradiance

In imaging systems, we are typically interested in the amount of radiant flux that is received by a certain area (e.g. a detector). This quantity is named irradiance (E) and is defined as

$$E = \frac{d\Phi}{dA} \quad [\text{W} \cdot \text{m}^{-2}]. \quad (2.4)$$

Although Eq. 2.4 is written as a differential quantity, it is important to note that irradiance can vary across a surface and therefore has an implicit spatial dependence, i.e. $E(x, y)$. The total radiant flux on a surface can be calculated by integrating the irradiance distribution over the surface area according to

$$\Phi = \int_{Area} E(x, y) dA \quad [\text{W}]. \quad (2.5)$$

If a source is not pointing directly nadir, but is tilted by an angle, θ , relative to the receiving object, then the projected area of the object must be used instead. This introduces a $\cos \theta$ factor, as given by

$$E_\theta = E_0 \cos \theta \quad [\text{W} \cdot \text{m}^{-2}]. \quad (2.6)$$

where E_θ is the irradiance on the projected surface and E_0 is the irradiance if the source were perpendicular to the surface. The irradiance over the projected area will necessarily be reduced, since the same incident radiant flux is spread over a larger area.

2.1.4 Radiant Intensity

Although irradiance details the amount of radiant flux per unit area, it provides no angular or directional information. In contrast, radiant intensity provides the angular dependence

of radiant flux with no spatial description. The angular dependence is described in terms of solid angle, which has units of steradians (sr), and is given by $d\Omega = dA/r^2 [\frac{\text{m}^2}{\text{m}^2} = \text{sr}]$, where dA can be thought of as the differential area projected onto a spherical surface of radius r . Radiant intensity is therefore defined as

$$I = \frac{d\Phi}{d\Omega} \quad [\text{W} \cdot \text{sr}^{-1}]. \quad (2.7)$$

2.1.5 Radiance

Radiance is a more complex quantity than those previously described, combining the spatial and angular dependencies of radiant flux into one term. Radiance is the flux per unit area per unit solid angle and is given by

$$L = L(x, y, \theta, \phi) = \frac{d^2\Phi}{\cos\theta \, dA \, \cos\sigma \, d\Omega} \quad [\text{W} \cdot \text{m}^{-2} \cdot \text{sr}^{-1}], \quad (2.8)$$

where θ and ϕ are the polar and azimuthal angles relative to the normal to the plane, respectively, and the $\cos\theta$ and $\cos\sigma$ factors are included to account for area projection effects of both the source and collector, respectively. Radiance is often used in radiometry due to its invariance over distance, assuming no transmission losses.

The radiant flux of a source with radiance L is calculated by integrating over both area and solid angle, i.e.

$$\Phi = \int_A \int_{\Omega} L(x, y, \theta, \phi) \cos\theta \, dA \, \cos\sigma \, d\Omega \quad [\text{W}]. \quad (2.9)$$

As with all of the other quantities defined in this section, radiance can have a spectral dependence. Spectral radiance, or the radiance rate of change with respect to wavelength,

evaluated at a specific wavelength is given by

$$L_\lambda = \frac{dL(x, y, \theta, \phi)}{d\lambda} = \frac{d^3\Phi}{\cos \theta \, dA \, \cos \sigma \, d\Omega \, d\lambda} \quad [\text{W} \cdot \text{m}^{-2} \cdot \text{sr}^{-1} \cdot \mu\text{m}^{-1}]. \quad (2.10)$$

Here we have deviated from strict usage of SI units to write the spectral radiance's wavelength dependence in terms of microns, μm . This is done because in optics wavelength is often measured in microns and this form more clearly expresses that distinction.

2.2 STRAY LIGHT

Stray light can be simply defined as unwanted radiation that reaches the focal plane of an optical system [17]. Stray light can affect optical systems used for a wide variety of applications, including astronomical and terrestrial remote sensing, medical imaging, head-mounted displays, and illumination. There are a number of general imaging scenarios that are particularly susceptible to stray light and its adverse effects. For example, stray light can be a significant problem when imaging high contrast scenes containing faint targets with bright sources nearby, as the stray light will reduce the image's contrast ratio, obscure the target signal, and possibly create false signals [64]. In remote sensing, this situation can occur when imaging areas of low reflectance (e.g. coastal water areas or boreal forest) that are adjacent to areas of high reflectance (e.g. bright beaches or snow), or when clouds are in or near the system's field of view (FOV) [18].

As is the case with the Landsat program, stray light is a particular concern when high-accuracy radiometric measurements are required, especially if the stray light is not well characterized and therefore cannot be easily compensated for through post-processing calibration. Users of Landsat imagery need the data to be radiometrically calibrated so that

the measured surface radiances represent the true Earth radiance. Stray light acts as a form of optical noise that obscures the actual Earth signal, thus leading to degraded scientific accuracy. In fact, the imagery may be completely unusable for certain scientific applications if the stray light contributions are a significant percentage of the measured radiances. Stray light can also cause adverse effects in high-energy laser systems, where even small amounts of stray light can damage hardware, in infrared systems which are susceptible to thermal self-emission of components, and in multispectral or hyperspectral systems which can suffer from spatial and spectral crosstalk between bands. In all of these susceptible scenarios, stray light can cause such problems that the system design is unable to meet its desired optical performance [64].

There are numerous examples of Earth-observing remote sensing systems that have suffered from stray light, often unexpectedly. The Sea-viewing Wide Field-of-view Sensor (SeaWiFS) and Moderate Resolution Imaging Spectroradiometer (MODIS) both suffered from unforeseen ghosting issues (a type of stray light that is spatially coherent with the source) that had to be corrected via post-processing [13, 31]. The Advanced Land Imager (ALI) instrument on NASA's Earth Observing-1 (EO-1), a technology demonstration satellite for Landsat 8's Operational Land Imager (OLI), experienced ghosting levels of 1% close to the edge of extended objects due to unexpected reflections. This 1% ghosting level amounted to a radiometric error of 16% when imaging a 5% reflectance target adjacent to an area with 80% reflectance, such as snow [65]. More recently, Landsat 8's Thermal Infrared Sensor (TIRS) suffers from a stray light issue caused by scattering off of a lens supporting structure [66]. The stray light manifests itself as a non-uniform banding artifact across Earth scenes and as a seasonal variation in absolute radiometric calibration error. Post-processing techniques have been developed to reduce the banding artifact magnitude

and absolute radiometric error to more reasonable levels [32, 58]. These examples highlight the importance of understanding a system's stray light performance early in the design process and the adverse effects that can result from unforeseen stray light issues.

2.2.1 Stray Light Paths

A light path is defined as the unique sequence of interactions that a beam of light undergoes as it propagates through an optical system. The designed optical path refers to the specific path the optical designer intended for light from object space to travel through the system, ending at the image plane. However, stray light is inevitable in any optomechanical system due to a number of physical mechanisms and leads to a large number of unintended light paths beyond the designed optical path. Although it is not possible to eliminate all of these unintended paths, it is important to reduce the total magnitude of stray light below the acceptable threshold for a given instrument and its user applications.

Stray light paths are characterized by their order, which refers to the number of stray light interactions that occur in the path [17]. For example, consider the stray light path shown in Fig. 2.1. Light leaves the sun, transmits through the first surface of a lens, ghost reflects off the second surface, ghost reflects off the first surface, and transmits through the second surface to the focal plane. This is a second-order path, since the two ghost reflections are stray light events. It is possible to have a zeroth-order stray light path (a "sneak path"), in which unwanted light directly illuminates the focal plane; this is usually the result of inadequate baffling of the optical system. The transmittance of a given path typically decreases as t^n , where t is a number less than 1 (due to reflections or transmissions) and n is the path order. Therefore, generally speaking, the lower a path's order, the more light it will transmit to the focal plane. The art of stray light control thus involves first

eliminating or reducing the contributions from lower order stray light paths and progressing to higher levels until the stray light requirement is met [17].

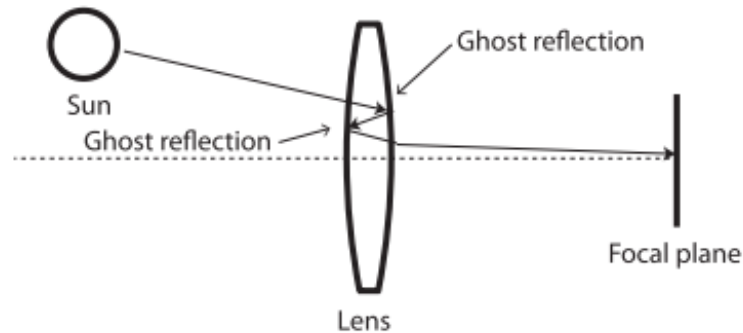


Figure 2.1: Example of a second-order stray light path [17].

2.2.2 Critical and Illuminated Surfaces

Somewhat counterintuitively, stray light analysis starts from the detector plane of an optical design. This is due to the fact that stray light arriving at the detector will have interacted with objects that the detector “sees”. It is important to include the full optomechanical system when considering the detector’s point of view, not each subsystem separately, so that all potential stray light paths are included [67]. A critical surface is defined as any surface that can be seen by the detector, while illuminated surfaces are those that are illuminated by a stray light source [17]. Critical surfaces are so significant in stray light analysis because all stray light must come from them; if a surface can not be seen by the detector, it will not contribute any stray light, even if it is heavily illuminated. Figure 2.2 shows an example optical system with the critical and illuminated surfaces labeled. All optical surfaces are typically critical in an optical system. Due to the importance of critical surfaces, unlike other users of optical systems, stray light analysts usually care more about

the scattering characteristics of an optical system's interior surfaces rather than the object field [68]. Optimum stray light design tries to eliminate the number of critical non-optical surfaces to reduce potential stray light paths [69]. Stops and baffles, conical or cylindrical objects used to block unwanted radiation paths, are often used to limit off-axis power on critical objects. Baffles are often outfitted with a series of concentric rings called vanes to further suppress stray light, as illustrated in Fig. 2.3.

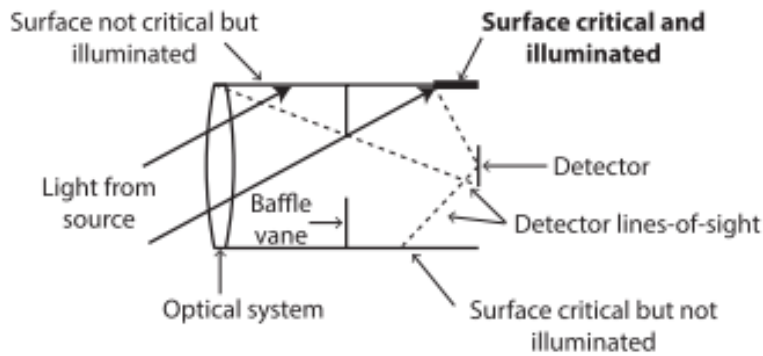


Figure 2.2: Optical system with critical and illuminated surfaces labeled [17].

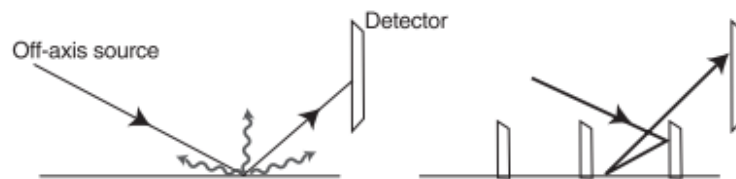


Figure 2.3: Off-axis source scatters off a critical baffle surface and to the detector (left). With vanes included, the light can now only reach the detector via multiple scattering, which greatly attenuates the stray light power (right) [67].

A surface must generally be both critical and illuminated in order for first-order stray light paths to exist (thermal self-emission stray light is an exception). An example of a first-order stray light path is shown in Fig. 2.2, where the baffle surface closest to the detector

is critical and illuminated, allowing light to propagate from the source to the detector after a single scattering event. First-order stray light paths are typically the largest sources of stray light. If these paths are eliminated, the total amount of stray light on the detector can often be decreased by two orders of magnitude or more [67].

2.2.3 In-Field and Out-of-Field Stray Light

Stray light that originates from sources located within a system's FOV is called "in-field" stray light, while stray light resulting from sources located outside the FOV is called "out-of-field" stray light [17]. In-field stray light often creates a halo-like profile around a point source, while out-of-field stray light leads to a diffuse, spatially-varying irradiance distribution across the focal plane. Ghost reflections like the one shown in Fig. 2.1 can be created by sources either within or outside of the FOV, though the sources in the out-of-field case are usually located very close to the edge of the FOV. Thermal self-emission of components in thermal imaging systems is another example of stray light that can be either in-field or out-of-field depending on the location of the self-emitting component.

2.2.4 Stray Light Mechanisms

As light propagates through an optical system, a number of physical mechanisms reduce the transmittance of the designed optical path and create unintended stray light paths. Stray light mechanisms can be categorized into one of two main categories: specular or scatter. Specular stray light is deterministic in nature, obeying either the law of reflection, Snell's law of refraction, or the grating equation. The law of reflection states that relative to the surface normal, a ray's angle of incidence, θ_i , will equal its angle of reflection, θ_r , i.e.

$$\theta_i = \theta_r. \quad (2.11)$$

Snell's law of refraction asserts that when a light ray travels through an interface between media with two different refractive indices, the angle of transmission, θ_t , is given by

$$n_i \sin \theta_i = n_t \sin \theta_t, \quad (2.12)$$

where n_i and n_t are the refractive indices for the incident and transmitting media, respectively, and θ_i is the angle of incidence. As with the law of reflection, both angles in Eq. 2.12 are referenced relative to the surface normal. Figure 2.4 illustrates the law of reflection and Snell's law of refraction for an incident ray. The ghost reflections off of the lens surfaces in Fig. 2.1 are examples of specular stray light mechanisms.

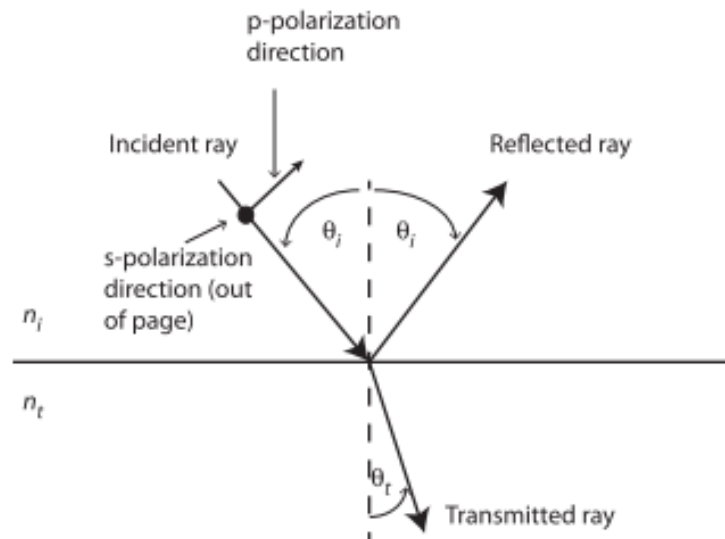


Figure 2.4: Specular reflection and refraction at an interface between two media [17].

Scatter mechanisms do not follow a deterministic equation, as a ray scattered from a surface can scatter into any direction. In reality, scatter will always be present, since light never undergoes a perfect specular reflection or transmission, even for highly polished optical surfaces. Scatter can have a significant impact on a system's stray light performance. A surface that diffusely scatters such that its radiance is independent of angle is said to be Lambertian. This means that the surface's apparent brightness is the same no matter what angle it is viewed from by an observer. Conversely, polished surfaces specularly reflect the majority of light, with a minimal amount of scattering centered around the specular direction. Most surfaces have scattering properties that lie somewhere between these two extremes [67].

2.2.5 Bidirectional Scattering Distribution Function (BSDF)

The scattering characteristics for a given surface can be described by the bidirectional scattering distribution function (BSDF), which relates the radiance of a scattering surface to the incident irradiance according to [70–72]

$$\text{BSDF}(\theta_i, \phi_i; \theta_s, \phi_s) = \frac{dL(\theta_i, \phi_i; \theta_s, \phi_s)}{dE(\theta_i, \phi_i)} \quad [\text{sr}^{-1}], \quad (2.13)$$

where dL is the differential radiance of the scattering surface, dE is the differential incident irradiance, θ_i and ϕ_i are the elevation and azimuth angles of the incident rays, and θ_s and ϕ_s are the elevation and azimuth angles of the scattered ray. Figure 2.5 displays each of these angles for an incident and scattered ray. In addition to being a function of the incident and scattered angles, BSDF is also a function of wavelength, polarization, and spatial position on a surface. Depending on the direction of the scattered light, BSDF can be split into two

separate components: the bidirectional reflectance distribution function (BRDF) and the bidirectional transmittance distribution function (BTDF). The BSDF will be greater than zero for any real surface and is a constant for a Lambertian surface (equal to ρ/π , where ρ is the surface's hemispherical reflectance).

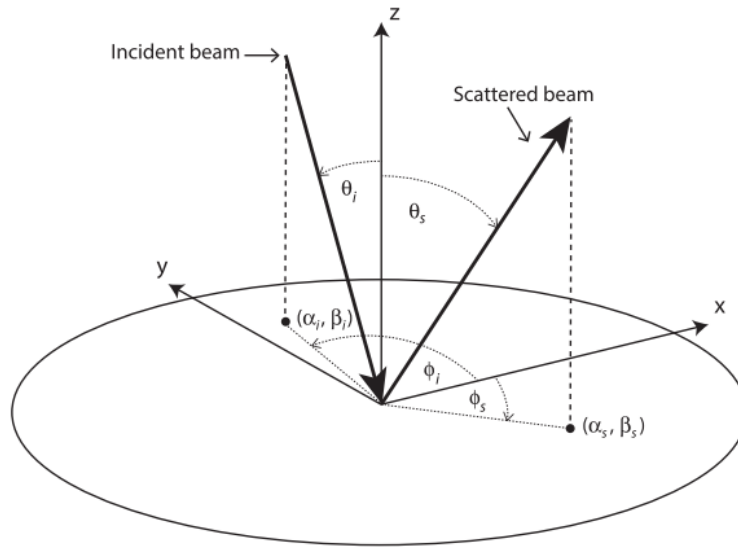


Figure 2.5: Incident and reflected angles used in describing a surface's bidirectional scattering distribution function (BSDF) [17].

It is important to accurately model the BSDF for the surfaces within an optomechanical system, since a system's stray light performance greatly depends on the BSDF of its components [17]. However, it is often very difficult to predict the BSDF of a particular surface to within more than a factor of two, especially with limited time and budget on a project [73]. Even estimating the uncertainty of a measured BSDF can be challenging with a limited number of measurements, given that BSDF can spatially vary over a surface. There is also a general lack of published BSDF data for surfaces commonly used in optical systems; in any case, taking sample BSDF measurements from the actual materials to be used in a

system will be more accurate than trusting a vendor's published BSDF information [17].

2.2.6 Stray Light Radiative Transfer Equation

Figure 2.6 shows the geometry for an incident ray scattering from a source area to a collector area. Starting with Eq. 2.8 and using this geometry, we can derive an important radiative transfer equation for stray light that specifies how much radiant flux is received by the collector.

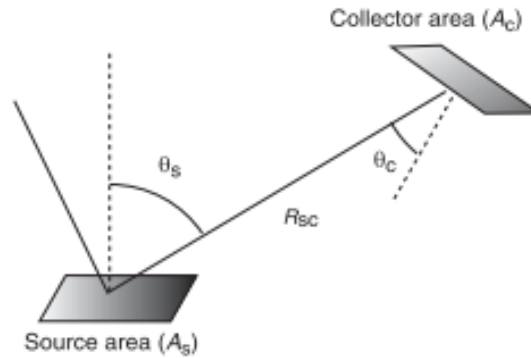


Figure 2.6: Geometry for scattering from a source area to a collector area [67].

$$L_s = \frac{d^2\Phi}{\cos\theta_s dA_s \cos\theta_c d\Omega} \quad (2.14)$$

$$d^2\Phi = L_s dA_s \cos\theta_s \cos\theta_c d\Omega \quad (2.15)$$

$$d^2\Phi = E_i dA_s \left(\frac{L_s}{E_i} \right) \cos\theta_s \cos\theta_c d\Omega \quad (2.16)$$

From Eq. 2.16, $E_i dA_s$ is simply the radiant flux incident on the source area, the quantity

$\left(\frac{L_s}{E_i}\right)$ is the source BSDF described in the previous section, and $\cos\theta_s \cos\theta_c d\Omega$ is the projected solid angle subtended by the collector as seen from the scattering source. The radiant flux on the collector can therefore be calculated by rewriting Eq. 2.16 as

$$\Phi_{collector} = \Phi_{source} \cdot \text{BSDF}(\theta_i, \phi_i; \theta_s, \phi_s) \cdot \Omega_{collector}. \quad (2.17)$$

The projected solid angle term, $\Omega_{collector}$, is often expressed in terms of a geometrical configuration factor (GCF) such that

$$\Omega_{collector} = \pi \text{GCF}_{collector}. \quad (2.18)$$

The GCF term is defined as

$$\text{GCF}_{collector} = \frac{A_c \cos\theta_s \cos\theta_c}{\pi R_{sc}^2}, \quad (2.19)$$

where R_{sc}^2 is the distance between the source and collector shown in Fig. 2.6. This term is independent of the source's incident radiant flux or scattering characteristics and only depends on the system geometry. The GCF has an important physical meaning in that if the source area were turned into a Lambertian emitter, then the fraction of the source's power incident on the collector would equal the GCF [67].

Equation 2.17 indicates that the scattered radiant flux transferred from one surface to another is proportional to the flux incident on the source area, the scattering characteristics of the source, and the geometrical relationship between the source and collector. The stray light performance of a system ultimately depends on only the multiplication of these three factors on a surface-by-surface basis. This result is significant for stray light control because

reducing or eliminating any of these factors will directly limit the amount of stray light received at the detector plane.

The third term, $\Omega_{collector}$, is the only factor that can be reduced to zero in Eq. 2.17. Although tilting the source and collector surfaces or increasing the distance between them will reduce this quantity, it can be eliminated altogether by either moving the collector surface out of the scattering surface's FOV or by placing a stop or baffle to block the line of sight between the two surfaces. Equation 2.17 therefore reveals the mathematical justification for why stray light analysis starts from the detector plane; by blocking off as many direct paths of unwanted radiation to the detector plane, the number of surfaces that are both critical and illuminated is reduced, along with the total amount of stray light. These “move it” and “block it” techniques can also be successfully applied to moving or blocking surfaces so that they are not illuminated, which prevents unwanted radiation from propagating deeper into the system in the first place [64].

The second term, $BSDF(\theta_i, \phi_i; \theta_s, \phi_s)$, can be reduced by painting, coating, or smoothing surfaces to reduce scatter or by applying anti-reflective coating on lenses to reduce ghost reflections. Many stray light analysts make the mistake of focusing first on this term by attempting to paint mechanical surfaces with the lowest scattering material or coat optical surfaces with the lowest-reflectance coating without knowing the true impact on stray light performance [64]. However, BSDF has angular, spatial, and wavelength dependence and can never go to zero like the collector solid angle as seen from the scattering surface [68]. This is not to say that reducing the BSDF term is not wise; if done with a proper understanding of the system, painting or coating critical surfaces or cleaning surfaces to remove particulate contamination can all greatly mitigate scatter and improve system stray light performance.

2.2.7 Stray Light as Noise

It is evident from Eq. 2.17 that for any given moment in time, the stray light flux received by each detector element at the focal plane is dependent on the radiant flux of all sources of stray light, along with the geometric relationship of every surface included in stray light paths. With this level of complexity, it can be quite difficult to know how much of the radiant flux received by each detector element is from stray light paths and how much is from the designed optical path for every possible imaging scenario. During an exposure, photons from a target object travel along the designed optical path and are collected by the detector wells along with stray light photons. These photons then generate electrons based on the quantum efficiency (QE) of each detector element, while thermally-generated detector dark current add additional electrons. The average number of dark current electrons can be subtracted from the total number of electrons in each well if the detector temperature is known, leaving a Johnson noise component due to the statistical variance of the dark current [74]. However, unless the target or stray light fluxes are well characterized for the specific imaging scenario, the exact number of stray light electrons per detector well remains unknown. Consequently, the stray light contribution for each detector well can not be subtracted and it remains as a bias noise that can significantly degrade performance [74].

2.2.8 Causes of Stray Light

Stray light can be caused by a number of different factors, including optical surface roughness, scratches or digs on optical surfaces, particulate contamination, residue left from cleaning, mechanical support structures and baffles, and aperture diffraction [75]. This section provides a brief overview of a few of these primary causes of stray light.

Scattering from optical surfaces and coatings

The grinding and polishing process for optical surfaces leaves residual surface roughness and subsurface damage that can cause scattering, along with cosmetic imperfections such as scratches and digs. Figure 2.7 provides a visualization of the marks left on a fused silica surface due to polishing and grinding. It can be rather difficult to model the surface roughness *a priori* since the exact profile depends on the manufacturing process.

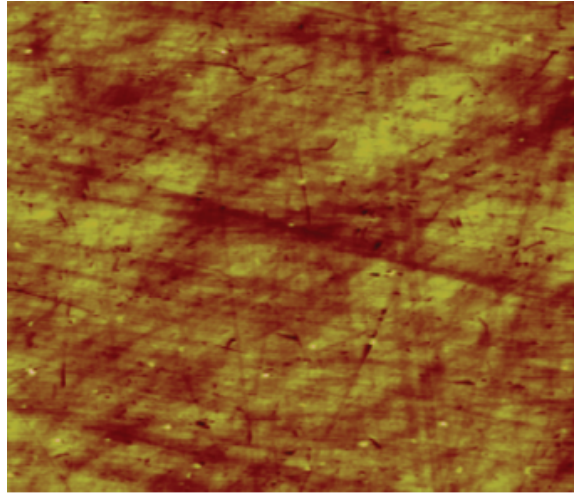


Figure 2.7: Microscope image of surface roughness on a fused silica surface due to grinding and polishing. The image is approximately 10 μm across, with an RMS surface roughness of 5 \AA [76].

Surface roughness profiles are most commonly specified according to their root-mean-square (RMS) variation in surface height, σ_{RMS} , which is typically on the order of 10^{-10} meters, i.e. angstroms (\AA) [67]. Power spectral density (PSD), which describes a surface's spatial frequency content, can also be used. Coatings that are added to an optical surface after manufacturing will increase the surface's roughness, along with altering its PSD profile and BSDF. The total integrated scatter (TIS), the ratio of the total scattered power to

incident power, scales as $(\sigma_{RMS}/\lambda)^2$ (where λ is the incident light's wavelength) for surfaces whose RMS surface roughness is much less than the wavelength of incident light [73, 77]. This indicates that shorter wavelength light will scatter exponentially more than longer wavelengths due to surface roughness.

As discussed in §2.2.5, the BSDF for a given surface can be a complicated function of incident and reflected angles, spatial position, and wavelength. It can therefore be convenient to use models to approximate the BSDF distribution in a functional form. The Harvey-Shack model [78, 79] is commonly used to describe the BSDF of smooth optical surfaces ($\sigma_{RMS} \ll \lambda$) over 2π steradians and is an empirically-derived function of the vectors β and β_0 , as defined in Fig. 2.8. The first vector, β , is the projection of the unit vector in the scattering direction onto the tangent plane, while the second vector, β_0 is the projection of the unit vector in the specular direction onto the tangent plane. This means that $\beta = \sin \theta$ and $\beta_0 = \sin \theta_0$, where θ and θ_0 are the scattered and specular reflection angles, respectively.

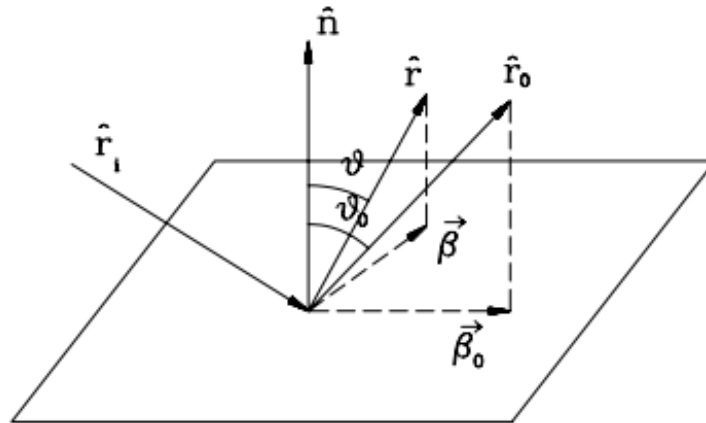


Figure 2.8: Vectors used in the Harvey-Shack scatter model [80].

The mathematical form of the Harvey-Shack scatter model is given by

$$\text{BSDF}(\beta, \beta_0) = b_0 \left(1 + \left(\frac{\beta - \beta_0}{L} \right)^2 \right)^{S/2}, \quad (2.20)$$

where L describes the location of the knee of the curve (typically between 0.0001 and 0.01 radians from specular), b_0 is the peak of the curve at $|\beta - \beta_0| = 0$, and S is the slope of the curve (typically between -0.5 and -2), as shown in Fig. 2.9 [81]. From this functional form, it is evident that scattered light from optical surface roughness is typically a Lorentzian angular distribution centered around the specular reflection direction [19]. The Harvey-Shack model is inherently linear shift-invariant since it is independent of the incident direction (i.e. it assumes an isotropic surface) and only a function of the difference $|\beta - \beta_0|$ between the specular and scattered rays. The model is also wavelength invariant, though limited wavelength scaling can be used with caution [81].

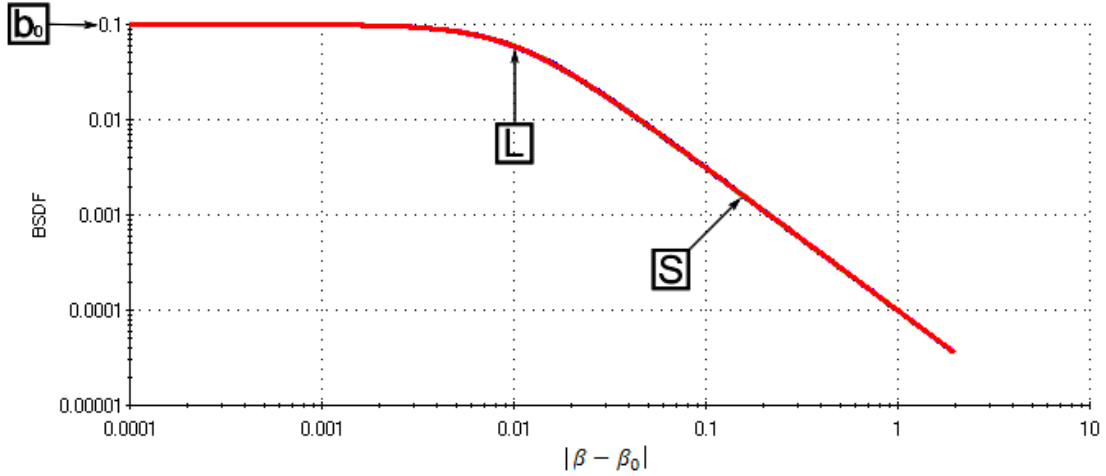


Figure 2.9: Example Harvey-Shack scatter model curve with $L = 0.01$, $b_0 = 0.1$, and $S = -1.5$. Assuming $\lambda = 0.55 \mu\text{m}$, these parameters correspond to an approximate surface roughness of $\sigma_{RMS} = 14.7 \text{ \AA}$ [81].

Scattering from particulate contaminants

All surfaces contain some level of particulate contamination (e.g. dust) that adds to the scattering from surface roughness. The type of clean room used for processing, the duration of exposure, and the geometric orientation of the optics all impact the amount of particulate contamination collected by the optical surfaces. In fact, for large optics, it is very difficult to keep the dust coverage areal fraction below a few percent [67]. Without regular cleaning, the amount of particulate contamination will only increase over time, leading to a two-fold harmful degradation; the increased particulates lead to a decrease in light on the designed optical path, while stray light levels rise due to the increased in-FOV scattering [38, 82]. Similar to optical surface roughness, particulate contamination also scatters out-of-FOV light into a system's FOV, further increasing levels of stray light.

The BSDF for particulate contamination is strongly based on $f(D)$, the particle density function, which details the projected area density of the particulate distribution as a function

of particle diameter, D [17]. The calculation of BSDF from $f(D)$ is done using Mie scatter theory [83–85]. The cleanliness level for optical surfaces is most widely defined according to the Institute of Environmental Sciences and Technology (IEST) CC1246D standard, which is derived from the now discontinued U.S. military specification MIL-STD-1246C [86, 87]. IEST-STD-CC1246D specifies the number of particles N_p (per 0.1 m^2) that have diameters greater than or equal to D according to [17]

$$N_p(S, CL, D) = 10^{|S|([log_{10}(CL)]^2 - [log_{10}(D)]^2)}, \quad (2.21)$$

where S is the particle distribution slope, CL is the cleanliness level of the surface, and D is the particle diameter in μm (the standard is only valid for $D \geq 1 \mu\text{m}$). Figure 2.10 shows example plots of N_p for CLs 200, 400, and 600 using the default particle distribution slope of -0.926 , which is representative of cleaned surfaces. For these cases, the cleanliness corresponds to the particle size in microns for which there is one particle per 0.1 m^2 (e.g. CL400 has one 400- μm particle per 0.1 m^2). The particle distribution slope is dependent on the specific environment to which an optical system is exposed and the specific cleaning processes used. The act of cleaning a surface will reduce the particle distribution slope, S , since the larger particles will be removed while the smaller ones remain [17]. The total amount of scatter from particulate contamination does not have a strong wavelength dependence for most typical particle density functions, so surface roughness will generally dominate below wavelengths of $2 \mu\text{m}$, whereas particulate contamination scatter will dominate above $2 \mu\text{m}$ [17]. The percent area coverage (PAC) is a metric based on a surface's cleanliness level that is used to describe what percentage of the surface is covered by particulates. This

is given by [17]

$$\text{PAC} = 10^{K+|S|[\log_{10}(D)]^2}, \tag{2.22}$$

where CL is the surface's cleanliness level and $K = -7.245$ if $|S| = 0.926$.

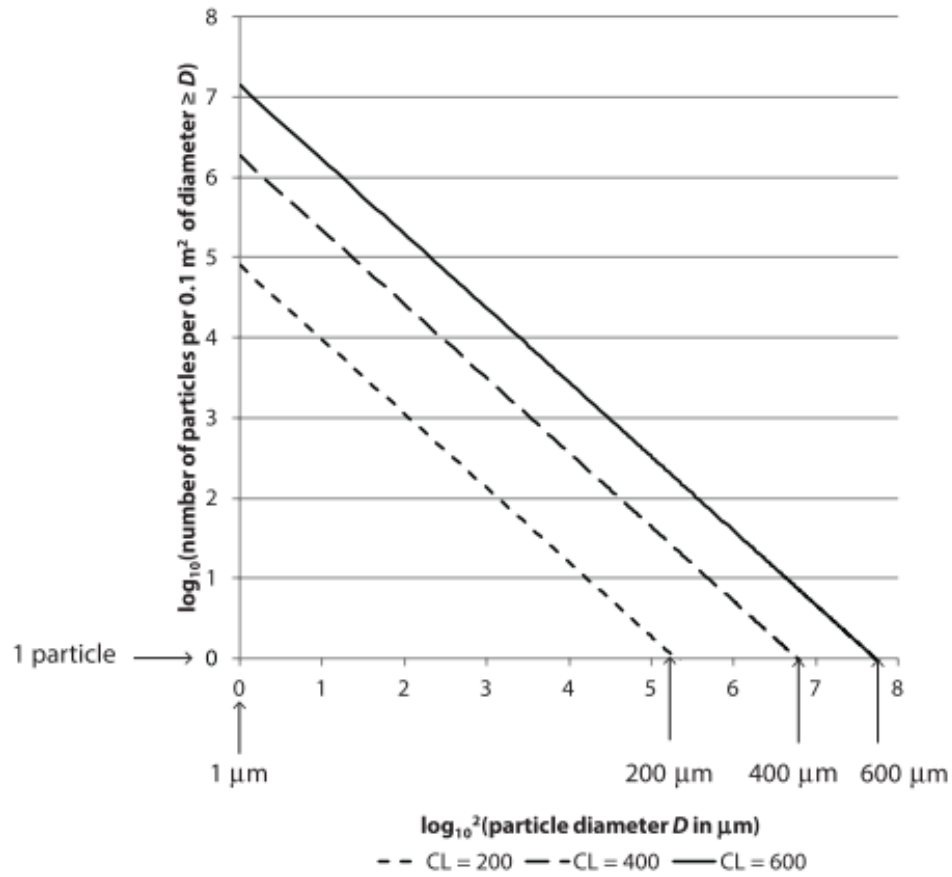


Figure 2.10: Number of particles of diameter $\geq D$ v. D according to IEST-STD-CC1246D for CLs 200, 400, and 600 [17].

Scattering from black surface treatments

Applying black surface treatments to reduce scatter and absorb light is one of the primary methods of stray light control for mechanical surfaces. This method is typically used for mechanical components near the optical path, such as baffles, vanes, struts, lens mounts, struts, stops, and sunshades. The closer these components are to the detector plane, the more imperative it is to control their scattering properties. Although reducing the scattering from mechanical surfaces can improve stray light performance, this will not overcome stray light performance deficiencies due to poor optical design or baffle placement [17]. Whereas optical surfaces are finely polished to reduce scatter, black surface treatments aim to minimize scatter by using highly absorbing materials, using dendrites or cavities to trap light, or by using particles to diffusely scatter incoming light. Anodized aluminum and Aeroglaze[®] Z306 [88], an absorptive polyurethane coating designed for application on substrates used in aerospace applications, are two of the most common black surface treatments. Note that surfaces that are “black” (i.e. have low scatter) in one spectral regime may not be black in other spectral regions, so care must be taken to use proper black surface treatments for a system’s operational waveband(s).

Figure 2.11 shows an example of how dendrites, such as those in anodized aluminum, are used to trap light. Note that less light is trapped for higher angles of incidence due to the shadowing effect; this increases the surface’s specularity and TIS for higher incidence angles, though this effect can be minimized through proper baffle placement and vane design [67]. The BRDF of black surface treatments can be difficult to predict *a priori* due to the differences in application method, environment, and chemistry, as well as the variability in dendrite or cavity structure, so direct measurements at a series of incident

angles are often the most useful [17].

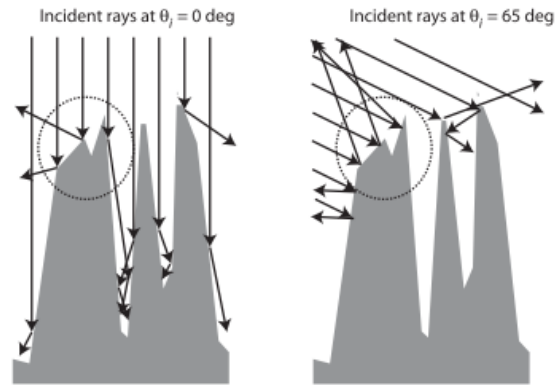


Figure 2.11: Example of how dendrites can be used to trap light. The angles of incidence are defined according to the macroscopic surface normal and not the variable dendrite profile. [17].

Aperture diffraction

Diffraction theory describes the relationship between a scene's electric field profile and the electric field distribution at the image plane [89]. Diffraction technically creates stray light, since it redirects light from its nominal path to undesired locations on the focal plane. Given the proportional relationship between diffraction and wavelength, it is not typically a major stray contributor in the ultraviolet (UV) or visible, but can be a significant factor in the longwave infrared (LWIR) [19]. The impact of diffraction on a system's PSF will be covered in more detail in the linear systems theory discussion in §2.3.

2.2.9 Stray Light Metrics

There are a number of quantitative metrics that can be used to compare the stray light performance of optomechanical imaging systems, the same system under different conditions,

or to write stray light performance requirements.

Point source transmittance

Point source transmittance (PST) is a transfer function relating the amount of stray light irradiance on the focal plane to the irradiance incident at a system's entrance aperture. PST is one of the oldest stray metrics and is known by a few other names, including normalized detector irradiance (NDI) and point source normalized irradiance transmittance (PSNIT) [68, 74]. The equation for PST is given by

$$PST = \frac{E_{SL}}{E_i}, \quad (2.23)$$

where E_{SL} is the stray light irradiance on the focal plane and E_i is the irradiance incident on the entrance aperture (or first optical element for systems without a clearly defined entrance aperture). This measurement can be performed by creating a collimated source of light (i.e. a point source located at infinity) that is incident at the entrance aperture and calculating the PST for a series of input angles. Since PST is an irradiance ratio rather than a power ratio, it is independent of the detector size and can therefore be used to compare the stray light performance of instruments of different sizes without scaling. Note that PST is simply an irradiance ratio for a given input angle and contains no explicit information about the stray light irradiance distribution on the focal plane.

PST is useful as a diagnostic tool to identify angles contributing unacceptable levels of stray light, which can inform a stray light analyst on which stray light mechanisms may be causing problems and where to focus mitigation efforts [19]. PST is often a strong function of the angle between the optical axis and the stray light source, so a number of

angles must be tested across the entrance aperture to characterize a system's stray light performance. Rotationally-symmetric systems can be tested in only one input plane, but systems with asymmetries due to their optical design, struts, etc. will need to have their PST measurements repeated across several different planes. Only a finite number of input angles can be tested even when taking these additional measurements, so there is always the risk that a significant unexpected stray light artifact is missed using this technique [90].

Veiling glare index

Veiling glare index (VGI) is a metric typically used to quantify the stray light performance of optical systems operating in the visible wavelength regime. VGI is given by

$$VGI = \frac{E_{out}}{E_{out} + E_{in}}, \quad (2.24)$$

where E_{out} is the stray light irradiance on the focal plane from Lambertian radiance outside the system's FOV and E_{in} is the irradiance on the focal plane due to the same Lambertian radiance inside the FOV [91]. As shown in Fig. 2.12, a special scene is created for this test consisting of a broad Lambertian screen with a black target that exactly subtends a system's FOV. The scene is illuminated with a bright source and the irradiance on the focal plane (E_{out}) is then measured with the black target in place. The black target is then removed, revealing a white, uniform Lambertian screen and the focal plane irradiance is measured again ($E_{out} + E_{in}$). VGI scenes can also be created with a target that is smaller than the FOV or a circular target with a background annulus, so it is important to understand the exact scene used when assessing this metric.

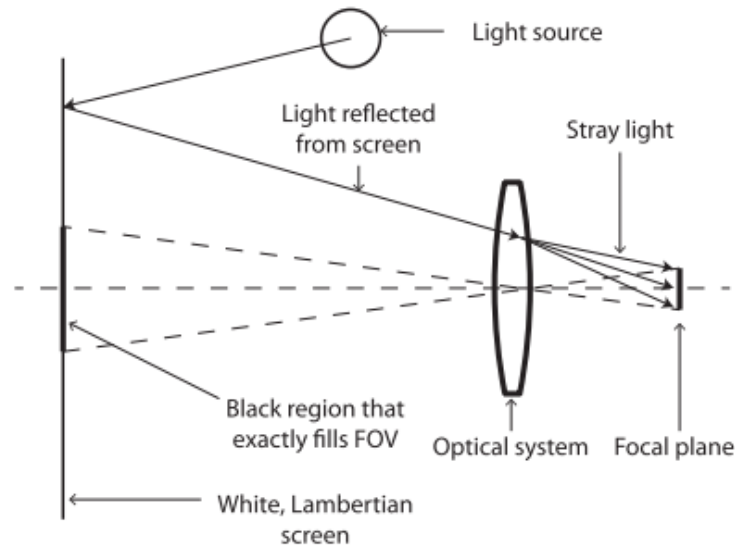


Figure 2.12: Setup used for a veiling glare test [17].

Percent stray light

Percent stray light is a single number that characterizes the stray light performance of a system. It is calculated by taking the ratio of the optical noise power from every stray light mechanism to the signal power of the intended target [19]. Therefore, it can be thought of as a reciprocal signal-to-noise ratio (SNR) measurement, though this metric does not include other photon- or electronics-induced noise effects. Although this metric will never go to 0% for any real system, a percent stray light of a few percent is typical for a well-baffled system [19].

Noise equivalent irradiance and delta temperature

All detectors have electronic noise due to a number of factors, including shot noise, Johnson noise, readout noise, etc. The magnitude of these combined noise factors can be specified by noise equivalent irradiance (NEI), which is the minimum irradiance on the detector that can be detected with the given sensor noise level. Noise equivalent delta temperature (NEDT)

is the synonymous term for infrared systems, i.e. the minimum temperature difference in the scene that can be discerned in the presence of the sensor noise. Both of these metrics can be used as a unit of measure when quantifying stray light irradiance levels (e.g. the stray light irradiance was $15 \times \text{NEI}$) [17].

2.2.10 Stray Light Requirements

Establishing stray light requirements for an imaging system is essential for optimal system performance. Setting a requirement for no stray light is not feasible since stray light inevitably exists in every system, whereas not setting a maximum limit will very likely lead to less than desirable results due to excessive levels of stray light. The specific stray light requirement set for any given system can be a complex balancing act between system performance, size, cost, complexity, time, etc. and requires an intimate knowledge of the system's purpose. In general, the more strict a stray light requirement is, the more expensive the necessary mitigation solutions will be to implement and the more difficult it will be to test. Once a stray light requirement is set, the systems engineering process flowchart displayed in Fig. 2.13 can be used to iteratively build a stray light system software model and assess the performance of both the software model and as-built system.

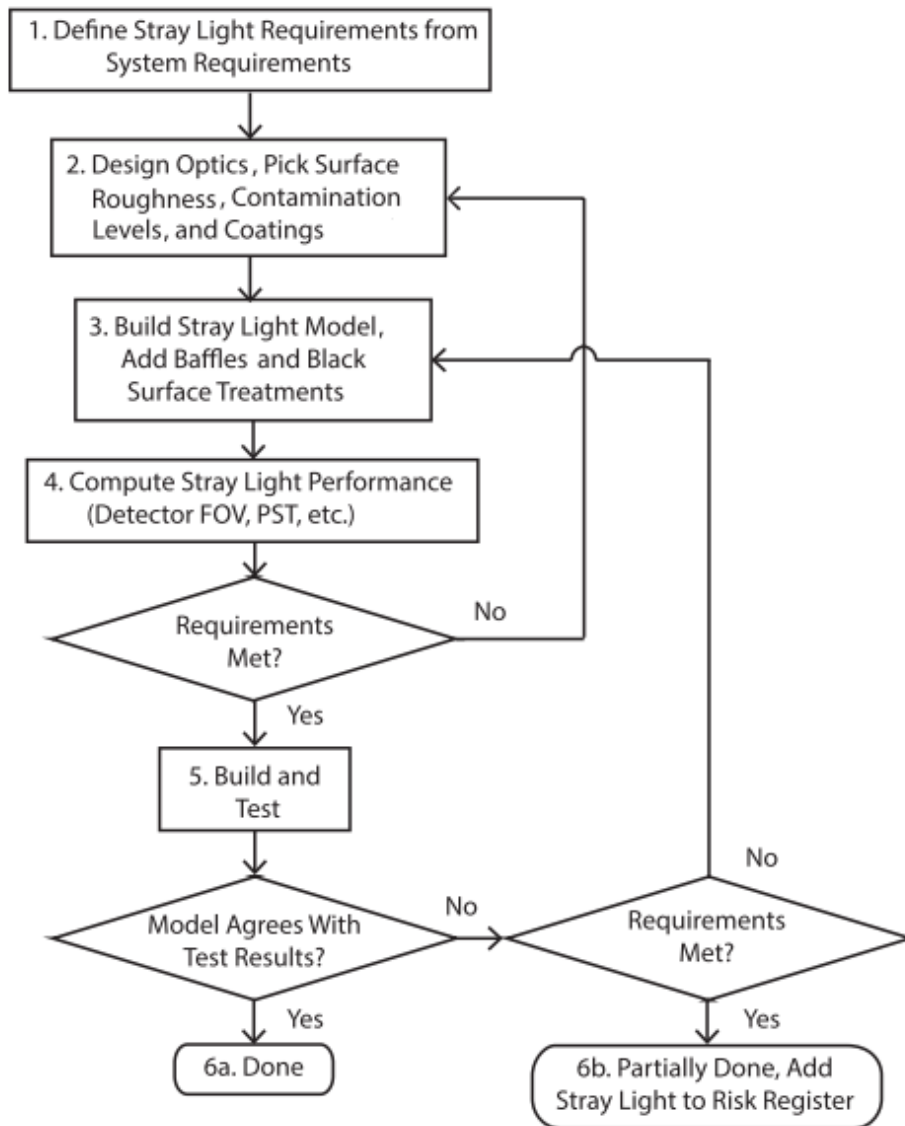


Figure 2.13: Stray light systems engineering flowchart illustrating the necessary steps from stray light requirements definition to final system build and model validation [17].

There are several different ways in which to define stray light requirements for a system, including relative radiometric measurements such as PST or VGI, or in absolute terms like the maximum allowed image plane stray light irradiance. PST is a design- and point

source-based requirement, since it defines a system's stray light performance at specific input angles, and can offer more control if operational conditions dictate required levels of stray light performance at particular off-axis angles. VGI on the other hand is an image- and extended scene-based requirement, which does not depend on which components or input angles are causing the stray light, only relying on how input radiance from a larger scene is translated to stray light at the focal plane. This provides an instrument designer with more control over the allocation of how much stray light specific components contribute to the focal plane and does not limit a system to a particular design type, albeit at the loss of the angular fidelity of the PST definition. Another common method is to set the maximum allowed image plane stray light irradiance requirement to the system's minimum detector irradiance, so that the stray light signal is below the detector noise level. This is usually accompanied by an exclusion angle requirement, which defines the minimum angle at which the maximum allowed image plane stray light irradiance requirement is met, since stray light irradiance on the detector typically increases as the source angle to the optical axis decreases [17]. Stray light requirements can be specified for the entire detector or for different detector regions, effectively limiting the stray light's spatial distribution to avoid sharp irradiance edges that can cause problems with image processing algorithms [17].

Stray light requirements can be divided into two main categories: near-field and far-field. Similar to the discussion of in-field and out-of-field stray light in §2.2.3, the near field describes stray light that originates near a given pixel's instantaneous field of view (IFOV), which is the angle subtended by a single detector element. The near field is generally considered to extend from the center of a pixel's IFOV out to 6–100 IFOV, whereas the far field lies beyond this angular extent [1]. Near-field stray light requirements are often defined in terms of an acceptable edge-response slope, which details how much a system will blur a

high-contrast edge in the scene. This performance metric depends on a system's PSF, which is mathematically detailed in §2.3. Efforts to model a system's PSF are further described in §2.4.1. Far-field stray light requirements include the PST and VGI-based requirements previously discussed, while maximum allowed image plane stray light irradiance includes both near-field and far-field stray light.

Since it can be very difficult to know how to quantify the specific stray light requirements for a given optomechanical system, heritage requirements are often used instead. If a new system's design is similar to a previous one, it can be easier to use heritage-derived requirements, than to define what level of stray light performance is actually needed for the new system. At best, setting stray light requirements in this manner runs the risk of overspecifying the necessary stray light requirements, leading to additional costs and delays. In the worst case scenario, the new system may actually require more stringent stray light performance and the heritage-derived requirements will not be sufficient, resulting in possible redesign of the entire system or else running the risk of a dissatisfied user community. In fact, in the case where the heritage-derived stray light requirements are more strict and the new system design is inherently more susceptible to stray light, it may not even be possible to meet the new requirements. This is more likely to be the case in the future as systems push the theoretical and manufacturing limits (e.g. compact systems, systems using freeform optics, etc.) [38]. It is clear that a method is needed to set more educated system stray light requirements that are based upon a clear quantitative linkage to the acceptable stray light levels for user applications, an issue this research aims to address.

The Landsat program provides an illustration of the growing importance of stray light requirements. Although the earliest Landsat missions applied good stray light control practices, no formal far-field system-level stray light requirements were set. It was not until the

development of the second-generation of Landsat satellites in the late 1970s (Landsat 4 and 5) that much consideration was given to the stray light performance of the Landsat imaging sensors [1]. Since that time, the only stray light performance characterizations for the majority of the Landsat imaging systems have been conducted using modeling. A notable exception to this has been the two Landsat 8 instruments: the Operational Land Imager (OLI), which is a multispectral instrument with bands in the visible, NIR, and SWIR, and the Thermal Infrared Sensor (TIRS), with two bands in the long-wave infrared (LWIR). Both of these systems were subjected to hardware stray light tests in addition to software modeling.

Stray light requirements have been better defined since the earliest Landsat missions, driving the need for testing and modeling efforts both pre-launch and on-orbit [1]. The Landsat far-field stray light requirements have typically been defined according to a veiling glare measurement, where the signal measured in the center of a dark circular region (radius of 0.25°) shall not change by more than a small percentage of the brightness difference when compared to a brighter surrounding annular region (radius of 25°). Although similar types of operational targets can be envisioned (e.g. a dark lake surrounded by brighter land), this is an extremely difficult requirement to test and provides limited insight into the expected levels of stray light for a given scene. Consequently, this stray light requirement for Landsat 8 OLI was allowed to be verified by analysis using component and subsystem data, along with system stray light modeling and the superposition of test data [18]. The entire assembled Landsat 8 flight telescope (minus the flight FPAs), was placed in a stray light facility and the system's PST was measured. These test results led to adjustments of the optomechanical system software model, which was used to verify the veiling glare requirement [18,92].

2.2.11 Critical Step in Design Process

The stray light performance of an optomechanical system depends on many different factors, including the optical system design, the mechanical design, the system's thermal characteristics, and the scattering and reflectance properties of the critical surfaces, so it is imperative to consider stray light performance early in the design process [68, 93]. Design decisions made early on are much more expensive to change later in the development process and it is too costly to conduct parallel studies based on an initial design [68]. In addition to the expense, it may not even be possible to add piecemeal stray light mitigation solutions to a design after it has reached a mature stage. Thus the necessity to control a system's stray light performance imposes basic design constraints on a system's first-order optical configuration that ensures it can meet its specified SNR requirements.

However, there is an unfortunate tendency to think only about the light we want, not the light we do not want, i.e. stray light [82]. This may be somewhat understandable since the light we want is more predictable (i.e. following the designed optical path), but stray light analysis can often be easy to neglect. Stray light mitigation hardware such as baffles are often not included in the original system software model since they are not required for initial image quality analysis, but it is crucial to include these features when conducting system stray light modeling and analysis [17].

2.2.12 Stray Light Analysis

There are two distinct methods for conducting stray light analysis: build and test or model and predict [68]. These methods have distinct advantages and disadvantages and can complement each other when performed correctly.

Building and testing involves first constructing the optomechanical system and then testing its stray light performance. If the as-built system is tested in its intended operational environment and performs satisfactorily, then it has passed the ultimate test [68]. However, it is often difficult if not impossible to test a system within its operational environment, so lab-based tests are performed instead. Although these tests are useful in better understanding the system's stray light performance, the test configuration and equipment can negatively or positively bias the results. These tests are also rarely designed to provide information about stray light propagation paths or what surfaces are contributing the most stray light; however, these are the details that are needed to drive stray light performance improvements [68]. As previously mentioned, any system modifications that must be made at this point in development will generally be high cost and may not be able to fully correct any issues found. That being said, experimental tests should be performed, but their limitations must be recognized. PST-based tests can be conducted on the as-built system with the angles tested near the optical axis being the most crucial. Stray light is typically attenuated less at these angles so the stray light noise will generally be much higher than the detector noise, while at off-axis angles the stray light signal may not be detectable.

The modeling and prediction method involves creating a software model of the optomechanical system and using an optical engineering software program to analyze the system's stray light performance. This is a key tool in risk reduction during system development and requires a firm grasp of the primary mission objective and the derived system requirements. The allowable trade space must be fully understood, since cost-benefit decisions must often be made in balancing stray light reduction and other competing requirements [38]. Major advances in computing power over the past few decades have greatly improved the ability to conduct raytraces with ever-increasing numbers of rays, providing more accurate stray light

results [38]. An optomechanical software model can also be used to more easily conduct system trade studies or sensitivity analyses on parameters of interest, or possibly explore alternate designs. This is likely the first time in the project that a full system model has been created, so the model can now serve as a system validation tool [38]. Since optical engineering software programs used for stray light analysis provide detailed ray path and surface information, the specific stray light problem areas in a system can be quickly identified and possible solutions developed. These recommended system improvements can then be incorporated into the overall system design before hardware production and assembly takes place, leading to large cost and schedule savings. The time spent conducting stray light modeling and analysis will be a valuable investment, especially for large projects.

Despite the many benefits, stray light modeling has its limitations as well. An optomechanical software model will not include every single component or detail of a complex system design; after all, it is only a model of the real system. Not including all of the relevant mechanical hardware can be a particular problem for stray light analysis. Due to time and budget constraints, only the optical components and a few of the major mechanical components might be included in a software model. However, if the more minor mechanical hardware components cause the worst stray light paths, these effects will never be seen in the stray light modeling analysis. The optomechanical system model can therefore only capture the performance of the components actually included in the model. System models are also created with precisely-sized, assembled, and aligned components, whereas the real-life manufacturing and assembly processes will inevitably result in errors, leading to differences between the software model and the as-built system. As previous discussed in §2.2.8, it can be very difficult to define the BSDF properties for surfaces and coatings *a priori*, so the scattering properties included in the system model will only be approximations. Performing

stray light modeling early on in the development process may be a challenge because many of the optical and mechanical design decisions have not been made yet; conversely, stray light analysis may be useful in informing those decisions [38]. Only a limited number of rays can be used when conducting raytraces with the system model compared to performing real-world tests on the as-built system, leading to potential differences in results. Large software models can also have large run times when conducting raytraces. Finally, user error in inputting system details or running the raytraces can lead to additional errors in analyzing a model's stray light performance. Since stray light is such a niche field in the optical engineering community, there simply are not many qualified, experienced stray light analysts [38]. Due to any number of these factors, the stray light software analysis may miss significant stray light paths that are present in the as-built system.

For optical designers, it would be considered quite unacceptable to perform image quality analysis of an optical design based on modeling and then not test the system once it is built [68]. However, given the improvements in stray light modeling, there is often the temptation to forgo hardware testing. Some program managers even refuse to perform stray light modeling, arguing that the schedule will not allow for any delays [38]. Nevertheless, as summarized in Fig. 2.14 the build-and-test and model-and-predict methods for conducting stray light analysis have complimentary strengths and weaknesses. For best results, both methods should be employed to gather the most comprehensive and accurate information about a system's stray light performance.

- The ability to assign scatter models to surfaces, representing surface roughness, particulate contamination, black surface treatments, or coatings. Measured BSDF or PSD surface data can also often be imported. This information is not usually included in the original mechanical CAD or image quality analysis models and so must be specified in the stray light analysis program [17].
- The ability to define coating reflectance and transmittance properties.
- The ability to model light from a variety of sources, including monochromatic or polychromatic, coherent or incoherent, and polarized or unpolarized.
- The ability to perform non-sequential raytraces, in which the physical properties of the geometry determine how rays propagate through a system.
- The ability to incorporate ray importance sampling, where only the scattered rays propagating to areas of interest are traced, providing better radiometric statistics and computational efficiency.
- The ability to collect detailed information about each individual ray path in a raytrace, which is especially useful when analyzing stray light paths.
- The ability to capture irradiance and radiant intensity distributions over regions of interest.
- The ability to write scripts that can automate the collection and analysis of raytrace data.

2.3 LINEAR SYSTEMS THEORY

In order to fully comprehend the validation tests and demonstrations presented in subsequent chapters, it is necessary to provide an overview of linear systems theory, including linear shift-invariant systems, linear shift-variant systems, the point spread function (PSF), and the modulation transfer function (MTF) [89, 99].

2.3.1 Linearity

A system can be described as a general operator, \mathcal{O} , that maps an input to an output. For an imaging system, these inputs and outputs can be real or complex-valued functions of a two-dimensional independent space variable at the entrance aperture and image plane. The output function $g[x, y]$ is therefore related to the input function $f[x, y]$ according to

$$\mathcal{O}\{f[x, y]\} = g[x, y]. \quad (2.25)$$

In order to solve many imaging problems, two useful restrictions can be placed on the general system operator, \mathcal{O} : linearity and shift-invariance. It is important to keep in mind that these restrictions are idealizations, since no realistic system is truly linear or shift-invariant. Linearity refers to the action of a system on the amplitude of a weighted sum (superposition) of input functions, $f_n[x, y]$, whose individual output functions are $\mathcal{O}\{f_n[x, y]\} = g_n[x, y]$. The general linearity criterion is then given by

$$\begin{aligned} \mathcal{O}\{a_1 f_1[x, y] + a_2 f_2[x, y]\} &= a_1 \mathcal{O}\{f_1[x, y]\} + a_2 \mathcal{O}\{f_2[x, y]\} \\ &= a_1 g_1[x, y] + a_2 g_2[x, y] \end{aligned} \quad (2.26)$$

where a_n are generally complex-valued constants. This statement indicates that a linear system acting on the weighted sum of input functions will have the same result as the sum of the system acting on each input function individually. The primary advantage of linearity is that the response of a system to an arbitrary input can be expressed as the linear combination of the system's response to a series of elementary functions into which the input has been decomposed [89]. An appropriate decomposition of an input function can be found using the sifting property of the Dirac delta function, which states

$$f[x, y] = \int_{-\infty}^{+\infty} \int_{-\infty}^{+\infty} f[\alpha, \beta] \delta[x - \alpha, y - \beta] d\alpha d\beta = f[x, y] * \delta[x, y], \quad (2.27)$$

where $*$ is the convolution operator and $\delta[x, y]$ is the Dirac delta function, defined as

$$\delta[x, y] = 0, \quad \text{for } x \neq 0 \text{ or } y \neq 0 \quad (2.28)$$

and

$$\int_{-\infty}^{+\infty} \int_{-\infty}^{+\infty} \delta[x, y] dx dy = 1. \quad (2.29)$$

Equation 2.27 shows that the input function $f[x, y]$ is simply a linear combination of weighted and shifted Dirac delta functions. With this new expression for $f[x, y]$ we can now rewrite Eq. 2.25 as

$$g[x, y] = \mathcal{O} \left\{ \int_{-\infty}^{+\infty} \int_{-\infty}^{+\infty} f[\alpha, \beta] \delta[x - \alpha, y - \beta] d\alpha d\beta \right\} = \mathcal{O}\{f[x, y] * \delta[x, y]\}, \quad (2.30)$$

It is apparent from Eq. 2.30 that $f[\alpha, \beta]$ is a weighting factor applied to $\delta[x - \alpha, y - \beta]$. Using the linearity property from Eq. 2.26, the system operator can be moved inside of the

integral to operate on the individual Dirac delta functions. Equation 2.30 then becomes

$$g[x, y] = \int_{-\infty}^{+\infty} \int_{-\infty}^{+\infty} f[\alpha, \beta] \mathcal{O}\{\delta[x - \alpha, y - \beta]\} d\alpha d\beta = f[x, y] * \mathcal{O}\{\delta[x, y]\}. \quad (2.31)$$

2.3.2 Point Spread Function (PSF)

We can denote $h[x, y]$ as the system's response at point $[x, y]$ of the output space to a Dirac delta function input at $[\alpha, \beta]$ of the input space by writing

$$h[x, y] = \mathcal{O}\{\delta[x - \alpha, y - \beta]\}. \quad (2.32)$$

The function h is known as the system's impulse response or, within an optics context, the system's point spread function (PSF). Using the PSF expression, Eq. 2.31 becomes

$$g[x, y] = \int_{-\infty}^{+\infty} \int_{-\infty}^{+\infty} f[\alpha, \beta] h[x - \alpha, y - \beta] d\alpha d\beta = f[x, y] * h[x, y]. \quad (2.33)$$

Equation 2.33 is known as the superposition integral, since it highlights the fact that a linear system can be completely described by the superposition of its responses to unit impulses. For an imaging system, this means that the output image for an arbitrary input scene can be determined simply by knowing the system's response to point sources located anywhere in the input space. The PSF therefore effectively describes the combined action of a system's components (lenses, mirrors, stops, struts, etc.) upon each of these point sources. Equation 2.27 shows the result for a perfect imaging system, i.e. one where the output image exactly replicates the input scene (ignoring the system's magnification). In this ideal case, the PSF is a Dirac delta function. In reality, aberrations, diffraction, and stray light will ultimately degrade the PSF in an optical system. This means that a point

source will not produce a point of light on the image plane; the PSF degradations will blur the point of light, create asymmetries, add diffraction rings or streaks, etc. that all act to distort the point source's irradiance distribution on the image plane.

2.3.3 Shift-Invariance

Shift-invariance implies that the system operator is independent of the absolute position of the input, i.e. a shift in the input function produces a corresponding shift in the output function. Mathematically, this means that given Eq. 2.25, then

$$\mathcal{O}\{f[x - x_0, y - y_0]\} = g[x - x_0, y - y_0] \quad (2.34)$$

for all x_0 and y_0 . This allows the system's impulse response to be written in a shift-invariant form, as shown in Eq. 2.32. For an imaging system, this indicates that the image of a point source changes only in location, not in functional form, for any point source in the object space.

2.3.4 Linear Shift-Invariant and Linear Shift-Variant Systems

Equation 2.33 provides the output for a linear, shift-invariant (LSI) imaging system, in which the output image is a convolution of the input scene with a single system PSF that does not change across the system's FOV. This approximation is often made for the purposes of simplification. However, in general, imaging systems are shift-variant, meaning that the PSF will change for point sources across the system's FOV and a different $h[x, y]$ must be used for each pair of spatial coordinates in Eq. 2.33. This is due to the fact that aberrations, diffraction, and stray light are typically a function of field angle. Despite this shift-variant

nature, the object field can often be divided into small regions called isoplanatic patches, over which the system is approximately shift-invariant. The system output is then the combination of the PSF for each isoplanatic patch convolved with its own unique small object field region. In addition to shift-variance, a system's PSF response is also a function of wavelength. Imaging systems can exhibit nonlinear responses as well, where the PSF is a function of the input radiance level.

2.3.5 Modulation Transfer Function (MTF)

The modulation transfer function (MTF) is a useful metric for analyzing the frequency response of a system and is found by computing the normalized magnitude of the system PSF's Fourier transform, given by

$$MTF[\xi, \eta] = \frac{|\mathcal{F}\{PSF[x, y]\}|}{\int_{-\infty}^{+\infty} \int_{-\infty}^{+\infty} PSF[x, y] dx dy} = \frac{\left| \int_{-\infty}^{+\infty} \int_{-\infty}^{+\infty} h[x, y] e^{-2\pi i(\xi x + \eta y)} dx dy \right|}{\int_{-\infty}^{+\infty} \int_{-\infty}^{+\infty} h[x, y] dx dy}, \quad (2.35)$$

where ξ and η are the spatial frequency domain variables and x and y are the spatial domain variables [89]. MTF provides information about the image quality of a system, since it describes the ability of a system to reproduce the spatial modulation of the scene. The MTF for an imaging system can also be written as

$$MTF[\xi, \eta] = \frac{E_{max}[\xi, \eta] - E_{min}[\xi, \eta]}{E_{max}[\xi, \eta] + E_{min}[\xi, \eta]}, \quad (2.36)$$

where $E_{max}[\xi, \eta]$ is the irradiance at the focal plane due to the maximum radiance of content in the scene with spatial frequencies ξ and η , while $E_{min}[\xi, \eta]$ is the irradiance at the focal plane due to the minimum radiance of the same spatial frequency content [17]. For a perfect

optical system, $E_{min} = 0$ and therefore $MTF = 1$. Stray light acts to degrade a system's MTF such that E_{min} is increased to $E_{min} + E_{SL}$, where E_{SL} is the additional stray light irradiance. This serves to reduce the contrast of an output image, as shown in Fig. 2.15.

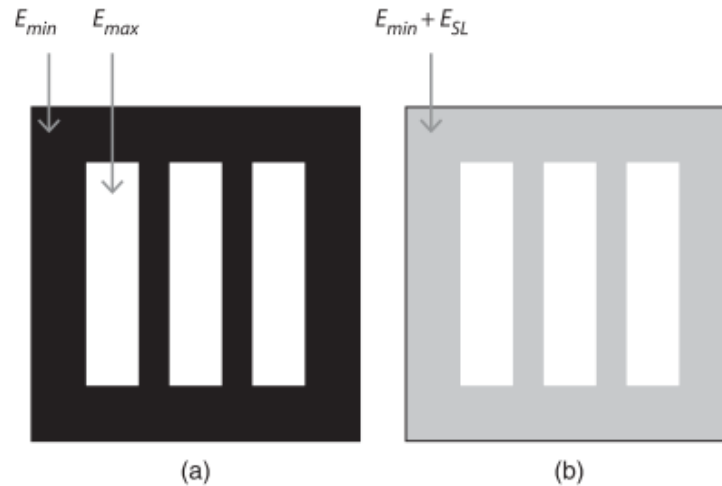


Figure 2.15: Image of a bar target (a) without stray light and (b) with stray light. Stray light acts to reduce the contrast of the bar target. [17].

2.4 MODELING AND SIMULATION OF OPTOMECHANICAL SYSTEMS

Modeling and simulation play critical roles in the development of remote sensing systems [100] and offer a unique systems engineering solution for understanding the quantitative linkage between system trade studies and their effects on user applications. During system development, optical engineers use software programs such as Zemax OpticStudio [94], CODE V [95], and OSLO [96] to create and optimize optical designs, and programs like FRED [61], ASAP [97], and TracePro [98] for more complete optomechanical system

analysis. Optical engineering software is particularly adept at modeling intricate optomechanical system details and producing data to characterize a system's imaging performance, including its MTF and stray light susceptibility.

With a focus on user end products, the remote sensing community employs forward modeling approaches using radiative transfer image simulation models during phase A/0 [101, 102] of system development to simulate synthetic data and assess system performance. Some of these models are end-to-end simulators (e2eS) [103, 104] for specific missions, such as the EnMAP end-to-end Simulation (EeteS) [105], the Sentinel-2 end-to-end Simulation (S2eteS) [106], the FLuorescence EXplorer end-to-end simulator (FLEX-E) [107], and the Selex Galileo (SG) simulator [108]. Other image and data simulation models are more general, including the Digital Imaging and Remote Sensing Image Generation (DIRSIG) model [62, 109–112], the Discrete Anisotropic Radiative Transfer model (DART) [113–117], the Software Environment for the Simulation of Optical Remote sensing systems (SENSOR) [118], the Parameterized Image Chain Analysis & Simulation Software (PICASSO) [119], MC-Scene [120], and the Advanced Modeling of the Earth for Environment and Scenes Simulation (MATISSE) [121]. These types of models incorporate the rest of the imaging chain [59] to varying degrees, including scene radiometry, vehicle motion and jitter, focal plane read-out effects, etc. The synthetic data they produce are not only useful for testing surface parameter retrieval algorithms and as a source of labeled training data for training deep learning networks, but they are also an invaluable resource for conducting system trade studies. However, integrating optomechanical system model performance data from optical engineering software with a radiative transfer image simulation model would greatly expand the number of optomechanical design parameters that can be analyzed compared to the system attributes already included in the image and data simulation models. This type

of novel end-to-end model integration would allow for system developers to view flight-like imagery in the design phase in order to predict and correct design parameters with a significant user application impact, thus avoiding the unfortunate task of developing costly and time-consuming reactive solutions after system assembly.

Much of the modeling and simulation work currently performed for optomechanical systems can be split into two categories: optical design or image analysis. Optical design modeling and simulation uses optical engineering software programs to analyze a specific system's optical design and verify that the system's imaging performance meets its requirements. On the other hand, image analysis modeling and simulation typically involves one of two approaches: (1) creating a virtual environment and using a parameterized model (e.g. PSF, effective focal length, FPA dimensions, pixel pitch, etc.) of an optomechanical system to simulate imaging performance, or (2) using or testing image processing algorithms to extract meaningful data for a given user application from either synthetic imagery generated by a parameterized optical system model or real imagery captured by an operational imaging system. While both optical design and image analysis modeling and simulation are successful in many ways, there is often minimal connection between the two. There is currently a capability gap that would allow for design changes to be made to a detailed 3-D CAD optomechanical system model and the resulting impact assessed on a realistic operational scene, particularly for stray light-related trade studies.

In this research, we demonstrate and validate an integration method that uses imaging performance data from an optomechanical system model to image high-fidelity scenes of operational environments created using a radiative transfer image simulation model. The following sections provide a general overview of previous system modeling and simulation efforts focused on stray light, along with an introduction to the DIRSIG model and its

capabilities.

2.4.1 Overview of PSF and Stray Light Modeling Efforts

One of the primary ways to analyze an imaging system's nominal or stray light performance is through the measurement or modeling of its PSF. No real-world system has a perfect Dirac delta function PSF, meaning that a significant portion of the signal recorded in a given detector element often originates from locations outside of the detector element's IFOV. The contributions from beyond a detector element's IFOV ultimately hinder the ability of users to extract meaningful surface information from images on a per-pixel basis [122]. A system's PSF can be used to verify certain spatial characterization and near-field stray light requirements, produce simulated imagery to analyze the system's expected imaging performance given an arbitrary scene, or post-process operational imagery to correct for the PSF's degrading effects. In regards to the second usage, image simulators are commonly developed during the design phase of imaging system acquisitions and take into account the system's PSF, detector characteristics, and flight path or orbital information [55]. This is especially important for space-based systems, which are typically very expensive with little to no opportunity for making system adjustments after launch.

To better understand the history and current state of optomechanical system modeling and simulation, particularly those efforts focused on characterizing stray light performance, it is once again necessary to distinguish between near-field and far-field stray light. The difference between the two and the importance of this distinction for stray light requirement definition is discussed in §2.2.10. The distinction is also critical for modeling and simulation purposes, since near-field and far-field stray light are typically created through different physical mechanisms and affect different aspects of a system's imaging performance. Near-

field stray light originates from sources in or near a pixel's IFOV and therefore depends on diffraction effects, aberrations, focus, the scattering properties of the system's optical surfaces and their associated particulate contamination, and any mechanical structures located in the way of the designed optical path (e.g. secondary mirror support struts) [1, 123]. The proximity of components to the focal plane affects the spatial distribution of the near-field stray light contributions due to optical surface and mechanical structure scattering effects. The scatter from components farther away from the focal plane will generally be distributed more uniformly across the system's FOV, while those components that lie closer to the focal plane will contribute more narrowly peaked scatter distributions [123]. It is important to note that a PSF only includes near-field stray light, since it measures a system's response to point sources in the FOV and is analyzed over a spatially-limited region surrounding the PSF peak.

Conversely, far-field stray light originates farther from a given pixel's IFOV and is impacted by optical surface roughness and particulate contamination scattering, baffle geometry, material properties, and black surface treatments, as well as any other critical surfaces with their associated specular and scattering properties [1]. Far-field stray light can be subdivided into diffuse stray light due to scatter which produces an overall diminished image contrast, and ghosting, which creates more localized irradiance peaks that often appear as spatially-displaced weaker images of the target [1]. Optical surface manufacturing has improved over the past several decades, along with the quality and effectiveness of cleanliness controls and black surface treatments, leading to better far-field stray light performance. Far-field stray light performance remains one of the most challenging criterion to verify via testing, although improvements in stray light modeling and simulation have led to better characterization of far-field stray light performance. It is often easier to measure, model, or

estimate a system's PSF than to extensively analyze its far-field stray light performance, so it should be no surprise that the majority of previous stray light modeling efforts have focused on PSF characterization. It is also commonly assumed that if a system is adequately baffled, the far-field stray light will be reduced to acceptable levels and more attention should be paid to the system PSF. Of course, this may be an invalid assumption if unforeseen stray light paths exist.

PSF Modeling Efforts

Three primary methods exist to estimate a system's PSF: direct measurement, image analysis, and mathematical modeling [48, 124]. Direct PSF measurement is an attractive option since the actual system hardware can be used along with all of its (hopefully minimal) assembly errors, real BSDFs, etc. and the full 2-D PSF is produced, but unfortunately this is often very difficult in practice. It is impossible to create a true point source since the source would have to be infinitely small in spatial extent, so any attempt to measure a system's PSF will only be an approximation. Furthermore, it is difficult to use a source with a high enough radiant intensity so that the low-signal broad wings of the PSF are above the detector's noise floor, while not saturating the pixels near the PSF peak [125]. The fact that a low source intensity leads to low SNR in the PSF wings is not only a challenge for lab-based measurements, but also when trying to use a natural source like a star [45]. Despite these difficulties, high dynamic range techniques have been attempted to make direct PSF measurements more practical [41].

The image analysis method consists of imaging an in-scene target either before or during a mission to determine the system's PSF. Three different types of scene elements can be used to estimate the system's PSF: an impulse characterized by a narrow-width 1-D contrast

difference, a step function with an abrupt change in contrast between two adjacent regions, or a rectangular pulse with a contrast change along two dimensions [42, 44]. Use of an impulse is a good option since it directly provides the shape of the PSF. Bridges or roads can be used as a target, but it can be difficult to find a discontinuity that is narrow enough to be approximated as an impulse; if the impulse is too wide, the resulting PSF will also be too wide. Landsat 7 successfully used images of the Lake Pontchartrain Bridge in Louisiana to assess the on-orbit PSF and MTF performance of its Enhanced Thematic Mapper Plus (ETM+) multispectral scanning radiometer, revealing degradation in several of the bands over the mission lifetime [1].

The most common means to estimate a PSF is using a step function in the scene, the so-called “knife-edge” method [1, 126]. This method can be implemented pre-mission, but is also extensively used to characterize the PSF of operational systems. The edge spread function (ESF) measures a system’s response to an edge that is oriented either horizontally or vertically and provides a 1-D integration of the system’s PSF along the given dimension (this is similar to the edge-slope requirement previously discussed in §2.2.10) [45]. Taking the derivative of the ESF produces a line spread function (LSF) in an easier manner than imaging an actual line, since edges are generally more prevalent than line targets in imagery. Assuming the overall PSF is separable, the PSF becomes the product of the LSFs along the x and y dimensions,

$$\text{PSF}(x, y) = \text{LSF}(x) \cdot \text{LSF}(y). \quad (2.37)$$

The knife-edge method can be especially beneficial for systems where the PSF is unknown and cannot be modeled, since in this case the PSF is empirically measured [127]. On-orbit systems can use a wide variety of natural and man-made objects as suitable edge

targets, such as coastlines and field boundaries. For example, McGillem et al. [42] estimated the PSF of Landsat 4's Thematic Mapper (TM) multispectral scanning instrument using field boundaries from imagery of rural Iowa in order to analyze the system's post-launch spatial resolution. Pre-launch LSFs have also been generated for all the Landsat sensors dating back to the beginning of the program and used to model the system PSFs [1, 43]. The knife-edge method can be more challenging to implement for thermal systems due to the difficulty in finding sufficiently sharp edge targets and the generally large IFOVs for sensor thermal bands, but several coastline locations in the Middle East and northern Africa have been successfully used for on-orbit PSF/MTF estimations of Landsat 8 TIRS [45]. For astronomical imaging, transits of the solar limb by the Moon, Venus, or Mercury can provide a sufficient boundary for estimating a system's PSF [46, 47, 128, 129].

It should be noted that the image analysis PSF estimation method only measures the PSF along two axes and makes the assumption that a system's PSF is rotationally symmetric, while real PSFs can have significant anisotropic components. Furthermore, the estimated PSF is assumed to be shift-invariant unless measurements are made across the sensor's FOV. In reality, the system's PSF response may have significant shift-variant dependencies across the FOV.

Mathematical modeling is the third major method used to estimate a system's PSF. Many of these techniques involve parametrically modeling the PSF as a finite summation of basis functions, with Gaussian functions being one of the most common functional forms. Yang et al. [48] propose first measuring a remote sensing system's LSF along the cross-track and along-track directions using the knife-edge method and then fitting 1-D Gaussians to each LSF in an effort to improve the accuracy of the PSF estimation. Cui et al. [50] conducted a spatial aliasing and spectral band requirement sensitivity study for future

Landsat missions using DIRSIG by modeling Landsat 8 OLI's cross-track LSF as a super-Gaussian and its detector and along-track LSFs as rectangle functions. Yeo et al. [46] successfully used a sum of five Gaussian functions whose amplitudes vary sinusoidally with azimuth to correct for stray light effects and improve granulation contrast in solar imagery captured by the Solar Dynamics Observatory's (SDO) Helioseismic and Magnetic Imager (HMI). For digital still imagery applications, Bitlis et al. [36] have developed a method to correct for stray light by modeling the PSF as a rotationally-invariant combination of two separate components: a Gaussian kernel that takes into account imperfections such as diffraction and aberrations and a scatter component that derives its form from the BRDF. The overall function resembles a 2-D Gaussian, Cauchy, or Voight function and is shift-variant across the system's FOV. Harvey et al. [49] use a similar approach to predict the image degradation due to scattering in a two-mirror extreme ultraviolet (EUV) system by dividing the PSF into four components in order to describe the specular (direct) and scattering interactions off of each mirror. Near-field stray light is especially important for short-wavelength applications where the surface roughness, σ_{RMS} , is not necessarily much less than the wavelength of light; using a wavelength of 93.9 Å, Harvey et al. [49] found that less than 20% of the total energy reaching the focal plane was in the specular beam (direct-direct component) for their EUV system, while 32% of the energy resided in the scattered-scattered component. In an extension of this work, Choi and Harvey [51] lay out the mathematical framework to describe a multi-element imaging system's PSF as the convolution of its geometrical PSF due to aberrations and the BRDFs of the individual surfaces, achieving a nearly identical PSF to that calculated via raytracing with optical engineering software.

While the shift-invariant PSF assumption is commonly used, shift-variant PSFs provide

a more accurate representation of the system's performance and may be required for certain systems with significant PSF variations across the FOV or for applications requiring high precision. Aberrations, misalignment, and differing stray light paths can cause a system's PSF to change significantly within the FOV. Achatzi et al. [41] present an experimental process for measuring the shift-variant PSFs of high-dynamic range cameras, where the broad stray light wings of the PSF are more likely to rise above the noise floor, greatly influencing image quality and limiting the achievable dynamic range [130]. Digital photography is another application area that often requires spatially-varying PSFs, so Wei et al. [52] have developed an efficient means to implement space-varying convolution using matrix source coding and modeled shift-variant PSFs. The structure of the PSF across the system's FOV also plays a major role for adaptive-optics (AO) systems due to the increasing error of the atmospheric correction farther away from the guide star's location. Lauer [131] addresses this problem for astronomical imagery by decomposing the shift-variant PSFs into basis functions with weighting factors and using the iterative Lucy-Richardson deconvolution algorithm to restore the images [132, 133]. Optical engineering software can also be used to measure a system's shift-variant PSFs across the focal plane.

Once a system's shift-invariant PSF or shift-variant PSFs have been estimated using any of the above methods, output imagery can be corrected for the effects of near-field stray light. The errors introduced by stray light contributions can be non-trivial, negatively impacting data both spatially and spectrally. For example, clouds over the ocean are a major problem for MODIS on board NASA's Aqua satellite, with half of the ocean pixels flagged for spatial stray light contamination. Applying the modeled MODIS Aqua PSF to artificial test scenes, it was found that the stray light contributions 10 km from a large cloud increased measured top-of-atmosphere (TOA) radiance levels significantly, from 1%

for band 11 (531 nm) up to 3% for band 13 (667 nm) [134, 135]. These are significant errors compared to the MODIS uncertainty requirements of 5% in radiance and 2% in reflectance [136]. Hardware tests with commercial charge-coupled device (CCD) cameras have also shown that spatial stray light can impact an instrument's radiometric calibration by up to 3.7% [137].

Several classical image restoration methods have been used to correct imagery, including Wiener filtering, regularized filtering, and the Richardson-Lucy algorithm, which all require an estimation of the system's PSF from one of the above methods. Many of the correction methods rely on deconvolution, assuming the system is LSI, though shift-variant PSF corrections do exist. Other stray light correction algorithms attempt to measure the statistical variations in pixel values to determine the stray light contributions on a per-pixel basis [138].

Spectrometers present a unique stray light case due to the spatial and spectral dimensional nature of their FPAs. Stray light can be the dominant source of error in a scientific-grade spectroradiometer, as spatial stray light can create a halo effect around bright objects, while stray light in the spectral dimension leads to the reduction of contrast in spectral features and error in surface reflectances [139, 140]. Stray light errors can be particularly significant when the instrument is measuring a target source which varies considerably from the calibration source [141]. Stray light correction of spectrometers typically rely on measuring a system's spectral line spread functions (SLSFs) using lasers. Stray light will broaden the wings of the SLFs due to scattering off of the grating, order-sorting filters, and other system components [139]. These SLSFs are then used to derive a stray light distribution function (SDF), a type of correction matrix that can be multiplied by raw data to reduce the degrading effects of spectral stray light by 1–2 orders of magnitude [34, 35].

Far-Field Stray Light Modeling Efforts

Almost all of the methods discussed so far to estimate a system's PSF only include near-field stray light from scattering, with little to no capability to incorporate ghost reflections or far-field stray light. This is largely due to the difficult nature of measuring far-field stray light; nevertheless, far-field stray light can be a significant contribution if not the most dominant form of stray light for a system. Despite the relative scarcity of far-field stray light modeling in the public domain, a few notable efforts have been made.

In work performed for the CHaracterizing ExOPlanet Satellite (CHEOPS) [142, 143], Kuntzer et al. [55] developed StrAy Light SimulAtor (SALSA), a tool to measure the amount of stray light contamination from the Earth for space-based observatories. Stray light is a particular concern for CHEOPS, since it will use high precision photometry to measure the transits of exoplanets across their host stars, where the SNR can be easily dominated by stray light. SALSA can provide a first-order estimate of stray light as a function of the satellite's orbital elements, the season, and the chosen pointing direction, making it a useful tool to optimize a satellite's observing sequence, set design constraints (e.g. PST stray light performance), or compare several system designs or mission concepts. Given the location of the Earth, the Sun, and the system's pointing direction, SALSA calculates the flux reflecting off the Earth's surface that reaches the telescope and reduces this signal by the instrument's PST to calculate the stray light contamination that reaches the detector [55]. Miller et al. [56] used a similar approach to integrate PST curves over all input angles to determine the stray light contribution from the sky continuum background. While these PST-based methods can provide a first-order stray light estimate, they do not take into account stray light susceptibility asymmetries and are limited to particular operational

scenarios and scenes of interest.

Lightsey and Wei [53] present a more robust method of far-field stray light estimation through their design and analysis work for the James Webb Space Telescope (JWST). JWST's open architecture allows light from the celestial sky to directly illuminate its optics or scatter and reflect from other components into the FOV [123]. Since JWST will observe in the long-wave visible out to medium-wave infrared (MWIR), the most significant stray light contributions are due to zodiacal light, reflected sunlight and thermal emissions from interplanetary dust along the ecliptic plane, and radiance from galactic stars, dust, nebulae, and external galaxies [144]. To calculate the total stray light background contribution, Lightsey and Wei used wavelength-dependent maps of the celestial sky radiance and system stray light susceptibility information captured from a reverse raytrace of a JWST software model [123]. This reverse raytrace technique relies on the principle of reciprocity by defining an extended uniform Lambertian source on the detector plane and tracing the rays out through the front of the system to determine the system's stray light susceptibility for all angles over the entire celestial sphere. Using the same grid coordinates, the total stray light flux contribution from the sky is then found by summing the point-by-point multiplication of the celestial sky radiance grid and the system stray light susceptibility map. This stray light flux is then equated to the flux at the detector from a uniform sky background in order to compute the equivalent uniform sky background radiance in the FOV. This method was used to compare the actual JWST stray light radiance requirement to the estimated stray light radiance levels for different orientations of the JWST observatory, various levels of particulate contamination on the primary and secondary mirrors, and adding a tubular baffle to the observatory [53].

2.4.2 Digital Imaging and Remote Sensing Image Generation (DIRSIG) Model

Although there are numerous commercial and open-source rendering programs that employ physics-driven approaches to produce conventional frame-oriented imagery, a more limited subset focus on data simulation for remote sensing applications in the visible through LWIR. These general-purpose remote sensing models include DART [114], MCScene [120], and MATISSE [121]. DIRSIG also falls into this category, with its particular strength being a sensor-driven approach that allows users to model the complexity of modern remote sensing systems [109].

Overview of DIRSIG

The DIRSIG model has been developed at RIT since the late 1980s as a 3-D simulation environment for generating passive broadband, multispectral, hyperspectral, low-light, and active laser radar datasets in the visible through thermal infrared regions ($\lambda = 0.2$ to $20 \mu\text{m}$) [109]. The software is employed internally at RIT and externally by a user community as a tool to aid in the evaluation of sensor designs, to produce imagery for algorithm-testing purposes, and for troubleshooting instrument behavior during initialization and operation. Key components of the model and some aspects of the model's overall performance have been gauged by several validation efforts over the model's evolution [145, 146].

As a physics-based image and data simulation model, DIRSIG allows users to create high-fidelity representations of complex scenes with spectral optical characteristics and material thermal properties and to model a wide variety of imaging and non-imaging instruments. To begin using DIRSIG, a scene's geometry is created or imported and material

properties are applied, describing each surface's optical and thermodynamic attributes (e.g. BRDF, spectral optical transmission, thermal emissivity, etc.). Once all of the scene elements are assembled, virtual sensors are defined according to engineering-level descriptions such as effective focal length, FPA dimensions, pixel pitch, pixel spectral response curves, per-pixel gain characteristics (linear or non-linear), timing and clocking information, etc. These individual instruments are then mounted onto a platform based on their unique locations and orientations relative to the platform coordinate system. The platform is next assigned flight path or orbital information, including dynamic motion such as sensor or vibrational motion, i.e. jitter. The simulation's collection date and time are provided, along with atmospheric data from the MODerate spectral resolution atmospheric TRANsmittance (MODTRAN) model, which is a computationally-rigorous radiation transfer model developed by the Air Force Research Lab (AFRL) in collaboration with Spectral Sciences, Inc. (SSI) [147]. Once the simulation is complete, the output imagery or data from the sensors can be analyzed, along with precise truth maps that are invaluable for assessing imaging system performance, quantitative evaluation of ground processing, or replicating and then correcting artifacts from actual sensor data [148]. Figure 2.16 shows an example DIRSIG simulation of the Port of Tacoma, WA imaged with a 2-D framing array on a commercial small satellite.



Figure 2.16: DIRSIG simulation of the Port of Tacoma, WA imaged with a 2-D framing array on a commercial small satellite [149].

DIRSIG has been used to successfully model a number of remote sensing systems pre-launch, such as Landsat 8’s TIRS and OLI instruments, in order to better understand the impact of design trades during the instrument build [148,150–154]. While TIRS contains two LWIR bands, OLI has 8 spectral bands in the visible and NIR, along with a panchromatic band. The registration of the TIRS and OLI multispectral bands was a particular challenge for Landsat 8 due to the mission’s pushbroom imaging design, which was a change from the previous Landsat whiskbroom architectures; registration was further complicated by the fact that TIRS and OLI are spatially separated on the satellite bus. The TIRS and OLI modeling efforts therefore involved the simulation of Level-0 class data (i.e. raw data) by testing focal plane calibration anomalies (e.g. spectral filter variations and gain characteristics across the subchip assemblies (SCAs)) and the various registration offsets (pixel-to-pixel, band-to-band, module-to-module, and instrument-to-instrument) present in operational data. These

results were then used in the development and testing of image reconstruction algorithms in order to verify the ground processing pipelines [109]. A detailed scene of the Lake Tahoe region was created for the TIRS and OLI simulations by using digital elevation models, high-resolution spatial and spectral variability data from satellite data, and atmospheric effects from MODTRAN, thus demonstrating DIRSIG's capability to develop high-fidelity operational scenes of interest.

The TIRS and OLI simulations utilized a DIRSIG feature known as a data-driven focal plane where the geometric and radiometric properties of each FPA pixel can be defined [148]. This includes the IFOVs and pointing angles at the aperture for each pixel, along with per-pixel descriptions of relative spectral and spatial responses, amplification (linear gains or bias, or a non-linear look-up table), and noise. Since the TIRS and OLI line-of-sight vectors were based on observed test chamber data, they incorporated each instrument's aberrations, distortions, and alignment errors.

The latest version of the DIRSIG model (version 5, and referred to here as DIRSIG5) leverages a unified path-tracing solution [109]. This approach is essentially a simultaneous, multi-dimensional Monte Carlo integral and the number of rays used to sample each pixel controls the overall numerical fidelity of the simulation. The sensor modeling facilities in the latest version were expanded to allow packaged and user-developed sensor plugins greater freedom to spatially and temporally sample the object field in order to improve DIRSIG's ability to incorporate optical and mechanical effects of imaging systems, as well as temporal scene effects such as motion and rapid changes in illumination conditions. Specifically, the BasicPlatform sensor plugin (the default sensor model in DIRSIG5) includes the basic components of a sensor model, including the ability to incorporate the optical system MTF as a PSF, spectral integration across arbitrary spectral responses, temporal integration,

system motion (both gross motion and fine-scale motion such as jitter), linear and non-linear transfer functions from photons to digital counts, and basic noise contributions [149].

Application of the PSF Importance Sampling Approach in DIRSIG

The spatial and temporal radiance contributions for a given FPA pixel are computed by sampling the contributing area in the object plane with the path tracing facility of the core radiometry engine. The launch time for the initial rays used by the path tracer can be uniformly distributed as a function of time to emulate the temporal integration. Rather than employing a post-processing convolution method, the incorporation of a measured PSF involves a 2-step spatial sampling method that can be directly incorporated into the ray tracing approach, as shown in Fig. 2.17. First, a uniformly-distributed random location within the geometric footprint of the pixel is generated (the option to supply an active area map is also available). Second, the PSF is supplied as some form of 2-D data (image, grid file, etc.) and these data are importance sampled such that grid elements with high magnitudes are proportionally more likely to be randomly drawn. This effectively treats the PSF as a discrete probability mass function (PMF) [155]; once a grid element is chosen via importance sampling, a uniformly random location is selected from within the grid element's spatial boundaries to provide a more continuous sampling of the PSF. These random grid locations are scaled into pixel space (using a supplied scale that defines the spatial support of the PSF) to create an offset to the initial pixel area location. Hence, each pixel sample involves combining a single random pixel location with a single random PSF offset. Since hundreds or thousands of samples are used per pixel, the resulting sampling effectively emulates the convolution of the detector element area and PSF of the system in the object plane.

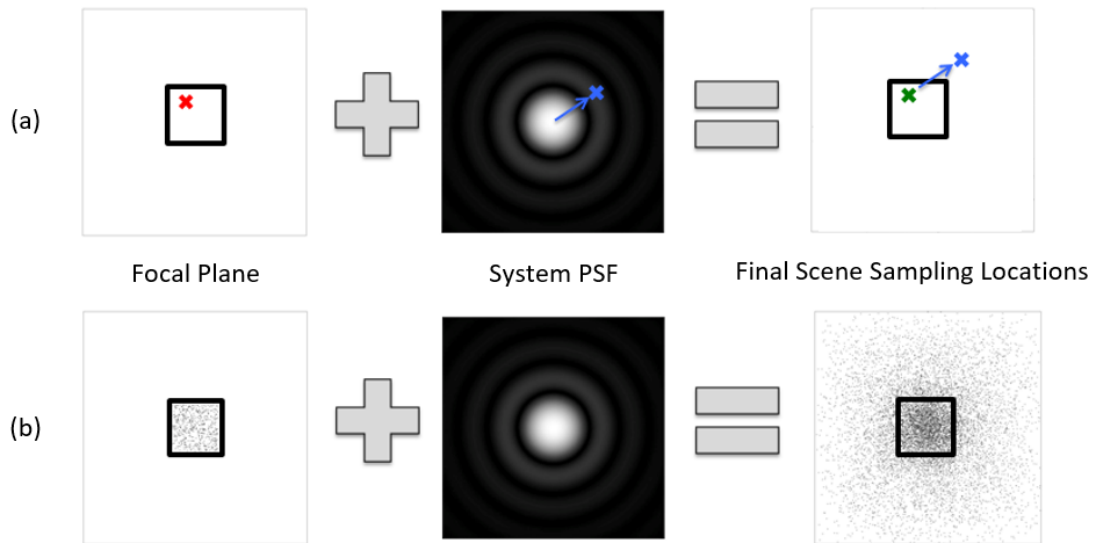


Figure 2.17: The 2-step PSF importance sampling process combines a single random pixel location with a single random PSF offset: (a) One initial and final ray sampling location. (b) Numerous initial and final ray sampling locations.

Figure 2.18 demonstrates the effect of imaging a 1951 U.S. Air Force (USAF) resolution test target and a helicopter with rotating rotor blades both with and without a Gaussian PSF and temporal integration. The Gaussian PSF has blurred the resolution test target in Fig. 2.18b to the point where the highest spatial frequency bars are indistinguishable. The time integration effects are also clearly noticeable in Fig. 2.18b, as the rotor blades are bent due to a rolling shutter, where rows in the FPA are independently integrated and then read out sequentially. Note that this imaging effect is directly a result of DIRSIG's time integration sampling process and not a post-processing effect. The goal of our integration methodology is to analyze the user application impact of these types of full system imaging effects.

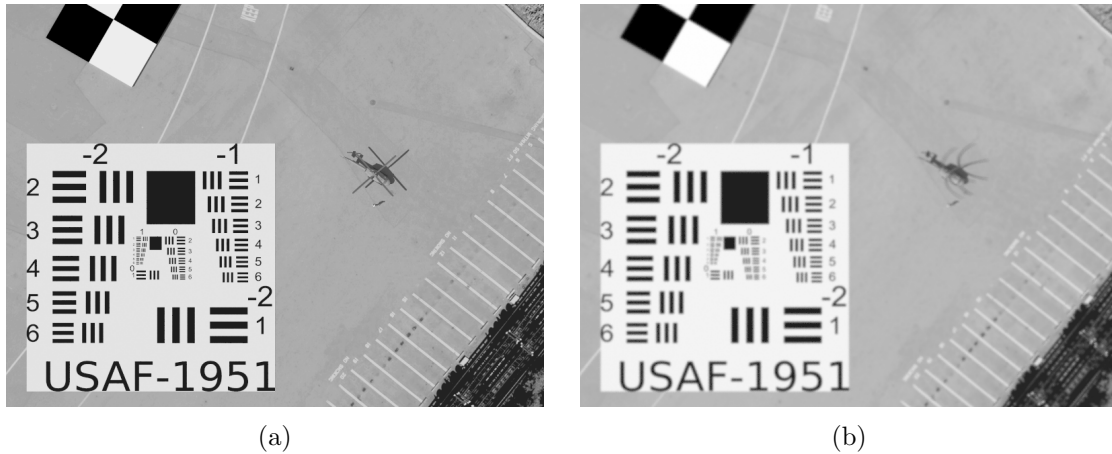


Figure 2.18: DIRSIG image of a resolution test target and a helicopter with rotating rotor blades: (a) No Gaussian PSF or time integration. (b) With a Gaussian PSF and time integration.

2.5 CONCLUSIONS

Modeling and simulation plays an important role in the design and analysis of imaging systems. Much of this work is focused on performance assessment and requirement verification rather than end-to-end modeling for trade study purposes, where design trades can be assessed based on their impact to operational imagery and user applications. This is especially true for stray light, where PSF estimation is used more to assess spatial resolution and near-field stray light performance (both before and during a mission) or to post-process operational imagery for PSF degradation effects, rather than to drive system changes during the design phase. Far-field stray light is largely ignored in this PSF-focused work. A few efforts have been made to model far-field stray light, though these have been applied to more limited operational scenarios and scenes of interest.

The trends of requirement verification, near-field stray light estimation, and lack of end-to-end stray light modeling are not surprising, since far-field stray light can be difficult to assess and, in general, modeling and simulation work takes time and money (not to

mention expertise). The schedule and budget may not exist to conduct robust modeling and simulation to validate that user needs are met with a given system design. There is often an inherent trust that the system requirements have been set by the program manager such that the system's performance will be satisfactory to the users if the system meets these requirements. The responsibility therefore rests with the program manager to ensure that informed system requirements are set. In the case of stray light, this can be quite difficult without the capability to efficiently analyze the potentially subtle impacts of various design options on stray light performance and ultimate user application impact.

There are a few notable exceptions to the lack of end-to-end system modeling, including the DIRSIG model. DIRSIG's parametric system model and data-driven focal plane capability can represent a wide range of highly-detailed space, airborne, and ground-based imaging or non-imaging systems, while its scene generation ability allows for the performance of these systems to be analyzed in dynamic environments. DIRSIG has an exceptional track record, having been successfully used to conduct NASA trade study analysis for Landsat missions, and enjoys a growing user community. The work presented in this research opens up even more system trade study and sensitivity analysis possibilities for DIRSIG by introducing a methodology for integrating optomechanical system software models with a radiative transfer image simulation model. There are many more trade studies and design changes that can be made to a high-fidelity 3-D CAD optomechanical system model than with a typical parameterized system model. The incorporation of a detailed system software model with a powerful scene generation and system simulation model addresses a true end-to-end system modeling capability gap within the systems engineering community, particularly for stray light.

Chapter 3

Integration Methodology

3.1 INTRODUCTION

In order to evaluate the overall performance of Earth-observing telescopes and conduct system trade studies, it is beneficial to incorporate detailed optical engineering tools that characterize a system's MTF, stray light, etc. into full system simulations. To fulfill this need, we have developed a methodology that integrates PSF and stray light performance data collected from a 3-D CAD optomechanical system model with a radiative transfer image simulation model to produce simulated imagery of a highly realistic scene description. Although throughout the work presented here we use FRED Optical Engineering Software [61] to collect PSF and stray light performance data from a Cassegrain telescope model and DIRSIG [62] to incorporate these data and produce synthetic imagery, the method can be generalized to any optical engineering software program and radiative transfer image simulation model.

As detailed in Fig. 3.1, this integration methodology leverages the ability of optical

engineering software to model the intricate details of an optomechanical design and characterize a system's nominal imaging and stray light performance, as well as the capability of a radiative transfer image simulation model to create high-fidelity scenes with accurate radiometry, incorporate unique sensor platform motion and focal plane characteristics, and produce physics-driven imagery. The end-to-end integration of these two types of models using the flowchart displayed in Fig. 3.2 provides system managers and designers with a valuable tool that greatly increases the system trade study and sensitivity analysis possibilities beyond those of each model individually and can be utilized in the drafting of more informed system requirements. There are many trade studies and design changes that can be made to a high-fidelity 3-D CAD optomechanical system model, especially those that influence stray light performance (e.g. baffle placement and geometry, black surface treatments, and particulate contamination levels) that can then be quantitatively evaluated for user application impact on a given scene using a radiative transfer image simulation model. This is particularly important for testing the impact of relaxing system stray light performance in a more constrained system design.

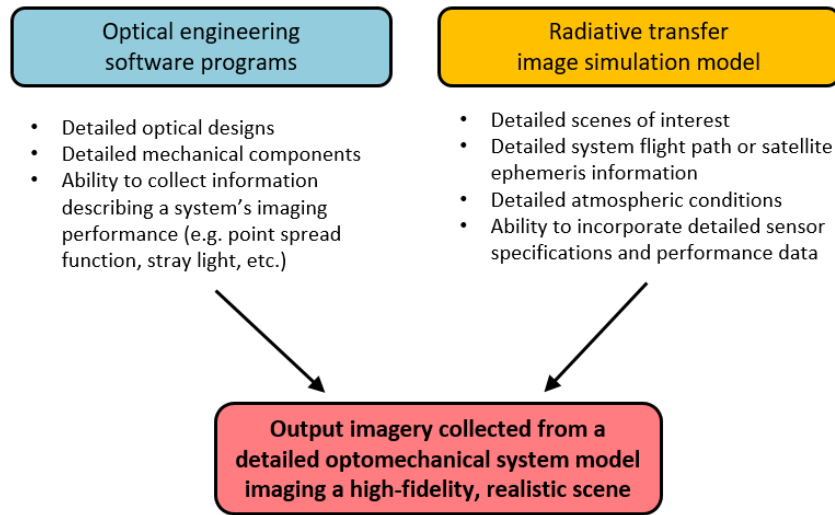


Figure 3.1: Integrating optical engineering software programs with a radiative transfer image simulation model combines the unique benefits of each type of software.

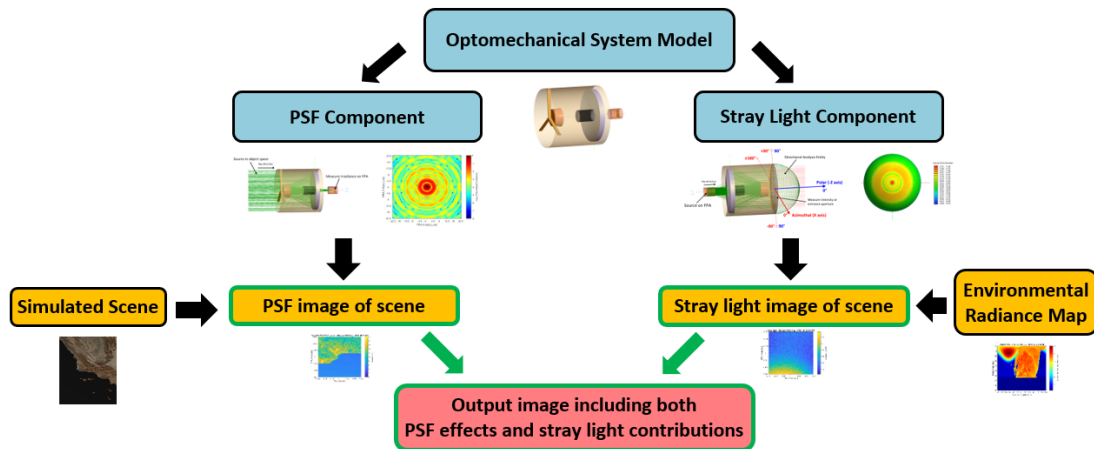


Figure 3.2: Integration method flowchart illustrating how system PSF and stray light performance data collected from an optomechanical system model in optical engineering software (blue steps) can be used to image a scene using a radiative transfer image simulation model (orange steps) to produce simulated output imagery.

The enhanced visualization and quantifiability of stray light in flight-like images, rather than a focus on laboratory-based abstract stray light requirement metrics, bolsters the

capability to predict stray light artifacts earlier in system development and minimize costly reactive solutions after system assembly. This allows optical designers and application scientists to collectively understand what impacts the system's stray light performance has on science data products. Additionally, this forward modeling capability aids in testing stray light correction algorithms pre-mission, so that decisions can be made to either change a system design for improved stray light performance or to correct for the observed levels of stray light via post-processing. Although stray light is the impetus for this research, our general methodology is versatile and can be used to analyze other system parameters, including image quality, the effect of aberrations and distortions, tolerancing and alignment of optomechanical components, optical component form errors, or component degradation expected during a system's operational lifecycle.

This chapter focuses on describing the basic radiometric framework of the integration methodology and introduces the PSF and stray light components. A detailed demonstration of how to collect and analyze stray light performance data from an optomechanical system software model for the integration method's stray light component is also included. Chapter 4 provides the in-depth validation of the PSF component, while Chapter 5 presents the detailed validation of the stray light component.

3.2 INTEGRATION METHODOLOGY FRAMEWORK

The basic radiometric framework of our integration method relies on the fact that the irradiance reaching each pixel of an FPA in an optomechanical system is the summation of two component contributions: the system PSF and stray light. Quantitatively, this can be

expressed as

$$E_{tot}(x, y) = E_{PSF}(x, y) + E_{SL}(x, y), \quad (3.1)$$

where x and y are focal plane spatial coordinates, $E_{tot}(x, y)$ is the total irradiance for a given FPA pixel, $E_{PSF}(x, y)$ is the irradiance from radiation traveling along the designed optical path influenced by the PSF, and $E_{SL}(x, y)$ is the irradiance from stray light paths. The PSF component incorporates diffraction and aberration effects for light propagating along the designed optical path. The stray light component encompasses all other contributions, but may include scattering from optical component surface roughness, particulate contamination, and mechanical components, as well as specular effects, which can result in ghosting. The raytrace data provided by the optical engineering software in our integration method is collected separately for these two component contributions.

3.2.1 PSF Component Radiance to Irradiance Conversion

Our integration methodology produces the PSF component by importing the PSF from an optomechanical system software model into a radiative transfer image simulation model and using it as a probability distribution to drive importance sampling of a scene, as described in §2.4.2. Some radiative transfer image simulation models like DIRSIG have historically provided at-aperture radiance output images for passive systems, with users conducting their own post-processing to incorporate optical system effects. However, we must convert these output images to irradiance when using a PSF to sample a scene, since we are now viewing the irradiance distribution at the focal plane. This radiance to irradiance conversion

is accomplished using the camera equation [59], which is given by

$$E = \frac{L}{G\#}, \quad (3.2)$$

where the $G\#$ [sr^{-1}] defines the throughput of the system when converting input radiance, L , to irradiance on the focal plane, E . The irradiance distribution can be converted to photons, electrons, or digital counts by incorporating the quantum efficiency (QE) and gain characteristics of the FPA. In general, a system's $G\#$ can be calculated using [59]

$$G\# = \frac{1 + 4(f/\#)^2}{\pi\tau}, \quad (3.3)$$

where the system's f-number ($f/\#$) is defined as the ratio of its focal length to aperture diameter and τ is the system's transmittance. Although a system's $G\#$ can have spectral and field angle dependencies, Eq. 3.3 provides the value along the optical axis for a typical operating wavelength.

The system $G\#$ can also be extracted from raytrace data using an optomechanical system software model. This is done by creating a source of known radiance at the system's entrance aperture that fills the system's FOV and calculating the average irradiance at the focal plane on the optical axis. It is important that scattering is included for this $G\#$ raytrace since the throughput of the system will be reduced by mirror surface roughness, particulate contamination, etc. If so desired, optical engineering software can also calculate spectral and field-dependent $G\#$'s by changing the source's wavelength and angular extent so that it only fills a given detector element's IFOV.

3.2.2 Integration Method Component Radiometry

Using the $G\#$ concept and dividing object space into M and N polar and azimuthal solid angles, respectively, we can further detail the PSF and stray light components by rewriting Eq. 3.1 as

$$E_{tot}(x, y) = \frac{L_{PSF,img}(x, y)}{G\#_{DOP}(x, y)} + \sum_{i=1}^M \sum_{j=1}^N \frac{L_{scene}(\theta_i, \phi_j)}{G\#_{SL}(x, y; \theta_i, \phi_j)}. \quad (3.4)$$

In general, Eq. 3.4 will have an in-band wavelength dependence, but here we show the result integrated over the bandpass of a single spectral channel for simplicity. The equation also separately applies to each spectral channel of a system with multiple spectral bands. For the PSF component, $L_{PSF,img}(x, y)$ is the radiance image produced through sampling the scene with a system PSF and $G\#_{DOP}(x, y)$ is the designed optical path's shift-variant $G\#$ for each FPA pixel extracted from a raytrace model. The stray light component consists of two separate terms: $L_{scene}(\theta_i, \phi_j)$ is the scene's mean at-aperture radiance profile over the object space solid angle centered on polar angle, θ_i , and azimuthal angle, ϕ_j , and $G\#_{SL}(x, y; \theta_i, \phi_j)$ is the system's separate stray light $G\#$ for every FPA pixel and object space solid angle (a single FPA pixel can potentially receive stray light from every direction in object space). The amount of stray light irradiance that reaches a system's focal plane is therefore a function of the scene at-aperture radiance and the system's stray light throughput, or equivalently, susceptibility to stray light. This summed product relationship means that significant stray light contributions can even result from low scene radiance if the system has high stray light susceptibility over that region of object space or from regions of low system stray light susceptibility if the scene radiance is high at those angles. In fact, large stray light contributions can be produced if both the system's stray light susceptibility and scene radiance are relatively low, but if the scene radiance extends across a substantial fraction of

object space. We can calculate the stray light irradiance component for each FPA pixel by summing over the quotient of L_{scene} and $G\#_{SL}$ for every solid angle in object space. Since L_{scene} and $G\#_{SL}$ are defined over all of object space, the stray light component includes both near-field stray light originating from sources in or near a pixel's IFOV, as well as far-field stray light from sources farther from the IFOV.

Environmental Radiance Map (ERM)

The scene's radiance profile, $L_{scene}(\theta_i, \phi_j)$, which we call an *environmental radiance map (ERM)* in our integration method, is captured using a radiative transfer image simulation model containing a detailed spatial and spectral representation of the scene. A user can capture an ERM in DIRSIG by conducting a raytrace of the scene using an entity known as a *spherical collector* and specifying the number of divisions along the collector's polar and azimuthal axes, along with the desired number of sampling rays per solid angle. The number of sampling rays defines the fidelity of sampling the scene's radiance profile and therefore its significant stray light contributors. Uniform sampling can be used, where each ERM solid angle grid element is sampled with the same number of rays. DIRSIG also supports an adaptive, radiometric convergence-based sampling method, where the number of sampling rays per solid angle grid element falls between a specified minimum and maximum range. Sampling continues for each grid element until either a pre-set radiometric convergence limit is achieved or the maximum number of rays is reached. Uniform or radiometric convergence-based sampling of the object space solid angles is used rather than an importance sampling-based approach as with our PSF component, due to the fact that significant stray light contributions can originate from sources across all of object space, not just where a system has high stray light susceptibility (e.g. high radiance sources at low system stray light

susceptibility angles would not be sufficiently sampled using an importance sampling-based approach). The uniform and radiometric convergence-based sampling methods also have the advantage of requiring only one ERM per scene capture rather than separate stray light scene sampling for every detector element as with the importance sampling approach.

Stray Light Angular Susceptibility Map (ASM)

The $G\#_{SL}(x, y; \theta_i, \phi_j)$ terms in Eq. 3.4, provide a measure of a system's stray light susceptibility across all of object space for each FPA pixel. Due to the invariance of throughput, these values can be determined by conducting reverse raytraces of an optomechanical system model (i.e. source on the focal plane) in optical engineering software. This reciprocal relationship exists due to the fact that radiance from a given solid angle of object space will propagate along certain paths through a system and result in a given amount of stray light radiant flux on an FPA pixel, whereas the same radiance originating from the pixel will travel along these same ray paths in the reverse direction and result in an equivalent radiant flux leaving the system through the given object space solid angle.

A Lambertian source of known radiance created over the spatial extent of an FPA pixel located at focal plane position x, y will produce a system's $G\#_{SL}$ values according to

$$G\#_{SL}(x, y; \theta_i, \phi_j) = \frac{A_{pixel} L_{src,SL}}{\Phi_{SL}(x, y; \theta_i, \phi_j)}, \quad (3.5)$$

where $L_{src,SL}$ is the radiance of the reverse raytrace source, $\Phi_{SL}(x, y; \theta_i, \phi_j)$ is the stray light radiant flux leaving the system at the object space solid angle centered on polar angle, θ_i , and azimuthal angle, ϕ_j , and A_{pixel} is the pixel area. Substituting Eq. 3.5 into Eq. 3.4

allows us to rewrite the stray light component as

$$E_{SL}(x, y) = \sum_{i=1}^M \sum_{j=1}^N \frac{\Phi_{SL}(x, y; \theta_i, \phi_j) \cdot L_{scene}(\theta_i, \phi_j)}{A_{pixel} L_{src, SL}}, \quad (3.6)$$

which demonstrates that the total amount of stray light irradiance reaching an FPA pixel is simply a product of a system's stray light susceptibility and the scene's at-aperture radiance profile summed over every object space solid angle. Figure 3.3 highlights this important radiometric relationship for stray light contributions. The $\Phi_{SL}(x, y; \theta_i, \phi_j)$ terms, which we call *stray light angular susceptibility maps (ASMs)* in our integration method, can be viewed as a set of weighting factors for each object space solid angle that determines the system's efficiency at converting at-aperture scene radiance to focal plane stray light irradiance for a given FPA pixel.



Figure 3.3: As detailed by the integration method's underlying radiometry, the stray light contributions reaching the focal plane of an optical system are inherently a product of the system's stray light susceptibility and the scene's at-aperture radiance profile.

Far-field Stray Light

As previously discussed in §2.4.1, many stray light modeling and simulation efforts are limited to including only near-field stray light performance via a system's shift-invariant PSF or shift-variant PSFs. This form of stray light modeling assumes that a system has no far-field stray light susceptibility, i.e. $\Phi_{SL}(x, y; \theta_i, \phi_j) = 0$ W for all solid angles that are not near the IFOV of the pixel located at focal plane position x, y . From Eq. 3.5, it

follows that $G\#_{SL}(x, y; \theta_i, \phi_j) \rightarrow \infty \text{ sr}^{-1}$ for these solid angles and that their stray light contribution is zero. Our integration method does not make this assumption and includes both near-field and far-field stray light, thus improving the modeling fidelity of system stray light susceptibility.

History has shown that far-field stray light from out-of-FOV sources can have a significant effect on a system's imaging performance, as evidenced by Landsat 8's TIRS. TIRS suffers from a far-field stray light path that allows out-of-scene radiance to scatter into the FOV off of a lens supporting structure, leading to the addition of a non-uniform, scene-dependent stray light signal in its two thermal bands that can be in excess of 8% [58, 66]. The non-uniform banding artifacts caused by this stray light issue can be seen in the TIRS image of the Red Sea shown in Fig. 3.4. Although this open water scene should be essentially uniform, stray light contributions from the surrounding land out of the FOV creates a banding effect between the three FPAs. Despite the fact that these types of far-field stray light effects can sometimes be minimized through the time-consuming development of post-processing techniques as with TIRS [58], it is far more advantageous to predict and correct such issues pre-mission, as opposed to developing reactive operational solutions. It is apparent that system far-field stray light susceptibility must be incorporated into our integration methodology in order to identify many potential problems, especially those originating from hard to predict far-field stray light paths. This is especially significant given the constrained design environments of future compact systems that may have elevated far-field stray light susceptibility.

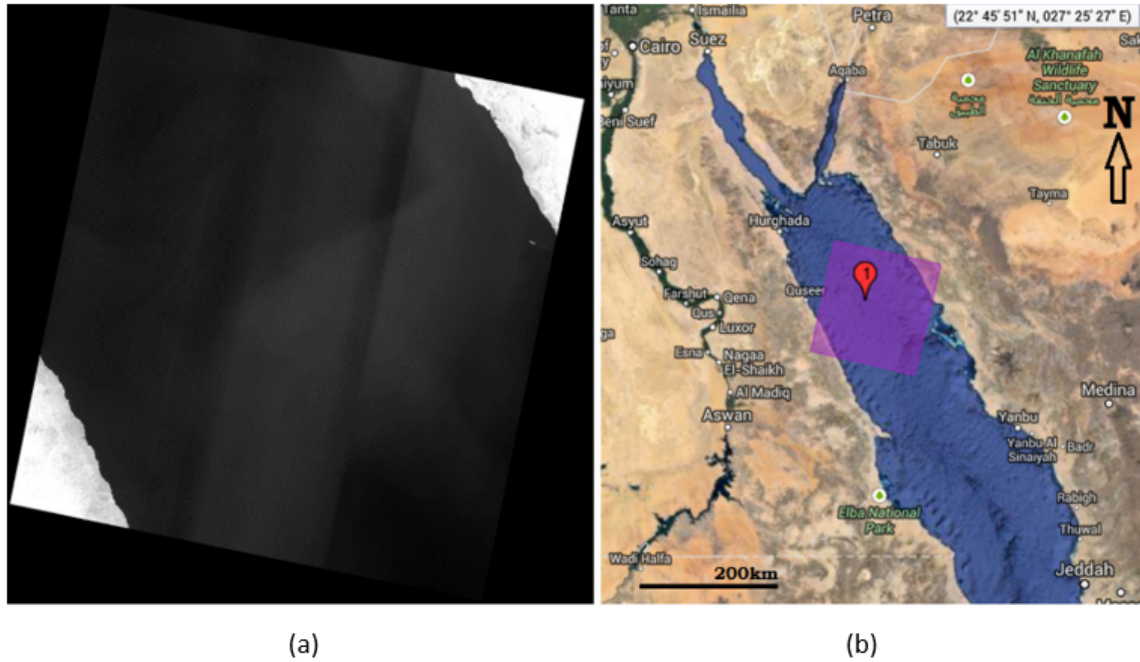


Figure 3.4: (a) TIRS band 11 (11.50–12.51 μm) image of the Red Sea with image intensity ranging from 8.5 to 11.5 $\text{W}/\text{m}^2/\text{sr}/\mu\text{m}$. Far-field stray light leads to a banding effect that is evident in the across-track direction between the three FPAs. (b) Map from USGS Earth Explorer showing the extent of the scene. Reproduced with permission, courtesy of Montanaro et al. (2014) [57].

3.3 STRAY LIGHT ANGULAR SUSCEPTIBILITY MAP (ASM)

As previously discussed, the $G_{\#SL}(x, y; \theta_i, \phi_j)$ terms in Eq. 3.4 provide a measure of a system's stray light susceptibility, which is inherent to a given set of system design conditions and independent of scene radiance. The $G_{\#SL}(x, y; \theta_i, \phi_j)$ terms are calculated according to Eq. 3.5, where $\Phi_{SL}(x, y; \theta_i, \phi_j)$ are the stray light ASMs for each FPA pixel and $L_{src,SL}$ is the radiance of the reverse raytrace source used to create the stray light ASMs. The stray light ASMs are the key factors contributing to the stray light component of the integration method and are the means through which different stray light susceptibility conditions can

be tested for a system.

3.3.1 Capture a Stray Light ASM

To demonstrate the capture of a stray light ASM, we use the Cassegrain telescope model displayed in Fig. 3.5, which has a Ritchey-Chrétien design form, an aperture of 10.16 cm (4 in), and a focal length of 51.364 cm (f/5.06 system). The designed optical path for this system is detailed in Table 3.1. Since scattering from mechanical structures dominates the stray light performance of this Cassegrain design, we have assigned a flat black paint scatter model to all of the mechanical surfaces (labeled in black). This scatter model is based on data from Aeroglaze[®] Z306 [88], which is largely Lambertian at normal incidence, but whose total integrated scatter (TIS) and specular nature increase with increasing incident angle. Although the flat black paint scatter model has a TIS = 2% at normal incidence, the TIS increases to 7.24% at an incident angle of 75° and 9.02% at a near-grazing incident angle. For the primary and secondary mirrors (labeled in blue in Fig. 3.5), we have assigned a Harvey-Shack scatter model [78, 79] ($b_0 = 0.1$, $L = 0.01$, and $S = -1.5$) that is representative of the residual surface roughness after optical surface polishing. These Harvey-Shack parameters provide the mirrors with a TIS = 0.11% at normal incidence and $\lambda = 0.55 \mu\text{m}$ and a surface roughness of $\sigma_{RMS} = 14.7 \text{ \AA}$. We have also assigned a Mie scatter model to the mirrors with a CL400 IEST-STD-CC1246D particle size distribution function to represent the particulate contamination level of freshly cleaned optics. This produces a TIS = 0.22% at normal incidence and $\lambda = 0.55 \mu\text{m}$ and a percent area coverage (PAC) = 0.1059%. Note that the complex refractive indices for this particulate distribution were defined according to approximated values for the visible wavelength regime. The Harvey-Shack surface roughness and Mie particulate contamination scatter models both act upon light incident on the two

mirror surfaces, so their scattering effects combine.

We have set the raytrace controls to allow up to second-order scattering off the mechanical components and first-order scattering off of the mirrors, since the TIS of the flat black paint is significantly higher than the total TIS of the optical surface scatter models. Second-order scattering from the mirrors is therefore relatively small in magnitude and can be excluded without a substantial loss in accuracy. For both the mechanical and optical surfaces, each incident ray that scatters results in ten scatter rays that then propagate through the system.

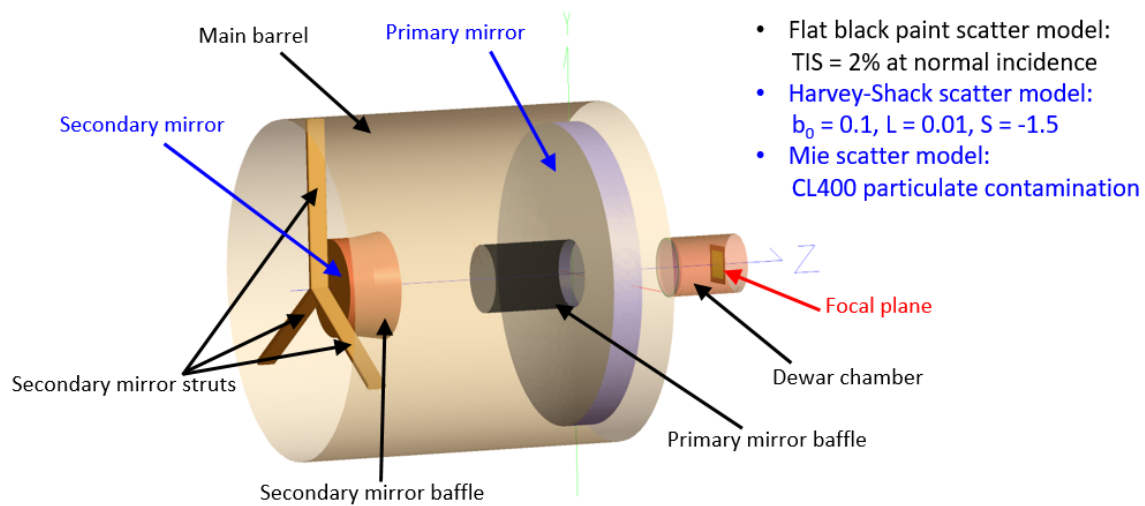


Figure 3.5: Cassegrain telescope FRED model with a flat black paint scatter model (TIS = 2% at normal incidence) assigned to the mechanical surfaces (labeled in black). A Harvey-Shack scatter model ($b_0 = 0.1$, $L = 0.01$, and $S = -1.5$) and Mie scatter model representing particulate contamination (CL400) have been assigned to the optical surfaces (labeled in blue).

Table 3.1: Cassegrain telescope designed optical path in the forward direction (object space to focal plane).

Event	Interaction	Entity
1	Reflection	Primary mirror reflecting surface
2	Reflection	Secondary mirror reflecting surface
3	Transmission	Dewar chamber window front surface
4	Transmission	Dewar chamber window back surface
5	Absorption	Detector

Although we can capture shift-variant and multispectral stray light ASMs, to simplify this demonstration, we use a single $50 \mu\text{m} \times 50 \mu\text{m}$ detector in the center of the focal plane and $\lambda = 0.55 \mu\text{m}$. Due to the invariance of throughput, we can conduct a reverse raytrace to capture the detector’s stray light ASM. We start by defining a $\lambda = 0.55 \mu\text{m}$, $1 \text{ W/m}^2/\text{sr}$ Lambertian source with 2 million initial rays over the spatial extent of the $50\text{-}\mu\text{m}$ detector. This source sends rays uniformly random into the full 2π steradians above the pixel. Scattering is not suppressed for this raytrace and the source is incoherent since the effects of surface scattering are represented statistically by the interaction between geometric rays and the surface BSDFs. Diffraction effects are therefore not included in the stray light ASM calculation. The rays are traced back through the system and captured as a radiant intensity $[\frac{\text{W}}{\text{sr}}]$ distribution at the entrance aperture through a special type of FRED analysis surface called a directional analysis entity (DAE), shown in Fig. 3.6. The DAE bins the rays according to their angular distribution, thus removing any information about their spatial distribution across the entrance aperture. We are able to capture only the rays from stray light paths by properly filtering the ray data captured by the DAE. A hemispherical DAE is appropriate for the Cassegrain system’s entrance aperture, although a spherical DAE could be used for a system with an open architecture. FRED saves the radiant intensity distribution information from the DAE in its custom `.fgd` file format (FRED Grid Data).

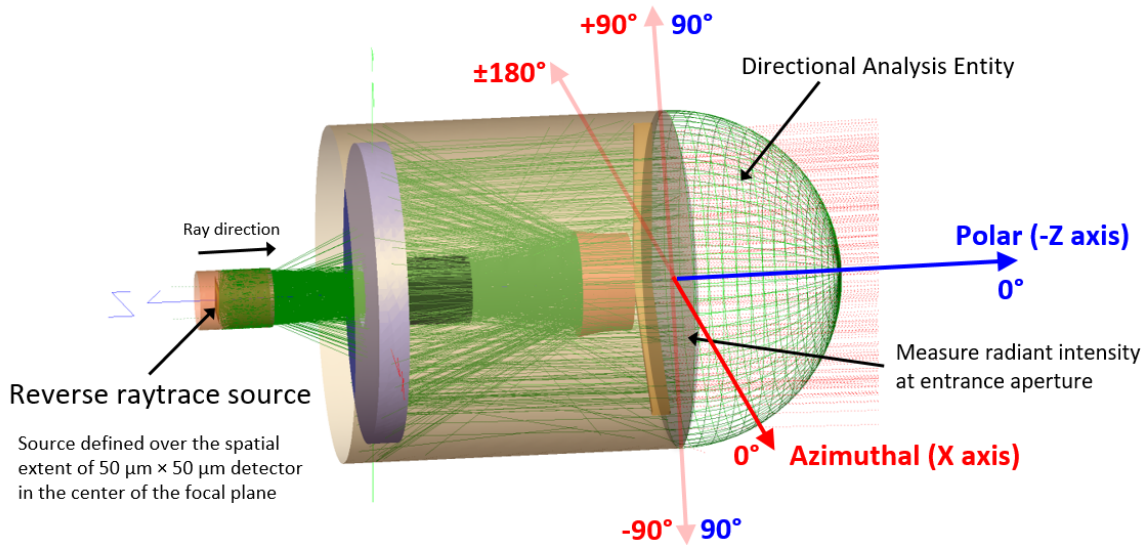


Figure 3.6: Reverse raytrace using the Cassegrain telescope model along with the stray light ASM coordinate system. The system’s stray light susceptibility data is captured at the entrance aperture as a radiant intensity profile by the DAE. These data are then converted to stray light radiant flux per grid element by multiplying by each DAE grid element’s solid angle.

We have oriented the DAE grid such that the zenith angle of the plot aligns with the Cassegrain telescope’s optical axis. This results in a higher angular sampling of the stray light distribution closest to the optical axis, where the system will have the highest magnitude and most structured stray light susceptibility. The stray light data must now be converted from radiant intensity to radiant flux to account for the fact that the ASM grid elements do not cover equal solid angles. Here we use a grid with $1^\circ \times 1^\circ$ grid elements, which results in grid elements with solid angles that are over two orders of magnitude larger along the edge of the entrance aperture compared to those closest to the optical axis. The stray light data is converted from radiant intensity to radiant flux by multiplying each ASM grid element by its solid angle. The stray light data now details the amount of stray light radiant flux leaving every solid angle at the entrance aperture for the $1\ \text{W}/\text{m}^2/\text{sr}$ source on our $50\text{-}\mu\text{m}$ detector. We call these plots *stray light angular susceptibility maps (ASMs)* since

they provide a map of which solid angles can contribute stray light radiant flux to the focal plane, with the stray light radiant flux per ASM grid element serving as a measure of the system's stray light susceptibility. The invariance of throughput states that the total stray light radiant flux that would reach the detector in the forward direction (i.e. from object space to the focal plane) from an infinite Lambertian plane of uniform $1 \text{ W/m}^2/\text{sr}$ radiance is simply the summation of the stray light radiant flux over every stray light ASM grid element (also integrating over the detector's spectral bandpass). Of course, in reality an arbitrary scene will not be of uniform radiance, so the scene's variable radiance distribution must be taken into account when calculating the total stray light reaching the detector using Eq. 3.6.

We have used an optical engineering software raytracing technique called importance sampling to increase the efficiency of our reverse raytrace and produce better statistics for our stray light ASM. Whereas DIRSIG's PSF importance sampling is used to sample a scene, this type of importance sampling deals with the directionality of scattered rays. A single ray incident on a surface will produce scattered rays with an angular distribution and flux values determined by the surface's BSDF. A very large number of scatter rays are required to accurately represent the full 4π -steradian scattering from a surface (including both reflection and transmission). Without any special directional scattering specifications, the vast majority of the scattered rays created in our stray light ASM reverse raytrace would not reach the entrance aperture. However, this version of importance sampling allows the user to specify the relevant solid angle into which a surface should scatter rays for raytracing purposes. The raytrace engine only generates scatter rays into the specified solid angle with the flux of each ray scaled according to the surface's BSDF definition, increasing the statistical sampling of the relevant solid angle and resulting in a better radiometric convergence

for a given number of initial rays. Figure 3.7 illustrates the benefit of defining directional importance sampling specifications for rays scattering from a surface. For our stray light ASM raytrace, we have set the Cassegrain telescope’s importance sampling specifications such that scattered rays are ultimately directed towards the entrance aperture.

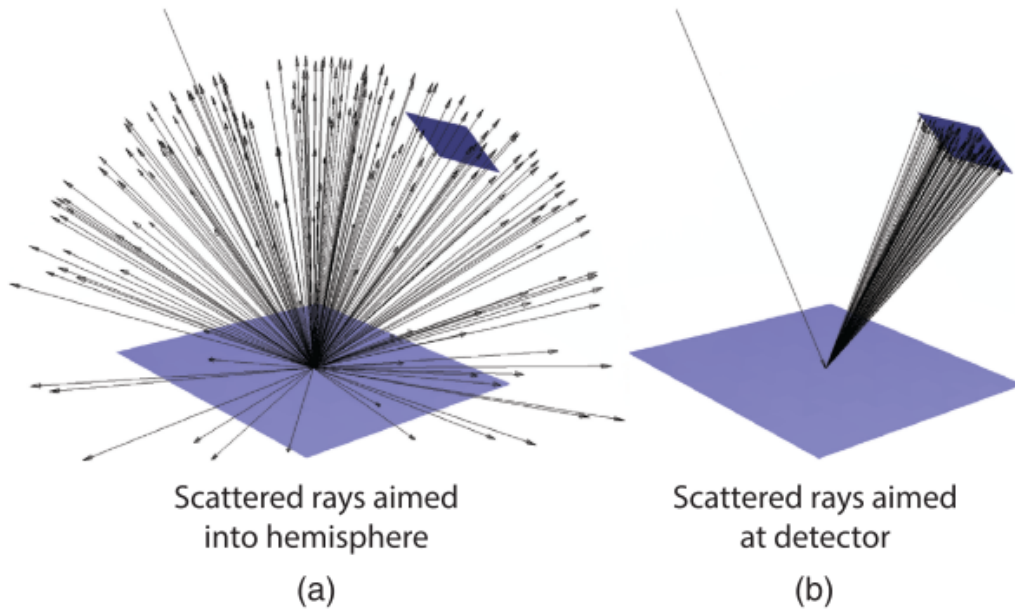


Figure 3.7: Scatter model importance sampling demonstration. (a) Scatter rays into the full hemisphere. (b) Scatter rays towards a detector. The latter case produces greatly improved radiometric results due to the increased numbers of rays scattered to the surface of interest [17].

In addition to specifying the solid angle scatter region of interest (the importance sample) for each surface, we also dictate how scattered rays are distributed within that importance sample. FRED’s default mode of operation is to uniformly sample the solid angle of interest with scattered rays whose power is proportional to the BSDF in a given ray’s direction. In this “uniform” sampling mode, each ray has the same statistical weight re-

ardless of the BSDF value in the ray's propagation direction. An alternative method of generating scattered rays is to use a Monte-Carlo mode, where the number of scattered rays generated in a given direction is proportional to the surface's BSDF. This means that more rays will be scattered towards angles where the surface's BSDF is higher, while fewer rays will be scattered towards angles where the BSDF is lower. Given that only a finite number of rays can be traced, when possible, it is often preferential to trace higher power rays than lower power rays. The Monte-Carlo method is particularly useful for surfaces with a BSDF containing significant variations over the importance sample region, since more rays will be directed towards those angles leaving a surface where the scattering power is higher and more likely to significantly impact radiometric calculations. If the uniform scattering option is used for these surfaces, the angles leaving the surface that have a high BSDF can be undersampled, while the angles with a low BSDF can be relatively oversampled. We have chosen the Monte-Carlo option for this demonstration in order to more efficiently trace scatter rays with the greatest opportunity of impacting our radiometric calculations.

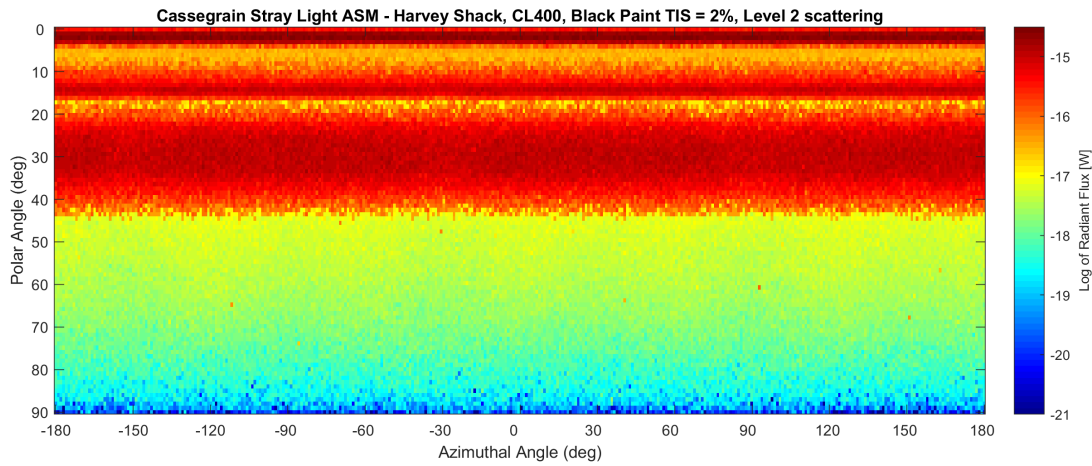
3.3.2 Stray Light ASM Analysis

Figure 3.8 displays the Cassegrain telescope's stray light ASM, with the top plot containing the log of stray light radiant flux data, whereas the bottom plot shows the log of the original radiant intensity data overlaid on the DAE grid in FRED. Although the 50- μm detector has a nominal specular FOV of only $0.00558^\circ \times 0.00558^\circ$, it is apparent that the system's stray light susceptibility due to scattering has increased its true FOV to cover almost the entire object space hemisphere. A stray light analyst can use this type of plot to easily identify where a system has hot spots, i.e. the angles from which the system is most susceptible to receiving stray light, in order to develop an effective strategy to mitigate significant stray

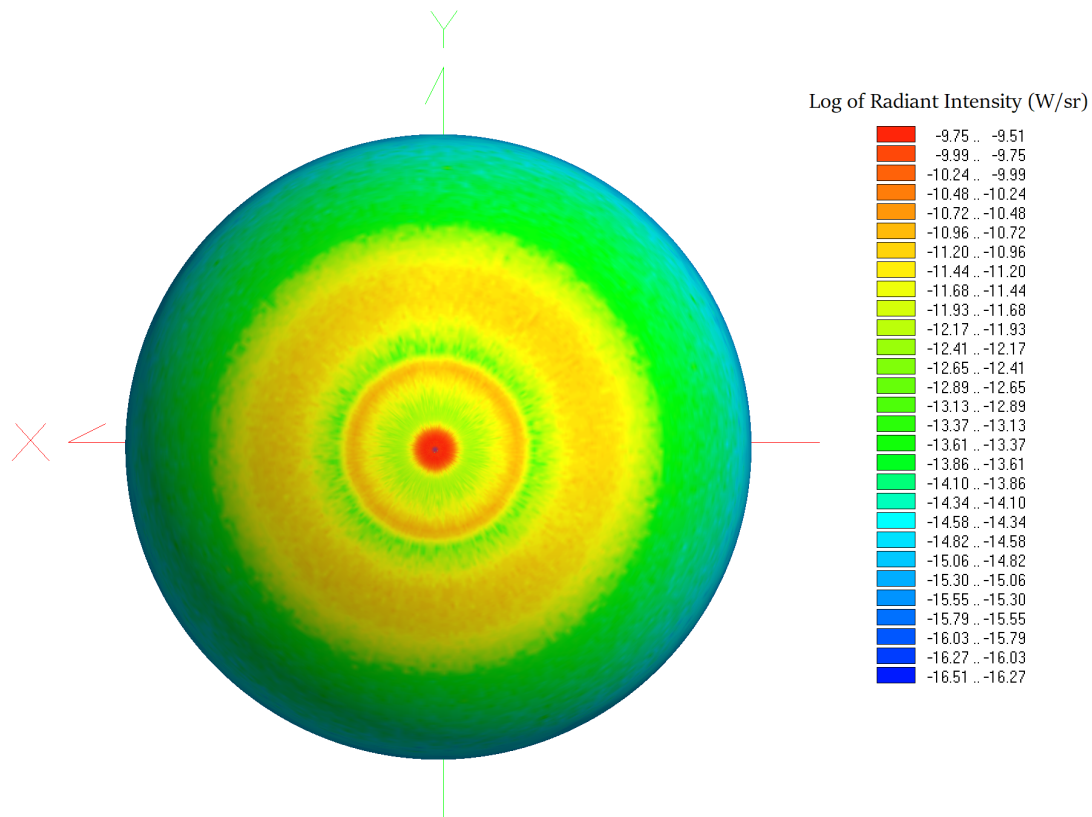
light paths.

The Cassegrain system's highest stray light susceptibility occurs within 5° of the optical axis, which is primarily the result of light that scatters off of the primary mirror baffle's inner wall and specularly reflects off both the primary and secondary mirrors. In fact, as shown in Table 3.2, over 60% of the stray light captured on the stray light ASM is from light that scattered from the primary mirror baffle's inner wall. Figure 3.9 provides a visualization of the Cassegrain's most susceptible stray light path, which alone is responsible for 46.9% of the total stray light radiant flux captured by the stray light ASM for this detector. In the forward direction, this stray light path is caused by light entering the Cassegrain telescope's entrance aperture and scattering off the primary mirror baffle inner wall directly to the detector.

The fact that the majority of the system's stray light susceptibility is a result of stray light paths that include the primary mirror baffle illustrates the difficulty of controlling and mitigating stray light. Although the primary mirror baffle blocks higher power stray light paths that would cause even more significant problems (a zeroth order stray light path would exist without it), its inclusion does create a large number of lower power stray light paths. Surfaces placed parallel to the designed optical path offer the opportunity for high incident angle, specular-like scattering, which is one of the reasons why vanes are typically placed along the inner diameter of baffles. Unfortunately, it is often true that mitigating one stray light issue creates other (hopefully less significant) stray light paths.



(a)



(b)

Figure 3.8: (a) Cassegrain system stray light ASM at $1^\circ \times 1^\circ$ resolution (log of radiant flux). (b) Visualization of the Cassegrain stray light ASM on the entrance aperture DAE grid in FRED (log of radiant intensity). Azimuthal angle $\phi = 0^\circ$ points in the positive x-axis direction, while $\phi = +90^\circ$ points towards the positive y-axis. Polar angle $\theta = 0^\circ$ points directly out of the page from the center of the entrance aperture, while polar angle $\theta = 90^\circ$ points along the entrance aperture edge.

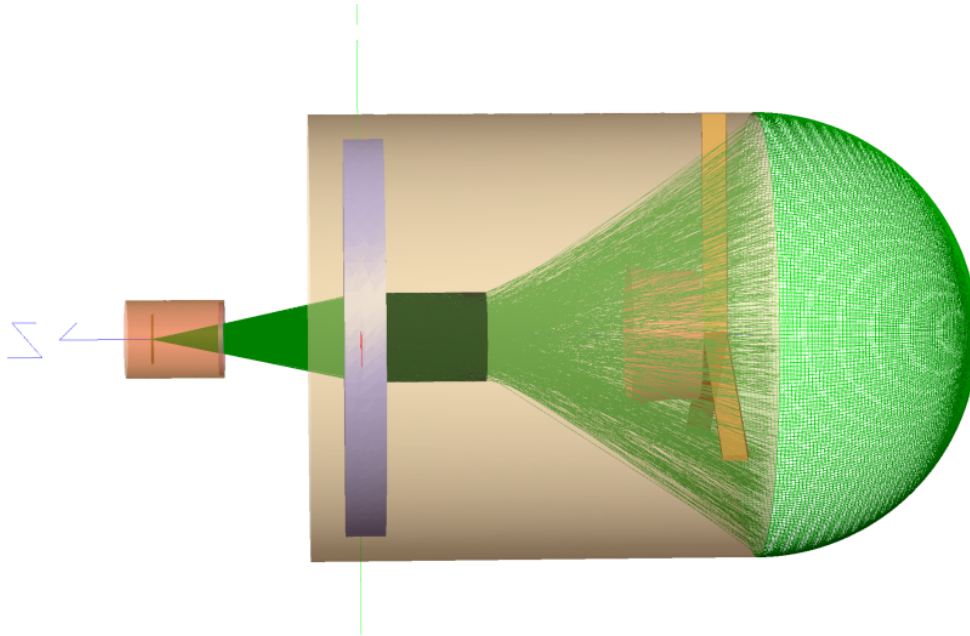


Figure 3.9: Visualization of the Cassegrain telescope’s highest susceptibility stray light path. In the forward direction, these rays enter the Cassegrain telescope’s entrance aperture and scatter off of the primary mirror baffle’s inner wall directly to the detector. In our reverse raytrace, this stray light path is solely responsible for 46.9% of the total stray light radiant flux captured by the detector’s stray light ASM.

Table 3.2: Percentage of the total stray light radiant flux on the detector’s stray light ASM from first-order stray light paths including significant scattering surfaces. The surfaces listed are where the single scattering event took place in each case. Since many unique first-order stray light paths can share the same scatter surface, these percentages are the summation of all first-order stray light paths for each scatter surface.

Scatter Surface	Percentage of Stray Light ASM Total Radiant Flux
Primary mirror baffle inner wall	60.09%
Dewar chamber inner wall	14.05%
Primary mirror hole inner wall	11.94%
Secondary mirror baffle	5.44%
Secondary mirror reflecting surface	1.78%
Primary mirror reflecting surface	1.59%

The Cassegrain telescope also has increased stray light susceptibility from polar angle $\theta = 10 - 17^\circ$, which is predominantly caused by scattering off of the dewar chamber inner wall and the secondary mirror baffle. The largest angular region of stray light susceptibility, which extends from $\theta = 19 - 44^\circ$, is primarily due to the highest susceptibility stray light path displayed in Fig. 3.9 that directly scatters off the primary mirror baffle inner wall, as well as light that directly scatters off the inner wall of the primary mirror hole. The lower magnitude stray light susceptibility beyond about $\theta = 45^\circ$ is largely due to second-order scattering off of the main telescope barrel and first-order scattering off the sides of the secondary mirror struts. The stray light susceptibility is so low beyond $\theta = 45^\circ$ that only 0.48% of the total stray light radiant flux on the entire stray light ASM is contained within this region, despite the fact that it constitutes 70.7% of the total object space solid angle. First-order scatter dominates overall, accounting for 95.49% of the total stray light radiant flux captured by the stray light ASM, with the remaining amount resulting from second-order scattering from the mechanical components.

As expected, the scattering from mechanical components is by far the most significant contributor of stray light, with 96.63% of the total stray light radiant flux on the detector's stray light ASM. Scattering from the primary mirror and secondary mirrors account for 1.59% and 1.78% of the total stray light radiant flux, respectively, as detailed in Table 3.2. From a stray light analyst's perspective, improving the stray light performance of the mechanical surfaces will lead to the greatest improvement. For remote sensing applications, it is the potentially significant stray light contributions resulting from out-of-FOV sources that is the primary concern based on analyzing the Cassegrain telescope's stray light ASM.

3.3.3 Shift-Variant Stray Light ASMs

It is possible to simply collect a single shift-invariant stray light ASM to characterize a system's stray light performance, i.e. only capture the stray light ASM for a single detector element and use this stray light ASM to compute the stray light contribution for every detector element at the focal plane. This will produce a single stray light contribution value, resulting in a uniform stray light bias across the focal plane. This assumption of system stray light susceptibility invariance may be useful for a quick estimate of the expected stray light level for a system, but runs the risk of missing significant stray light paths contributing to detector elements other than the one for which the stray light ASM was captured.

In general, shift-variant stray light ASMs should be collected across the focal plane, since a system's stray light susceptibility has a focal plane spatial dependence. Shift-variant stray light ASMs will produce a 2-D stray light irradiance distribution across the focal plane that is more representative of the system's true stray light performance. Collecting shift-variant stray light ASMs becomes even more meaningful when imaging heterogeneous scenes with large contrast changes. This is due to the fact that the product of $\Phi_{SL}(x, y; \theta_i, \phi_j)$ and $L_{scene}(\theta_i, \phi_j)$ in Eq. 3.6 will change considerably across the focal plane with any change in the magnitude or distribution of $\Phi_{SL}(x, y; \theta_i, \phi_j)$. Given the large amount of raytracing required, GPU raytracing for optical engineering software presents a critical new capability to facilitate the timely capture of large numbers of shift-variant stray light ASMs. We demonstrate this capability with our stray light-focused system trade studies presented in Chapter 6.

The collection of shift-variant stray light ASMs depends on several factors, including the spatial sampling interval on the focal plane, the radiometric fidelity and noise level of

each individual stray light ASM, the total capture time for a set of stray light ASMs, and the total data size of the output files. The spatial sampling interval determines the distance between individual stray light ASM samples at the focal plane, e.g. capturing the stray light ASM for the center detector element of every 5×5 grid of detector elements at the focal plane. In the maximum limit, the stray light ASM for every detector element can be captured, but this may prove to be prohibitive in terms of total collection time and data size. This is especially true if several sets of stray light ASMs for different system stray light susceptibility conditions are being collected for a large number of detector elements in order to conduct a system trade study. One option is to collect a sparse set of shift-variant stray light ASMs and use interpolation techniques to create the stray light ASMs for the detector elements that have not been explicitly sampled. The downside to this approach is that it approximates the system's stray light susceptibility between the sampled detector elements. It may be unnecessary to use a very fine focal plane spatial sampling if the system's stray light susceptibility has minimal variation over relatively small regions at the focal plane. However, as with the shift-invariant case, stray light ASM spatial samplings that are too sparse do run the risk of missing important stray light paths. This is especially true for unforeseen stray light paths caused by specular glints or specular-like high incident angle scattering. Ultimately some level of risk must be accepted when using a sparse sampling, but the benefits will usually outweigh the risks. If this integration method is being used later in a system's development, hardware testing can be used to help reduce the uncertainty of missing any anomalous stray light paths and update the optomechanical system software model for validation purposes.

It should be noted that the collection of shift-variant stray light ASMs should not be the primary method of discovering anomalous stray light paths. The purpose of including

the stray light component in the integration method is to determine the impact of stray light on user applications and is not intended as a replacement of traditional stray light analysis. Other raytracing techniques should first be applied to an optomechanical system model using optical engineering software to characterize its general stray light performance. One of the most common methods is to perform a reverse raytrace for the entire FPA at once [17]. This will identify the system's critical surfaces and the most significant low-order stray light paths. Although every system has expected stray light, this full-detector method can also be useful in diagnosing anomalous stray light paths that were not anticipated in the initial optomechanical design. Further reverse raytraces of specific regions of the focal plane can be conducted to gain further insight into how the system's stray light susceptibility changes across the focal plane. This type of general knowledge about a system's stray light performance is very useful in determining the proper spatial sampling of shift-variant stray light ASMs across the focal plane.

The radiometric fidelity and statistical noise level of the stray light ASMs depends on the number of initial rays used to conduct the reverse raytraces, the number of scatter rays created during each scattering event, and the levels of scatter allowed in the model. In general, the more initial rays and the more stray light rays captured by the DAE will lead to stray light ASMs with higher radiometric fidelity and lower noise. Radiometric fidelity can be assessed by setting the system's raytrace conditions and collecting stray light ASMs for a single detector element using different numbers of initial rays. Statistics on the convergence of each stray light ASM grid element solid angle to its true stray light radiant flux value can then be used to determine the optimal number of initial rays for the reverse raytraces. This can be accomplished by creating a delta stray light ASM consisting of the radiant flux differences between stray light ASMs captured using different numbers

of initial rays. Equation 3.6 can then be used in conjunction with the ERM of a particular scene to determine the change in detector stray light irradiance between using the different numbers of initial rays for the stray light ASM reverse raytrace. If this change in stray light irradiance is below a desired radiometric threshold, then the lower number of rays can be used. A similar technique can be utilized when comparing how many levels of scatter to include. If the increase in detector stray light irradiance when including second-order, third-order, etc. scatter is below the detector's noise floor or other minimal standard, then the higher-level scatter rays are unnecessary.

3.4 INTEGRATION METHOD VALIDATION TESTS

It is important to understand the objective of the integration method PSF and stray light component validation tests in Chapters 4 and 5 within the overall context of system development. Figure 3.10 displays the three levels of validation required when using an optomechanical system software model to predict the performance of a physical system that is either in development or already operational. The first level involves validating the optomechanical system software model by iteratively comparing its imaging performance in optical engineering software to actual hardware data. If the system is still in the preliminary design phase, then these system model updates will be based on vendor component measurements (e.g. component sizes, surface coatings, BSDFs, etc.) or data from previous missions. If the system is further along in development, then the data from lab-based tests can be used to adjust the system model. In this way, the system model's performance begins to more closely replicate the actual physical system. Once the model's performance has achieved a sufficient match to the physical system, the system model can then be used to help verify

system requirements, as previously described in §2.2.10 with Landsat 8 OLI.

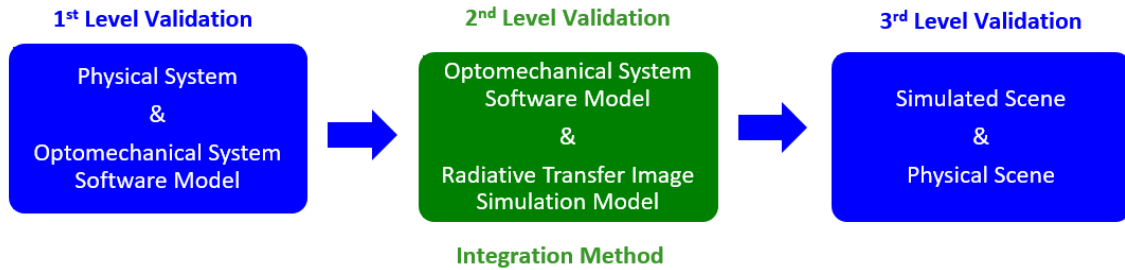


Figure 3.10: Validation levels for end-to-end system modeling and simulation. Work supporting the 2nd level of validation is presented in this dissertation, whereas the 1st and 3rd levels have system and scene dependencies and are therefore left to the users of this integration method.

At this point, the integration method presented here can be used to collect PSF and stray light susceptibility data from the model. This data can then be used in conjunction with a radiative transfer image simulation model to emulate the system model’s performance imaging any scene of interest. Just as the system model is an approximation of the physical system, the PSF and stray light susceptibility data collected from the optomechanical system model are approximations of the model’s performance. Although the system model is theoretically capable of producing continuous data, the PSFs and stray light ASMs must be captured on discrete grids with raytraces using a finite number of rays. Certain assumptions are also necessary when collecting the data, such as how many orders of scatter to include when capturing the stray light ASMs. These factors introduce errors in how well the PSF and stray light ASM data represent the system model’s true performance. There are additional approximations that must be made when using the collected data to sample a scene in a radiative transfer image simulation model, given that only a finite number of

rays can be traced for each detector element to compute the scene radiance. Ignoring these realities, the ideal performance of the integration method would be to exactly replicate the system model's imaging performance within a radiative transfer image simulation model. The goal of the PSF and stray light validation tests in Chapters 4 and 5, respectively, is therefore to characterize the fidelity with which the integration method can replicate the system model's PSF and stray light performance. This is a critical step in providing users with confidence that this tool is capable of providing accurate radiometric results, no matter the system and its user applications.

With this assurance, the PSF and stray light susceptibility data collected from the system model can be used to image a scene created using a radiative transfer image simulation model. However, a third level of validation must be performed to ensure that the created simulated scene is a faithful representation of the intended scene. This may be relatively simple for modeling a lab-based scene with known targets, but can become more complicated when creating an Earth-observing remote sensing scene complete with a model of the Earth and atmosphere. Approximations must also be made with modeling such a scene (e.g. the spatial and spectral resolution of the data used to create the scene, atmospheric conditions, etc.) and care should be taken to minimize any errors compared to the real scene. Once this has been conducted, the PSF and stray light susceptibility data can be used to image the scene. Now that all three validation steps have been performed, the simulated imagery complete with stray light contributions can be viewed as an acceptable representation of the physical system imaging the real scene. This imagery can then be used as a prediction of the expected imagery produced by a system still in development or for comparison to the imagery produced by an operational system.

The first and third levels of validation described in this end-to-end system modeling

and simulation process are ultimately left to users of the integration method. These steps are entirely system and scene dependent, whereas this work is focused on validating the integration method itself. However, performing the first and third validation steps will help limit their contribution to the overall system modeling and simulation error. It is important to note that the integration method validation tests presented in the following chapters in support of the second level of validation do not account for user error or compensate for errors introduced through the first or third validation levels. The integration method will also only reflect the PSF and stray light performance of whatever data is collected, so users of the method should ensure that the data is collected at the desired level of fidelity. Performing the first and third validation levels, while taking care to properly collect PSF and stray light susceptibility, will produce the highest fidelity end-to-end results.

3.5 CONCLUSIONS

This chapter has supported research objective 1 from §1.2 by presenting the basic radiometric framework of our method for integrating optomechanical system models from optical engineering software with a radiative transfer image simulation model. This framework consists of a PSF and stray light component to best incorporate both system effects. The integration method improves upon other stray light modeling approaches by including near-field and far-field stray light within the stray light component. This provides a comprehensive characterization of a system's stray light susceptibility across all of object space, thus aiding in assessing the impact of out-of-FOV stray light sources that can cause significant stray light contributions at the focal plane. This is a key capability for analyzing the stray light performance of Earth-observing satellites such as future Landsat designs. We have also

demonstrated how to collect system stray light susceptibility data using FRED and analyzed a stray light ASM from the Cassegrain telescope model. This type of stray light data can be collected across the focal plane, providing the opportunity to produce stray light irradiance images invaluable for performing system trade studies. Validation tests for the integration method's PSF and stray light components are contained in Chapters 4 and 5, respectively, in order to provide confidence in each component's radiometry.

Chapter 4

Point Spread Function Component Validation

4.1 INTRODUCTION

This chapter focuses on the integration method’s PSF component, including how PSF data must be collected from an optomechanical system software model and how these data are then used in conjunction with a radiative transfer image simulation model to generate synthetic imagery. Most radiative transfer image simulation models rely on convolutional techniques to produce system output imagery with PSF effects included (these PSFs are also often only Gaussian approximations) [106, 118]. This requires spatially oversampling a scene, convolving the oversampled data with a PSF (or performing this operation as a multiplication in the spatial frequency domain), and downsampling to the desired pixel grid. Another common approach is to take an existing 2-D image captured by another system and to use this as the input “scene” to which the desired system PSF is to be applied. Although

there are many approaches to deconvolving the effects of the imaging system that produced the candidate input scene, the linear shift variance of real systems results in a less realistic scene. To improve upon this method, we use the innovative importance sampling-based approach rooted in probability theory [155] described in §2.4.2 to directly incorporate a PSF from an optomechanical system software model into a radiative transfer image simulation model. Although importance sampling methods are currently used in optical engineering and remote sensing software to efficiently model surface scattering, applying a similar approach to PSF sampling in a radiative transfer image simulation model has a number of major advantages over convolution.

The primary benefit of PSF importance sampling is that it efficiently emulates convolution in-the-loop of the simulation, producing Level-0 type (raw) data without the need for a potentially massive intermediate image file (i.e. the oversampled image). This increases the speed at which system trade studies and sensitivity analyses can be performed on parameters of interest. Additionally, the initial capture of the oversampled image inherently introduces errors through the sampling process when the convolution would ideally be performed on the scene itself. Convolution has several other significant downsides in that it assumes a shift-invariant PSF, is limited to a 2-D gridded data array, and fails to take into account certain geometrical and dynamic scene effects. Many modern imaging systems have modular focal planes divided into sub-chip assemblies (e.g. pushbroom systems) that do not directly produce 2-D data products unless the data is first orthorectified, which can introduce interpolations before convolution. Scene elements at different altitudes or scene dynamics will also lead to different results when conducting PSF sampling within the loop-of-the simulation versus through convolution. What appears in neighboring pixels in an intermediate image may not actually correspond to what is next to a given pixel at the

time of capture due to projection effects that can only be captured during the simulation itself. Finally, importance sampling can effectively adapt to an arbitrary PSF probability distribution, though PSFs with larger dynamic range require more rays to adequately sample.

4.2 CAPTURE SYSTEM PSF

The Cassegrain PSF test presented in this chapter uses the Cassegrain telescope shown in Fig. 4.1, which once again has a Ritchey-Chrétien design form, an aperture of 10.16 cm (4 in), and a focal length of 51.364 cm (f/5.06 system). Although the integration method supports the input of spectral and field-dependent PSF data, a basic implementation assuming a monochromatic, shift-invariant PSF is used here for the purpose of validating the methodology and the importance sampling approach. The system PSF is calculated in the optomechanical software, FRED, by creating a coherent, monochromatic, on-axis plane wave that enters the telescope's entrance aperture and propagates through the system to the focal plane, as shown in Fig. 4.2. We use an arbitrary source power of 1 W since the PSF will be normalized in DIRSIG later in the process. No stray light mechanisms (e.g. scattering, ghosting, etc) are enabled during computation of the PSF component. Although future work will expand the spectral capability of the integration method, the basic procedure uses a single spectral channel; for these validation tests, we have chosen a source wavelength of 0.55 μm . The PSF is captured on a fine-resolution analysis surface, as shown in Fig. 4.3, with FRED saving the PSF distribution in its `*.fgd` file format. We use a 75×75 pixel analysis surface with 0.6 μm -wide pixels and a 100% fill factor, with each pixel having 100% spectral responsivity and uniform spatial response. This analysis

surface can be viewed as the central 5×5 pixel region of an FPA with $9\text{-}\mu\text{m}$ pixels and 15×15 subsamples per pixel; the box in Fig. 4.3 denotes the extent of the center $9\text{-}\mu\text{m}$ pixel area. Although the analysis surface's fine-resolution $0.6\text{ }\mu\text{m}$ pixel size is unrealistic for a real FPA, we must use a sufficient spatial resolution to resolve the PSF's features.

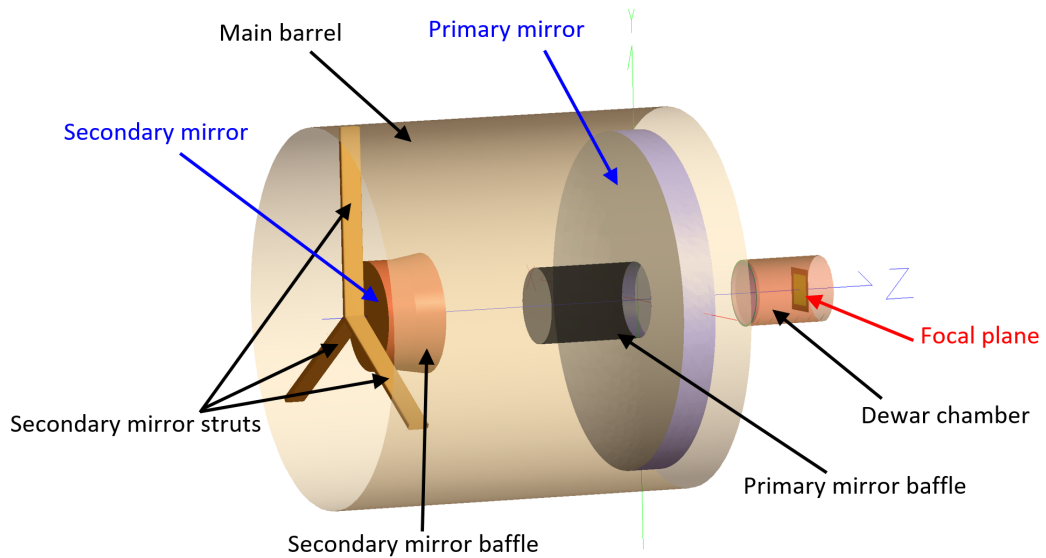


Figure 4.1: Cassegrain telescope FRED model. The optical surfaces are labeled in blue and the mechanical surfaces are labeled in black [60].

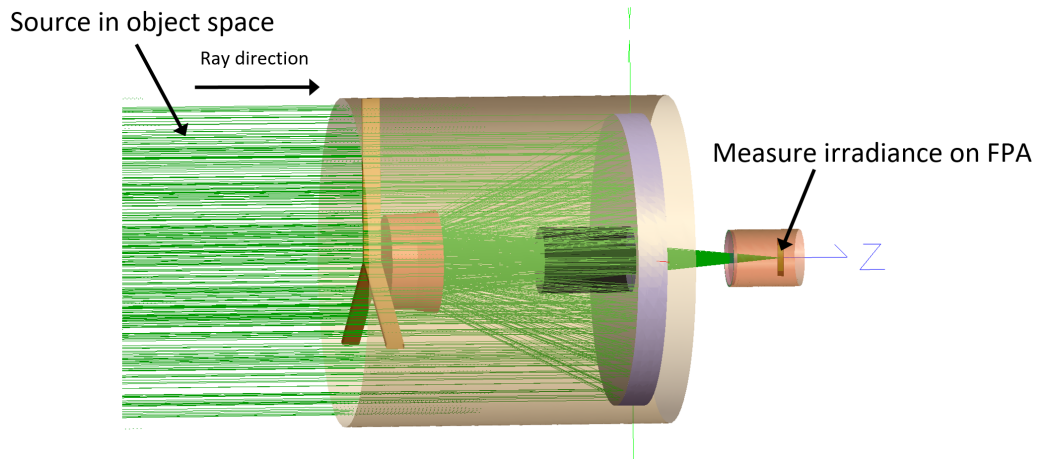


Figure 4.2: Forward raytrace to capture the Cassegrain telescope's on-axis PSF [60].

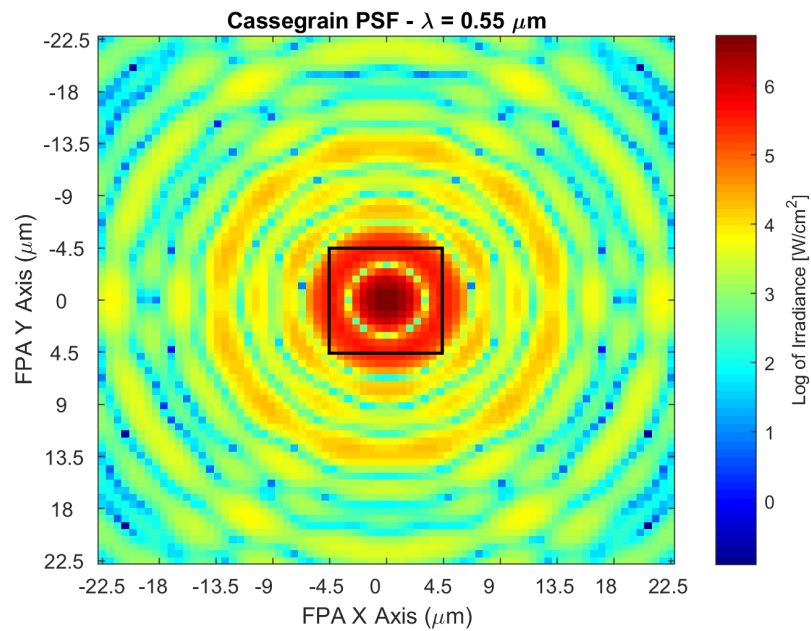


Figure 4.3: Irradiance plot of the Cassegrain system on-axis PSF at $\lambda = 0.55 \mu\text{m}$ (log scale). The black box denotes the spatial extent of a 9- μm FPA pixel [60].

As shown in Fig. 4.3, diffraction from the telescope's entrance aperture produces concentric rings that decrease in magnitude from the PSF center, whereas the six subtle, yet

distinguishable, radial lines are a result of diffraction from the three secondary mirror struts. The fine spatial sampling of these PSF features ensures that DIRSIG will include their impact when sampling a scene, resulting in a more accurate representation of the system's imaging performance. Note that the captured portion of the PSF includes almost eight orders of magnitude; due to the importance sampling approach, spatially-extended PSFs with large dynamic ranges will require significantly more sampling rays to capture the low magnitude contributions.

4.3 METHODOLOGY

The goal of the two PSF tests presented in this chapter is to validate both the PSF importance sampling process and the successful integration of optical engineering software with a radiative transfer image simulation model. For both of these tests, we begin by modeling a 75×75 pixel fine-resolution FPA in DIRSIG with a pixel pitch of $p = 0.6 \mu\text{m}$ and 100% fill factor. We must use this subsampled version of the central 5×5 pixel region of an FPA with $9\text{-}\mu\text{m}$ pixels in DIRSIG, so that we can resolve fine-resolution image details at the focal plane for the purposes of these two validation tests. The ground instantaneous field of view (GIFOV), i.e. the projection of an FPA pixel onto the ground at nadir, is given by

$$\text{GIFOV} = h \cdot \text{IFOV} = \frac{hp}{f}, \quad (4.1)$$

where h is the altitude of the system, p is the pixel pitch, and f is the system's focal length. As shown in Figure 4.4, we have placed the FPA at an altitude slightly over 1 km ($h = 1.02728$ km) and pointing in the nadir direction, thus producing a GIFOV of 1.2 mm for the fine-resolution FPA pixels. Both of the PSF tests were conducted using an

instantaneous image capture (i.e., no integration time is specified). All of the FPA pixels were assigned a uniform, 100% responsivity spectral bandpass of $0.10\ \mu\text{m}$ centered on $0.55\ \mu\text{m}$. No atmospheric effects were included since our goal was to validate the integration method's ability to capture the Cassegrain telescope's performance.

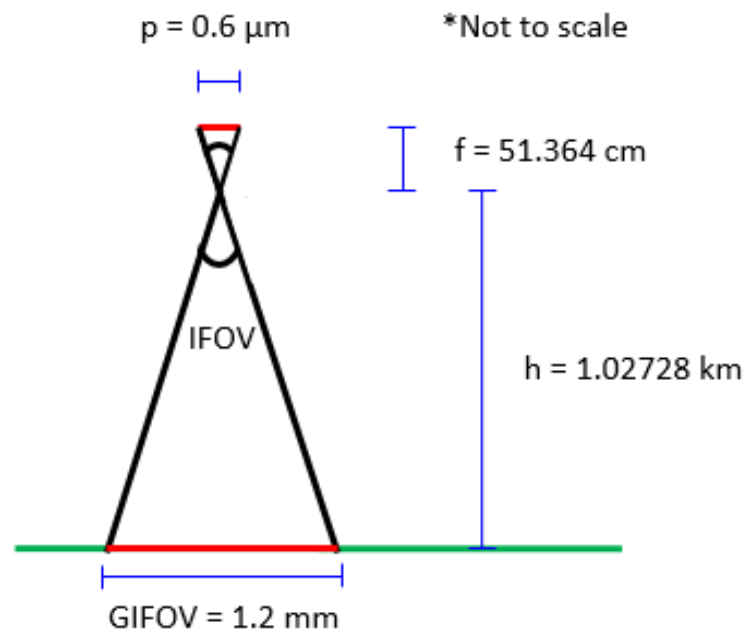


Figure 4.4: System setup for the PSF validation tests.

4.3.1 2-D RECT Function PSF Validation Test

The first validation test provides a validation of the PSF importance sampling process by using a geometric-based PSF and target, thus producing a clear mathematical solution for the ideal output image. We use versions of a 2-D rectangle (RECT) function test target

and PSF, where the 2-D RECT function is defined as [99]

$$RECT \left[\frac{x}{a}, \frac{y}{b} \right] = RECT \left[\frac{x}{a} \right] RECT \left[\frac{y}{b} \right] \quad (4.2)$$

with

$$RECT \left[\frac{x}{a} \right] = \begin{cases} 0, & \text{if } |x| > \frac{a}{2} \\ \frac{1}{2}, & \text{if } |x| = \frac{a}{2} \\ 1, & \text{if } |x| < \frac{a}{2} \end{cases} \quad (4.3)$$

and

$$RECT \left[\frac{y}{b} \right] = \begin{cases} 0, & \text{if } |y| > \frac{b}{2} \\ \frac{1}{2}, & \text{if } |y| = \frac{b}{2} \\ 1, & \text{if } |y| < \frac{b}{2} \end{cases} \quad (4.4)$$

The test target is a 3 cm \times 3 cm (25 \times 25 GIFOV) Lambertian square with a uniform spectral radiance of 100 W/m²/sr/ μ m across the visible and a zero radiance background. The target's radiance therefore forms a 2-D RECT with $a = b = 3$ cm; when projected to the focal plane this becomes $a = b = 15$ μ m. The target is placed directly below the FPA so that the Cassegrain telescope's optical axis is aligned with the center of the target. This test uses a 75 \times 75 pixel artificial PSF (0.6 μ m fine-resolution pixels, the same size as the Cassegrain PSF analysis surface) that contains a 25 pixel \times 25 pixel RECT function of non-zero irradiance with $a = b = 15$ μ m. When projected to the focal plane, the target therefore matches the size of the non-zero portion of the PSF. Although the 2-D RECT function PSF does not represent the impulse response of a real system, we use an arbitrary shift-invariant $G\# = 40$ sr⁻¹ (this is very close to the Cassegrain telescope's on-axis $G\#$)

to convert the output images from radiance to irradiance in accordance with Eq. 3.2 (note that the $G\#$ has no impact on the evaluation metrics used for this validation test).

As discussed in §2.3, the output of a linear, shift-invariant (LSI) system is given by the convolution of the system input and the system's impulse response, which is the PSF for an imaging system [89]. For this validation test, we must also include a convolution with the RECT function representing the FPA pixel since the continuous system output is captured by a discrete grid. The ideal result is therefore the convolution of two 2-D RECT functions (along with an additional convolution with the fine-resolution pixel area), which is approximately a 2-D triangle (TRI) function [99]. This can be expressed as

$$g[x, y] = \frac{L_{\lambda, target} \Delta\lambda}{G\#} \cdot RECT \left[\frac{x}{a}, \frac{y}{b} \right] * \frac{1}{|ab|} RECT \left[\frac{x}{a}, \frac{y}{b} \right] * \frac{1}{|p^2|} RECT \left[\frac{x}{p}, \frac{y}{p} \right] \quad (4.5)$$

$$= \frac{100 \cdot 0.10}{40} \cdot TRI \left[\frac{x}{a}, \frac{y}{b} \right] * \frac{1}{|p^2|} RECT \left[\frac{x}{p}, \frac{y}{p} \right] \quad \left[\frac{W}{m^2} \right], \quad (4.6)$$

$$= 0.25 \cdot TRI \left[\frac{x}{a} \right] TRI \left[\frac{y}{b} \right] * \frac{1}{|p^2|} RECT \left[\frac{x}{p}, \frac{y}{p} \right] \quad \left[\frac{W}{m^2} \right], \quad (4.7)$$

where $L_{\lambda, target}$ is the target's spectral radiance, $\Delta\lambda$ is the spectral bandpass of the FPA fine-resolution pixels, $G\#$ is the conversion factor for converting at-aperture radiance to irradiance, $a = b = 15 \mu\text{m}$, the pixel pitch, $p = 0.6 \mu\text{m}$, and

$$TRI \left[\frac{x}{a} \right] = \begin{cases} 1 - |x|, & \text{if } |x| < |a| \\ 0, & \text{if } |x| \geq |a| \end{cases} \quad (4.8)$$

$$TRI \left[\frac{y}{b} \right] = \begin{cases} 1 - |y|, & \text{if } |y| < |b| \\ 0, & \text{if } |y| \geq |b| \end{cases}. \quad (4.9)$$

Note that the PSF RECT function in Eq. 4.5 has been normalized by its area so that its cumulative probability is one.

4.3.2 Cassegrain PSF Validation Test

The second test uses the Cassegrain PSF from Fig. 4.3 to validate the ability of a radiative transfer image simulation model like DIRSIG to incorporate a PSF from an optical engineering software program such as FRED through the importance sampling approach. The target for this test is a $1.2 \text{ mm} \times 1.2 \text{ mm}$ (1×1 GIFOV) Lambertian RECT function with a uniform spectral radiance of $10 \text{ W/cm}^2/\text{sr}/\mu\text{m}$ across the visible and a zero radiance background. The target center is aligned with the Cassegrain telescope's optical axis as with the first test. Given its small angular extent ($1.17 \mu\text{rad} \times 1.17 \mu\text{rad}$), this target is approximately a point source to the Cassegrain telescope. Eq. 2.27 in §2.3 shows that a Dirac delta function PSF produces a replicated input; however, in this case, it is the input scene, $f[x, y]$ that is the Dirac delta function, and the system impulse response, $h[x, y]$, is the Cassegrain PSF. Using the commutative property of convolution, which states that the order in which two functions are convolved is not important, the expected output $g[x, y]$ is thus given by

$$g[x, y] = \delta[x, y] * h[x, y] = h[x, y] * \delta[x, y] \quad (4.10)$$

$$g[x, y] = \int_{-\infty}^{+\infty} \int_{-\infty}^{+\infty} h[x, y] \delta[x - \xi, y - \eta] d\xi d\eta = h[x, y], \quad (4.11)$$

i.e., according to linear systems theory, imaging a point source produces the system impulse response. In the case of our Cassegrain PSF validation test, the ideal output image is a

replication of the Cassegrain PSF. However, DIRSIG is not performing an actual convolution operation, but instead importance sampling the scene with a finite number of rays and the 1×1 GIFOV target is only approximately a Dirac delta function. It is thus more accurate to state

$$g[x, y] \approx h[x, y]. \quad (4.12)$$

We therefore expect our output to more accurately replicate the Cassegrain PSF as the number of DIRSIG sampling rays increases. Using the Cassegrain telescope's on-axis $G\# = 39.17 \text{ sr}^{-1}$ determined via a raytrace of the model, we are able to convert the output images for this test from radiance to irradiance.

4.3.3 Evaluation Metrics

As outlined in Table 4.1, we simulated nine separate test cases using increasing numbers of DIRSIG sampling rays per FPA pixel in order to evaluate how the output images converge to the ideal results both spatially and radiometrically. Although DIRSIG does have an adaptive sampling capability to determine a sufficient number of sampling rays within a specified range based on a radiometric convergence criterion, in these cases, we are forcing DIRSIG to sample the scene with the specified number of rays. Each test case was run ten times so that statistics for each test case could be evaluated.

Any test case above at least 5,625 sampling rays would theoretically allow for uniform sampling of the PSF fine-resolution pixels (our 75×75 pixel PSFs contain 5,625 total fine-resolution pixels) when determining the scene's radiance contribution for a given FPA pixel. However, this method would not easily incorporate the convolution with the FPA pixel in-the-loop of the simulation as with the PSF importance sampling approach. Significantly

more rays, each with their own initial FPA pixel offset, would be required to uniformly sample each PSF fine-resolution pixel in order to capture the FPA pixel convolution effect, thus leading to a considerable increase in simulation run time. One of the primary design goals of DIRSIG5 is to provide users with a single fidelity factor, i.e. the number of samples per FPA pixel, rather than tying the number of sampling rays to the PSF size and resolution. Although DIRSIG simulations do not typically use the highest numbers of sampling rays in Table 4.1, we include these cases for these validation tests to better illustrate the spatial and radiometric convergence of the PSF importance sampling process.

Table 4.1: Number of DIRSIG sampling rays per FPA pixel tested for the PSF validation tests.

of Sampling Rays
250
500
1,000
2,500
5,000
10,000
25,000
50,000
100,000

For spatial comparison of each simulation result, we calculated the 2-D correlation coefficient, r , which is given by

$$r = \frac{\sum_{m=1}^M \sum_{n=1}^N (D_{mn} - \bar{D})(I_{mn} - \bar{I})}{\sqrt{\left(\sum_{m=1}^M \sum_{n=1}^N (D_{mn} - \bar{D})^2\right) \left(\sum_{m=1}^M \sum_{n=1}^N (I_{mn} - \bar{I})^2\right)}}, \quad (4.13)$$

where D_{mn} and I_{mn} are the irradiance values in the DIRSIG output image D and the ideal

output image I at row m and column n , and \bar{D} and \bar{I} are the mean irradiance values of D and I , respectively. The approximate TRI function in Eq. 4.7 is the ideal output image, I , for the first PSF validation test, whereas the Cassegrain PSF from FRED convolved with a detector element is I for the second test. Perfectly correlated data will produce $r = 1$. For both tests, r should converge to 1 as more DIRSIG sampling rays are used and the variance over the ten simulations at each number of rays should decrease. The root-mean-square error (RMSE) provided by Eq. 4.14 was also calculated for each of the ten simulations in every test case to quantify the deviation from the ideal result. RMSE is calculated according to

$$RMSE = \sqrt{\frac{1}{N} \sum_{n=1}^N (x_n - \hat{x})^2}, \quad (4.14)$$

where x_n is the n th simulated value (2-D correlation coefficient for this first metric) for a given test case, \hat{x} is the ideal simulated value (one for the 2-D correlation coefficient), and N is the total number of simulations (ten for each of these validation tests).

Our second metric is a ratio of the total irradiance in each output image to the total irradiance of the ideal image for each validation test. These total irradiance values are calculated by separately summing all of the individual pixel irradiance values in the output images and the targets projected to the focal plane. The ratio of the total irradiance in each output image and the irradiance of the ideal image should also converge to one as more DIRSIG sampling rays are used per FPA pixel. As with the previous metric, the RMSE for each simulation was calculated.

Although we have converted the output images to irradiance for both validation tests to demonstrate the radiometric conversion detailed in §3.2.1, the arbitrary $G\#$ for the 2-D RECT function test and the Cassegrain $G\#$ have no impact on the test results. The

calculation of the spatial correlation coefficient metric in Eq. 4.13 is unaffected by positive image scaling factors and the $G\#$ cancels out when calculating the irradiance ratio. The results for each validation test are therefore based solely on the incorporation of the PSF data through the importance sampling process, not the radiometric conversion factor.

The spatial and radiometric statistics produced by these tests do not provide universal results for any arbitrary imaging scenario. The exact spatial and radiometric errors for any given imaging scenario are a function of the given system's PSF spatial distribution, resolution, support, and dynamic range, the scene's spatial and radiometric characteristics, and the number of sampling rays per pixel. These tests validate the PSF importance sampling process, while highlighting general convergence trends that provide insight into other imaging scenarios.

4.4 RESULTS

4.4.1 2-D RECT Function PSF Validation Test Results

Figure 4.5 displays the log-scaled ideal result of imaging the 25×25 GIFOV RECT target with the RECT PSF (calculated using the `conv2` function in MATLAB [156]), along with sample output images from the simulations conducted for five of the test cases. All of these images are in irradiance units and plotted on a common 0–0.25 W/m² scale. Qualitatively, it is evident that the output images more closely match the ideal result as the number of sampling rays per FPA pixel increases. As shown in Fig. 4.5b, with 250 sampling rays per pixel and the corresponding statistical noise, the output image exhibits a TRI function with the proper spatial dimensions and a maximum irradiance near 0.25 W/m². By the time 10,000 sampling rays per FPA pixel are used, the output image becomes almost visually

indistinguishable from the “ideal” MATLAB result. Figure 4.6 shows the difference image between the ideal result in Fig. 4.5a and the image with 10,000 sampling rays per FPA pixel in Fig. 4.5e, highlighting the minimal variations between the two images. This simple geometric-based validation test illustrates that imaging a scene using a PSF as a probabilistic distribution driving importance sampling effectively emulates the convolution of a scene with a PSF and FPA pixel area.

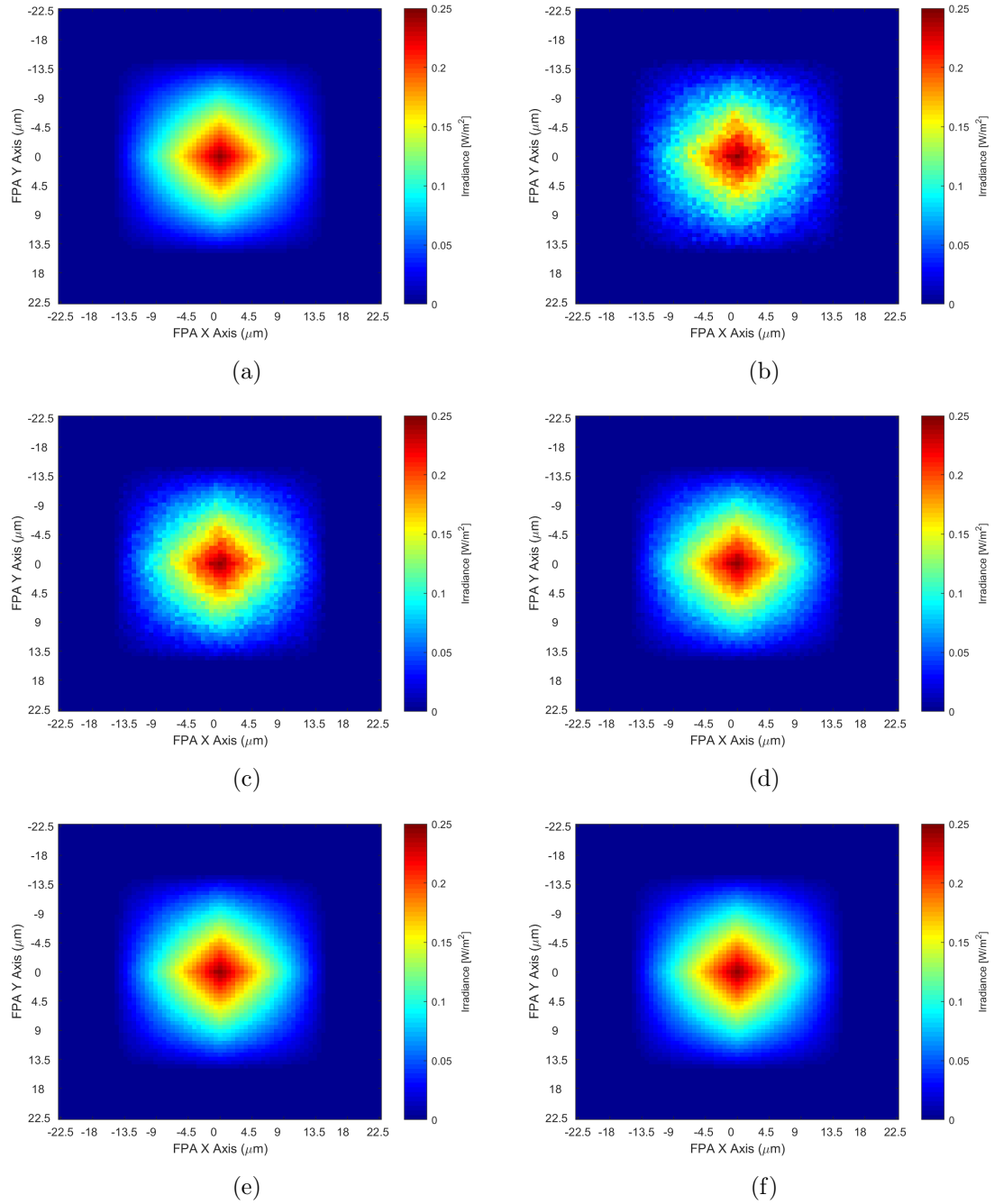


Figure 4.5: Ideal result and DIRSIG output images for the 2-D RECT function PSF validation test: (a) Ideal result. (b) 250 sampling rays per FPA pixel. (c) 500 sampling rays per FPA pixel. (d) 1,000 sampling rays per FPA pixel. (e) 10,000 sampling rays per FPA pixel. (f) 100,000 sampling rays per FPA pixel.

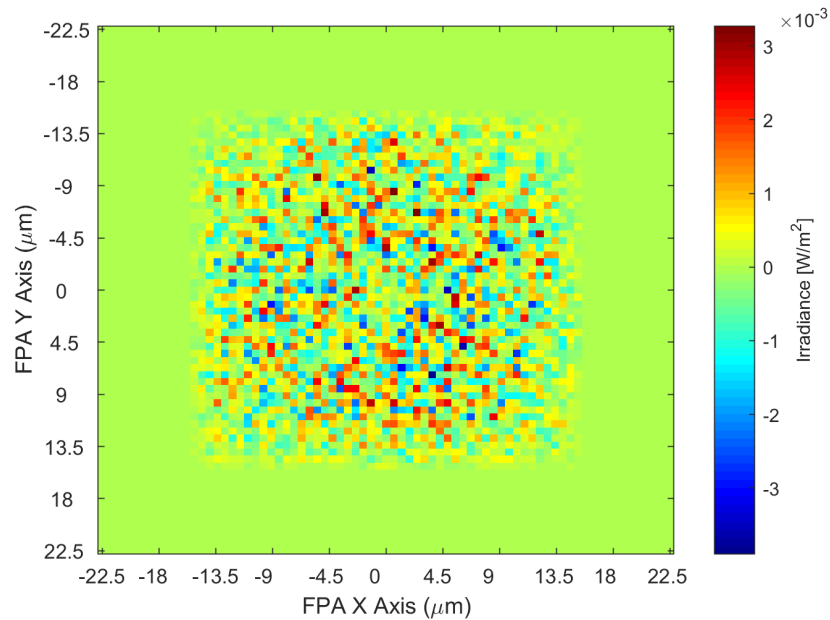


Figure 4.6: Difference image between the ideal result and the DIRSIG image with 10,000 sampling rays per FPA pixel for the 2-D RECT function PSF validation test.

We can quantitatively analyze the spatial convergence of the output images to the ideal result from the 2-D correlation coefficients, r , for each test case in Fig. 4.7 and the RMSE for these values in Fig. 4.8. Each data point in Fig. 4.7 shows the mean of the ten simulations conducted for each test case along with error bars denoting the extent of one standard deviation (σ) in either direction. The 2-D correlation coefficients converge to one with extremely small variances as the number of sampling rays increases, whereas the RMSE is reduced by approximately $\frac{1}{n}$, where n is the number of DIRSIG sampling rays per FPA pixel.

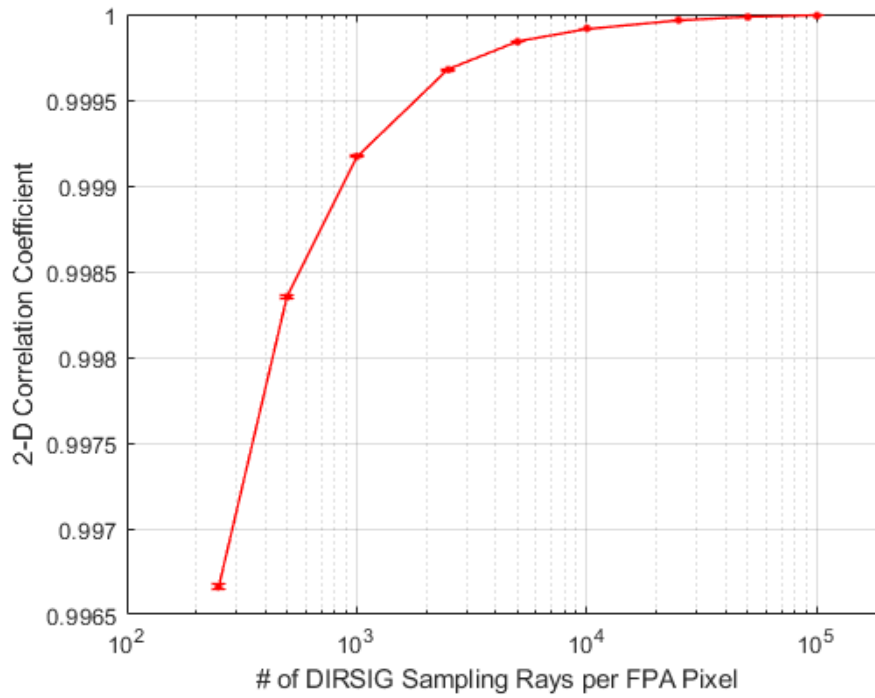


Figure 4.7: 2-D correlation coefficient between the ideal result and the DIRSIG images for each test case of the 2-D RECT function PSF validation test. The data points indicate the mean value of the ten simulations conducted for each test case, with the error bars extending plus or minus one standard deviation.

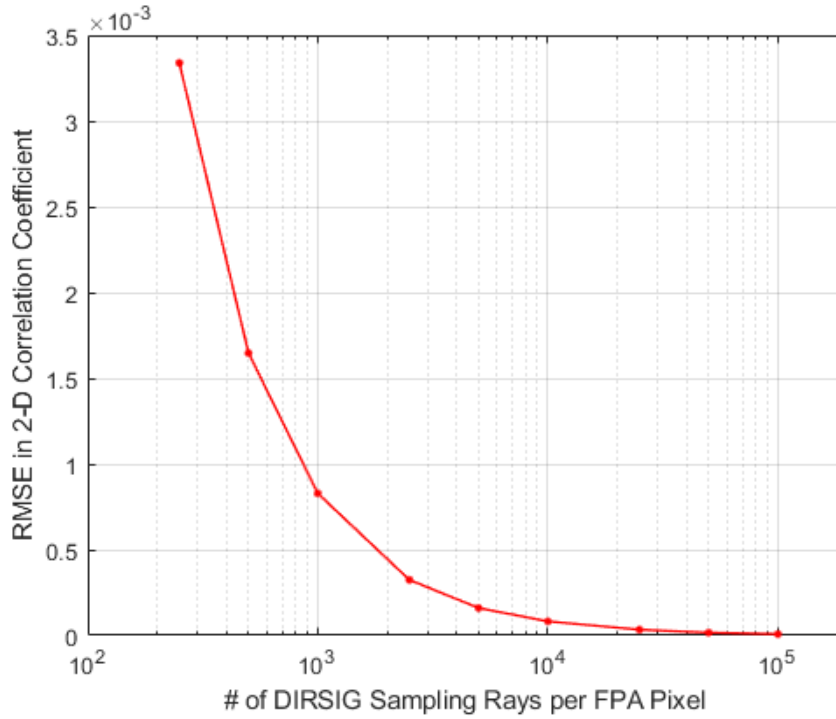


Figure 4.8: RMSE in 2-D correlation coefficient v. number of DIRSIG sampling rays for the 2-D RECT function PSF validation test.

Figure 4.9 shows the mean irradiance ratio for each test case, along with error bars extending $\pm \sigma$, whereas Fig. 4.10 provides the RMSE values. The irradiance ratio fluctuates by roughly $\pm 0.05\%$ at lower numbers of sampling rays before rising towards the ideal value of 1, with the variance decreasing as the number of rays increases. Minor fluctuations in the irradiance ratio are to be expected given the various statistical factors at play (e.g. PSF spatial distribution, resolution, support, and dynamic range, target spatial and radiometric characteristics, number of sampling rays, etc.), though we are still investigating how each of these factors influence the trend of radiometric convergence for a given scenario. The RMSEs are minuscule for all of the test cases, with the 250 ray test case producing an irradiance ratio error on the order of 0.06%. The irradiance ratio RMSE falls at a faster rate as the number of rays increases, although the 500 ray case is an exception due to the fact that the mean

irradiance ratio lies close to 1. In conjunction with the 2-D correlation coefficient results, these data demonstrate the importance sampling approach's effectiveness at producing both spatial distribution and radiometric convergence as the number of sampling rays per FPA pixel increases.

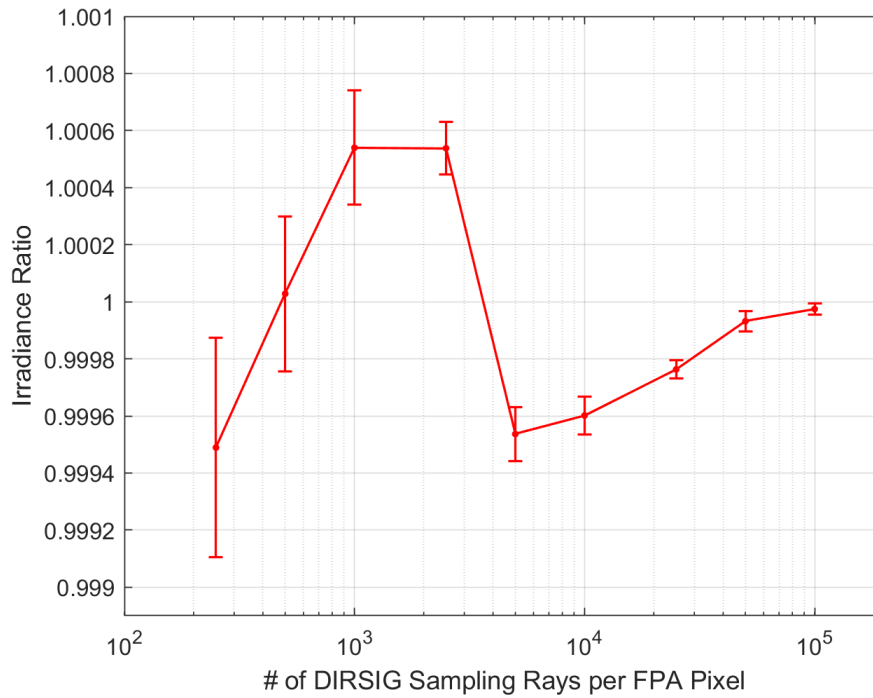


Figure 4.9: Irradiance ratio for each test case of the 2-D RECT function PSF validation test. The data points indicate the mean value of the ten simulations conducted for each test case, with the error bars extending plus or minus one standard deviation.

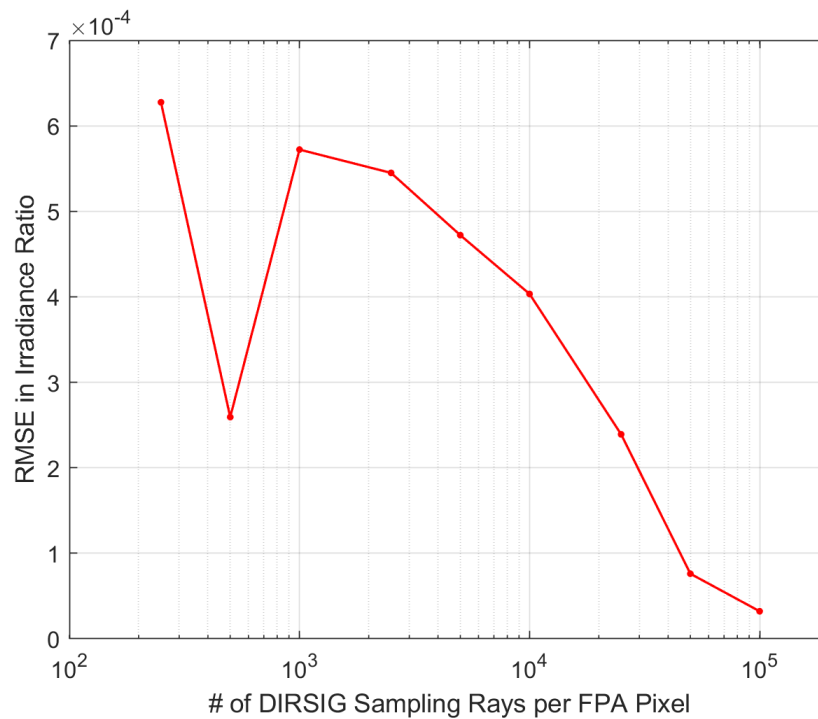


Figure 4.10: RMSE of the irradiance ratio v. number of DIRSIG sampling rays for the 2-D RECT function PSF validation test.

4.4.2 Cassegrain PSF Validation Test Results

The Cassegrain PSF validation test builds upon these results by using the Cassegrain system's PSF to demonstrate the integration of optical engineering software models with a radiative transfer image simulation model. Figure 4.11 displays the log-scaled Cassegrain PSF from FRED (i.e. the ideal result), along with images of the 1×1 GIFOV target imaged with the Cassegrain PSF data in DIRSIG for one simulation from five different test cases. For visualization purposes, all of the plots have been normalized to their maximum irradiance values and plotted on an 8-decade log scale. Similar to the 2-D RECT function PSF test, the output images approach the ideal result as more sampling rays are used per FPA pixel. Even at the lowest numbers of sampling rays, the importance sampling

approach has very closely replicated the large magnitude core of the PSF along with the first major diffraction ring. The details of the outer diffraction rings that are 3–4 orders of magnitude below the PSF maximum progressively appear with larger numbers of sampling rays. Due to the probabilistic nature of PSF importance sampling, the order of magnitude of the number of sampling rays per FPA pixel is directly linked to how many PSF orders of magnitude are sampled. Consequently, more of the PSF will be spatially sampled for larger numbers of sampling rays.

Once again, it should be noted that this PSF test is only an approximation of imaging a point source. The error introduced by imaging a small RECT target rather than a true Dirac delta function target can be seen by comparing the output images, where the gaps between the diffraction rings are filled in by the emulated convolution with the target area, to the FRED Cassegrain PSF. Despite this test limitation, these images indicate that a radiative transfer image simulation model can incorporate PSF data collected from an optomechanical system software model to emulate the system model's performance imaging a scene.

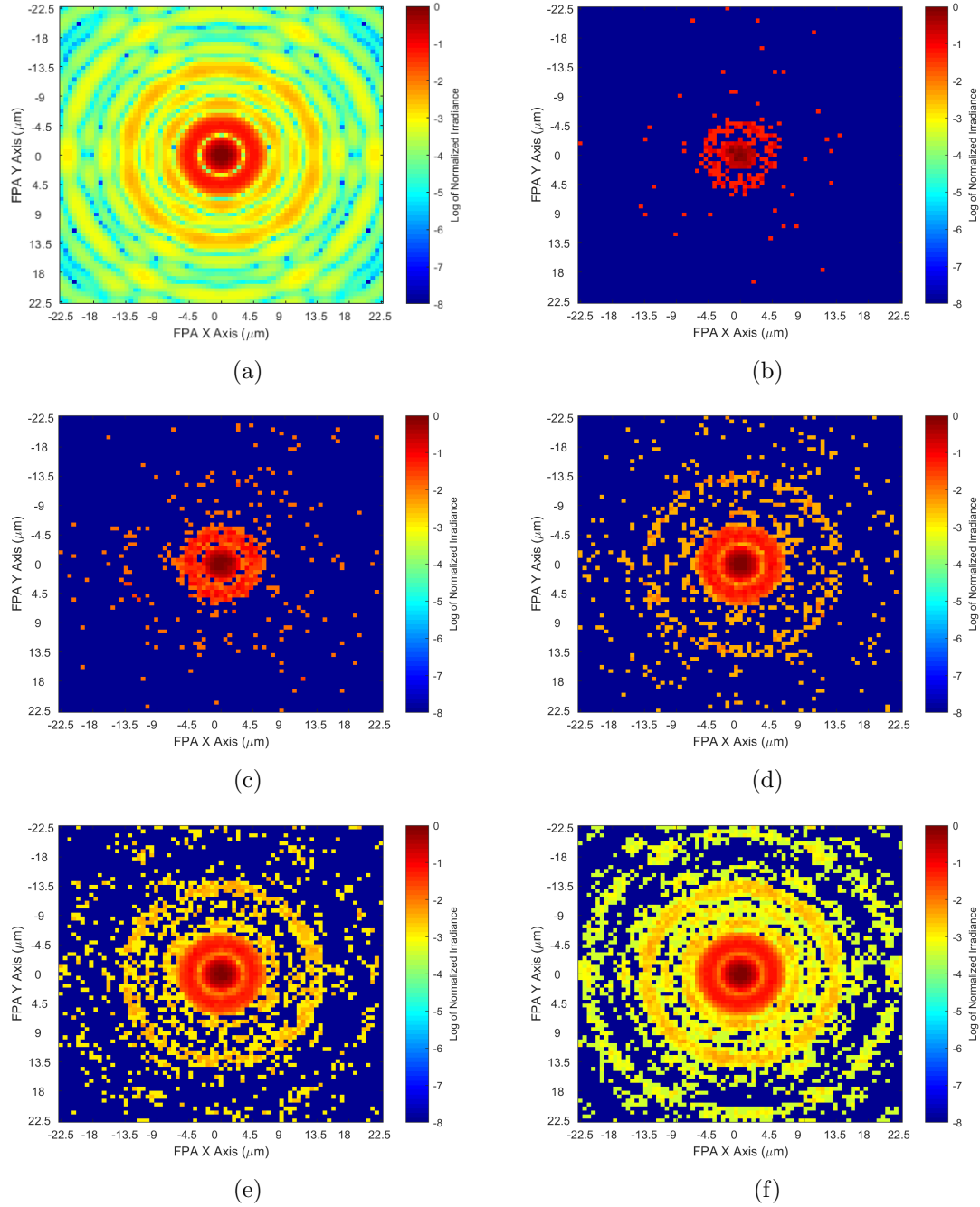


Figure 4.11: Ideal result and DIRSIG output images for the Cassegrain PSF validation test (log scales): (a) FRED Cassegrain PSF. (b) 500 sampling rays per FPA pixel. (c) 2,500 sampling rays per FPA pixel. (d) 10,000 sampling rays per FPA pixel. (e) 25,000 sampling rays per FPA pixel. (f) 100,000 sampling rays per FPA pixel.

We examine the 2-D correlation coefficients, r , in Fig. 4.12, with the RMSE for these values displayed in Fig. 4.13. Each data point in Fig. 4.12 indicates the mean of the ten simulations conducted for each test case, with the error bars denoting $\pm \sigma$. As with the 2-D RECT function PSF test, r converges to one and the variance for each test case decreases with increasing numbers of DIRSIG sampling rays per FPA pixel. However, it is important to understand the performance differences between the 2-D RECT function and Cassegrain PSF validation tests, since our integration method ultimately uses PSFs from system models and not generic geometric-based PSFs. For the Cassegrain PSF test, the r values start out much lower and have significantly higher variances. The reduction in r and increase in variance for all Cassegrain PSF test cases is due to several factors, including the much smaller target size required for the Cassegrain PSF test and both the larger dynamic range and spatial support of the Cassegrain PSF compared to the uniform probability and smaller non-zero 25×25 fine-resolution pixel portion of the 2-D RECT function PSF. Regarding the target size, there is only at most a one pixel overlap on the focal plane between the 1×1 GIFOV target and Cassegrain PSF when conducting the importance sampling for any given FPA pixel (in contrast, the 25×25 GIFOV target projects to 625 FPA pixels). This greatly reduces the probability that the 1×1 GIFOV target will be sampled by any individual sampling ray, leading to more sparse spatial replications of the Cassegrain PSF and reduced r values, especially at lower ray counts. The Cassegrain PSF's large dynamic range plays a role in reducing r and creating higher variance due to the fact that there is a lower probability that the target will be sampled when the lower magnitude PSF regions are overlapping the 1×1 GIFOV target (i.e. when collecting the irradiance contributions for pixels farther from the FPA's center). Many more DIRSIG sampling rays would therefore be needed to achieve the same r value for the Cassegrain PSF test compared to the 2-D

RECT function PSF test. Similarly, the larger spatial support of non-zero fine-resolution pixels in the Cassegrain PSF means that more sampling rays are required to recreate the full spatial extent of the PSF than the 2-D RECT function PSF.

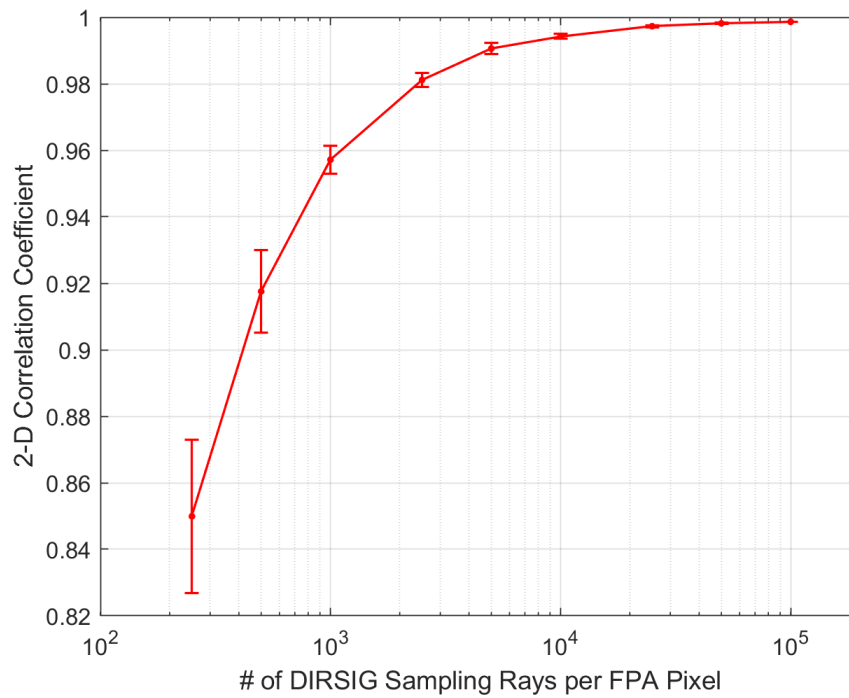


Figure 4.12: 2-D correlation coefficient between the FRED Cassegrain PSF and the DIRSIG images for the Cassegrain PSF validation test. The data points indicate the mean value of the ten simulations conducted for each test case, with the error bars extending one standard deviation in each direction.

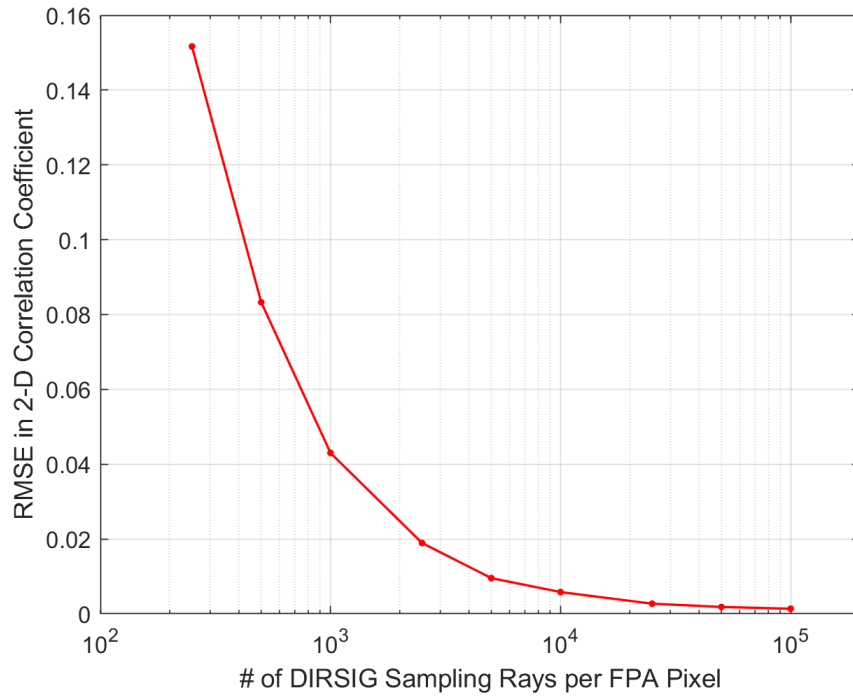


Figure 4.13: 2-D correlation coefficient RMSE v. number of DIRSIG sampling rays for the Cassegrain PSF validation test.

The RMSE in r once again approximately falls as $\frac{1}{n}$, where n is the number of DIRSIG sampling rays per FPA pixel. Despite the overall increased spatial RMSEs for this test, the 2,500 sampling ray case in Fig. 4.11c illustrates the importance sampling approach's success at recreating the Cassegrain PSF's central core and first diffraction ring. Although much of the outer PSF regions that are orders of magnitude below the maximum are not sampled at this sampling count, by far the most significant portions of the PSF have already been sufficiently sampled. On a linear scale, the regions beyond the first diffraction ring are barely discernible. This reveals an important insight when using an optomechanical system's PSF; due to the importance sampling approach, a relatively small number of rays are needed to sample the highest magnitude PSF regions, even for PSFs with a large dynamic range. This efficient sampling approach leads to diminishing returns with increasing numbers of

sampling rays, as evidenced by the exponential decrease in the spatial RMSE.

Since irradiance contributions for a given FPA pixel depend on both a system's susceptibility (i.e. PSF probability) and the scene's radiance at a given object space angle, high radiance sources at low susceptibility angles (outer PSF regions) may still provide meaningful contributions. More sampling rays can be used to capture the spatial impact of such high radiance sources. However, high source radiance, low susceptibility angle contributions are less of a concern for the integration method's PSF component than the stray light component for two primary reasons. First, in general, PSF magnitude falls off by orders of magnitude over relatively small distances from the PSF center, thus limiting the object space angles that can provide meaningful irradiance contributions for a given FPA pixel. Second, the PSF importance sampling approach results in sub-IFOV sampling around the IFOV of the particular FPA pixel being sampled (using typical FPA pixels and not the subsampled, fine-resolution pixels we use here in our validation tests). This reduces the angular extent of a high radiance source at a low susceptibility angle that can still provide a meaningful irradiance contribution at the focal plane while not being sampled; this is especially true for higher resolution systems. Ultimately, it is the user's decision as to how many sampling rays to use per FPA pixel based on the given imaging scenario and the desired simulation fidelity and run time.

Figure 4.14 displays the mean irradiance ratio for each test case of the Cassegrain PSF validation test, with Fig. 4.15 containing the irradiance ratio RMSEs. As with the 2-D correlation coefficients, the irradiance ratios converge to one and have lower variance as the number of DIRSIG sampling rays increase. However, the Cassegrain PSF irradiance ratios have much larger variances and RMSEs than the RECT PSF test cases. In addition to the smaller target size, larger PSF dynamic range, and increased PSF spatial support, this

elevated RMSE can also be attributed to a radiometric sampling effect related to the law of large numbers.

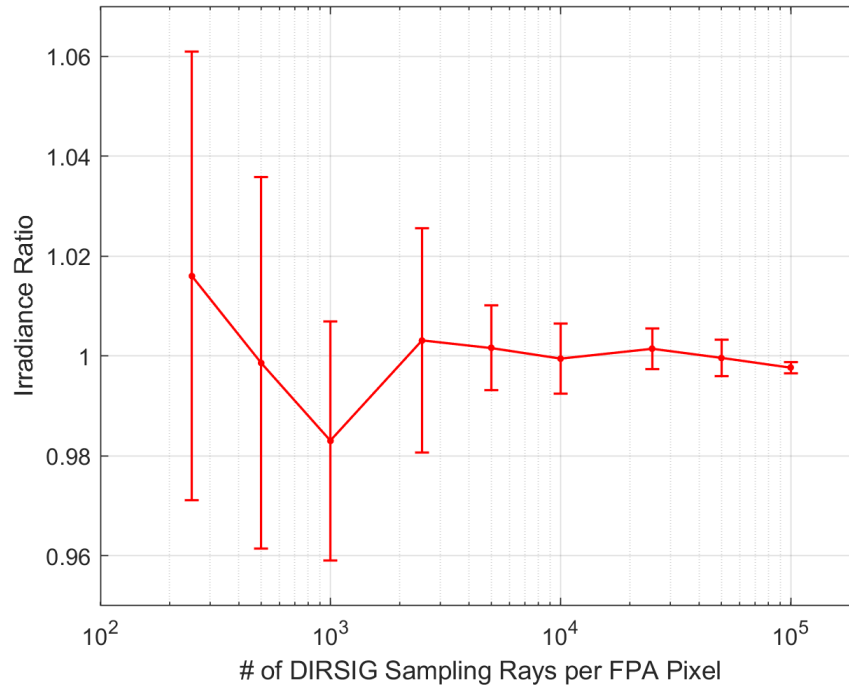


Figure 4.14: Irradiance ratio for each test case of the Cassegrain PSF validation test. The data points indicate the mean value of the ten simulations conducted for each test case, with the error bars extending plus or minus one standard deviation.

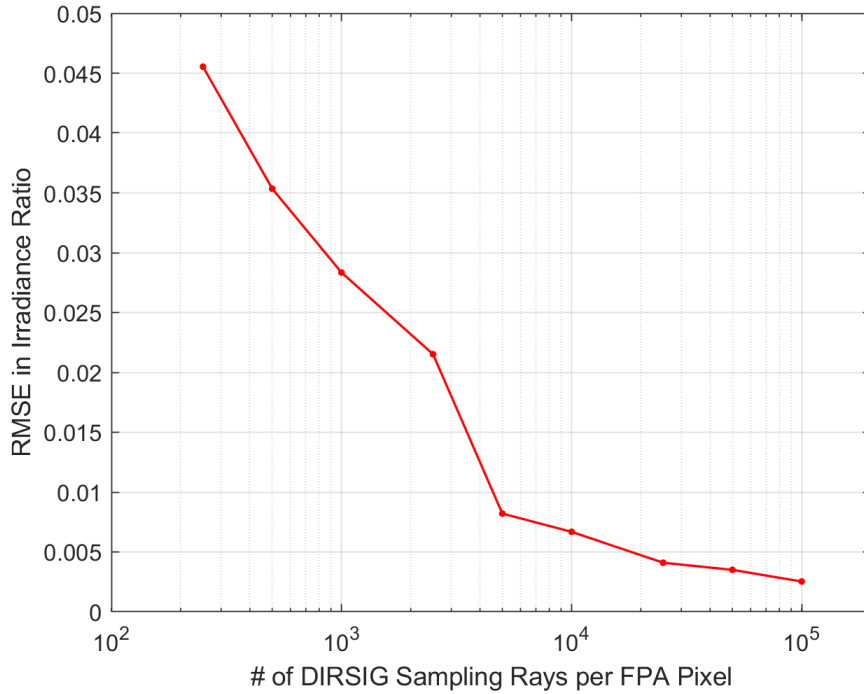


Figure 4.15: RMSE of the irradiance ratio v. number of DIRSIG sampling rays for the Cassegrain PSF validation test.

If we examine the results in Fig. 4.11 on a per-pixel basis and assume the FPA has a dynamic range matching the magnitude of the output images, 500 sampling rays are needed in order for the mean individual pixel radiometric error to fall below the quantization level of an 8-bit system, whereas 25,000 sampling rays reduce the error below a 10-bit system's quantization level. Note that these statistics are dependent on a given system's PSF and the specific scene being imaged, so these results will vary for an arbitrary imaging scenario. In general, PSFs with narrower, higher-magnitude cores and smaller spatial support will require fewer sampling rays to achieve a mean individual pixel radiometric error below a certain quantization level. This is due to the fact that a large percentage of the sampling rays for each FPA pixel sample the high magnitude core of the PSF, more accurately representing the true radiometric contribution of these PSF regions. Although many of the

fine-resolution pixels in the lower magnitude regions of the PSF are not sampled at lower sampling ray counts, they typically will not provide meaningful contributions regardless (exception: very high radiance sources), thus resulting in a minimal increase in radiometric error. In the most extreme case of an approximate Delta function PSF, all of the DIRSIG sampling rays will sample within the given pixel's IFOV, resulting in a very low radiometric error.

4.4.3 PSF Importance Sampling and the Law of Large Numbers

When DIRSIG samples a scene for a given FPA pixel using a PSF, the radiance contributions from all of the individual ray samples are averaged to calculate the pixel's radiance, which is then converted to irradiance using the system's $G\#$. Since the PSF fine-resolution pixels have a non-uniform probability distribution for a real system, the number of times each pixel is selected via importance sampling acts as a weighting factor for the average radiance calculation. As more sampling rays are used per FPA pixel, the distribution of the number of times each PSF pixel is sampled relative to the total number of samples more closely resembles the PSF's actual probabilistic distribution. This phenomenon can be explained by a generalized case of Borel's strong law of large numbers [155, 157]. If an experiment is performed many times independently and under identical conditions, then the proportion of times a specific event, E , occurs will converge to its probability of occurrence on any given trial. This can be written as

$$\lim_{n \rightarrow \infty} \frac{N_n(E)}{n} \rightarrow p, \quad (4.15)$$

where E denotes the specific event, n is the total number of trials, $N_n(E)$ is the number of times that event E occurs in n trials, and p is the probability of the event's occurrence on a single trial. The error between $\frac{N_n(E)}{n}$ and p for each FPA pixel is therefore greatest when n is small, i.e. in our case, at low numbers of sampling rays [155].

We can see evidence of this effect in Fig. 4.11, where the radiometric error is most noticeable in the images using the lowest numbers of sampling rays. For example, in Fig. 4.11b the sparse pixels in the outer regions of the FPA have approximately 5% of the irradiance of the center FPA pixels and are caused by 1 out of 500 rays sampling the 1×1 GIFOV target (i.e. $\frac{N_n(E)}{n} = \frac{1}{500}$). In reality, from observing Fig. 4.11a, the outer FPA pixel irradiance values should be at least three orders of magnitude below the center of the FPA, since $p = 10^{-5}$ to 10^{-4} for the corresponding fine-resolution PSF pixels that overlap the target for these FPA pixels. As more sampling rays per FPA pixel are used, the irradiance of the outer FPA pixels starts to fall to lower orders of magnitude that are more in line with their expected levels from the Cassegrain PSF, i.e. $\frac{N_n(E)}{n} \rightarrow p$. This process repeats itself as even lower magnitude PSF regions are sampled at higher numbers of sampling rays, resulting in more diminished irradiance ratio rises and falls. Similar to the spatial distribution analysis, the dynamic range of the optomechanical system software model's PSF directly correlates to how many sampling rays per FPA pixel should be used to achieve the highest fidelity radiometric results. These same issues do not appear in the 2-D RECT function PSF test cases because of the uniform probability of the 2-D RECT function PSF. In general, the radiometric error is also scene dependent; heterogeneous scenes will lead to comparatively more error than homogeneous scenes. For any arbitrary scene, there is an interplay between the number of DIRSIG sampling rays per FPA pixel and the PSF's probability distribution, dynamic range, and spatial support. The Cassegrain PSF test provides an example of

one system imaging a simple target, but is not an exhaustive study of all possible imaging scenarios.

4.5 SUMMARY AND CONCLUSIONS

In this chapter, we have focused on the first milestone in our integration methodology, the incorporation of PSF data from an optomechanical system software model and its correct usage in a radiative transfer image simulation model. This fulfills research objectives 1 and 2 from §1.2 in demonstrating a general methodology for integrating optomechanical system models from optical engineering software with a radiative transfer image simulation model, as well as validating the integration method's capability to accurately incorporate the PSF component. Although PSF integration could be accomplished with scene oversampling, a convolution, and downsampling, this assumes that it is possible to convolve the PSF with a large 2-D image. Many modern remote sensing systems are not 2-D arrays and an oversampled scene data product can be massive. To avoid these limitations, we have introduced a two-step importance sampling process to emulate the PSF convolution in-the-loop of the simulation. Importance sampling effectively adapts to arbitrary probability distributions, but PSFs with larger dynamic range and spatial support require more rays to properly sample due to the law of large numbers. It is important that the user consider the desired simulation fidelity when determining the size of the included PSF and the number of sampling rays. Future work should test methods that reduce the error due to the law of large numbers by limiting PSF dynamic range while still preserving sufficient spatial sampling to capture important PSF features. Despite the statistical challenges, the results presented here validate the capability of a radiative transfer image simulation

model to properly incorporate a PSF from an optomechanical system software model and use importance sampling to image a scene and produce accurate spatial and radiometric results. The integration of imaging performance data from high-fidelity 3-D CAD optomechanical system models significantly expands the system analysis capability of radiative transfer image simulation models by increasing the number of system design parameters that can be modified and whose impact can be directly assessed in user end products.

Chapter 5

Stray Light Component Validation

5.1 INTRODUCTION

In order to provide a rigorous validation of the stray light component radiometry in Eq. 3.6, we have conducted several stray light validation tests using FRED Optical Engineering Software and DIRSIG. The goal of the first test is to validate FRED's capability to produce highly accurate scatter radiometry for a single source-collector area pair (with FRED serving as a proxy for optical engineering software in general). The second test further validates FRED's stray light radiometry, as well as the Cassegrain telescope model used in the remaining tests, by comparing stray light forward raytrace results (from object space to the focal plane) of a simple target to analytical equations for calculating in-field scatter in an optical system provided by Peterson [158]. This is not strictly necessary to prove the validity of the integration method itself, but does provide additional support that FRED follows the basic stray light radiative transfer equation in Eq. 2.17 on a surface-by-surface basis within a detailed optomechanical system model. This is especially important given that

the stray light contributions for an arbitrary system and scene cannot be readily calculated analytically for validation purposes. Combined with the first test, this second test provides confidence in the absolute stray light radiometry of FRED for any arbitrary system, which is a key step in trusting the radiometric fidelity of the stray light ASM data used in the integration method. The third test demonstrates the Cassegrain model's reciprocity, validating the integration method's foundational stray light radiometric principle, i.e. that reverse raytrace (focal plane to object space) stray light susceptibility data are equivalent to a system's stray light susceptibility in the forward direction. This in turn justifies using reverse raytrace system stray light susceptibility data to estimate stray light contributions at the focal plane from an arbitrary scene in the forward direction. Finally, the last test implements the integration method by capturing the Cassegrain's stray light ASM for a small detector and the environmental radiance map (ERM) of a DIRSIG target scene to estimate the total stray light captured by the detector. The integration method results are then compared to the FRED raytrace results to prove that the integration method has successfully emulated the Cassegrain telescope's performance within DIRSIG.

These tests ultimately radiometrically validate the method of integrating stray light susceptibility data captured from an optomechanical system software model with a scene's at-aperture radiance profile from a radiative transfer image simulation model to accurately estimate the stray light contributions for a detector given an arbitrary system and scene. This provides confidence to optical engineers, remote sensing application scientists, and program managers alike that this modeling and simulation-based integration method can be used to perform system trade studies that quantitatively link specific design parameters to user application impact. Chapter 6 builds upon this stray light validation work by demonstrating how the integration methodology can be used to perform stray light-related

system trade studies and produce useful quantifiable metrics to assess the impact of stray light on user applications.

5.2 METHODOLOGY

As shown in Fig. 5.1, the first stray light test uses a simple setup of two parallel aligned square surfaces to validate FRED's capability to produce very accurate scatter radiometry. Both surfaces are $2\text{ cm} \times 2\text{ cm}$ in area and placed 5 cm apart. The source area is modeled as a Lambertian surface with a TIS = 100% that scatters light to the collector area. Since the BSDF of a Lambertian surface is given by $\text{BSDF} = \text{TIS}/\pi$, the source surface's BSDF = $1/\pi\text{ sr}^{-1}$. The source area is directly illuminated by a 1-W, 0.55- μm source with 10 million initial rays located just above the surface. The source's rays directly impinge upon the source surface, creating ten scatter rays for every incident ray. Importance sampling specifications ensure that the scattered rays that are traced are directed towards the collector for the sake of raytrace efficiency and higher fidelity radiometric results.

In order to analytically calculate the expected scatter radiant flux on the collector using the basic stray light radiative transfer equation in Eq. 2.17, we must first calculate the geometric configuration factor (GCF) of the collector as seen by the source surface. Fortunately, our simple setup allows this GCF to be easily calculated using numerical integration. Note that the GCF calculation is much more complex for arbitrary source and collector surfaces and their associated geometry. This highlights the difficulty of analytically calculating the stray light performance of a detailed system with any geometric configuration and set of scatter models. Demonstrating the capability for FRED to produce highly accurate scatter radiometry for this simple setup which can be analytically validated thus provides solid

evidence of FRED's ability to accurately model the scatter between surfaces with much more complicated geometries, where analytical validation is much more difficult.

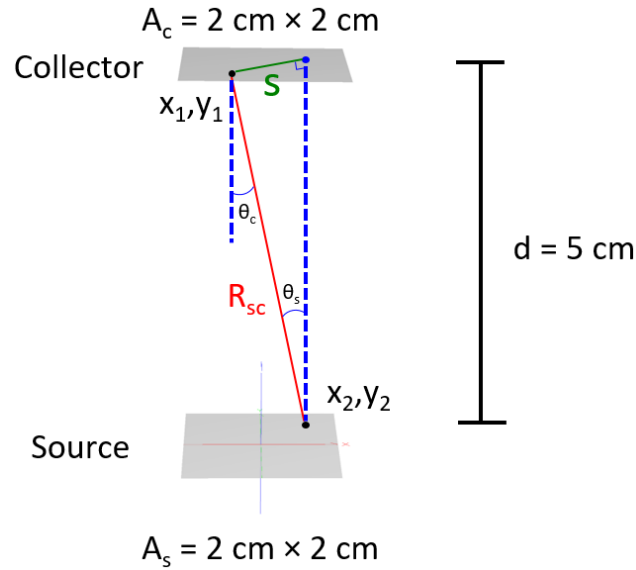


Figure 5.1: Simple FRED setup of two parallel aligned square surfaces for use in the first stray light validation test. A source placed directly above the source area illuminates the Lambertian source surface, scattering rays towards the collector. The scatter radiant flux captured by the collector during a series of FRED raytraces can then be compared to the analytically calculated value.

We begin our derivation of the GCF expression for the source-collector setup by starting with the general GCF equation in Eq. 2.19,

$$\text{GCF}_{\text{collector}} = \frac{A_c \cos \theta_s \cos \theta_c}{\pi R_{sc}^2}, \quad (5.1)$$

where A_c is the collector area, R_{sc} is the distance between a point x_1, y_1 on the collector surface and x_2, y_2 on the source surface, and θ_s and θ_c are the angles from the surface normals to the line connecting the two points on the source and collector surfaces, respectively.

Since both the source and collector surfaces are extended areas, we must express Eq. 5.1 in differential form and integrate over both areas, producing

$$\text{GCF}_{collector} = \frac{1}{\pi A_s} \int_{y_2} \int_{x_2} \int_{y_1} \int_{x_1} \frac{\cos \theta_s \cos \theta_c}{R_{sc}^2} dx_1 dy_1 dx_2 dy_2. \quad (5.2)$$

From Fig. 5.1 we can see that for this scenario

$$R_{sc}^2 = s^2 + d^2 \quad (5.3)$$

and

$$s^2 = (x_2 - x_1)^2 + (y_2 - y_1)^2. \quad (5.4)$$

The distance R_{sc} can therefore be expressed as

$$R_{sc} = (s^2 + d^2)^{1/2} = ((x_2 - x_1)^2 + (y_2 - y_1)^2 + d^2)^{1/2} \quad (5.5)$$

and

$$\cos \theta_s = \cos \theta_c = \frac{d}{R_{sc}} = \frac{d}{((x_2 - x_1)^2 + (y_2 - y_1)^2 + d^2)^{1/2}}. \quad (5.6)$$

Plugging the previous two expressions into Eq. 5.2 produces the final equation for the GCF of the collector as seen by the source,

$$\text{GCF}_{collector} = \frac{1}{\pi A_s} \int_{y_2} \int_{x_2} \int_{y_1} \int_{x_1} \frac{d^2}{(d^2 + (x_2 - x_1)^2 + (y_2 - y_1)^2)^2} dx_1 dy_1 dx_2 dy_2. \quad (5.7)$$

Equation 5.7 can be numerically integrated to find the value of $\text{GCF}_{collector}$. Since $\Omega_{collector} = \pi \text{GCF}_{collector}$, all of the values are now known to analytically calculate the collector's scat-

ter radiant flux using Eq. 2.17. This result can then be compared to FRED raytrace results of the source-collector setup to quantify FRED's scatter radiometry capability.

For the remaining stray light validation tests, we have created a simplified version of the Cassegrain telescope FRED model in Fig. 3.5 with a single $50 \mu\text{m} \times 50 \mu\text{m}$ detector (uniform spectral bandpass $\Delta\lambda = 0.10 \mu\text{m}$ centered on $0.55 \mu\text{m}$) located in the center of the focal plane. A Lambertian scatter model with a TIS = 10% has been assigned to the primary and secondary mirrors (total reflectance $\rho = 1$ for both mirrors) and no scatter model has been assigned to the mechanical surfaces. This simplified system is used to image a source located at the Cassegrain telescope's entrance aperture with radiance $L_{src} = 10 \text{ W/m}^2/\text{sr}$ and $\lambda = 0.55 \mu\text{m}$. The source sends rays into the system uniformly random at angles within 0.10° of the optical axis, which is equivalent to imaging an on-axis circular target located at infinity with a radius of 0.10° from the perspective of the Cassegrain telescope. Despite the fact that we are using a single $50\text{-}\mu\text{m}$ detector with a $0.00558^\circ \times 0.00558^\circ$ FOV to capture stray light radiant flux in these validation tests, the Cassegrain telescope design can support an FPA that covers an approximately $0.72^\circ \times 0.72^\circ$ FOV. The 0.10° radius circular target is therefore an in-field target for the Cassegrain system as a whole.

Although we are limiting these validation tests to a small in-field target source, excluding mechanical component scattering, and using a Lambertian scatter model that is not realistic for polished mirrors, this simplified system setup allows us to analytically calculate the stray radiant flux expected on the detector. Although analytical stray light calculations can be useful for first-order performance estimates, in general, it is extremely difficult to analytically calculate the expected amount of stray light on a detector for an arbitrary imaging system and scene. This is largely due to the fact that there are thousands of

possible stray light paths in even the simplest of imaging systems. Including a larger target source and mechanical component scattering would exponentially increase the complexity of any analytical solution due to the complicated geometric relationship between the stray paths, the surface BSDFs, and the number of surfaces involved. Assigning a Lambertian scatter model to the mirrors helps to simplify the scatter calculations by creating a constant BSDF, thus removing the variable of BSDF as a function of incident and scatter angle. Optical engineering software is extensively used nowadays to conduct stray light analysis in optomechanical systems instead of analytical calculations due to its ability to model complicated geometry and rapidly compute the stray light paths and radiometry in complex systems. However, for the purpose of our stray light validation, it is useful to compare optical engineering software raytracing results to analytical stray light calculations. If the analytical calculations match the stray light performance of the simplified Cassegrain system and in-field source target configuration, then we can gain confidence that FRED will produce accurate stray light ASMs when implementing the integration method for any system.

For our simplified imaging scenario, we calculate the detector's expected stray light radiant flux using Peterson's analytical expression for in-field scattered light in multi-element imaging systems [158]. In-field scattered light can often be an important form of stray light to characterize in a system considering that a bright in-field source cannot be easily blocked via baffling. In order to help set specifications on optical component quality and cleanliness, Peterson developed equations to compute the magnitude and distribution of stray light at the focal plane given the BSDF of the optical elements [158]. These expressions have been previously numerically validated using optical engineering software [49, 159]. By taking into account the conservation of radiance and the Lagrange invariant of first-order imaging theory [160], Peterson [158] shows that the scattered irradiance at the focal plane

of an imaging system from the j^{th} element for a small, bright in-field source is given by

$$E(r)_{S,j} = \pi (NA)^2 T \frac{a_{ent}^2}{a_j^2} \text{BSDF}_j \left(NA \frac{r}{a_j} \right) E_{ent}, \quad (5.8)$$

where r is the distance on the focal plane away from the bright source image, NA is the system's numerical aperture, T is the system transmittance, a_{ent} is the beam semi-diameter at the first element, a_j is the beam semi-diameter at the j^{th} element, BSDF_j is the BSDF of the j^{th} element (a function of r , which correlates to scatter angle), and E_{ent} is the irradiance from the source at the first element. The total scatter irradiance at the focal plane is simply the sum of the stray light contributions from each optical element in the system. The total stray light irradiance largely depends on two quantities: the BSDF of each optical element (with the stray light irradiance at the focal plane from each element having the same functional form as the element's BSDF) and the beam radius at each optical element [158]. Equation 5.8 makes a number of assumptions and approximations, including assuming an axial optical system with rotational symmetry, an external medium with refractive index $n = 1$, a target object close to the optical axis, a paraxial raytracing approximation which neglects mirror curvature, a smooth surface assumption ($\sigma_{RMS} \ll \lambda$) for the optical elements, no contribution from structural elements, no multiple scattering, and no ghosting. In addition, the $\pi (NA)^2$ term assumes that the projected solid angle of the illuminated area of each optical element as seen by the detector is constant and also does not account for mirror curvature.

Since our system has only two optical components, we can rewrite Eq. 5.8 as

$$\Phi_S = \pi (NA)^2 a_{ent}^2 E_{ent} A_{det} \left(\frac{T_{PM} \text{TIS}_{PM}}{\pi a_{PM}^2} + \frac{T_{SM} \text{TIS}_{SM}}{\pi a_{SM}^2} \right), \quad (5.9)$$

where Φ_S is the detector's total scatter radiant flux, T_{PM} and T_{SM} are the system's transmittance in the forward direction up to the primary mirror and secondary mirror, respectively, $\text{TIS}_{PM} = \text{TIS}_{SM} = 0.1$ as previously specified, a_{PM} is the beam semi-diameter at the primary mirror, and a_{SM} is the beam semi-diameter at the secondary mirror. We have used the fact that the BSDF of a Lambertian scattering surface is given by $\text{BSDF} = \text{TIS}/\pi$ to rewrite BSDF_{PM} and BSDF_{SM} . Note that the constant BSDF terms mean that Eq. 5.9 has no dependence on r , thus allowing us to simply multiply by the detector area, A_{det} to convert from focal plane stray light irradiance to radiant flux. Unlike Peterson's original Eq. 5.8, we must also use separate system transmittance values for each mirror due to the fact that we are using a larger TIS value than normal for both mirrors to produce an increased stray light signal. This results in a system transmittance that is sufficiently different at each mirror. Assuming an incident plane wave, the system transmittance at the primary mirror, T_{PM} is simply the obscuration ratio of the primary mirror and secondary mirror strut geometry, which produces $T_{PM} = 0.853$. The system transmittance at the secondary mirror $T_{SM} = (1 - \text{TIS}_{PM})T_{PM} = 0.767$ since it must also take into account the scattering loss from the primary mirror. Peterson's analytical expression only includes single scattering, so scatter can only be generated at the secondary mirror by the specular rays coming from the primary mirror.

Using the source-collector test setup, the derived analytical expression for in-field scatter in Eq. 5.9, and our simplified Cassegrain telescope model, the validation of the integration method's stray light component can be accomplished with a four-step process:

1. Compute the expected collector scatter radiant flux for the source-collector test setup. Conduct twenty raytraces using the setup in FRED and capture the collector scatter radiant flux for each raytrace. Compare the detector scatter radiant flux from the

analytical calculation to the raytraces. Since this type of analytical calculation cannot be easily performed for any arbitrary geometry of source and collector surfaces, this step instills confidence in FRED's capability to accurately produce the absolute scatter radiometry for any surface geometry.

2. Calculate the detector stray light radiant flux estimated by the analytical expression in Eq. 5.9. Conduct twenty forward raytraces of the simplified Cassegrain system using the circular target source with ten million initial rays and record the stray light radiant flux on the detector for each raytrace. Compare the detector stray light radiant flux from the analytical calculation to the forward raytraces. Some discrepancies can be expected due to the assumptions and approximations made in Peterson's analytical expression. We can account for the most significant assumptions to produce a corrected Peterson analytical expression to compute a detector stray light radiant flux value that more closely matches the FRED forward raytrace results. This step provides a validation of both the Cassegrain model and FRED's stray light raytracing radiometry for an arbitrary optomechanical system model.
3. Compare the forward raytrace detector stray light radiant flux results from the previous step with the stray light radiant flux from twenty reverse raytraces. These reverse raytraces are conducted by defining a source with $L_{src} = 10 \text{ W/m}^2/\text{sr}$ and $\lambda = 0.55 \text{ }\mu\text{m}$ over the spatial extent of the $50\text{-}\mu\text{m}$ detector (10 million initial rays). The rays are traced back through the system and captured by a directional analysis entity (DAE) covering the angular region less than or equal to 0.10° from the optical axis. Due to the invariance of throughput, the total stray light radiant flux captured by the DAE should match the detector stray light radiant flux from the forward raytraces.

Along with demonstrating the reciprocity of the Cassegrain model, this supports the integration method's foundational principle of using system stray light susceptibility captured from a reverse raytrace to estimate stray light contributions from arbitrary scene radiance entering the system in the forward direction.

4. Conduct twenty reverse raytraces to capture the 50- μm detector's stray light ASM from the Cassegrain telescope using a $L_{src} = 1 \text{ W/m}^2/\text{sr}$ and $\lambda = 0.55 \text{ }\mu\text{m}$ over the spatial extent of the 50- μm detector (10 million initial rays). Use DIRSIG to capture the ERM of the 0.10° radius test target with spectral radiance $L_{src,\lambda} = 100 \text{ W/m}^2/\text{sr}/\mu\text{m}$ (when integrated over the detector's uniform spectral bandpass this becomes $L_{src} = 10 \text{ W/m}^2/\text{sr}$) and a zero radiance background. Although the choice is arbitrary, we have placed the spherical collector for this test at Landsat 8's altitude of 705 km (the test target radius is therefore $\approx 1.23 \text{ km}$ so that it extends 0.10° from the telescope's optical axis). No atmospheric effects are included for this test. We can use Eq. 3.6 to compute the integration method's estimated detector stray light radiant flux for the Cassegrain system and circular in-field target source. These results can then be compared to the forward raytraces from step 2 to determine the radiometric fidelity of the integration method.

In order to produce a corrected Peterson analytical expression for step two, the primary assumptions that affect the difference in detector stray light radiant flux between the analytical calculation in Eq. 5.9 and the FRED raytraces must be addressed, namely those related to the mirror curvatures and the system transmittance. To gain better insight into these assumptions, we can use the basic stray light radiative transfer radiometry in Eq. 2.17

to rewrite Eq. 5.9 as

$$\Phi_s = \Phi_{PM,i} \text{BSDF}_{PM} \Omega_{det,PM} + \Phi_{SM,i} \text{BSDF}_{SM} \Omega_{det,SM}, \quad (5.10)$$

where $\Phi_{PM,i}$ and $\Phi_{SM,i}$ are the incident radiant fluxes on the primary and secondary mirrors, respectively, BSDF_{PM} and BSDF_{SM} are the BSDFs for each mirror, and $\Omega_{det,PM}$ and $\Omega_{det,SM}$ are the projected solid angles of the detector as seen from each mirror. Using the relationship between $\Omega_{collector}$ and GCF from Eq. 2.18, Eq. 5.10 becomes

$$\Phi_s = \Phi_{PM,i} \text{BSDF}_{PM} \pi \text{GCF}_{det,PM} + \Phi_{SM,i} \text{BSDF}_{SM} \pi \text{GCF}_{det,SM}, \quad (5.11)$$

where $\text{GCF}_{det,PM}$ and $\text{GCF}_{det,SM}$ are the GCFs for the detector as seen by the primary and secondary mirrors, respectively. We can further break down Eq. 5.11 by replacing $\Phi_{PM,i}$ and $\Phi_{SM,i}$ with their constituent components such that

$$\Phi_s = (T_{PM} E_{ent} \pi a_{ent}^2) \text{BSDF}_{PM} \pi \text{GCF}_{det,PM} + (T_{SM} E_{ent} \pi a_{ent}^2) \text{BSDF}_{SM} \pi \text{GCF}_{det,SM}. \quad (5.12)$$

Given that BSDF_{PM} and BSDF_{SM} are constant in our simplified system configuration, the mirror incident radiant fluxes and GCFs are the only factors that may be influenced by assumptions that cause the analytical calculation and raytrace results to differ. The geometric configuration factors, $\text{GCF}_{det,PM}$ and $\text{GCF}_{det,SM}$, depend on the geometric relationship between each mirror and the detector, which intrinsically includes the effect of mirror curvature. We must find the true values for $\text{GCF}_{det,PM}$ and $\text{GCF}_{det,SM}$, since mirror curvature is not accounted for in Peterson's original analytical expression. We can use FRED as a numerical integrator to compute $\text{GCF}_{det,PM}$ and $\text{GCF}_{det,SM}$ because the Cassegrain model

contains the curved mirrors and therefore the correct projected solid angles for the detector as seen by each mirror. As previously described in §2.2.6, this can be accomplished by turning the primary and secondary mirrors into 100% Lambertian emitters. The GCF for the detector-mirror geometry in each case is the fraction of the source power collected by the detector.

It is also apparent from Eq. 5.12 that the incident radiant fluxes depend on the system transmittances at each mirror, T_{PM} and T_{SM} . Our initial system transmittance calculations assumed a plane wave when incorporating the obscuration ratio of the secondary mirror and its supporting struts. However, the true values need to take into account the extended circular target source and the resulting projection effects from the mechanical elements. This plays a smaller role than the initial no mirror curvature assumption, but is still significant enough that it must be addressed. FRED can again be used to calculate the system transmittances since the Cassegrain model contains the correct source and system geometry. We do this by conducting forward raytraces using the circular target source with and without the mechanical elements. The system transmittance at each mirror is then found by taking the ratio of the total radiant flux on the mirror with the mechanical elements included in the model to the radiant flux on the mirror with these elements removed.

5.3 RESULTS

Plugging in the values for the source-collector test setup shown in Fig. 5.1 into Eq. 5.7 and using MATLAB [156] to compute the numerical integration produces $GCF_{collector} =$

0.046137. Using Eq. 2.17, the expected collector scatter radiant flux is therefore

$$\Phi_{collector} = (1 \text{ W}) \left(\frac{1}{\pi} \text{ sr}^{-1} \right) (\pi \cdot 0.046137 \text{ sr}) = 0.046137 \text{ W}. \quad (5.13)$$

Table 5.1 compares this analytically calculated collector scatter radiant flux value to the FRED raytrace results. The analytical value and the mean raytrace collector scatter radiant flux are an extremely close match, only differing by 0.0064%. This simple test setup demonstrates that FRED is capable of producing highly accurate scatter radiometry. This is significant because it is very difficult to perform analytical calculations to validate the stray light performance of an arbitrary system. Since the source area is essentially serving as a Lambertian emitter with a power of 1 W, the magnitude of the collector radiant flux is also equivalent to $\text{GCF}_{collector}$, the collector's GCF as seen by the source area. This means that the value of $\text{GCF}_{collector}$ produced by FRED differs from the analytical calculation by 0.0064% as well, validating the usage of FRED as a numerical integrator to compute the updated values for $\text{GCF}_{det,PM}$ and $\text{GCF}_{det,SM}$ in the second test.

Table 5.1: Comparison between the collector scatter radiant flux analytical calculation and the FRED raytrace results for the source-collector test setup. The FRED raytrace results display the mean and standard deviation of the collector scatter radiant flux across the twenty raytraces conducted. The difference from analytical indicates the percentage difference between the mean raytrace collector scatter radiant flux and the analytically calculated value.

	Collector Scatter Radiant Flux (mW)	Difference from Analytical
Analytical calculation	46.137	
FRED raytraces	46.140 ± 0.012	+0.0064%

For the second test, after plugging in the values for the Cassegrain system and circular

in-field target source into the two-mirror analytical expression in Eq. 5.9, the primary mirror contributes $1.995\text{E-}16$ W of stray light radiant flux to the detector and the secondary mirror provides $2.873\text{E-}15$ W, for a total of $3.073\text{E-}15$ W. The fact that approximately 93.5% of the total detector scatter radiant flux is a result of the secondary mirror and only 6.5% is from the primary mirror highlights the importance of controlling stray light performance of components closer to the focal plane. Note that these scatter radiant flux values are very small and may be below the noise limit of a real system. This does not matter for our validation purposes because the integration method's stray light component radiometry is independent of system noise limitations and stray light radiant flux magnitude.

Table 5.2 compares the analytical calculation to the FRED forward and reverse raytrace results, which display the mean stray light radiant flux plus or minus the standard deviation across the twenty raytraces for each case. We can see that the FRED forward and reverse raytraces match extremely well, with their mean values differing by only 0.03%. This very close match is even more noteworthy considering that the stray light radiant flux levels for these imaging scenarios are over five orders of magnitude lower than the designed optical path radiant flux. The standard deviations are small in both cases, at 1.22% and 0.39% of the mean detector scatter radiant flux values for the forward and reverse raytraces, respectively. The standard deviations differ slightly due to the fact that the importance sampling specifications are separately optimized for the forward and reverse directions and are not exact geometric reciprocals. The reverse raytrace is expected to be more efficient since the DAE covers a larger angular area than the small detector at the focal plane.

Overall, the forward and reverse raytrace results provide significant confirmation that the integration method's approach of using system stray light susceptibility data from reverse raytraces is acceptable for estimating stray light performance in the forward direction

for an arbitrary scene. This is particularly important because reverse raytracing is much more efficient than forward raytracing for determining comprehensive system stray light performance, given that only one raytrace is required to capture a detector element's stray light susceptibility across all of object space. This is why reverse raytracing is such a key method in general for conducting stray light analysis [17, 68].

Table 5.2: Comparison between the detector scatter radiant flux for the original analytical calculation, FRED forward raytraces, and FRED reverse raytraces. The FRED raytrace results display the mean and standard deviation of the detector scatter radiant flux across the twenty raytraces conducted in each case.

	Detector Scatter Radiant Flux (W)	Difference from Analytical
Analytical calculation	3.073E-15	
FRED forward raytraces	$2.914\text{E-}15 \pm 0.035\text{E-}15$	-5.17%
FRED reverse raytraces	$2.913\text{E-}15 \pm 0.012\text{E-}15$	-5.20%

Although the FRED forward and reverse raytraces results match very well, they differ from the analytical calculation by 5.17% and 5.20%, respectively. These are reasonably close matches, given the mirror curvature and system transmittances assumptions present in the original analytical calculation. Table 5.3 shows a comparison between the original mirror GCFs calculated through rearranging terms in the original Peterson analytical equation and the corrected GCFs computed using FRED. The GCFs for both mirrors have fallen from the original approximated values, though the change in $\text{GCF}_{det,SM}$ has a much more significant effect on the total detector stray light radiant flux due to its larger magnitude.

Table 5.4 contains a similar comparison between the system transmittances at each mirror used in the original Peterson analytical equation and the corrected values from FRED. The projection effects from the target source and the mechanical components have

slightly reduced the system transmittances for both mirrors, which will in turn reduce the total detector stray light radiant flux.

Table 5.3: Comparison of the mirror GCFs in the original Peterson analytical equation and the corrected GCFs from FRED for the detector as seen by each mirror.

	Original GCF	Corrected GCF	Percent Difference
Primary mirror	3.016E-9	2.851E-9	-5.49%
Secondary mirror	4.826E-8	4.624E-8	-4.20%

Table 5.4: Comparison of the system transmittances at each mirror used in the original Peterson analytical equation and the corrected system transmittances from FRED taking into account projection effects from the target source and mechanical components.

	Original System Transmittances	Corrected System Transmittances	Percent Difference
Primary mirror	0.853	0.850	-0.35%
Secondary mirror	0.767	0.765	-0.36%

Taking into account the updated GCFs and system transmittances at each mirror, the corrected analytical equation in Eq. 5.12 produces a primary mirror detector scatter contribution of 1.879E-16 W and secondary mirror contribution of 2.743E-15 W, for a total detector scatter radiant flux of 2.914E-15 W. Table 5.5 compares the corrected analytically calculated result with the original analytical calculation and the FRED forward raytrace results. The corrected detector scatter radiant flux has dropped and now only differs from the forward raytrace mean value by 0.57%, which is within the limits of the statistical variations of the raytraces (the standard deviation of the forward raytrace detector scatter radiant flux is 1.22% of the mean value across the raytraces). This provides solid evidence that FRED is in fact following the basic stray light radiative transfer radiometry in Eq. 5.12

on a surface-by-surface basis.

Table 5.5: Comparison between the detector scatter radiant flux for the original and corrected analytical calculations and the FRED forward raytrace. The FRED raytrace results display the mean and standard deviation of the detector scatter radiant flux across the twenty raytraces conducted in each case.

	Detector Scatter Radiant Flux (W)	Difference from Corrected
Original analytical calculation	3.073E-15	+4.85%
Corrected analytical calculation	2.931E-15	
FRED forward raytraces	2.914E-15 \pm 0.035E-15	-0.57%

Although FRED itself was used to calculate the corrected GCF and system transmittance values, the first test convincingly illustrated that FRED can produce highly accurate absolute scatter radiometry and GCF calculations. In any case, it is valuable to demonstrate that the most significant assumptions from the original Peterson analytical expression are the primary cause of the differences between the original analytical calculation and the raytrace results. This highlights the point that analytical calculations must make more general assumptions for simplification purposes (e.g. no curved optical elements), but that optical engineering software often does not have these same limitations. In general, more and more assumptions can be removed from stray light analytical equations to improve their accuracy, but it can become an increasingly difficult task to determine the proper corrections. As seen here, the calculation of the GCFs with mirror curvature included must take into account an extended area detector and the curvature of hyperbolic mirrors. These are very difficult integrals to solve analytically. It should come as no surprise that the original Peterson analytical expression instead uses approximations for the projected solid angles. However, the true GCFs were easily calculated using FRED as a numerical integrator. This

emphasizes why optical engineering software is used for stray light calculations in the first place and illustrates the value of including optical engineering software in the integration method workflow.

In order to better understand the integration method implementation in the final validation test, Fig. 5.2 visually displays Eq. 3.6, the multiplication of system stray light susceptibility data with at-aperture scene radiance in graphical form, for this imaging scenario. The top plot in the figure is the Cassegrain stray light ASM from one raytrace converted to radiant flux by multiplying each grid element by its solid angle. The statistical noise in the radiant flux variations is particularly noticeable for this stray light ASM since each grid element covers an extremely small solid angle (polar angle $\Delta\theta = 0.01^\circ$, azimuthal angle $\Delta\phi = 1^\circ$). Although stray light ASMs can be captured for small regions of interest in object space (as here, with our single target source), each grid element will typically cover a larger solid angle (e.g. $1^\circ \times 1^\circ$) with the stray light ASM covering all of object space. The middle plot shows the DIRSIG ERM of the 0.10° circular target source integrated over the detector's spectral bandpass to convert spectral radiance to radiance. This plot only includes the region within 0.10° of the optical axis, which has a uniform radiance from the circular source target, whereas the rest of the ERM from 0.10° – 90° that is not displayed contains zero radiance. The bottom plot is the grid element-by-grid element multiplication of the two previous plots, which produces the stray light radiant flux contribution map for our simplified Cassegrain system imaging this particular scene. This plot provides a visualization of how much stray light radiant flux the detector receives from each solid angle in object space. In this case, the stray light contribution map is simply a scaling of the stray light ASM by the scene's uniform ERM. As a result, the grid elements farther from the optical axis contribute more stray light radiant flux to the detector due to their larger

solid angle size. The summation of these individual stray light radiant flux contributions produces the total stray light radiant flux reaching the detector.

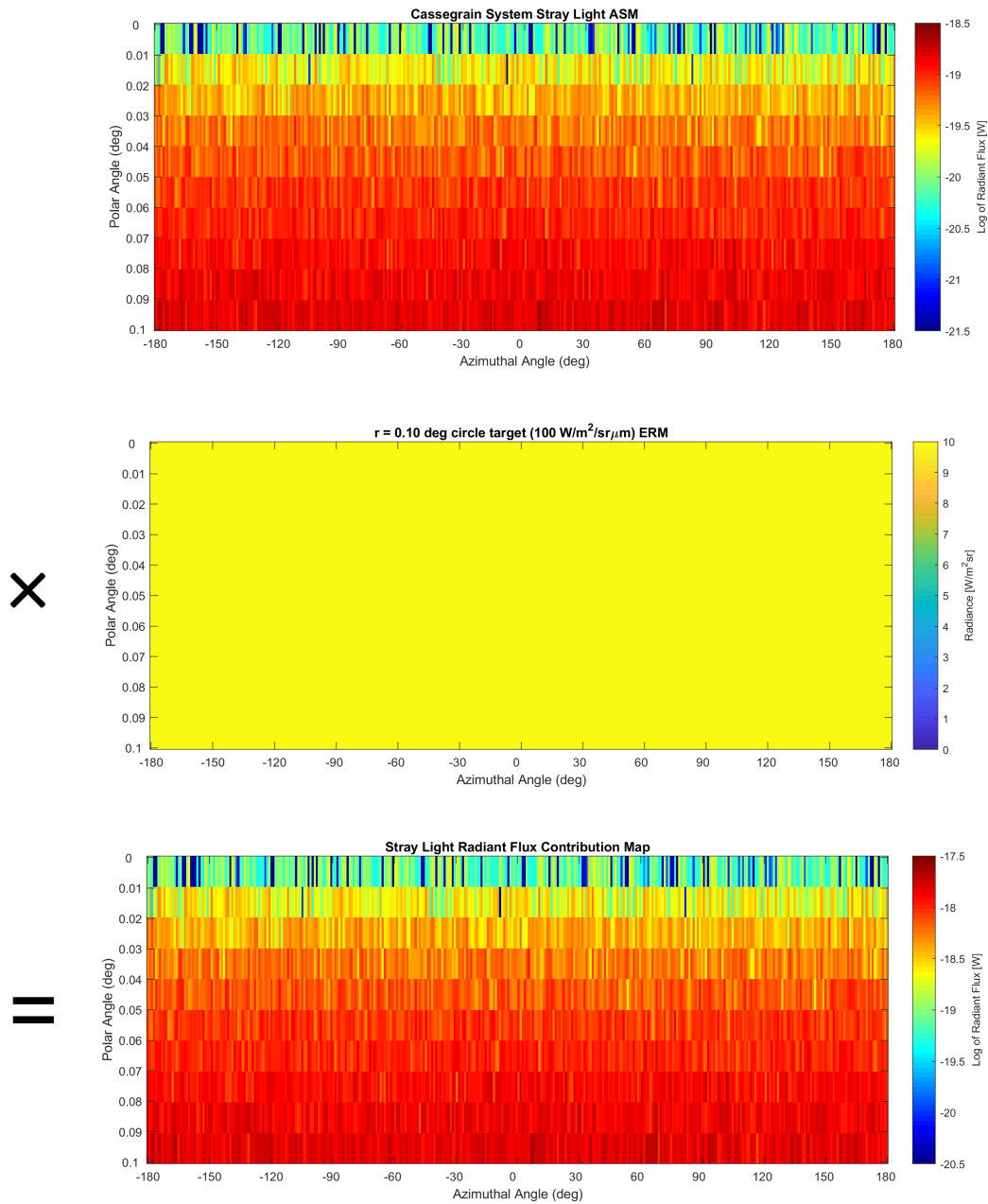


Figure 5.2: Integration method stray light radiant flux contribution equation in graphical form: (top) Cassegrain stray light ASM converted to radiant flux. (middle) 0.10° circle target source ERM from DIRSIG integrated over the detector's spectral bandpass. (bottom) Stray light radiant flux contribution map. The summation of the stray light radiant flux contribution map provides the detector's total stray light radiant flux.

Table 5.6 contains the results for the integration method applied to the simplified Cassegrain telescope and circular target source imaging scenario. The integration method's mean detector stray light radiant flux differs from the forward raytrace mean by only 0.25%, which is well below the statistical variations in either case (the standard deviation is 1.22% of the mean detector scatter radiant flux for the forward raytraces and 0.39% for the reverse raytraces) . This confirms that implementing the integration method via Eq. 3.6 produces the same detector stray light irradiance as conducting a forward raytrace of the scene directly in FRED or, equivalently, imaging the scene in DIRSIG with the 3-D CAD Cassegrain telescope model. Of course, neither of these capabilities are directly possible within each type of software separately. It is only through the integration of an optomechanical system model from optical engineering software and the scene creation and imaging capabilities of a radiative transfer image simulation model that we are able to realize this possibility. This simplified imaging scenario provides the radiometric justification that Eq. 3.6 will hold true for any arbitrary system and scene.

Table 5.6: Comparison between the FRED forward and reverse raytrace results and the integration method applied to the simplified Cassegrain telescope and circular target source imaging scenario. Each set of results display the mean and standard deviation of the detector scatter radiant flux across the twenty raytraces conducted in each case.

	Detector Scatter Radiant Flux (W)	Difference from Forward
FRED forward raytraces	2.914E-15 ± 0.035E-15	
FRED reverse raytraces	2.913E-15 ± 0.012E-15	-0.03%
Integration method estimates	2.921E-15 ± 0.013E-15	+0.25%

5.4 SUMMARY AND CONCLUSIONS

In this chapter, we have validated the integration method's stray light radiometry using a series of tests to evaluate FRED's absolute scatter radiometry, compare FRED raytrace result to analytical calculations, and analyze raytrace results in the forward and reverse directions. The absolute scatter radiometry test demonstrated FRED's capability to match the analytically calculated result to within 0.0064% for a simple source-collector area setup. In subsequent tests, the FRED forward raytrace detector stray light radiant flux matched the corrected analytical value to within 0.57%, providing strong evidence that FRED follows the basic stray light radiative transfer equations on a surface-by-surface basis. The FRED forward and reverse raytrace stray light radiant flux values differed by only 0.03%, indicating the reciprocity of the Cassegrain telescope model and justifying the use of reverse raytrace stray light performance data for estimating the stray light contributions at the focal plane for an arbitrary scene. Finally, the integration method applied to the simplified Cassegrain telescope and circular target source produced a detector stray light radiant flux that differed from the FRED forward raytraces by only 0.25%. This proved the integration method's stray light radiometric approach and justified its implementation for an arbitrary system and scene. The work in this chapter fulfills research objectives 1 and 3 from §1.2 in demonstrating a general methodology for integrating optomechanical system models from optical engineering software with a radiative transfer image simulation model, as well as validating the integration method's capability to accurately incorporate the stray light component.

Chapter 6

System Trade Study

Demonstration

This chapter builds off the stray light component validation work by demonstrating the integration method's system trade study capability through the assessment of the Cassegrain system's stray light performance imaging a remote sensing scene. Various system stray light susceptibility and scene conditions are tested to assess a range of system design and operational mission planning options. The data produced from these system trade studies are then used to generate quantitative stray light metrics that provide insight into user application impact. In addition to meeting the higher-level research objectives, this work also demonstrates the integration method's shift-variant and far-field stray light capabilities. Stray light ASMs are collected across the Cassegrain telescope's focal plane to produce a 2-D stray light irradiance distribution, which includes contributions originating from sources far from each pixel's nominal IFOV. In order to rapidly collect the large amount of shift-variant stray light ASMs, we use FRED's new graphics processing unit (GPU) raytracing

capability. This allows for thousands of processing units to run in parallel and presents a revolutionary opportunity for collecting very detailed system performance data for use in system trade studies, especially those related to stray light. The system trade study results presented here also highlight the benefits gained by the integration method's inclusion of far-field stray light contributions over PSF-only modeling approaches that are limited to near-field stray light.

Testing a series of system stray light susceptibility and scene conditions to assess performance and user application impact provides valuable information that can be used in driving system design or mission changes. This type of modeling and simulation-based systems engineering analysis is particularly useful because it can be conducted before hardware is built, thus potentially saving cost and shortening the schedule. Once a design reaches a certain level of maturity, it is also very important to understand how design issues affect operational performance in order to inform redesign or mitigation decisions.

A number of significant design decisions will impact a system's stray light performance, including optical surface polishing and cleanliness standards, mechanical component black surface treatments, and baffle design and placement. The specific technique or amount of optical surface polishing impacts the residual surface roughness and can leave characteristic patterned spatial frequencies that increase scattering. Cleanliness standards specify the distribution and amount of particulate contamination, which influence scattering off the optical components. Black surface treatments and baffling impact the levels of mechanical scattering that can dominate the stray light performance of a system. All of these stray light considerations must be taken into account when designing an imaging system that maximizes performance.

Ideally, a system would have the most expertly polished and contamination-free mirrors,

the most stray light-reducing black surface treatments, and the best designed and placed baffles, all completed at the lowest price and in record time. Unfortunately for program managers, the engineering adage “faster, better, cheaper – pick any two” often holds true. Improved mirror polishing quality, establishing and maintaining higher cleanliness standards, and the best performing black surface treatments combined with the addition of more baffles can all cost more time and money. Compromises must ultimately be made to balance system stray light performance with the overall mission budget and schedule, while ensuring the system still meets all of its performance requirements, including those related to stray light. Understanding the interplay of the available stray light control options and how their combined performance impacts user applications can be critical in making difficult stray light-focused system trades.

6.1 METHODOLOGY

6.1.1 System Stray Light Performance Conditions

The demonstrations presented in this chapter once again use the Cassegrain telescope design in Fig. 6.1, but with several different combinations of stray light performance conditions applied to provide a system trade study scenario. Each row of Table 6.1 provides a different combination of these system conditions. Since baffles are one of the primary means of controlling low-order stray light paths, this Cassegrain system has primary and secondary mirror baffles that block the zeroth-order stray light path, along with a main baffle which limits direct illumination of the primary mirror from out of the FOV. The flat black paint scatter model based on Aeroglaze[®] Z306 [88] has been applied to all of the mechanical surfaces. This scatter model is Lambertian-like at normal incidence, but its “specularity”

and TIS increase with increasing incident angle. Two versions are used here to represent different levels of stray light performance. The first version has a TIS = 2% at normal incidence, which increases to TIS = 7.24% at an incident angle of 75° and TIS = 9.02% at a near-grazing angle. The better performing version has the same BSDF functional form, but is scaled down in magnitude. This version has a TIS = 1% at normal incidence, 3.62% at a 75° incident angle, and 4.51% at near-grazing angles. These two flat black paint versions will be referred to by their TIS values at normal incidence throughout this chapter for the sake of simplicity. The baffles and flat black paint are particularly significant design choices due to the fact that mechanical scattering dominates this Cassegrain design.

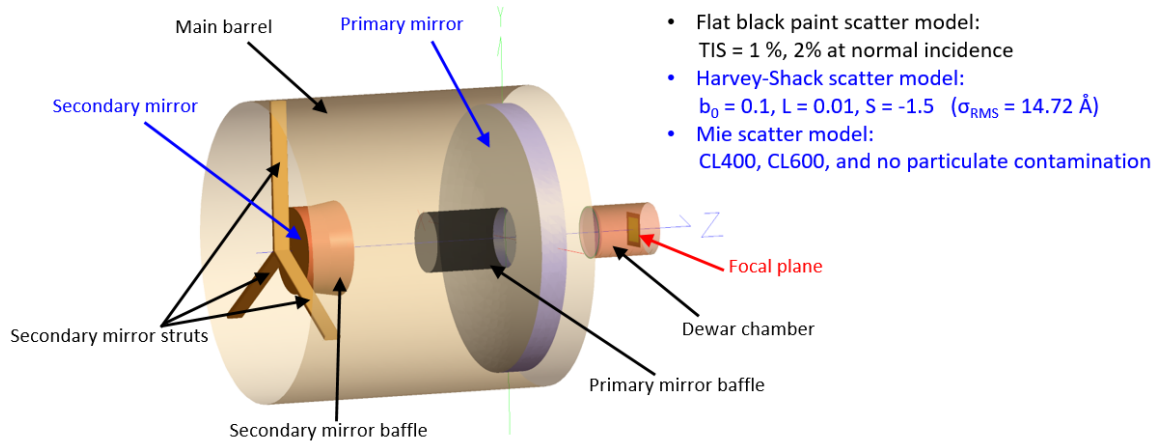


Figure 6.1: Different scatter models applied to the Cassegrain telescope's optical and mechanical surfaces to represent various stray light performance conditions.

Table 6.1: Different combinations of stray light performance conditions. All cases include the same Harvey-Shack scatter model ($b_0 = 0.1$, $L = 0.01$, and $S = -1.5$; $\sigma_{RMS} = 14.7$ Å) for optical surface roughness. The flat black paint TIS percentages refer to the value at normal incidence.

Mirror Polishing	Particulate Contamination	Flat Black Paint
Harvey-Shack	CL400	TIS = 1%
Harvey-Shack	CL400	TIS = 2%
Harvey-Shack	CL600	TIS = 1%
Harvey-Shack	CL600	TIS = 2%
Harvey-Shack	None	TIS = 2%

The primary and secondary mirrors have been assigned a Harvey-Shack model [78, 79] ($b_0 = 0.1$, $L = 0.01$, and $S = -1.5$) that models the residual surface roughness after optical surface polishing. These parameters provide the mirrors with TIS = 0.11% at normal incidence and a surface roughness of $\sigma_{RMS} = 14.7$ Å assuming $\lambda = 0.55$ μm. In addition, three different particulate contamination distributions based on the IEST-STD-CC1246D particle size distribution function have been applied to the mirrors using a Mie scatter model, including CL400 and CL600. The case of no particulate contamination (i.e. perfectly cleaned mirrors) is also modeled as a reference case to demonstrate the impact of including particulate contamination in system trade studies. Particulate contamination models can be included in optomechanical system models to represent initial cleanliness levels or particulate build up throughout a system’s lifecycle, which can decrease system performance over the course of a mission. The CL400 particulate contamination has a TIS = 0.14% at normal incidence ($\lambda = 0.55$ μm) and a PAC = 0.1059%, whereas CL600 is noticeably dirtier with TIS = 1.09% at normal incidence ($\lambda = 0.55$ μm) and a PAC = 0.7980%. Note that the particulate real and imaginary refractive indices for these distributions were defined according to reasonable values derived from Jennings et al. [161]. The Harvey-Shack surface roughness and Mie particulate contamination scatter models combine to act upon light that

is incident on the mirrors.

6.1.2 DIRSIG Scene and Conditions

We used DIRSIG5 for these demonstrations and focused our attention on a DIRSIG scene of central and southern California centered on 34.5° N latitude and 119.5° W longitude, which lies just north of Carpinteria, CA. Shown in Fig 6.2, this so-called “LA scene” (since it includes Los Angeles, CA and covers a large area) was created by Dr. Mike Gartley of RIT using Landsat 8 OLI and TIRS data in conjunction with NASA Shuttle Radar Topography Mission (SRTM) digital elevation data. The Landsat data were used to segment the scene into an eight material class map. Each class was then assigned spectral data according to a matching entry from within a spectral library. The scene covers 450×375 km ($33^\circ \times 28^\circ$ from an altitude of 705 km) at 100-m spatial resolution, extending from just south of Monterey, CA in the northwest of the scene to Anaheim, CA in the southeast corner. This scene is a particularly stressing scene for stray light due to its high contrast with the dark water and bright land. This scenario presents a particular problem for scientists who study near-coastal water regions, where the out-of-FOV stray light contributions can be significant compared to the relatively low desired signal received from the water.

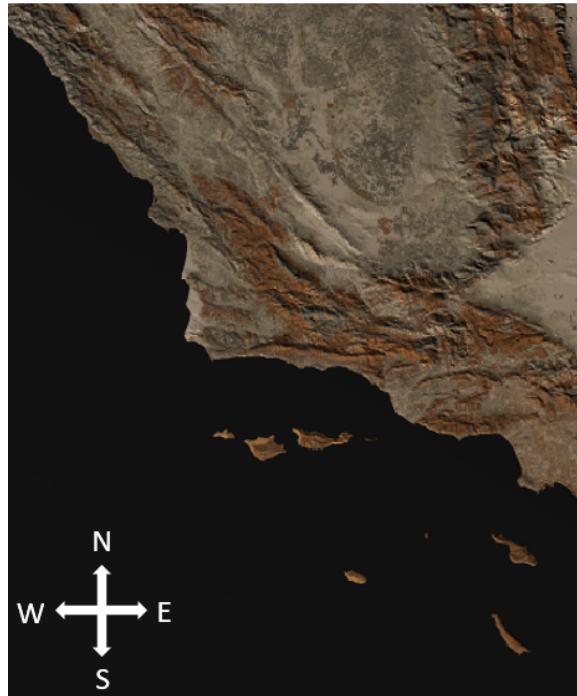


Figure 6.2: DIRSIG “LA scene” covering 450×375 km of central and southern California.

Although the LA scene covers a substantial area, we have added the scene to a background consisting of a lower-resolution model of the Earth created by Jared Van Cor for his master’s thesis work at RIT [162]. This 3-D Earth model was built using MODIS imagery and provides the additional out-of-FOV extent of the Earth, which can provide significant amounts of stray light for the Cassegrain system. Fig. 6.3 displays the LA scene with the added Earth background, along with an inset outlining the location of the higher spatial resolution LA scene. Ross-Li BRDF models were used to model the different land surface classifications, with the parameters fit to each material class. This model implements the kernel-based BRDF in Wanner et al. [163] with kernels developed by Ross [164] and Li [165] and is useful for capturing the aggregate reflectance of vegetated land surfaces at large spatial scales (≥ 100 m).

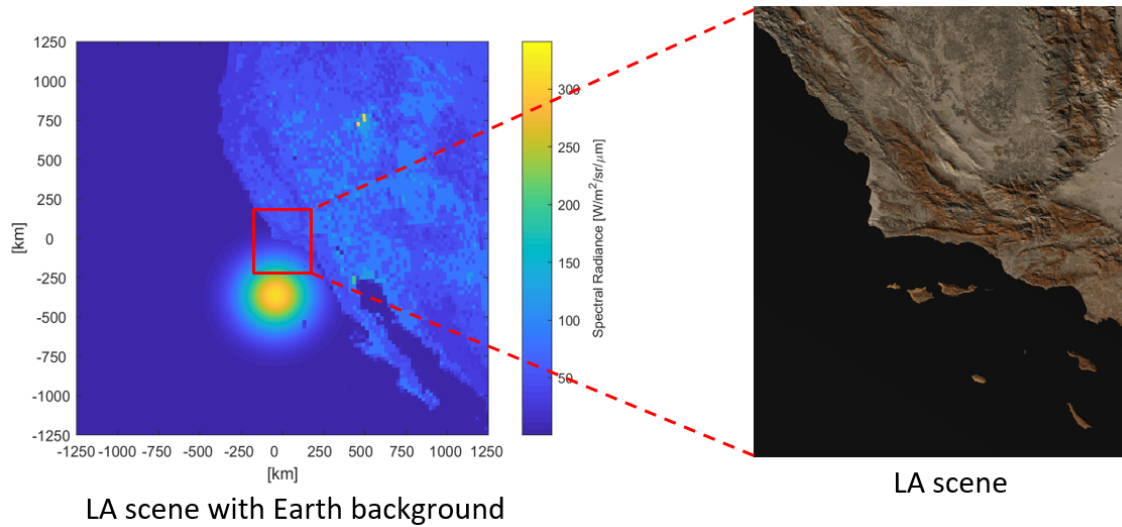


Figure 6.3: Wide-area view of the DIRSIG LA scene with lower-resolution Earth background and inset outlining the LA scene location.

The water in the combined scene was modeled using an uncontaminated seawater reflectance of 2% (at normal incidence) [166] and the Ward BRDF model [167]. The effect of wind speed (WS) on the ocean surface roughness was modeled using crosswind and up/downwind mean-square slope surface components for different wind speeds derived from ocean observational data collected by Cox and Munk [166]. These parameters were then applied to the Ward BRDF model in DIRSIG to provide a variable ocean surface. The ocean surface roughness plays a particularly important role in altering the ocean's specular sun glint shape and magnitude, which can provide a significant source of out-of-FOV stray light. Note that although the specular reflectance parameter does not change with incident angle in the Ward BRDF, we limit the sun zenith angle in these demonstrations. This ensures that the ocean's specular reflectance does not change substantially within the range of incident sun angles tested or due to multiple reflectances from the rough ocean surface.

To image this scene, the Cassegrain telescope used a 720×720 pixel FPA with a $9\text{-}\mu\text{m}$ pixel pitch. This FPA was placed at an altitude of 705 km in DIRSIG to match Landsat

8's altitude. The Cassegrain telescope in these demonstrations is not intended to replicate Landsat 8, but serves as a useful test example to better understand the scattering effects in a familiar optomechanical design. Placing the sensor at the same orbital altitude as Landsat 8 provides a relevant comparison for this telescope's Earth-observing stray light performance. The Cassegrain telescope has an approximately $0.72^\circ \times 0.72^\circ$ FOV and a GIFOV of 12.35 m from 705 km. This spatial resolution is less than the scene's spatial detail of 100 m, but this does not pose a problem for these demonstrations because they are intended to assess basic stray light metrics and not spatial-resolution dependent metrics such as image quality, MTF, etc. The FPA pixels were all modeled with a single spectral channel centered on $0.55 \mu\text{m}$, a bandpass of $0.10 \mu\text{m}$, and a 100% uniform spectral response across the entire bandpass. As shown in Fig. 6.4, the telescope was oriented so that its optical axis was pointing nadir and centered on Stearns Wharf in Santa Barbara, CA (34.41° N, 119.69° W). This provides a coastline view that includes both land and ocean pixels that can be separately evaluated for how much they are impacted by stray light contributions.

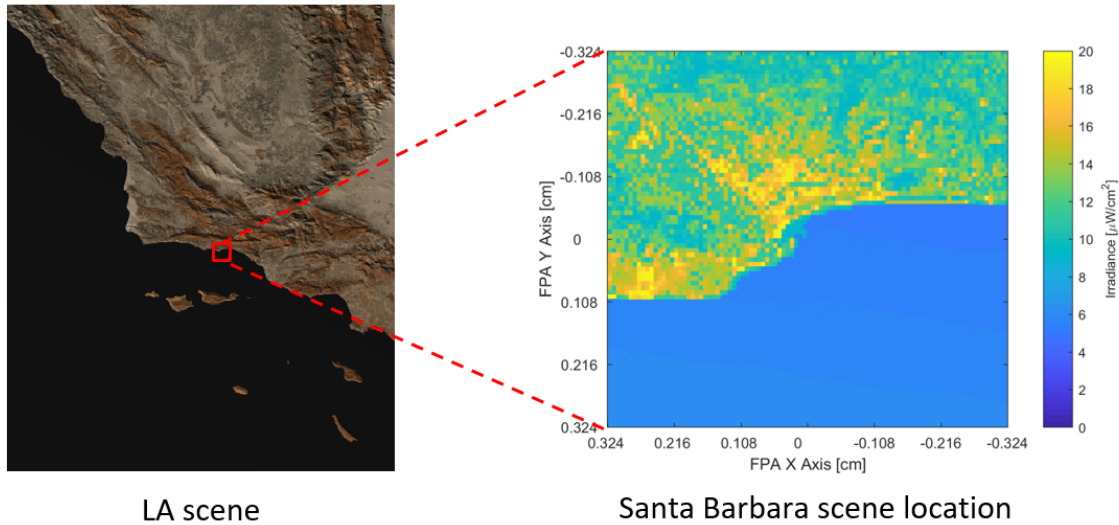


Figure 6.4: DIRSIG LA scene with Santa Barbara scene location within the Cassegrain telescope's FOV.

In addition to testing a range of Cassegrain telescope's stray light susceptibility conditions, these system trade study demonstrations vary the scene conditions to provide further insight into the system's operational stray light performance. Each set of system stray light susceptibility conditions was tested with each combination of scene conditions to produce a matrix of results for system trade study purposes. Table 6.2 lists the different combinations of scene conditions, whereas Fig. 6.5 provides a wide-area visualization of the LA scene with Earth background for each combination (plotted on common log scales). Two different dates were selected for testing, which change the sun's zenith angle and therefore the illumination conditions and specular sun glint shape and location on the Earth. This provides further knowledge of how the system's stray light performance fluctuates based on time of year. A MODTRAN mid-latitude summer atmosphere was modeled to provide realistic atmospheric conditions for these times of year, though this does not include spatial scattering effects of atmospheric aerosols. As shown in Fig. 6.5, the sun glint location on the ocean surface has shifted farther south and away from the Cassegrain's FOV over Santa

Barbara for the April date compared to August. Two different times of day were tested, which also impacts the sun’s location and glint pattern. These times are listed in local time, which is Pacific Daylight Time (PDT) for the dates selected. The 11:30 a.m. time corresponds to the fly-over time for Landsat 8 passing over Santa Barbara, CA in August. Fig. 6.5 illustrates the fact that higher magnitude portions of the sun glint pattern are over the ocean near Santa Barbara for 1:15 p.m. compared to 11:30 a.m., when the peak has shifted to the Gulf of California. As we will demonstrate, the 1:15 p.m. time also places the sun glint at a location where its angular extent overlaps with a higher region of stray light susceptibility for the Cassegrain telescope, representing a worst-case glint scenario. The effect of the wind speed on the sun glint pattern was assessed by testing a steady wind speed of 2.5 m/s (5.59 mph) and 7.5 m/s (16.78 mph), blowing from directly west to east. The wind speed of 7.5 m/s corresponds to a typical wind speed for coastal southern California [168] and produces a rougher surface. This leads to a lower magnitude sun glint peak with a broader spatial extent, as seen in Fig. 6.5b. The slower wind speed of 2.5 m/s provides a calmer surface, which produces a more specular sun glint peak that is higher in magnitude and narrower in spatial extent, as displayed in Fig. 6.5a.

Table 6.2: Different combinations of DIRSIG scene conditions. All times of day are listed in Pacific Daylight Time (PDT).

Date	Time of Day	Wind Speed
1 August 2019	1:15 p.m.	2.5 m/s
1 August 2019	1:15 p.m.	7.5 m/s
1 August 2019	11:30 a.m.	7.5 m/s
1 April 2019	1:15 p.m.	7.5 m/s

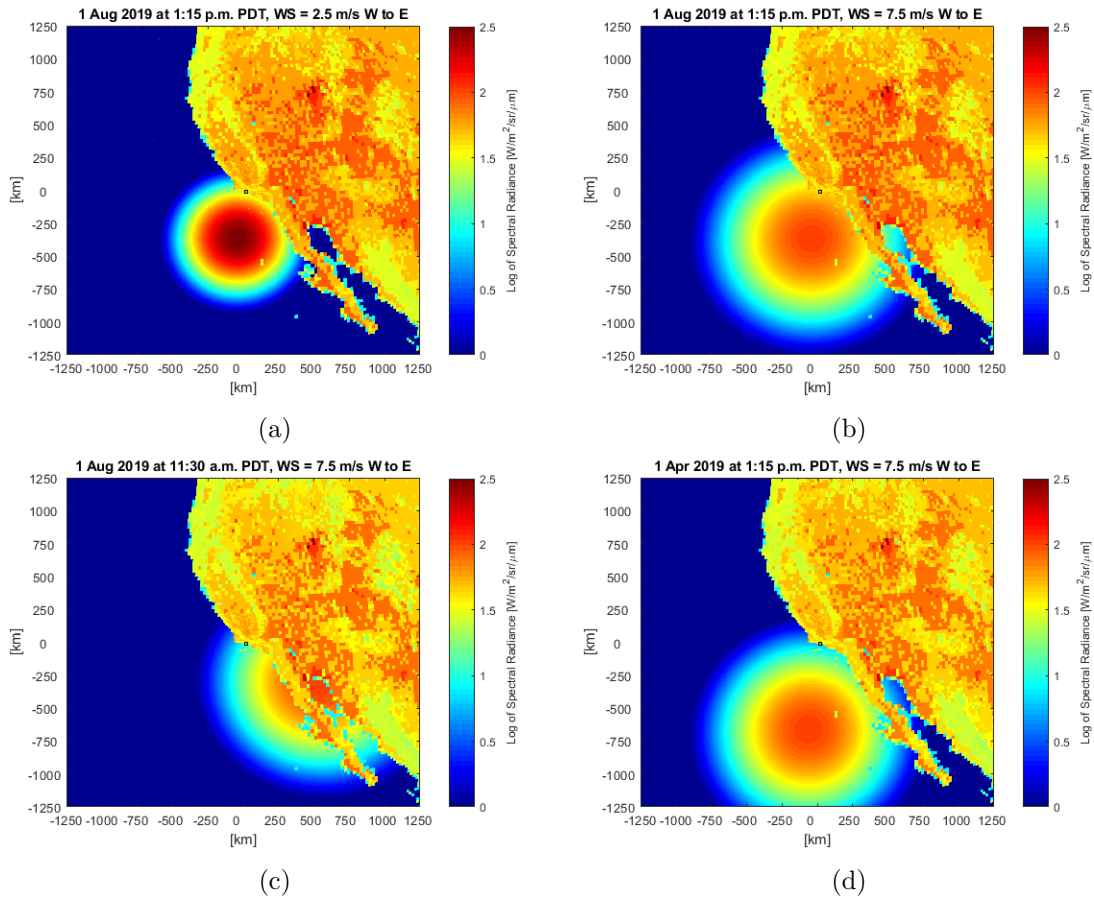


Figure 6.5: LA scene with Earth background for the different combinations of DIRSIG scene conditions (common log scales of spectral radiance at $\lambda = 0.55 \mu\text{m}$). The very small black box near the center of each scene marks the Cassegrain telescope's nominal FOV over Santa Barbara, CA. (a) 1 Aug 2019 at 1:15 p.m. PDT with wind speed = 2.5 m/s W to E. (b) 1 Aug 2019 at 1:15 p.m. PDT with wind speed = 7.5 m/s W to E. (c) 1 Aug 2019 at 11:30 a.m. PDT with wind speed = 7.5 m/s W to E. (d) 1 Apr 2019 at 1:15 p.m. PDT with wind speed = 7.5 m/s W to E.

6.1.3 Nominal Irradiance Images

A nominal image was taken of the Santa Barbara scene location for each set of DIRSIG scene conditions. The raytraces were performed in DIRSIG using geometric raytracing without the Cassegrain's PSF, since in these demonstrations we wish to isolate the effects of the

stray light contributions provided by Eq. 3.6. These nominal images include only light that has traveled along the designed optical path. Optical surface roughness and particulate contamination play a two-fold detrimental role in that they scatter light away from the designed optical path, some of which reaches the focal plane and increases the stray light level.

In order to take into account the reduction in light from the designed optical path to produce proper radiometry and to convert the DIRSIG image from radiance to radiance, we must use Eq. 3.2 to compute the system's $G\#$ for each set of optical surface conditions. Although the mechanical components play a factor in this computation due to their obscuration reducing the light on the designed optical path, their scattering does not impact the result, so we are only concerned with the optical surface stray light conditions. In general, the $G\#$ will change for individual pixels and also exhibit spectral dependencies. These field-dependent and spectral $G\#$'s can all be uniquely captured in FRED if so desired. For this Cassegrain telescope, the $G\#$ only changes by approximately 0.35% from the center of the FPA to the corners with $\lambda = 0.55 \mu\text{m}$, so we use the optical-axis value as $G\#_{DOP}$ for all FPA pixels in Eq. 3.4. The $G\#$'s for each set of optical surface conditions are calculated in FRED by creating a $1 \text{ W/m}^2/\text{sr}$, $\lambda = 0.55 \mu\text{m}$ source at the entrance aperture of the Cassegrain telescope. The source sends rays only into the angles corresponding to the IFOV of one of the center FPA pixels. The irradiance from the designed optical path is filtered out and the $G\#$ is then calculated for each case.

6.1.4 Cassegrain Shift-Variant Stray Light ASMs

Sets of stray light ASMs must now be collected from the Cassegrain telescope for each combination of system stray light susceptibility conditions. This was done by creating a

separate version of the FRED model for each set of system conditions and running a FRED script to shift the reverse raytrace source to the desired FPA pixels, conduct the raytraces, and save the output files in a standardized file-naming format. Figure 6.6 displays the pixel numbering convention used to track which stray light ASM corresponds to which FPA pixel. This is an important consideration to ensure that the correct nominal and stray light irradiance values are added together when combining images. The stray light ASM source was defined as a Lambertian source with $\lambda = 0.55 \mu\text{m}$, $L_{src,SL} = 1 \text{ W/m}^2/\text{sr}$, and 10 million initial rays over the spatial extent of a $9 \mu\text{m} \times 9 \mu\text{m}$ FPA pixel. Only single scattering was included for the stray light ASM raytraces since this captures more than 95% of the Cassegrain's total stray light radiant flux on the stray light ASMs. This also allows for faster raytracing, which is an important consideration when capturing large numbers of stray light ASMs. As illustrated in Fig. 3.8, much of the second-order scatter in this Cassegrain telescope is captured at angles greater than polar angle $\theta = 45^\circ$ on the stray light ASMs, which will mostly point off into space for our Earth-observing imaging scenario.

A FRED script captured the stray light ASM ($1^\circ \times 1^\circ$ angular resolution) for the center FPA pixel within every 9×9 pixel region across the Cassegrain's 720×720 pixel FPA. The Cassegrain telescope does not have any specular glint stray light paths, so this is a sufficient spatial sampling to observe the changing stray light irradiance distribution across the focal plane. This sampling interval results in a 80×80 pixel sparse sampling of the FPA, for a total of 6,400 total stray light ASMs for each set of system stray light susceptibility conditions. The stray light ASM capture script runs 80–110 times faster using FRED's GPU raytracing capability rather than CPU raytracing, demonstrating the benefits gained from the additional computational power.

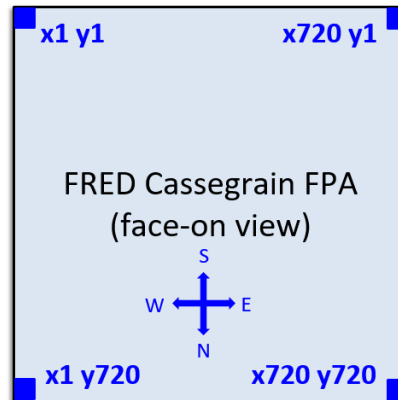


Figure 6.6: Face-on view of the Cassegrain FPA detailing the pixel numbering scheme used in FRED for capturing the shift-variant stray light ASMs. This is necessary to keep track of which stray light ASM was collected for each FPA pixel.

Note that a slightly different type of raytracing was used here than the stray light ASM capture demonstrated in §3.3.1. Whereas the previous raytrace used a ray splitting mode in which an incident ray produced ten scatter rays at a scattering surface, these stray light ASMs were captured using a Monte-Carlo mode that follows the “one ray in, one ray out” approach. Instead of splitting an incident ray into multiple scatter rays, the Monte-Carlo raytracing mode determines a ray’s future (i.e. specular reflection, scatter reflection, specular transmission, etc.) based on probability. This has the effect of suppressing the increase in number of rays that normally results from ray splitting. The Monte-Carlo mode was used due to a few characteristics of FRED’s current GPU raytracing capability that involve ray filtering. So although the stray light ASM raytraces here use ten million initial rays and the previous stray light ASM demonstration in §3.3.1 used two million initial rays, the stray light ASM displayed in Fig. 3.8 incorporates the data from more rays than the shift-variant stray light ASMs captured here.

6.1.5 DIRSIG ERM

The ERMs for each combination of scene conditions were captured by creating a spherical collector in DIRSIG at an altitude of 705 km and pointing nadir at the Santa Barbara scene location. The spherical collector extends from a polar angle of 0° along the nadir direction (i.e. the Cassegrain telescope's optical axis) to 90° (the edge of the telescope entrance aperture) and covers 360° azimuthally. Both the polar and azimuthal axes are divided into 1° divisions that match the angular resolution of the Cassegrain telescope's stray light ASMs. The spherical collector is oriented such that azimuthal angle $\phi = 0^\circ$ points directly east and $\phi = 90^\circ$ points directly north, based on the Cassegrain telescope's coordinate system in Fig. 3.6. The ERMs were captured by conducting raytraces in DIRSIG using between 500 and 1,000 rays per grid element solid angle based on a radiometric convergence criterion. In general, more rays per steradian sample the ERM grid element solid angles closest to the optical axis since they each cover a smaller angular range.

6.1.6 Stray Light Radiant Flux Contribution Maps

The stray light irradiance contributions at the focal plane were calculated for every combination of system stray light susceptibility and scene conditions using Eq. 3.6. As detailed in Fig. 6.7 and visually displayed in Fig. 5.2, the multiplication of each individual stray light ASM and ERM produces a unique stray light radiant contribution map. The summation of the stray light radiant flux contributions on these plots produces the final stray light irradiance distributions at the focal plane, so in reality there are an infinite number of system stray light susceptibility and scene radiance profile combinations that will produce the same stray light irradiance value.

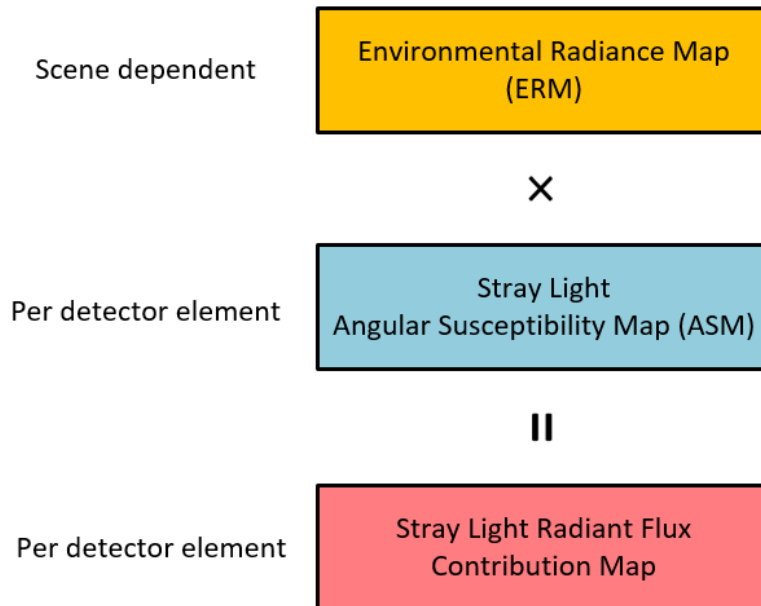


Figure 6.7: Block diagram of the integration method’s stray light radiant flux contribution equation. The ERM of a scene is multiplied solid angle grid element-by-solid angle grid element with a detector element’s stray light ASM for a given set of system stray light susceptibility conditions to produce the detector element’s stray light radiant flux contribution map. The summation of the stray light radiant flux contributions for each solid angle grid element across the contribution map provides the detector element’s total stray light radiant flux.

Observing the stray light irradiance distributions at the focal plane is certainly useful, but does not directly reveal what solid angles contributed the most stray light for each FPA pixel. However, stray light radiant flux contribution maps are produced as an intermediate data product of the integration method and show these “uncollapsed” views of the stray light contributions for each given pixel. This provides very detailed information regarding the interaction of a system’s stray light susceptibility with a particular scene. This moves a step beyond the information included within a stray light ASM, which only characterizes a system’s stray light susceptibility independent of any scene. Stray light contribution maps can be used as a diagnostic tool to better understand how a stray light irradiance

distribution is formed at the focal plane for a certain imaging scenario and can ultimately help guide both system design and mission planning. The combination of system stray light susceptibility and scene data is a critical attribute and novel contribution of the integration method resulting from its marriage of optical engineering software and radiative transfer image simulation models.

6.1.7 Stray Light Irradiance Images

The summed stray light radiant flux contribution maps from the previous step produce the stray light contributions only for the FPA pixels for which stray light ASMs were captured. For the purposes of these demonstrations, we made the approximation of assigning each calculated stray light irradiance value to all of the FPA pixels within its 9×9 pixel region, thus effectively producing a lower spatial resolution stray light irradiance image. Using this method, a separate stray light irradiance image was created for every combination of system and scene conditions. This again reveals the benefits of our modeling and simulation-based integration method, since a purely stray light component image can not be produced in real-world imaging. Producing both nominal and stray light images enables these contributions to be separately analyzed.

6.1.8 Combination of Nominal and Stray Light Irradiance Images

We must combine the nominal and stray light irradiance images to produce the Cassegrain's final output image for each set of system and scene conditions. Note that in the case presented here, the at-aperture radiance that produced both the nominal and stray light irradiance images is top-of-atmosphere (TOA) radiance and has not been atmospherically compensated. It should be noted that our approach has the potential to include a range of

atmospheric transmission and scattering effects and compare their impact to the instrument stray light to introduce that factor into design decisions. Before we combine the images, we must verify the orientation between the DIRISG FPA used to capture the nominal irradiance image and the FRED FPA contained within the Cassegrain telescope model. This is accomplished by conducting several raytraces in FRED and DIRSIG to correlate how object space maps to the focal plane. In FRED, a single ray source can be separately traced into the system from each quadrant of object space and captured on the FPA, thus matching object space and focal plane quadrants. A similar test can be performed in DIRSIG by creating distinct targets in each quadrant of a test scene and using the resulting output image to determine how the object space quadrants map to the focal plane. With this information, the stray light irradiance image can be flipped or rotated so that the FPA pixels being added together correspond to the same object space IFOV. The combined irradiance image can then be converted to photons, electrons, or digital counts as desired, but here we leave the images in irradiance for comparison of the various system and scene conditions.

6.1.9 Percent Stray Light Images

We computed the percent stray light image for each imaging scenario by taking the ratio of the stray light irradiance image to the nominal irradiance image. This produces percentages relating the relative amount of stray light in the combined output image on a per pixel basis, which depends on both the levels of stray light and the scene's illumination conditions. Equivalently, percent stray light details the increase in irradiance between the nominal image and the combined image including stray light. This provides a quantitative means to assess the importance of including the stray light image, which largely consists of out-

of-FOV stray light contributions, and the benefits over the PSF-only stray light modeling approaches. Since the Santa Barbara coastline provides a clear delineation, we have also calculated the average percent stray light for the land and water regions. This is useful for comparing the effect of stray light on different scientific applications viewing land and near-coastal water imagery. We expect the percent stray light to change significantly between land and water due to their different reflectances and therefore nominal signals.

6.1.10 Contrast Reduction

The final metric that we calculated for these demonstrations was the contrast reduction produced by the Cassegrain telescope's stray light performance. This effect is visually evident and can be quantified by comparing the contrast of the ideal image of a scene (i.e. no stray light) to the contrast of its combined nominal and stray light image. The ideal images are calculated by dividing the nominal radiance image for each scene condition by the system's G# calculated without any scattering included. The equation for contrast is given by [169]

$$C = \frac{E_{max} - E_{min}}{E_{max} + E_{min}}, \quad (6.1)$$

where E_{max} is the maximum irradiance in an image and E_{min} is the minimum irradiance. The Santa Barbara scene naturally has a fairly large contrast between the land and water and the addition of stray light adds a variable bias. This increases both E_{max} and E_{min} , resulting in a reduction in C . This contrast reduction is assessed for all of the different system and scene conditions.

6.2 RESULTS

6.2.1 Nominal Irradiance Images

Table 6.3 contains the Cassegrain telescope G#'s computed for each set of optical surface conditions. It is evident that more relaxed particulate contamination conditions lead to a higher G# due to the reduced nominal focal plane irradiance produced by the increase in scattering during the G# measurement. This in turn produces nominal irradiance DIRSIG output images with slightly lower irradiance for dirtier mirror conditions.

Table 6.3: The Cassegrain telescope G#'s for different optical surface conditions. Note that these G#'s are all calculated for the center of the focal plane. The Harvey-Shack scatter model includes $b_0 = 0.1$, $L = 0.01$, and $S = -1.5$, which corresponds to $\sigma_{RMS} = 14.7 \text{ \AA}$ at $\lambda = 0.55 \text{ \mu m}$.

Mirror Polishing	Particulate Contamination	G# [sr ⁻¹]
Harvey-Shack	None	39.16
Harvey-Shack	CL400	39.28
Harvey-Shack	CL600	40.30

Figure 6.8 displays the nominal irradiance images for the Harvey-Shack mirror surface roughness and CL400 particulate contamination conditions plotted on a common irradiance scale. This figure clearly illustrates the impact that the scene conditions have on the illumination levels, particularly over the water. These illumination differences play a factor when calculating the percent stray light per pixel.

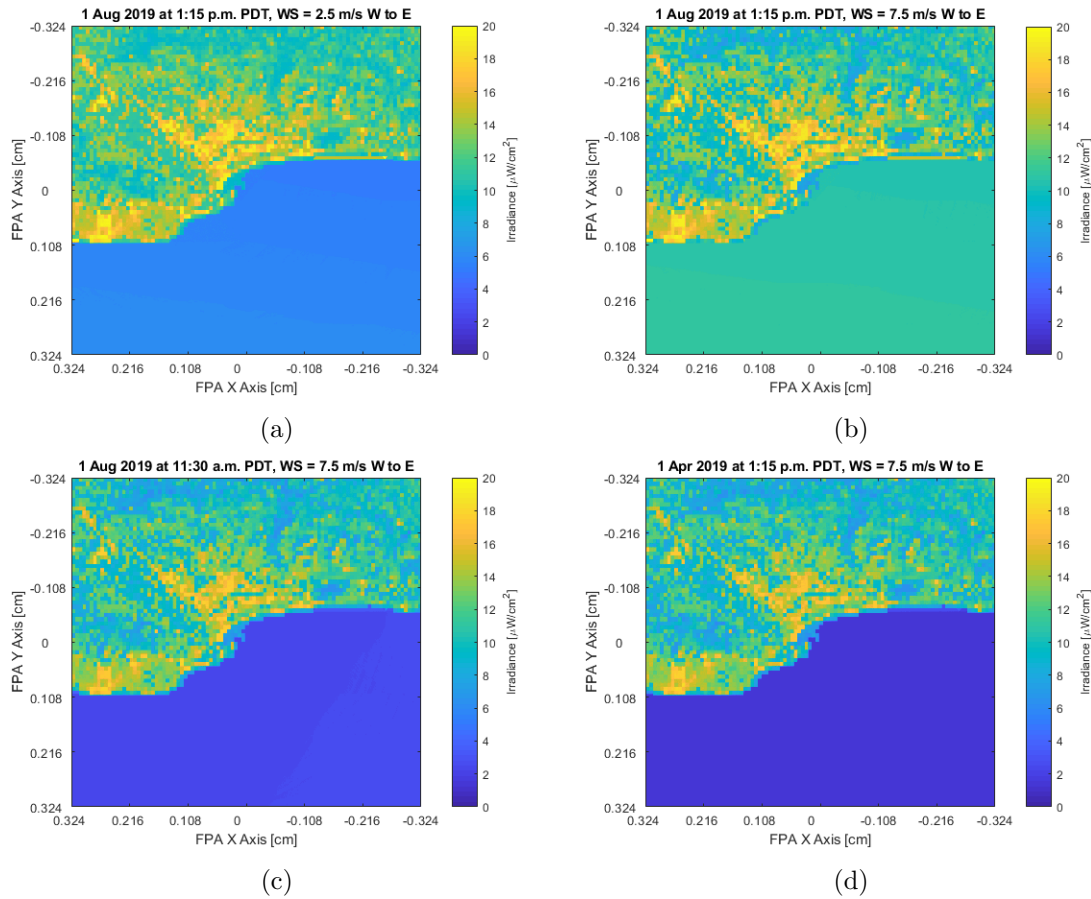


Figure 6.8: Nominal irradiance images for Harvey-Shack mirror surface roughness ($\sigma_{RMS} = 14.7 \text{ \AA}$) and CL400 particulate contamination (common irradiance scale). (a) 1 Aug 2019 at 1:15 p.m. PDT with wind speed = 2.5 m/s. (b) 1 Aug 2019 at 1:15 p.m. PDT with wind speed = 7.5 m/s. (c) 1 Aug 2019 at 11:30 a.m. PDT with wind speed = 7.5 m/s. (d) 1 Apr 2019 at 1:15 p.m. with wind speed = 7.5 m/s.

6.2.2 Cassegrain Shift-Variant Stray Light ASMs

Fig. 6.9 displays the stray light ASM for FPA pixel x356 y356 near the center of the FPA using 10 million initial rays (top) and 100 million initial rays (bottom) for comparison. These stray light ASMs were produced with the system stray light susceptibility conditions including Harvey-Shack scatter model mirror surface roughness ($\sigma_{RMS} = 14.7 \text{ \AA}$), CL400

particulate contamination, and flat black paint TIS = 2%. The vast majority of the scattering included in these plots is contained within approximately 45° of polar angle $\theta = 0^\circ$ (i.e. the optical axis) due to the limitation of single scattering for both the optical and mechanical surfaces. This stands in contrast to Fig. 3.8a, which includes second-order mechanical component scattering contributions beyond $\theta = 45^\circ$. Nevertheless, the major regions of system stray light susceptibility have been efficiently captured, clearly indicating that the Cassegrain system's stray light performance is dominated by single-order scattering from mechanical components.

Similar to the example in Fig. 3.8a, the highest stray light susceptibility from $\theta = 0 - 5^\circ$ results from scatter off the primary baffle's inner wall. The susceptibility region from $\theta = 10 - 17^\circ$ is due to scatter from the dewar chamber inner wall and the secondary mirror baffle, while the largest elevated region of susceptibility from $\theta = 19 - 44^\circ$ is direct scatter from the primary mirror baffle inner wall and hole. All of these most significant regions of stray light susceptibility lie outside of the Cassegrain system's FOV and would not be included in a PSF-only stray light modeling approach. This demonstrates the importance of characterizing a system's far-field stray light performance and including stray light contributions from these angular regions in system modeling and simulation. This is especially true when considering the constrained design environment of compact systems that does not allow for ample baffling that can block these out-of-FOV stray light paths. In these cases, it may no longer be valid to assume that a system is adequately baffled and that the far-field stray light performance is negligible.

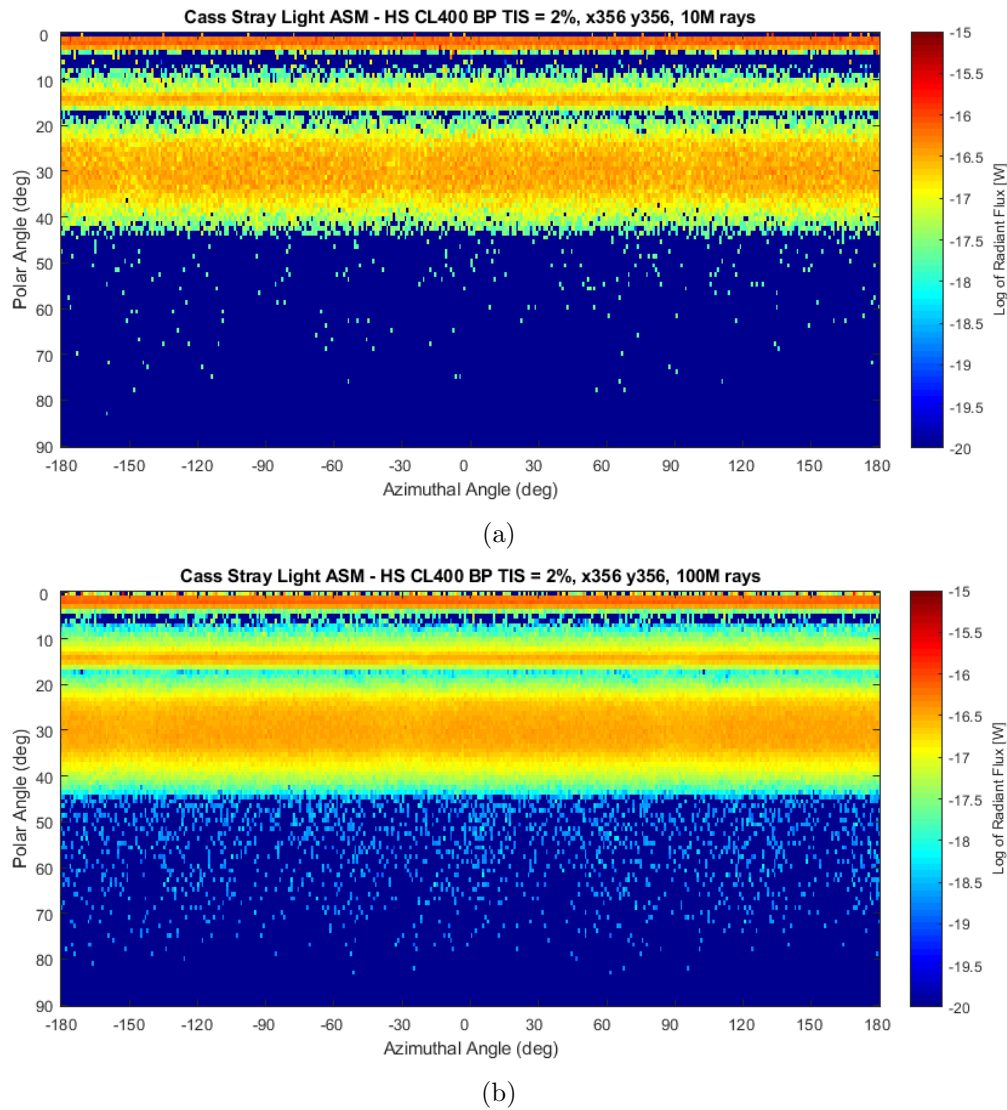


Figure 6.9: Cassegrain telescope stray light ASMs for a pixel near the center of the FPA (x356 y356) with system stray light susceptibility conditions including Harvey-Shack mirror surface roughness ($\sigma_{RMS} = 14.7 \text{ \AA}$), CL400 particulate contamination, and flat black paint TIS = 2% (common log of radiant flux scale). (a) 10 million initial rays. (b) 100 million initial rays. The greater number of rays traced in the latter case has reduced the statistical noise of the system stray light susceptibility data.

Comparing the plots shown here, the 100 million ray case provides a less noisy stray light ASM, but this comes at the expense of an increase in capture time. The lower noise

may not be worth the extra acquisition time depending on the desired level of stray light radiometric accuracy desired and the fidelity of the system model itself with its scatter models. Producing several of these plots for a given pixel with different numbers of initial rays can help characterize the noise and radiometric fidelity of the stray light ASMs for a system and its stray light susceptibility conditions. The higher number of rays also fills in more of the detail for lower magnitude susceptibility regions, though this may not be significant for a particular imaging scenario if the additional stray light contributions provided by these regions are minimal.

Figure 6.10 compares the stray light ASMs for pixel x356 y356 across several different system stray light susceptibility conditions. The impact of the flat black paint can be seen by comparing Fig. 6.10a, which includes the system with flat black paint TIS = 2% (at normal incidence), to Fig. 6.10b, where the flat black paint TIS = 1% (at normal incidence). The magnitude of all three major azimuthal bands of stray light susceptibility have all visibly decreased, thus considerably reducing the system's overall stray light susceptibility. We can look at the bottom two figures to evaluate the effect of particulate contamination, where Fig. 6.10b includes CL400 particulate contamination and Fig. 6.10c has CL600. The difference is most apparent at $\theta < 5^\circ$, where the dirtier CL600 stray light ASM has a slight increase in stray light radiant flux. This increase occurs at low polar angles because any light that single scatters off the mirrors must enter the system at angles fairly close to the optical axis in order to illuminate the mirrors.

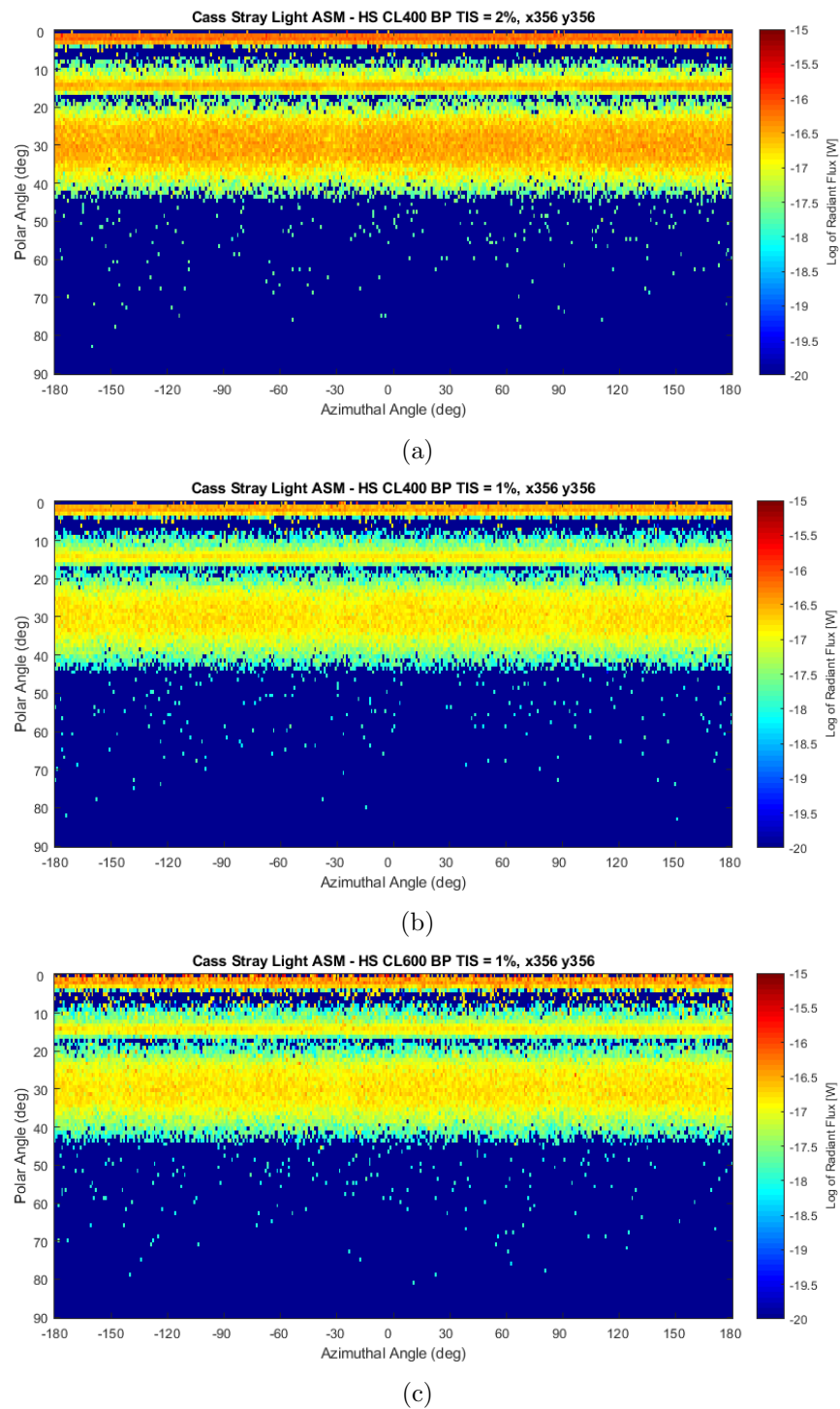


Figure 6.10: Cassegrain telescope stray light ASMs for a pixel in the center of the FPA (x356 y356) with varying system stray light susceptibility conditions: (common log of radiant flux scale). All of the system conditions have Harvey-Shack mirror surface roughness ($\sigma_{RMS} = 14.7 \text{ \AA}$) included. (a) CL400 particulate contamination and flat black paint TIS = 2%. (b) CL400 particulate contamination and flat black paint TIS = 1%. (c) CL600 particulate contamination and flat black paint TIS = 1%.

Beyond the visual comparisons, we can quantitatively evaluate the impact of the different system stray light susceptibility conditions using the metrics in Table 6.4. These metrics are useful because they provide single numbers to quickly approximate the relative stray light performance of different system conditions independent of any scene. However, it should be noted that since they do not take into account any operational scene or shift-variant system stray light susceptibility information (we only show the metrics for one FPA pixel), the full user application impact of the system's stray light performance cannot be evaluated. The total stray light radiant flux is simply the summation of the stray light radiant flux from each grid element of a stray light ASM. Due to reciprocity, this is equivalent to the amount of stray light radiant flux the particular FPA pixel (here we use x356 y356) would receive when imaging an infinite plane with a uniform radiance of $1 \text{ W/m}^2/\text{sr}$ (in this case, a spectral radiance of $10 \text{ W/m}^2/\text{sr}/\mu\text{m}$ at $\lambda = 0.55 \mu\text{m}$ integrated over the pixel's spectral bandpass). Note that this radiance value of $1 \text{ W/m}^2/\text{sr}$ at $\lambda = 0.55 \mu\text{m}$ is the same as the reverse raytrace source used to create the stray light ASM. This type of hypothetical uniform scene is almost analogous to the veiling glare scene described in §2.2.9 (minus the radiance within the pixel's IFOV). Extended uniform radiance scenes are often used to test or write requirements for a system's far-field stray light response, so this metric is especially relevant.

Table 6.4: Total stray light (SL) radiant flux and pixel percent stray light for a pixel (x356 y356) near the center of the Cassegrain telescope’s FPA under different system stray light susceptibility conditions. “BP” refers to the flat black paint scatter model assigned to the mechanical components and the TIS values are for normal incidence. All of the system conditions include Harvey-Shack mirror surface roughness ($\sigma_{RMS} = 14.7 \text{ \AA}$).

Conditions	Total SL Radiant Flux (W)	Pixel % SL
No particulates, BP TIS 2%	2.64E-13	12.74%
CL400, BP TIS 1%	1.36E-13	6.57%
CL400, BP TIS 2%	2.65E-13	12.79%
CL600, BP TIS 1%	1.73E-13	8.63%
CL600, BP TIS 2%	3.06E-13	15.26%

The total stray light radiant flux values indicate that including the CL400 particulate contamination over no particulates slightly increases stray light. Lowering the cleanliness standard from CL400 to the dirtier CL600 has a much more noticeable impact, raising the stray light radiant flux by 15% for the flat black paint TIS = 2% configuration and 27% for the flat black paint TIS = 1% configuration. The latter percentage is much higher because the particulate contamination contribution to the total stray light is larger when the better performing black paint decreases the mechanical component contribution. Including particulate contamination in a system model can therefore play a significant role, especially with less stringent cleanliness standards, which is often the case for cubesats and other small satellites intended for use in constellations. The different flat black paints have an even more substantial impact from TIS = 1% to TIS = 2%, increasing the total stray light radiant flux by almost 95% for the CL400 configuration and 77% for the CL600 configuration. These percentages are so high due to the fact that mechanical scattering by far dominates in the Cassegrain system (which is also detailed by the percentages in Table 3.2).

The pixel percent stray light metric compares the total amount of stray light radiant flux on the stray light ASM for a given pixel to the amount of radiant flux at the en-

trance aperture on the designed optical path during the stray light ASM reverse raytrace. Equivalently, this is the ratio of stray light to target signal for a given pixel when imaging the hypothetical infinite, uniform radiance scene. This metric reveals the same trends as with the total stray light radiant flux, but also shows that the stray light percentages are rather high for this system in its current configuration. The effects of this poor stray light performance will be seen in the results imaging the LA scene.

To aid in comparing how the stray light ASMs vary across the focal plane, Fig. 6.11 provides the stray light ASMs for four pixels near the corners of the FPA and one near the center. The stray light ASMs are displayed in the relative locations of their pixels as if viewing the Cassegrain FPA face-on within the FRED model (i.e. pixel x5 y5 near the top left, x716 y5 near the top right, x356 y356 near the center, etc.) and are plotted on a common log of radiant flux scale. It is immediately apparent that the system has asymmetric stray light susceptibility across the focal plane. Whereas the center pixel has mostly uniform azimuthal bands of stray light susceptibility, the corner pixels exhibit asymmetries from $\theta = 0 - 5^\circ$ and $\theta = 10 - 17^\circ$. The areas of higher susceptibility for the corner pixels are 90° out of phase azimuthally due to their locations on the focal plane. In general, stray light susceptibility asymmetries arise because the geometry of a system changes when viewed from different focal plane locations. This in turn introduces object space directional dependencies for certain stray light paths that either increase or decrease their scattering efficiency. These shift-variant stray light ASM asymmetries are fundamentally what lead to variable irradiance distributions at the focal plane.

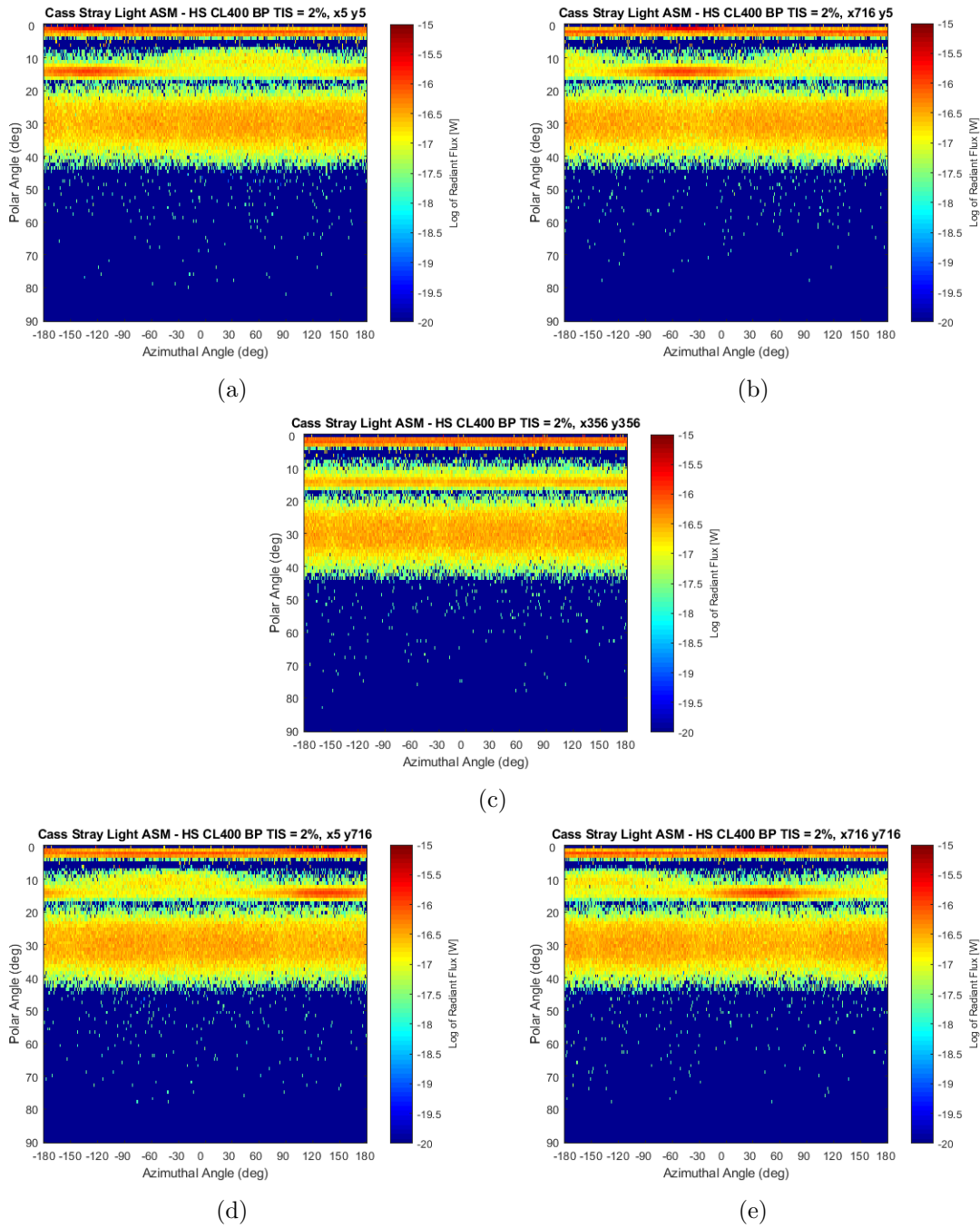


Figure 6.11: Cassegrain telescope shift-variant stray light ASMs for various pixels across the FPA (common log of radiant flux scale). The system stray light susceptibility conditions include Harvey-Shack mirror surface roughness ($\sigma_{RMS} = 14.7 \text{ \AA}$), CL400 particulate contamination, and flat black paint TIS = 2%. All FPA pixel locations are based on viewing the FPA face on in the FRED model (y-axis pointing up, x-axis pointing to the left). (a) top left corner (pixel x5 y5). (b) top right (pixel x716 y5). (c) center (pixel x356 y356). (d) bottom left (pixel x5 y716). (e) bottom right (pixel x716 y716).

6.2.3 DIRSIG ERMs

Fig. 6.12 displays the DIRSIG ERM containing the at-aperture spectral radiance profile at $\lambda = 0.55 \mu\text{m}$ for each of the four scene conditions. The non-zero radiance in each ERM extends to approximately polar angle $\theta = 64^\circ$ since this corresponds to the limb of the Earth from an altitude of 705 km. The contribution from the atmosphere beyond the Earth limb is not included since the MODTRAN atmosphere is not configured to provide accurate radiometry for this angular region. This is acceptable given the Cassegrain telescope's very low stray light susceptibility at high polar angles. The specular sun glint on the ocean is noticeable in all of the ERMs and changes location, size, and magnitude with the different scene conditions. The highest magnitude glint occurs in Fig. 6.15a with the wind speed of 2.5 m/s producing a calmer ocean surface. The glint lies relatively close to the Santa Barbara scene location (marked by a black circle in each ERM), which will cause problems for FPA pixels with strong stray light susceptibility in this direction. A large portion of the sun's direct illumination for the 11:30 a.m. case in Fig 6.12c falls over the land, thus reducing its potential as a stray light source. The western United States (U.S.) is visible in all of the ERMs and provides another major stray light source, especially due to the bright desert regions.

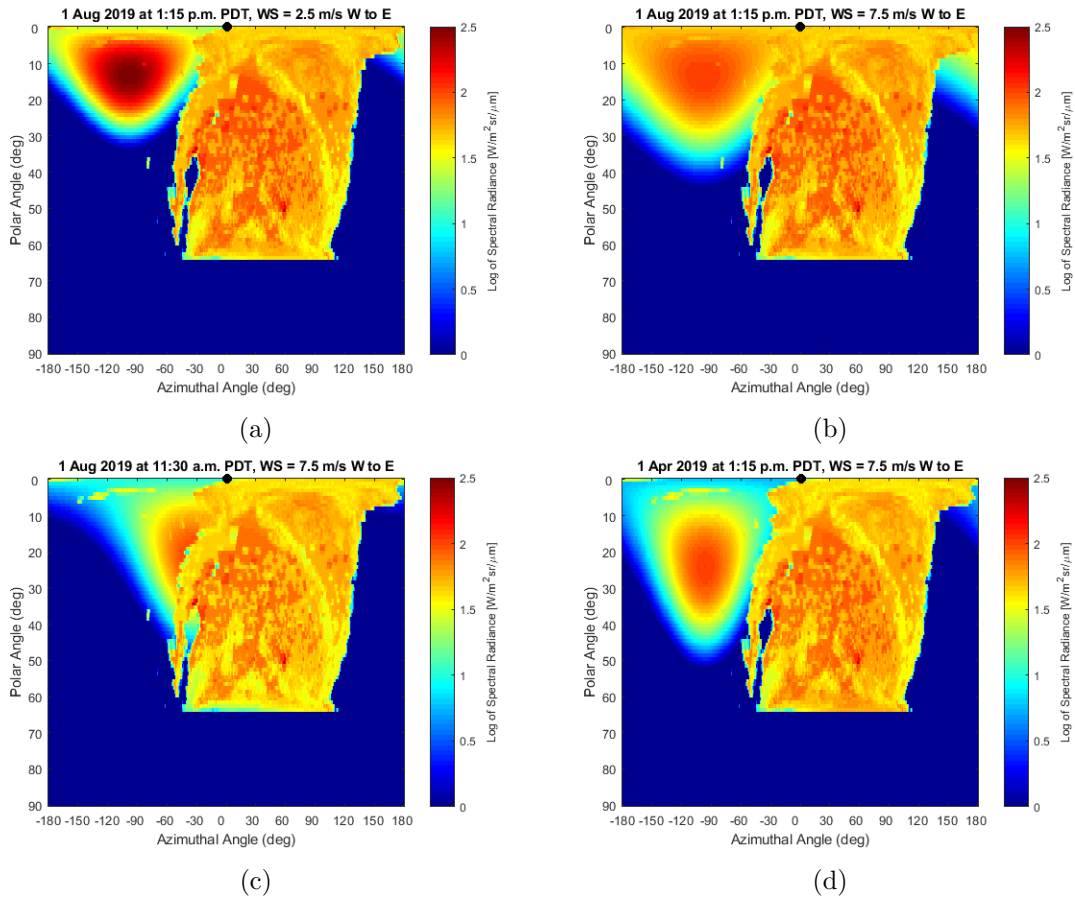


Figure 6.12: DIRSIG ERM for the different scene conditions (common log of spectral radiance scale). The black circles at the top center of each plot marks the Santa Barbara scene location for reference. (a) 1 Aug 2019 at 1:15 p.m. PDT with wind speed = 2.5 m/s. (b) 1 Aug 2019 at 1:15 p.m. PDT with wind speed = 7.5 m/s. (c) 1 Aug 2019 at 11:30 a.m. PDT with wind speed = 7.5 m/s. (d) 1 Apr 2019 at 1:15 p.m. with wind speed = 7.5 m/s.

6.2.4 Stray Light Irradiance Images

In order to interpret the stray light irradiance images, it is useful to consider how the stray light susceptibility asymmetries of the pixels across the Cassegrain telescope's FPA map to the scene. Fig. 6.13 illustrates the azimuthal angles of highest stray light susceptibility for the four corner FPA pixels (orange arrows), along with the stray light ASM azimuthal

angles mapped to the scene (red arrows). The scene displayed here for reference is 1 Aug 2019 at 1:15 p.m. with wind speed = 2.5 m/s plotted on a linear spectral radiance scale. The sun glint peak reflects off the ocean at an azimuthal angle $\phi \approx -110^\circ$. The figure also includes the face-on view of the Cassegrain FPA in FRED with the four corner pixels labeled. Note that the scene and FRED Cassegrain FPA would be facing each other in this imaging scenario. Each corner pixel is most susceptible to stray light originating from a direction mirrored through the system's focal point. For example, if viewing the Cassegrain FPA face-on in FRED, the top left corner pixel x1 y1 has the highest susceptibility to stray light from angles behind and to the bottom right in object space. We must also take into account the orientation of the DIRSIG FPA to the FRED FPA when viewing the stray light images. Fig. 6.14 shows that the FRED FPA must be flipped vertically to match the DIRSIG FPA output images.

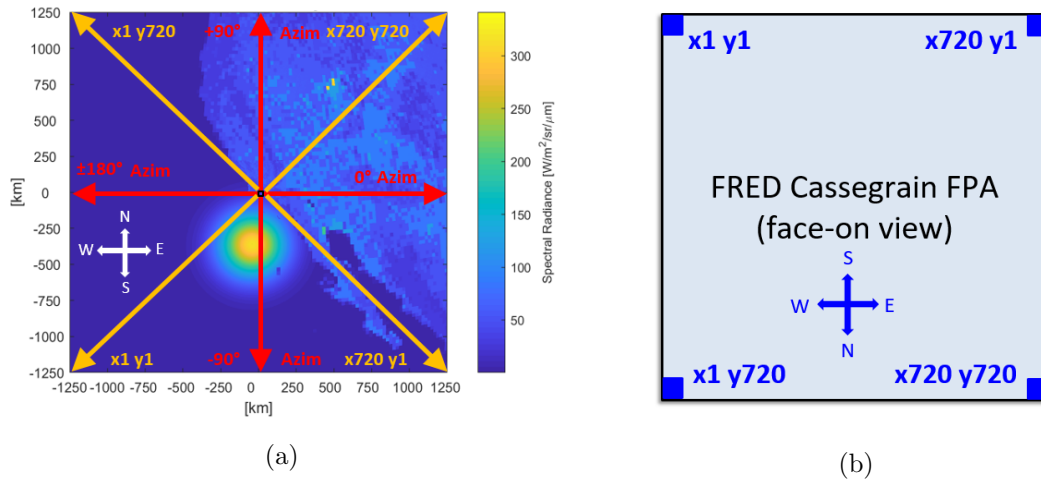


Figure 6.13: Illustration of how the azimuthal angles where different FPA pixels have their highest stray light susceptibility map to the scene. The scene shown is 1 Aug 2019 at 1:15 p.m. with wind speed = 2.5 m/s plotted on a linear spectral radiance scale. (a) The orange arrows mark the azimuthal angle of highest susceptibility for the labeled FPA corner pixels. The red arrows map the Cassegrain telescope's stray light ASM azimuthal angles to the scene (polar angle $\theta = 0^\circ$ points directly into the page). The very small black box in the center of the scene outlines the Cassegrain telescope's nominal FOV over Santa Barbara, CA. (b) Face-on view of the Cassegrain FPA within the FRED model with the corner pixel locations labeled and scene cardinal directions mapped to the FPA.

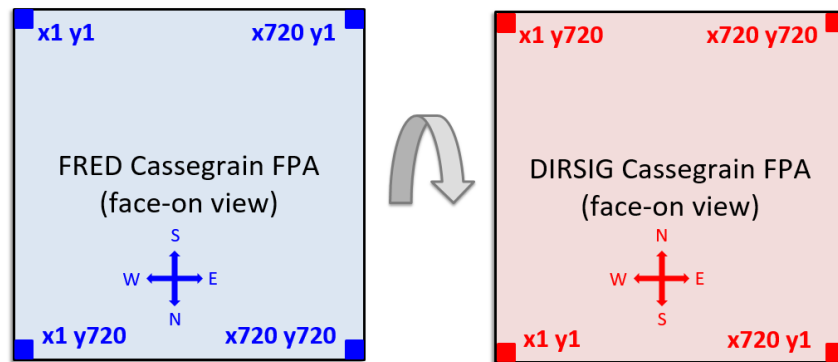


Figure 6.14: Orientation of the Cassegrain FPA within the FRED model to the DIRSIG FPA used to produce the nominal, stray light, and combined final output images. The Cassegrain FPA must be flipped vertically to match the DIRSIG FPA. As detailed by the cardinal directions, this specific orientation of the DIRSIG FPA was chosen so that north in the Santa Barbara scene points up, east points to the right, etc. for improved visualization of the output images.

Different system stray light susceptibility conditions

Fig. 6.15 displays the stray light irradiance images of the 1 Aug 2019 at 1:15 p.m. PDT, wind speed = 2.5 m/s scene with the system under different stray light susceptibility conditions. These images are all plotted on different linear irradiance scales to best highlight their distributions. Table 6.5 provides the mean irradiance from each of these images to aid in their quantitative comparison. As expected, the shift-variant stray light ASMs have resulted in non-uniform stray light distributions for each case. The peak of stray light irradiance near the bottom left of each image is immediately apparent and is produced by the highest regions of asymmetric stray light susceptibility for those pixels overlapping the sun glint on the ocean. The top left corner and right edge pixels generally have the lowest stray light irradiance, as these point to the open ocean northwest of the main California coast and along the Santa Barbara coastline, respectively. Both of these regions have much lower scene radiance than either the sun glint peak off the ocean surface or the western U.S. landmass.

The effect of particulate contamination can be witnessed with the three images in the right column of Fig. 6.15, which all include flat black paint TIS = 2%. As the amount of particulate contamination increases from the top image to the bottom image, the particulates cause more light to diffusely scatter across the focal plane. Similar to the stray light ASM results, there is a slight quantitative difference between no particulates and CL400 for the flat black paint TIS = 2% configuration, but a more substantial difference between the CL400 and CL600 particulate contamination scenarios. Changing from CL400 to CL600 increases the mean stray light irradiance by roughly 27% for the flat black paint TIS = 1% configuration and 13% for flat black paint TIS = 2%. The flat black paint has an even more significant impact when progressing from TIS = 2% to TIS = 1%, reducing the mean stray light irradiance by 49% for the CL400 configuration and 42% for CL600. This clearly demonstrates that the differences in system stray light susceptibility witnessed in the stray light ASMs independent of scene are also manifested when imaging a realistic Earth scene.

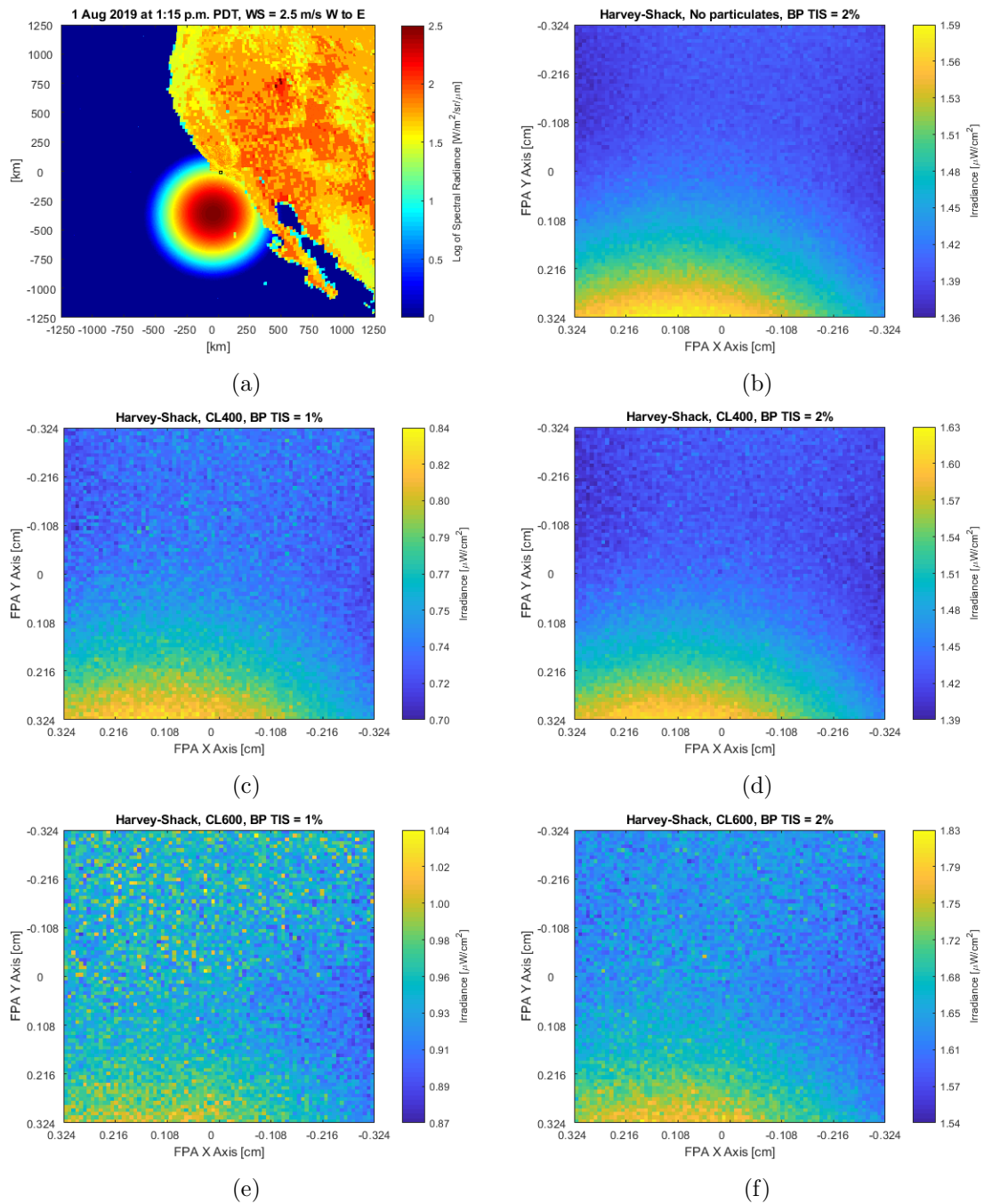


Figure 6.15: Stray light irradiance images for the 1 Aug 2019 at 1:15 p.m. PDT, wind speed = 2.5 m/s scene with different system stray light susceptibility conditions. Note that every image has a different irradiance scaling to best highlight its unique distribution. All system stray light susceptibility conditions include Harvey-Shack mirror surface roughness ($\sigma_{RMS} = 14.7 \text{ \AA}$). (a) Large-area view of the scene for 1 Aug 2019 at 1:15 p.m. PDT with wind speed = 2.5 m/s for reference. The small black box in the center of the scene outlines the Cassegrain telescope's FOV. (b) No particulate contamination, flat black paint TIS = 2%. (c) CL400, flat black paint TIS = 1%. (d) CL400, flat black paint TIS = 2%. (e) CL600, flat black paint TIS = 1%. (f) CL600, flat black paint TIS = 2%.

Table 6.5: Mean irradiance values for the stray light images of the 1 Aug 2019 at 1:15 p.m. PDT, wind speed = 2.5 m/s scene with different system stray light susceptibility conditions.

System SL Conditions	Mean Stray Light Irradiance [$\mu\text{W}/\text{cm}^2$]
No particulates, BP TIS 2%	1.43
CL400, BP TIS 1%	0.75
CL400, BP TIS 2%	1.46
CL600, BP TIS 1%	0.95
CL600, BP TIS 2%	1.65

Different scene conditions

Fig. 6.16 shows the stray light irradiance images for the system stray light susceptibility conditions with Harvey-Shack mirror surface roughness ($\sigma_{RMS} = 14.72 \text{ \AA}$), CL400 particulate contamination, and flat black paint TIS = 2% for each of the different scene conditions. Table 6.6 details the mean stray light irradiance for each of these scenarios. These stray light images exhibit more variability due to the changing scene conditions. Fig. 6.16a and Fig. 6.16b still have the same general pattern, since the change in wind speed does not impact the location of the sun glint on the ocean surface. However, the peak stray light irradiance does extend slightly farther to the bottom left corner of the FPA in Fig. 6.16b. This is due to the fact that the more diffuse sun glint pattern for wind speed = 7.5 m/s has a higher magnitude directly to the southwest of the Santa Barbara scene location, where the bottom left corner FPA pixels have their highest stray light susceptibility.

Unlike the first two images, the stray light image for the 1 Aug 2019 at 11:30 a.m. PDT scene in Fig. 6.16c has a stray light minimum in the bottom left corner. Since the sun glint has shifted to the Gulf of California for this time of day, the region of highest stray light susceptibility for these pixels is now the open ocean and thus produces low amounts of stray light. In fact, this scene has the lowest mean stray light irradiance due to the fact that much

of the sun glint overlaps the land. The sun glint has shifted farther south in the 1 April 2019 case shown in Fig. 6.16d and now overlaps lower regions of stray light susceptibility for the pixels in the bottom of the image. As a result, there are still elevated stray light levels at the bottom of the image, but they are diminished in magnitude compared to the 1 Aug 2019 at 1:15 p.m. PDT cases in the top two images. The minimum in the bottom right corner of the 1 Apr 2019 image is due to the lower amount of sun glint directly southeast of Santa Barbara caused by the shift in sun glint location. Both the 1 Aug 2019 at 11:30 a.m. and 1 Apr 2019 at 1:15 p.m. cases in the bottom two images have a stray light irradiance gradient from the top to the bottom due to the stray light contributions from the California coastline which runs east-west at Santa Barbara.

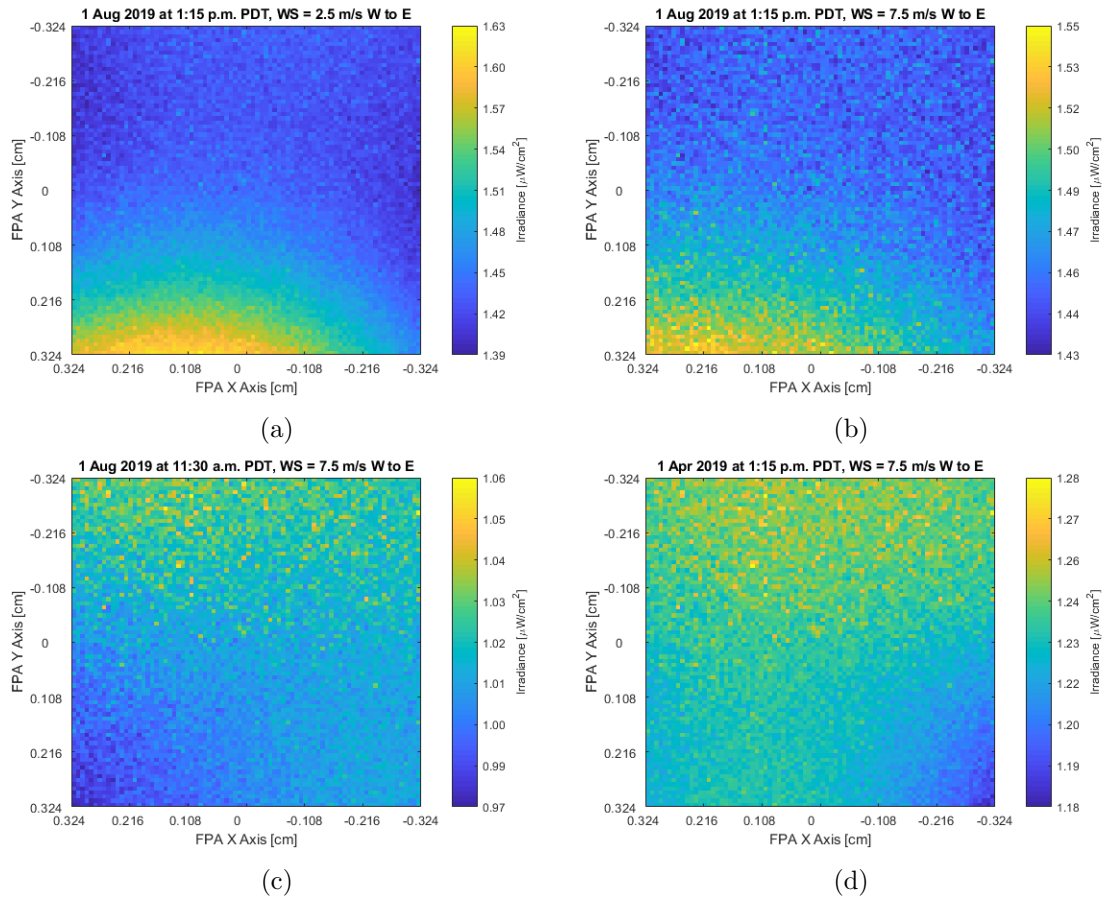


Figure 6.16: Stray light irradiance images for the stray light susceptibility conditions with Harvey-Shack mirror surface roughness ($\sigma_{RMS} = 14.7 \text{ \AA}$), CL400 particulate contamination, and flat black paint TIS = 2% for each of the different scene conditions. Note that every image has a different irradiance scaling to best highlight its unique distribution. (a) 1 Aug 2019 at 1:15 p.m. PDT, wind speed = 2.5 m/s. (b) 1 Aug 2019 at 1:15 p.m. PDT, wind speed = 7.5 m/s. (c) 1 Aug 2019 at 11:30 a.m. PDT, wind speed = 7.5 m/s. (d) 1 Apr 2019 at 1:15 p.m. PDT, wind speed = 7.5 m/s

Table 6.6: Mean of the irradiance values for the stray light images with Harvey-Shack mirror surface roughness ($\sigma_{RMS} = 14.7 \text{ \AA}$), CL400 particulate contamination, and flat black paint TIS = 2% for each of the different scene conditions.

Scene Conditions	Mean Stray Light Irradiance [$\mu\text{W}/\text{cm}^2$]
1 Aug 2019 at 1:15 p.m. PDT, WS = 2.5 m/s	1.46
1 Aug 2019 at 1:15 p.m. PDT, WS = 7.5 m/s	1.47
1 Aug 2019 at 11:30 a.m. PDT, WS = 7.5 m/s	1.01
1 Apr 2019 at 1:15 p.m. PDT, WS = 7.5 m/s	1.23

6.2.5 Stray Light Radiant Flux Contribution Maps

To provide better insight into how Eq. 3.6 produces the stray light irradiance value for each FPA pixel, Fig. 6.17 contains the graphical product of the DIRSIG ERM of the 1 Aug 2019 at 1:15 p.m. PDT, wind speed = 2.5 m/s scene with the stray light ASMs for pixel x5 y5 and x716 y716. For reference, this is the implementation of the block diagram stray light radiant flux contribution map equation displayed in Fig. 6.7. The stray light ASMs were produced with the Harvey-Shack mirror surface roughness ($\sigma_{RMS} = 14.7 \text{ \AA}$), CL400 particulate contamination, and flat black paint TIS = 2% system stray light susceptibility conditions. The end results are the stray light radiant flux contribution maps for each pixel, which detail the “uncollapsed” views of their stray light contributions. For reference, the stray light radiant flux contribution maps displayed here are for the pixels in the bottom left of the stray light image in Fig. 6.15d (pixel x5 y5) and the top right (pixel x716 y716). It can be seen in Fig. 6.15d that pixel x5 y5 has a greater stray light irradiance than pixel x716 y716. This difference arises because pixel x5 y5 has its highest stray light susceptibility regions at angles directly overlapping the sun glint on the ocean, whereas pixel x716 y716 has its regions of highest stray light susceptibility overlapping the western U.S. landmass, which has a lower radiance than the sun glint.

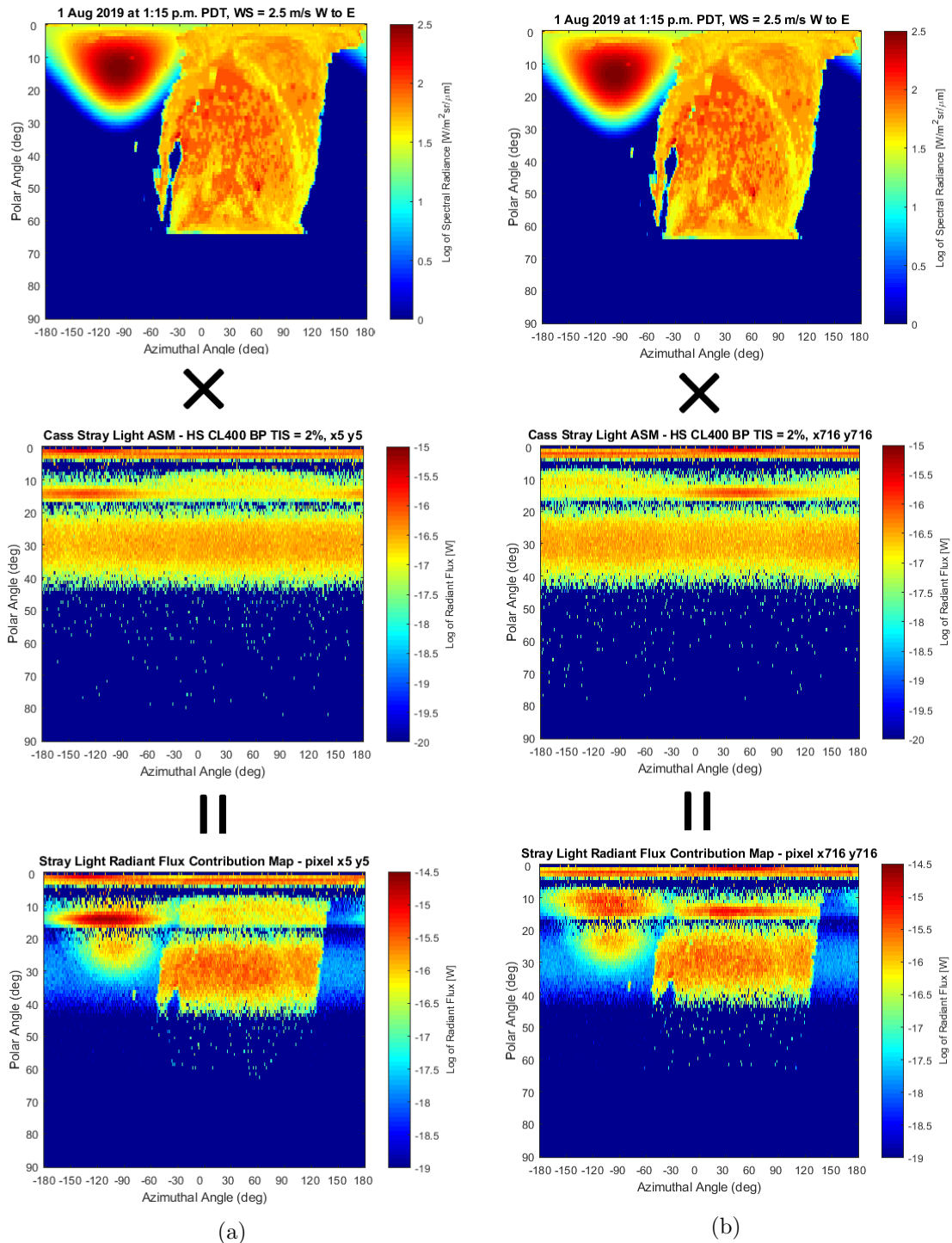


Figure 6.17: Stray light radiant flux contribution maps for the 1 Aug 2019 at 1:15 p.m. PDT, wind speed = 2.5 m/s scene and system stray light susceptibility conditions with Harvey-Shack mirror surface roughness ($\sigma_{RMS} = 14.7 \text{ \AA}$), CL400 particulate contamination, and flat black paint TIS = 2% (common log of radiant flux scales). The summation of these stray light radiant flux contribution maps provides the total stray light radiant flux for the given FPA pixel. (a) Pixel x5 y5 (bottom left of DIRSIG Cassegrain FPA) (b) Pixel x716 y716 (top right of DIRSIG Cassegrain FPA).

In addition to providing a visualization of the stray light contributions, stray light radiant flux contribution maps are a valuable source of information regarding the percentage of a pixel's total stray light irradiance contributed by specific stray light paths, system components, or scene elements. This information can then be used to either drive system changes or alter operational mission plans. Tables 6.7 and 6.8 detail the percentage of total stray light irradiance contributions across different polar angle ranges from different system components for pixel x5 y5 and x716 y716, respectively. From these results, it is evident that although the highest magnitude regions of system stray light susceptibility occur from polar angle $\theta = 0 - 5^\circ$ and $\theta = 10 - 17^\circ$ in the Cassegrain telescope, the greatest actual stray light contribution comes from the western U.S. landmass and the lower portion of ocean sun glint overlapping the $\theta = 19 - 44^\circ$ region. This illustrates the important fact that stray light contributions not only depend on a system's stray light susceptibility magnitude, but also its solid angle extent. The large western U.S. landmass does not change location across the different scene conditions and therefore provides a large stray light bias level for all of the pixels across the focal plane. These data also show that single scattering from the primary mirror baffle inner wall is the dominant stray light contributor from among the stray light paths that lead to approximately 70% of the total stray light irradiance for both pixels. Single scattering from the dewar chamber inner wall and secondary mirror baffle are the primary stray light contributors among the paths responsible for another roughly 30%. In addition to a percentage-based analysis, the magnitude of the stray light contribution from each component can also be separately analyzed for their specific impact on user applications.

Table 6.7: Percentage of the total stray light irradiance for pixel x5 y5 that originates from sources within the given polar angle ranges in object space. These data are for the 1 Aug 2019 at 1:15 p.m. PDT, wind speed = 2.5 m/s scene and system stray light susceptibility conditions with Harvey-Shack mirror surface roughness ($\sigma_{RMS} = 14.7 \text{ \AA}$), CL400 particulate contamination, and flat black paint TIS = 2%. The components causing scatter are the major scatter contributors for each polar angle range.

Polar Angle Range	Component(s) Causing Scatter	% of Total E_{SL}
0 – 5°	Primary mirror baffle inner wall (specular off mirrors)	21.1
10 – 17°	Dewar chamber inner wall, secondary mirror baffle	31.2
19 – 44°	Primary mirror baffle inner wall and hole (direct scatter)	46.1

Table 6.8: Percentage of the total stray light irradiance for pixel x716 y716 that originates from sources within the given polar angle ranges in object space. These data are for the 1 Aug 2019 at 1:15 p.m. PDT, wind speed = 2.5 m/s scene and system stray light susceptibility conditions with Harvey-Shack mirror surface roughness ($\sigma_{RMS} = 14.7 \text{ \AA}$), CL400 particulate contamination, and flat black paint TIS = 2%. The components causing scatter are the major scatter contributors for each polar angle range.

Polar Angle Range	Component(s) Causing Scatter	% of Total E_{SL}
0 – 5°	Primary mirror baffle inner wall (specular off mirrors)	25.5
10 – 17°	Dewar chamber inner wall, secondary mirror baffle	27.5
19 – 44°	Primary mirror baffle inner wall and hole (direct)	45.2

6.2.6 Combined Nominal and Stray Light Irradiance Images

Fig. 6.18 shows an example of how the nominal and stray light images are combined to produce the final output image. This output image includes both the stray light contributions and the reduction in designed optical path light due to scattering off the optical surfaces, effectively emulating the FRED Cassegrain telescope’s performance in the DIRSIG scene (in this case, ignoring PSF effects). The effect of the stray light contribution is most noticeable over the water in the bottom left of the image, though the increase in the land’s irradiance is also discernible. These final output images can be used to test algorithms to determine

the scientific impact on user applications when including the stray light contributions. This performance can then be evaluated against different system-scene configurations or compared to ideal images of the scene taken while assuming the system has no stray light. It may be necessary to interpolate the stray light irradiance values for those pixels that did not have a stray light ASM captured, rather than assigning the same stray light value to the surrounding pixels as we have done here. Having a lower-resolution stray light image could potentially cause issues with algorithm processing due to the mismatch in resolution with the nominal or PSF-produced image.

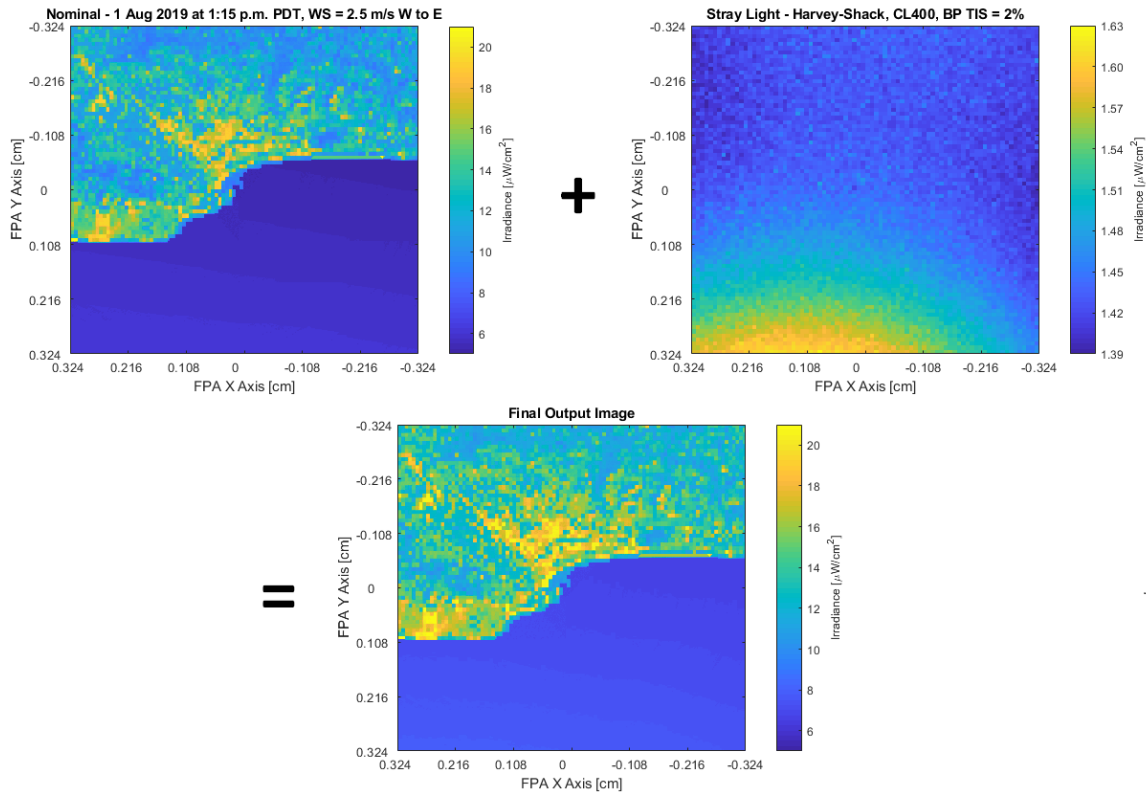


Figure 6.18: The nominal (top left) and stray light (top right) images for a given set of system stray light susceptibility and scene conditions are added together to form the final output image (bottom center). This example is for the 1 Aug 2019 at 1:15 p.m. PDT, wind speed = 2.5 m/s scene and system stray light susceptibility conditions with Harvey-Shack mirror surface roughness ($\sigma_{RMS} = 14.7 \text{ \AA}$), CL400 particulate contamination, and flat black paint TIS = 2%. Note that the nominal and final output images are plotted on the same irradiance scale.

6.2.7 Percent Stray Light Images

Another important quantitative stray light output that can be produced by the integration method are percent stray light images, which take the ratio between the stray light and nominal irradiance images. In addition to the images themselves, we have also computed the average percent stray light over the land and water regions for our Santa Barbara scene. These values are displayed in Table 6.9 across all of the different system stray light

susceptibility and scene condition combinations. Due to the higher nominal signal from the land, the mean land pixel percent stray light values are considerably lower than the water. This presents an issue for any near-coastal water scientific application users who would want to use the imagery from this system to perform ocean color analysis, measure chlorophyll or dissolved organic matter concentrations, etc.

The best stray light susceptibility conditions tested here of Harvey-Shack mirror surface roughness ($\sigma_{RMS} = 14.7 \text{ \AA}$), CL400 particulate contamination, and flat black paint TIS = 1% produce mean land percent stray light values ranging from 5.0–6.6% across the different scenes. Since percent stray light can be viewed as a kind of reciprocal SNR measurement (though it does not include noise from other sources), these stray light levels would range from SNR = 15–20. For reference, the Landsat 8 OLI green band (0.53–0.59 μm) SNR requirement was 100 [170]. A 5% mean land percent stray light (SNR ≈ 20) may be acceptable performance for this first-order system design, assuming some of the previously recommended stray light mitigation improvements are made. If higher cleanliness standards are not within the mission's cost and budget, or if the intended mission goal is to launch a constellation of these cheaper telescopes with lower cleanliness standards, the mean land percent stray light values rise to 6.7–8.8% for the CL600, flat black paint TIS = 1% case. However, the mean water percent stray light values for CL400, flat black paint TIS = 1% range from 7% all the way up to 43.1% for the different scene conditions, which reveals the impact of the illumination conditions on percent stray light. The 11:30 a.m. daily flyover time has the best overall performance numbers for the land pixels, so this may be preferential if land observation is a priority.

Table 6.9: Mean percent stray light values for the land and water pixels across all combinations of system stray light susceptibility and scene conditions.

HS, No particulates, BP TIS = 2%	Mean Land Pixel % SL	Mean Water Pixel % SL
1 Aug 2019, 1:15 p.m., WS = 2.5 m/s	11.5	25.4
1 Aug 2019, 1:15 p.m., WS = 7.5 m/s	12.6	13.3
1 Aug 2019, 11:30 a.m., WS = 7.5 m/s	9.5	40.3
1 Apr 2019, 1:15 p.m., WS = 7.5 m/s	11.9	83.6
HS, CL400, BP TIS = 1%	Mean Land Pixel % SL	Mean Water Pixel % SL
1 Aug 2019, 1:15 p.m., WS = 2.5 m/s	6.1	13.3
1 Aug 2019, 1:15 p.m., WS = 7.5 m/s	6.6	7.0
1 Aug 2019, 11:30 a.m., WS = 7.5 m/s	5.0	21.0
1 Apr 2019, 1:15 p.m., WS = 7.5 m/s	6.2	43.1
HS, CL400, BP TIS = 2%	Mean Land Pixel % SL	Mean Water Pixel % SL
1 Aug 2019, 1:15 p.m., WS = 2.5 m/s	11.8	25.9
1 Aug 2019, 1:15 p.m., WS = 7.5 m/s	12.9	13.8
1 Aug 2019, 11:30 a.m., WS = 7.5 m/s	9.8	40.9
1 Apr 2019, 1:15 p.m., WS = 7.5 m/s	12.2	84.7
HS, CL600, BP TIS = 1%	Mean Land Pixel % SL	Mean Water Pixel % SL
1 Aug 2019, 1:15 p.m., WS = 2.5 m/s	8.0	16.9
1 Aug 2019, 1:15 p.m., WS = 7.5 m/s	8.8	9.3
1 Aug 2019, 11:30 a.m., WS = 7.5 m/s	6.7	25.9
1 Apr 2019, 1:15 p.m., WS = 7.5 m/s	7.9	51.1
HS, CL600, BP TIS = 2%	Mean Land Pixel % SL	Mean Water Pixel % SL
1 Aug 2019, 1:15 p.m., WS = 2.5 m/s	13.8	29.7
1 Aug 2019, 1:15 p.m., WS = 7.5 m/s	15.1	16.0
1 Aug 2019, 11:30 a.m., WS = 7.5 m/s	11.5	46.3
1 Apr 2019, 1:15 p.m., WS = 7.5 m/s	14.0	93.5

Assuming a validated optomechanical system software model has been created and an operational scene has been correctly modeled, percent stray light images offer the potential for use in calibration or correction of on-orbit data. Although it is very difficult and sometimes impossible to decouple the stray light and desired signals for a real-world operational system, the percent stray light images produced by the integration method provide this decoupling. The stray light portion of a measured signal from the physical system imaging the real scene can therefore be readily determined and subtracted for compensation. This capability could be tested by validating an optomechanical system model for an on-orbit system and creating several high-fidelity scenes modeling real calibration sites. The on-orbit imagery could be compared to simulated images of the calibration sites created by implementing the integration method and including stray light contributions. If the results are a close match, then the simulated percent stray light images of the locations can be used to compensate for the stray light in the on-orbit images of the scenes. This process could

be repeated for any scene location without having to develop another post-processing stray light correction method.

Different stray light susceptibility conditions

Fig. 6.19 displays the percent stray light images for the 1 Aug 2019 at 1:15 p.m. PDT, wind speed = 2.5 m/s scene with the system under different stray light susceptibility conditions. These images are all plotted on the same percent stray light scale to aid in their comparison. The flat black paint TIS = 1% cases are immediately recognizable in Fig. 6.19b and Fig. 6.19d due to their much smaller percent stray light values for both land and water. This illustrates the importance of using a high quality black surface treatment for telescope designs where mechanical scattering is the dominant stray light contributor. The impact between the various particulate contamination levels is once again most noticeable over the water and in the flat black paint TIS = 1% images, due to the larger particulate contamination impact on the overall stray light levels.

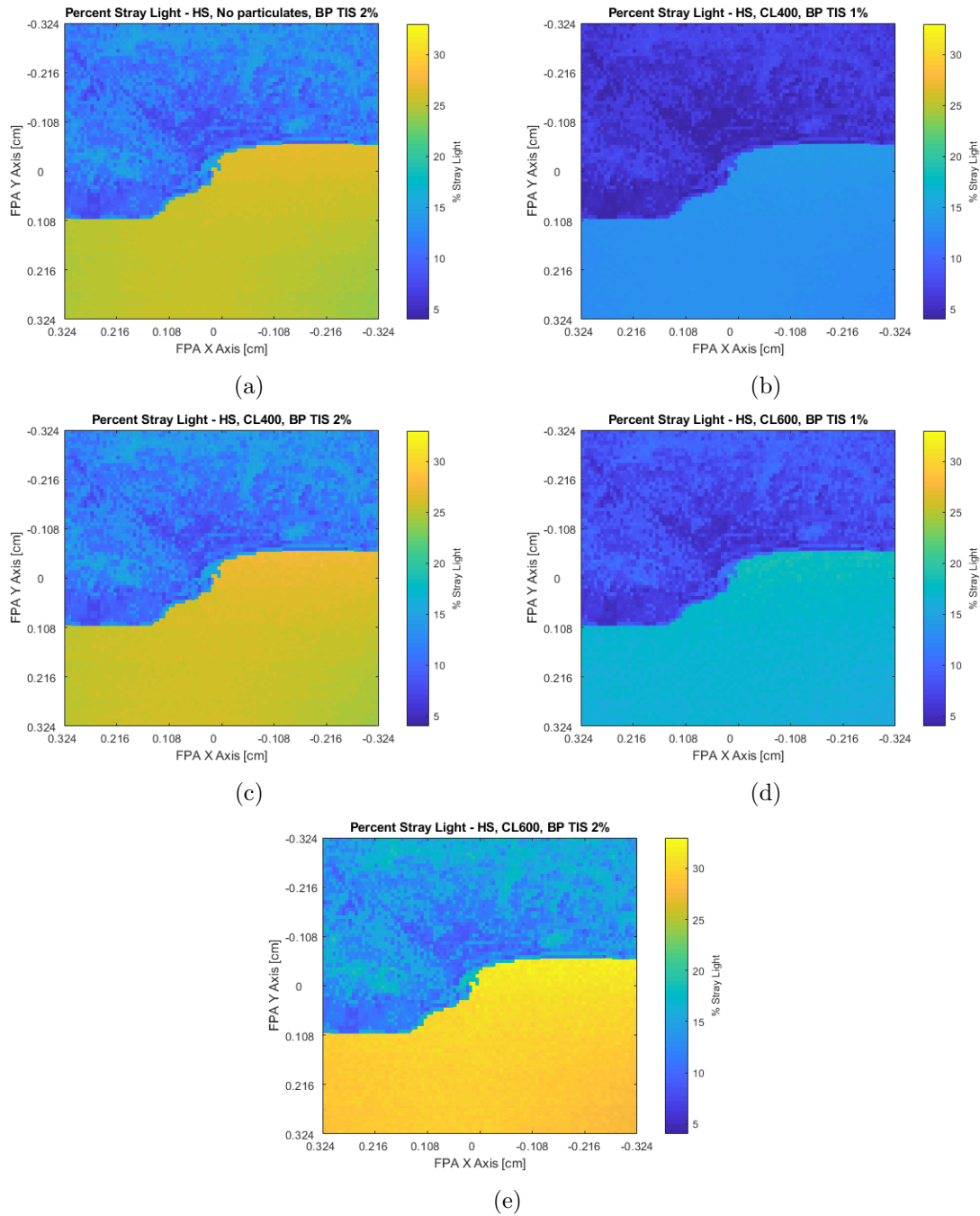


Figure 6.19: Percent stray light images for the 1 Aug 2019 at 1:15 p.m. PDT, wind speed = 2.5 m/s scene with different system stray light susceptibility conditions (common percent stray light scaling). All system stray light susceptibility conditions include Harvey-Shack mirror surface roughness ($\sigma_{RMS} = 14.7 \text{ \AA}$). (a) No particulate contamination, flat black paint TIS = 2%. (b) CL400, flat black paint TIS = 1%. (c) CL400, flat black paint TIS = 2%. (d) CL600, flat black paint TIS = 1%. (e) CL600, flat black paint TIS = 2%.

Different scene conditions

The percent stray light images for the Harvey-Shack mirror surface roughness ($\sigma_{RMS} = 14.7$ Å), CL400 particulate contamination, and flat black paint TIS = 1% system stray light susceptibility conditions with each of the scene conditions are shown in Fig. 6.20. Each image is plotted on a different percent stray light scale for comparison. The top two figures illustrate the percent stray light change that can occur based on wind speed, while Fig. 6.20c highlights the low land percent stray light of the 1 Aug 2019 at 11:30 a.m. PDT scene. The higher water percent stray light for this scene is the result of reduced illumination of the water at this time of day in August.

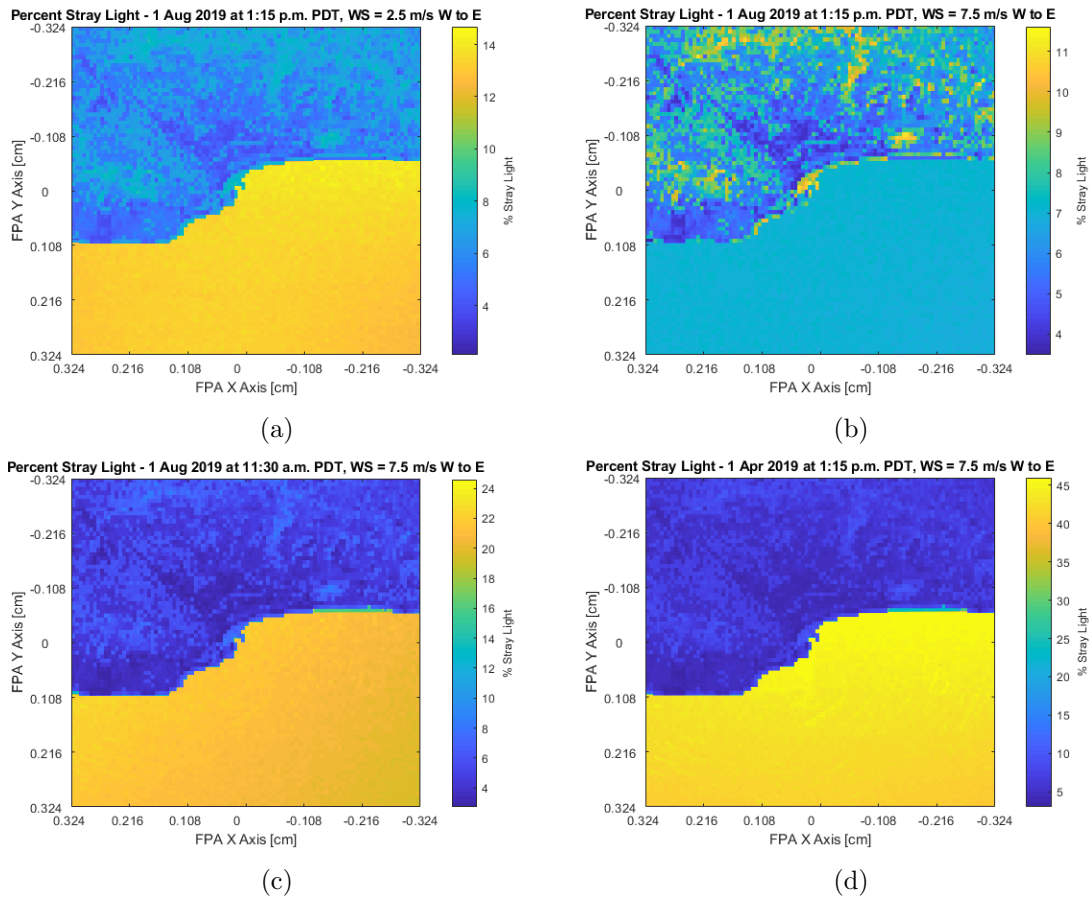


Figure 6.20: Percent stray light images for the system stray light susceptibility conditions with Harvey-Shack mirror surface roughness ($\sigma_{RMS} = 14.7 \text{ \AA}$), CL400 particulate contamination, and flat black paint TIS = 1% across the different scene conditions. Note that every image has a different irradiance scaling to best highlight its unique distribution. (a) 1 Aug 2019 at 1:15 p.m. PDT, wind speed = 2.5 m/s. (b) 1 Aug 2019 at 1:15 p.m. PDT, wind speed = 7.5 m/s. (c) 1 Aug 2019 at 11:30 a.m. PDT, wind speed = 7.5 m/s. (d) 1 Apr 2019 at 1:15 p.m. PDT, wind speed = 7.5 m/s.

6.2.8 System Trade Study Analysis

Taking into account the detailed system-scene stray light radiant flux contribution map data in Tables 6.7 and 6.8, a system designer can see that the inner wall of the primary mirror baffle needs particular attention if this telescope is to be used for an Earth-observing

mission. The majority of the stray light that scatters from the primary mirror baffle inner wall originates from the out-of-FOV western U.S. landmass for this scene and, in general, an Earth-observing satellite can often expect to have large regions of land outside of its nominal FOV. Adding vanes to the inside of the primary mirror baffle would considerably reduce the stray light contributions originating from large off-axis angles by eliminating the surface's near-specular single scattering path. The vanes would ensure that multiple scattering events are required to transmit stray light from the primary mirror baffle inner surface to the focal plane. An additional option would be to use either the flat black paint with $TIS = 1\%$ instead of $TIS = 2\%$ or another better performing black surface treatment, even if just for the primary mirror baffle. Adding a field stop with a reimaging stage or switching to an off-axis telescope design are other options, though those design changes would increase the size and cost of the system, which may be undesirable if the goal is a cheaper, more compact design. However, depending on the stray light requirements for the given scientific applications, the Cassegrain design may ultimately not be sufficient. As far as operational mission changes, stray light can be reduced by choosing a sun-synchronous orbit with a fly-over time in the morning. Table 6.6 shows that an 11:30 a.m. flyover time produces a mean stray light irradiance that is 31% lower than 1:15 p.m. due to the sun glint location.

It is important to note that in the specific case of this Cassegrain system, it has already been demonstrated that the primary mirror baffle inner wall is by far the largest contributor to the system's total stray light (see Table 3.2) and that the system's overall stray light performance is a concern in its current physical configuration (see Table 6.4). The data presented in these previous analyses were based on the more traditional approach of conducting stray light analysis within an optical engineering software program. However,

since the previous analyses were entirely based on stray light ASM data, they neglected to take into account any information regarding an operational scene. Therefore, the system's stray light performance impact on different user applications (and in particular, the primary mirror baffle inner wall's stray light impact) remained unclear. In general, there may be cases where further insights into recommended design changes to improve a system's stray light performance are provided by the integration method that were not as readily apparent from the stray light ASM data by itself.

Although it is true that stray light ASM data can be viewed as a system's response to a scene of uniform radiance, operational scenes exhibit heterogeneity (both spatially and spectrally) that can vary by orders of magnitude and, combined with a system's shift-variant and heterogeneous stray light susceptibility, dramatically impact a system's stray light performance. Additionally, since a stray light ASM only contains the data for a single detector element (as with the data in Tables 3.2 and 6.4), a system's shift-variant system stray light susceptibility will also remain unknown unless the stray light ASMs for a number of detector elements across the focal plane are analyzed. The complex interplay of scene radiance heterogeneity and system stray light susceptibility shift variance and heterogeneity means that stray light ASM data alone provides an incomplete picture of a system's stray light performance. Importantly, stray light ASM data on its own also lacks a means to quantitatively validate whether a specific design change (e.g. adding vanes to the primary mirror baffle inner wall) would sufficiently improve system stray light performance for user applications. This is especially significant since the heterogeneity of scene radiance impacts how different user applications are affected by stray light (e.g. water has a lower nominal signal than land and so near-coastal water scientific applications will be less tolerant of stray light).

The detailed stray light performance data produced by our integration method (e.g. stray light irradiance images, stray light radiant flux contribution maps, percent stray light images, etc.) provide a much more comprehensive view of a system's operational stray light performance and the resulting user application impact by incorporating the rest of the imaging chain. This combination of system stray light susceptibility and scene data provides the crucial linkage between a system's specific configuration (physical design, black surface treatments, cleanliness level, etc.) and its operational stray light performance. This moves beyond simply verifying that a system's stray light meets a given stray light requirement to validating that the system meets user application needs.

From a systems engineering perspective, by taking into account both the system and the scene, our integration method helps answer the critical question of what design change is sufficient for different user applications. Whereas the stray light ASM analysis in Table 3.2 detailed the relative contribution of individual components to the Cassegrain system's stray light performance (for one detector element imaging a uniform radiance scene), the comprehensive stray light performance data produced by the integration method quantifies the overall stray light magnitude for each detector element when imaging an operational scene. How much of the stray light for each detector element was created by particular system components or stray light paths can then be examined in detail. This in turn helps quantify the stray light performance impact of particular components or ray paths user applications. In the Cassegrain system case study presented here, different vane designs could be added to the primary mirror baffle inner wall to determine how much the stray light contributions at the focal plane are reduced both in magnitude and in percentage of the nominal signal. The determination of whether a given vane design is a sufficient improvement for user applications would therefore be based on analyzing simulated end product data, not solely on

verifying that the system meets a more abstract stray light requirement.

6.2.9 Contrast Reduction

We can visually and quantitatively observe the reduction in image contrast due to the addition of the stray light signal through our integration method. As we have previously shown for this imaging scenario, the western U.S. landmass provides a certain bias level of stray light for the different scenes, while the location and magnitude of the sun glint provides an additional variable amount. These effects act together to reduce the contrast of the combined final output images across all of the system stray light susceptibility and scene combinations, as detailed in Table 6.10. The contrast reductions from the ideal image (assuming no system scattering) to the combined nominal plus stray light images directly correlate to the stray light susceptibility conditions. As expected, the higher particulate contamination and flat black paint TIS conditions all lead to larger contrast reductions. This loss of contrast can have negative consequences for user applications, such as algorithms attempting to detect or track small target signals that get lost in the noise.

Table 6.10: Contrast values and reductions from the ideal images to final output images (nominal + stray light images) across every combination of system stray light susceptibility and scene conditions. All of the system stray light susceptibility conditions include Harvey-Shack mirror surface roughness ($\sigma_{RMS} = 14.7 \text{ \AA}$).

1 Aug 2019, 1:15 p.m., WS = 2.5 m/s	Ideal	Nominal + SL Image	Contrast Reduction
No particulates, BP TIS = 2%	0.789	0.745	-0.044
CL400, BP TIS = 1%	0.789	0.766	-0.023
CL400, BP TIS = 2%	0.789	0.745	-0.044
CL600, BP TIS = 1%	0.789	0.760	-0.029
CL600, BP TIS = 2%	0.789	0.739	-0.050
1 Aug 2019, 1:15 p.m., WS = 7.5 m/s	Ideal	Nominal + SL Image	Contrast Reduction
No particulates, BP TIS = 2%	0.542	0.493	-0.049
CL400, BP TIS = 1%	0.542	0.515	-0.027
CL400, BP TIS = 2%	0.542	0.492	-0.050
CL600, BP TIS = 1%	0.542	0.509	-0.033
CL600, BP TIS = 2%	0.542	0.486	-0.056
1 Aug 2019, 11:30 a.m., WS = 7.5 m/s	Ideal	Nominal + SL Image	Contrast Reduction
No particulates, BP TIS = 2%	0.791	0.723	-0.068
CL400, BP TIS = 1%	0.791	0.754	-0.037
CL400, BP TIS = 2%	0.791	0.722	-0.069
CL600, BP TIS = 1%	0.791	0.747	-0.044
CL600, BP TIS = 2%	0.791	0.715	-0.076
1 Apr 2019, 1:15 p.m., WS = 7.5 m/s	Ideal	Nominal + SL Image	Contrast Reduction
No particulates, BP TIS = 2%	0.870	0.775	-0.095
CL400, BP TIS = 1%	0.870	0.819	-0.051
CL400, BP TIS = 2%	0.870	0.775	-0.095
CL600, BP TIS = 1%	0.870	0.809	-0.061
CL600, BP TIS = 2%	0.870	0.765	-0.105

Fig. 6.21 provides a visualization of the contrast reduction for 1 Aug 2019 at 1:15 p.m., wind speed = 2.5 m/s scene across all of the system stray light susceptibility conditions. Fig. 6.21a displays the ideal output image case without any system stray light for comparison. The loss in contrast is most apparent for the poorest performing stray light susceptibility conditions, especially over the water. The effect is also more noticeable for the differences in the flat black paint compared to the differences in particulate contamination levels.

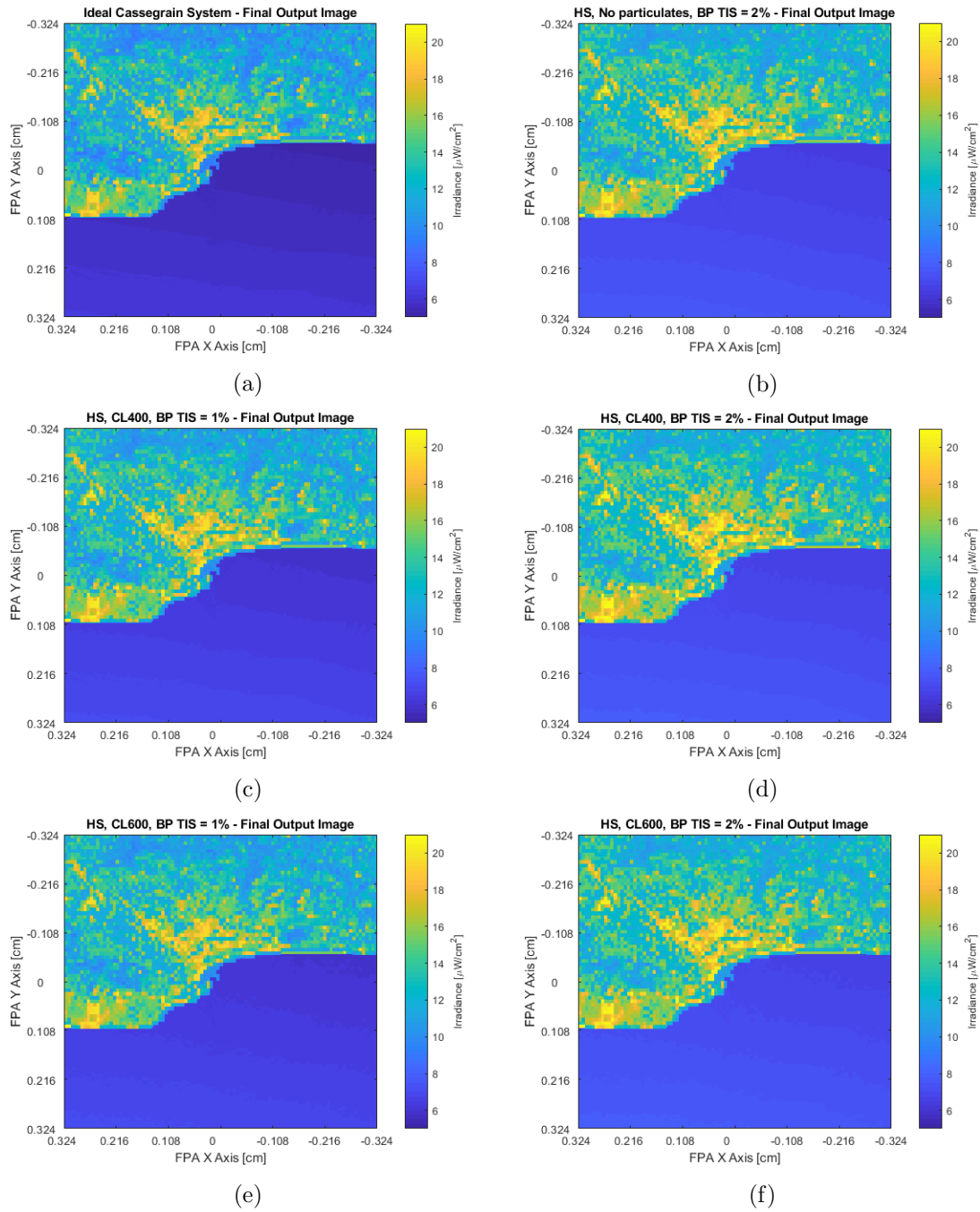


Figure 6.21: Ideal Cassegrain telescope final output image and the final output images (nominal + stray light image) of 1 Aug 2019 at 1:15 p.m. PDT, wind speed = 2.5 m/s scene under different stray light susceptibility conditions (common irradiance scale). All system stray light susceptibility conditions include Harvey-Shack mirror surface roughness ($\sigma = 14.7 \text{ \AA}$). Note that every image has the same irradiance scaling to best highlight the contrast reduction compared to the ideal image. (a) Ideal Cassegrain system. (b) No particulates, BP TIS = 2%. (c) CL400, BP TIS = 1%. (d) CL400, BP TIS = 2%. (e) CL600, BP TIS = 1%. (f) CL600, BP TIS = 2%.

6.3 CONCLUSIONS

This chapter has presented an in-depth stray light-focused system trade study demonstration and analysis through implementing the integration method. This case study was performed for the FRED Cassegrain telescope model and the DIRSIG Santa Barbara scene location, but these results provide insight into the use of this integration method for an arbitrary system and scene. This work meets research objectives 1, 4, and 5 from §1.2 by demonstrating a general methodology for integrating optomechanical system software models with a radiative transfer image simulation model, demonstrating the integration method's system trade study capability with various system stray light susceptibility and scene conditions, and demonstrating the quantitative metrics that can be produced by the integration method to evaluate the impact of stray light on user applications.

Several innovative contributions were included in this work that will enhance the modeling and simulation of system stray light performance. The capture of shift-variant system stray light susceptibility data using the new GPU raytracing capability of optical engineering software represents a significant advancement. The dramatic increase in computational power provided by GPU raytracing allowed us to collect detailed stray light performance data across the focal plane 80–110 times faster than with traditional CPU raytracing. The resulting shift-variant stray light ASMs provide a wealth of information about how the system's stray light susceptibility changes down to the per-pixel level.

The sets of shift-variant stray light ASMs we collected enabled us to produce stray light irradiance images for any given combination of system stray light susceptibility and scene conditions. These stray light irradiance images represent a substantial innovative contribution to the modeling and simulation of Earth-observing systems. Whereas traditional

modeling and simulation-based stray light analysis is largely performed exclusively within optical engineering software, the stray light irradiance images produced here critically incorporate both system stray light susceptibility and scene data. By combining stray light performance data from an optomechanical system model with a radiative transfer image simulation model, any combination of system stray light susceptibility and scene conditions can be tested. This is particularly useful for performing stray-light focused system trade studies and testing a system's performance on stressing stray light scenes. It is also not possible to create these stray light-only images in the real world to aid in system evaluation, since the stray light contributions cannot be separated from the designed optical path light once integrated at the focal plane. The stray light images produced by our integration method can be separately analyzed or used to generate secondary data products like percent stray light images. Additionally, they can be combined with nominal or PSF images to produce flight-like images for any arbitrary system and scene conditions. These final output images with stray light contributions included are a much more tangible end product to show program management than more abstract stray light metrics such as a PST curve or veiling glare measurements, which alone do not capture the complexity of the entire imaging chain. The combined final output images can further be used to test various retrieval or detection algorithms to determine how they are affected by the inclusion of stray light.

This integration method offers further benefits over typical PSF-only stray light modeling and simulation approaches. Many of these approaches are limited to near-field stray light, implicitly assuming that a system's far-field stray light susceptibility is negligible due to sufficient baffling or other stray light mitigation techniques. Although these methods do have the ability to produce final output images through convolutional means (which often assumes shift invariance), these images lack contributions from potentially impactful sources

of stray light. The approaches themselves also lack the flexibility to incorporate far-field stray light contributions if so desired. The relatively few stray light modeling methods that do incorporate some measure of far-field stray light susceptibility produce single stray light values at the focal plane, not stray light images and final output images including stray light contributions for any Earth-observing scene. However, as we have demonstrated here, far-field stray light susceptibility can lead to large amounts of stray light that produce variable irradiance distributions at the focal plane. This may be especially true in future lower cost, more compact optical designs used in small satellites for Landsat or other missions. The constrained design environments of these systems mean that many of the assumptions about far-field stray light performance may no longer be valid. At the very least, far-field stray light performance should be incorporated into the modeling and simulation of these systems to determine its impact on user applications. Our integration method includes contributions from near-field and far-field stray light across the entire focal plane, along with the effects of diffraction and aberrations through PSFs. This provides the most detailed and comprehensive method for incorporating stray light contributions to determine their impact on user applications.

Beyond the stray light irradiance images produced by this integration method, this work has also demonstrated the valuable performance data that can be produced to assess the stray light contributions from specific stray light paths or system components on a per-pixel basis. The stray light radiant flux contribution maps provide this enhanced visualization and quantifiable data in a way that clearly illustrates the interplay between a system's stray light susceptibility and a given scene. This is a major improvement over stray light modeling methods that either do not incorporate far-field stray light or do so in a way that only produces single, shift-invariant stray light values for the entire focal plane. This

also represents a further development upon traditional stray light susceptibility analysis conducted within optical engineering software (i.e. full detector reverse raytracing, PST, veiling glare, etc.) by integrating the interaction of a dynamic scene. As we have shown here with the LA scene, different scenes certainly change the stray light contributions even for the same instrument stray light susceptibility conditions.

The system trade study presented here revealed that the Cassegrain telescope model in its current configuration produces stray light contributions that are too high for most user applications, especially those involving near-coastal water regions. Several stray light mitigation solutions were discussed, including adding vanes to the inner diameter of the primary mirror baffle, using a higher performing black paint on the mechanical surfaces (especially the primary mirror baffle), redesigning the Cassegrain telescope with a field stop and reimaging stage, or switching to an off-axis design if the Cassegrain's stray light performance does not meet requirements. This determination was not made by only assessing the system's stray light susceptibility within optical engineering software, but by observing simulated stray light images and metrics of the Cassegrain system imaging a stressing stray light scene and comparing the results to user application needs. The integration method is not intended as a replacement for traditional stray light analysis within optical engineering software, which is extremely valuable in its own right, but rather as a complement. The enhanced visualization and insight gained through the integration method's system-scene modeling and simulation allows system designers to predict any negative impacts of system stray light performance on user applications and avoid costly hardware redesign further into the development process.

It is this end-to-end capability of the integration method that offers one final major benefit for drafting system stray light requirements. Creating stray light requirements that

are specifically written for the stray light performance required for a given mission and its user applications is an inexact science at best, so heritage-derived requirements are often used. However, without a clear linkage between the required user performance and a specific stray light requirement, this method of setting requirements runs the risk of over or underspecifying. This could lead to cost and schedule overruns in meeting a stray light requirement that is too strict (assuming the requirement can be met with the given system design) or a dissatisfied user community if the requirement is too relaxed. This integration method offers a means to better understand how stray light requirements written in more abstract optical engineering terms such as PST or veiling glare translate into a system's operational performance, both visually and quantifiably. Optical engineering software can be used to verify that a system meets the more abstract stray light requirements, while the end-to-end integration method validates that the system meets user needs. The knowledge gained from this verification and validation process can help inform the drafting of informed stray light requirements that connect to the user application impact.

As with any modeling and simulation, it should be noted that the results from this integration method will only be as good as the validated optomechanical system software model, the scatter models provided, the efficiency of the model's importance sampling specifications, etc. BSDFs for materials are notorious for varying by an order of magnitude from theoretical values and can vary significantly from component to component. Particulate contamination BSDFs can change for the same particle distribution based on varying refractive index and other factors. This emphasizes the importance of continued model validation as system development proceeds and vendor material measurements are available or hardware components are assembled. Even when using a lower fidelity system model earlier in the design process, where there is less confidence that the model's absolute stray

light radiometry matches the physical system it represents, the relative change in system stray light performance when making specific design changes can still prove very useful. Nevertheless, modeling and simulation play a substantial role in the system design and development process and can offer many benefits for evaluating system stray light performance and determining its impact on user applications.

Chapter 7

Summary and Conclusions

Chapter 1 introduced the context of this research through the discussion of the Landsat program's history and current challenges. The need to understand the stray light performance of future Landsat systems, especially for potential lower cost, more compact designs, was presented as a primary research motivation. Deficiencies of current stray light performance evaluation and modeling and simulation techniques were reviewed as additional motivating factors leading to the solutions developed by this dissertation work. Research objectives were defined, including: 1) demonstration of a general methodology for integrating optomechanical system software models with a radiative transfer image simulation model, 2) validation of the integration method's PSF component, 3) validation of the integration method's stray light component, 4) demonstration of the integration method's capability to perform system trade studies with varying system stray light susceptibility and scene conditions, and 5) demonstration of the quantitative metrics that the integration method can produce to evaluating the impact of stray light on user applications.

Chapter 2 contains a detailed background on stray light, starting with the fundamen-

tal radiometric principles and mechanisms, and progressing through the primary causes, including scattering from optical surfaces and coatings, scattering from particulate contamination, scattering from black surface treatments, and diffraction. Various stray light metrics were then discussed, along with stray light's role in the systems engineering process through requirement definition and analysis using build-and-test and optical engineering software modeling approaches. A review of linear system theory was included next to provide context for the PSF-based work. Finally, current PSF and stray light modeling efforts were described in detail, along with the DIRSIG radiative transfer and image simulation model and its importance sampling-based approach for incorporating system PSFs.

Chapter 3 introduced the basic radiometric framework of the integration method, including its PSF and stray light components. The integration method's primary radiometric equations were used as a means to introduce the $G\#$ concept for properly scaling the PSF component and the stray light ASM and ERM breakdown of the stray light component. The fundamental principle that stray light contributions are the product of system stray light susceptibility and scene at-aperture radiance on a per-pixel basis was discussed. The stray light component was then covered in more detail in order to highlight this key aspect of the integration methodology. This first involved demonstrating how stray light susceptibility data can be collected from an optomechanical system model using optical engineering software. Critical concepts such as importance sampling for scatter calculations in optical engineering software were discussed as a part of this demonstration. The resulting data were analyzed to show how they can be used in assessing a system's stray light performance. Shift-variant stray light ASMs were then introduced as a means to collect stray light susceptibility data across a system's focal plane using optical engineering software's new GPU raytracing capabilities. Finally, the dissertation's work on validating the inte-

gration method was placed within the context of the other forms of validation required to perform an end-to-end simulation of the expected imagery produced by a system still in development or for a comparison between simulated imagery of a given system and scene to actual operational imagery.

Chapter 4 introduced the details of the integration method's PSF component. This involved a description of how PSFs can be captured using optical engineering software along with helpful acquisition details. Two separate tests were then presented to validate the importance sampling-based approach for incorporating system PSFs and to validate the successful integration of a system PSF from an optomechanical system software model into a radiative transfer image simulation model. This produced convincing results in both cases, but also revealed areas of further research to better characterize the effect of the law of large numbers on probability-based PSF importance sampling.

Chapter 5 focused on the integration method's stray light component. Validation tests were presented using two parallel aligned square surfaces along with a simplified Cassegrain telescope model to compare raytrace results to analytical stray light calculations. These tests demonstrated FRED's high fidelity absolute scatter radiometry and the reciprocity of the Cassegrain telescope in the forward and reverse directions, validating the integration method's foundational principle of using reverse raytrace stray light susceptibility data to estimate stray light contributions for a given scene in the forward direction. These tests also confirmed that FRED's scatter radiometry follows the basic equations of stray light radiative transfer. As a last step, the integration method was implemented for a test target in DIRSIG and the results matched the FRED forward raytrace within the statistical noise of the raytraces. This proved that the integration method effectively emulates the stray light performance of an optomechanical system software model within a radiative transfer

image simulation model.

Chapter 6 built upon the stray light component validation work by demonstrating the integration method's stray light-focused system trade study capability using the FRED Cassegrain telescope model and a DIRSIG scene of the southern California coastline around Santa Barbara, CA. Several different combinations of system stray light susceptibility and scene conditions were tested to evaluate the Cassegrain telescope's stray light performance in different imaging scenarios. The collection of the shift-variant stray light susceptibility data for each type of system condition demonstrated the advantage of collecting this detailed performance data across the focal plane, which was greatly aided by FRED's GPU raytracing capabilities. The integration method's output images and quantitative metrics were then evaluated for the different system and scene combinations. A number of these data, including stray light irradiance images and stray light radiant flux contribution maps, are innovative contributions to existing stray light modeling and simulation approaches. Many insights were presented on how the integration method's stray light data products can be used for conducting a system trade study.

7.1 CONCLUSIONS

Stray light is often an afterthought during the imaging system design and development process, with emphasis placed on meeting other system requirements. However, it is all too often that systems reach flight operations and only then, when imagery is first collected, are the detrimental effects of stray light realized. At this point, the only option is to invest the necessary time and money in the attempt to develop a reactive solution.

Regardless of whether or not it is taken seriously, stray light presents a significant

risk to the radiometric fidelity of imagery collected by remote sensing systems. This is a particular concern of the Landsat program in its development of future systems, especially when considering lower cost, more compact designs that may be more susceptible to stray light. However, this problem is not unique to Landsat, as there is a general push towards smaller satellites for a variety of applications and freeform optics are allowing improved image quality within more compressed optomechanical designs.

In an effort to better understand the quantitative linkage between system stray light performance and the impact to user applications, we have developed a general modeling and simulation-based methodology that integrates optomechanical system models from optical engineering software with a radiative transfer image simulation model. This solution takes advantage of the unique benefits of both types of models to effectively emulate the PSF and stray light imaging performance of detailed optomechanical models within high-fidelity, physics-based scenes. This integration represents an important achievement for conducting system trade studies and sensitivity analyses for a number of reasons. Many more system design changes can be analyzed for their end-to-end impact on user applications when using a 3-D CAD optomechanical system model compared to the more typical parameterized system models used within radiative transfer image simulation models. This is especially true for stray light-focused changes, since a system's stray light performance depends on the complicated geometry and scattering characteristics of its various components. Using this integration method, the contributions of stray light from specific components and ray paths can be assessed to determine their impact on user applications. This predictive knowledge can then be used to develop efficient stray light mitigation strategies for a particular system without costly hardware redesign. Beyond just stray light, this integration method offers the versatility to analyze the final output imagery and user application impact of other

parameters of interest, such as image quality, the effects of aberrations and distortions, tolerancing and alignment of components, and the degradation expected during a system's operational lifecycle.

The validation work presented in this dissertation provides confidence that the integration method can successfully incorporate PSF and stray light susceptibility data from an optomechanical system software model into a radiative transfer image simulation model and produce correct radiometry. This is critical, since anyone using this integration method as a tool to assess system performance needs to understand the fidelity of the tool. It is important to note that this validation work has focused on the integration method itself, i.e. proving that using the method is functionally equivalent to having a 3-D optomechanical system software model within a radiative transfer image simulation model and imaging scenes. However, as with any system modeling and simulation, users of this integration method are still responsible for validating the optomechanical system software model if they desire its performance to model that of a real system in development. The integration method will replicate the performance of whatever system model is used, regardless of whether or not the model's performance matches the real system. Similarly, the scene must also be validated in the radiative transfer image simulation model if imagery from an operational system imaging a specific scene is to be compared to simulated imagery produced through this integration method.

These considerations aside, the innovative contributions of this integration method offer many new possibilities for system modeling and simulation, especially for stray light. The inclusion of far-field stray light contributions and shift-variant stray light susceptibility data captured by optical engineering software's GPU raytracing capability significantly improve upon current stray light modeling approaches. The production of stray light irradiance

and percent stray light images, along with the detailed system-scene information contained within stray light radiant flux contribution maps on a per-pixel basis provide valuable information for system trade studies that also goes far beyond current capabilities. Finally, this integration method can play a crucial role in determining how specific stray light requirements translate to stray light user application impact.

7.2 FUTURE WORK

The work presented here in developing, validating, and demonstrating the integration method has laid a solid foundation for a number of future efforts to expand this novel capability. The following list details a few of these options.

- Test the integration method with the validated telescope model of an operational system and compare end-to-end simulated imagery with real imagery produced by the system. This would require validating the telescope optomechanical system software model to the real system and the scene created using a radiative transfer image simulation model to the real scene. This work would be useful in proving that the integration method can be used as a key step in successfully replicating the performance of an operational system.
- Demonstrate the integration method's shift-variant PSF capability. This would allow for the changing impact of a system's diffraction and aberrations across the focal plane to be captured in imagery. Final output imagery could then be produced using both shift-variant PSF and stray light susceptibility data to produce more realistic results.
- Demonstrate the integration method's PSF and stray light spectral capabilities. Al-

though the results presented in this dissertation used a single spectral channel, the method applies the same to multiple spectral channels. The spectral effects of stray light then can then be analyzed in detail.

- Demonstrate the integration method for a system operating in the thermal wavelength regime. This would require the modeling of component thermal self-emission that must be included as part of the system stray light susceptibility data. As seen with Landsat 8's TIRS, stray light can be a significant problem at thermal wavelengths and this integration method can be a valuable tool for those systems as well.
- Investigate how the law of large numbers affects PSF radiometric results when using low numbers of sampling rays. This work should test methods that reduce this error by limiting PSF dynamic range, while still preserving sufficient spatial sampling to capture important PSF features.
- Test the integration method using system PSF and stray light performance data from other optical engineering software programs such as CODE V, Zemax OpticStudio, TracePro, ASAP, etc. This would help expand the method's versatility to other types of systems and user communities.

Bibliography

- [1] B. L. Markham, T. Arvidson, J. A. Barsi, M. Choate, E. Kaita, R. Levy, M. Lubke, and J. G. Masek, “Landsat program,” in *Comprehensive Remote Sensing* (S. Liang, ed.), pp. 27–90, Oxford: Elsevier, 2018.
- [2] Irons, James R., “Landsat 1.” NASA Goddard Space Flight Center, 2018. <https://landsat.gsfc.nasa.gov/landsat-1/>. (Accessed: 16 September 2018).
- [3] D. Daniels, “Landsat project report,” 2015. Given to the Landsat Ground Station Operations Working Group, #44, Paris, France.
- [4] S. Goward, D. Williams, T. Arvison, L. Rocchio, J. Irons, C. Russell, and S. Johnston, *Landsat’s Enduring Legacy: Pioneering Global Land Observations from Space*. Bethesda, MD: American Society for Photogrammetry and Remote Sensing, 2017.
- [5] D. L. Williams, S. Goward, and T. Arvidson, “Landsat: Yesterday, today, and tomorrow,” *Photogrammetric Engineering and Remote Sensing*, vol. 72, no. 10, pp. 1171–1178, 2006.

- [6] D. L. Williams and S. Goward, "Landsat and earth systems science: Development of terrestrial monitoring," *Photogrammetric Engineering and Remote Sensing*, vol. 63, no. 7, pp. 887–900, 1997.
- [7] Irons, James R., "A Landsat Timeline." NASA Goddard Space Flight Center, 2018. <https://landsat.gsfc.nasa.gov/a-landsat-timeline/>. (Accessed: 16 September 2018).
- [8] Miller, Holly, "Users and Uses of Landsat 8 Satellite Imagery - 2014 Survey Results." U.S. Geological Survey, 2016. <https://pubs.usgs.gov/of/2016/1032/ofr20161032.pdf>. (Accessed: 10 February 2019).
- [9] Z. Wu, G. Snyder, C. Vadnais, R. Arora, M. Babcock, G. Stensaas, P. Doucette, and T. Newman, "User needs for future Landsat missions," *Remote Sensing of Environment*, vol. 231, p. 111214, 2019.
- [10] M. A. Wulder, T. R. Loveland, D. P. Roy, C. J. Crawford, J. G. Masek, C. E. Woodcock, R. G. Allen, M. C. Anderson, A. S. Belward, W. B. Cohen, J. Dwyer, A. Erb, F. Gao, P. Griffiths, D. Helder, T. Hermosilla, J. D. Hipple, P. Hostert, M. J. Hughes, J. Huntington, D. M. Johnson, R. Kennedy, A. Kilic, Z. Li, L. Lyburner, J. McCorkel, N. Pahlevan, T. A. Scambos, C. Schaaf, J. R. Schott, Y. Sheng, J. Storey, E. Vermote, J. Vogelmann, J. C. White, R. H. Wynne, and Z. Zhu, "Current status of Landsat program, science, and applications," *Remote Sensing of Environment*, vol. 225, pp. 127–147, 2019.
- [11] Irons, James R., "Landsat 9." NASA Goddard Space Flight Center, 2018. <https://landsat.gsfc.nasa.gov/landsat-9/>. (Accessed: 5 February 2019).

- [12] J. Masek, “NASA SLI-Technology Studies,” 2016. Given to the Landsat Science Team, Brookings, SD.
- [13] C. F. Schueler, “Satellite-instrument system engineering best practices and lessons,” in *Proc. SPIE*, vol. 7458, p. 745807, 2009.
- [14] S. Wills, “Freeform optics: Notes from the revolution,” *Optics & Photonics News*, pp. 35–41, 2017.
- [15] J. P. Rolland and K. P. Thompson, “Freeform optics: Evolution? No, revolution!,” *SPIE Newsroom*, pp. 10–12, 2012.
- [16] K. P. Thompson and J. P. Rolland, “Freeform optical surfaces: A revolution in imaging optical design,” *Optics & Photonics News*, vol. 23, no. 6, pp. 30–35, 2012.
- [17] E. Fest, *Stray Light Analysis and Control*. Bellingham: SPIE Press, 2013.
- [18] P. W. Dabney, R. Levy, L. Ong, E. Waluschka, and F. Grochocki, “Ghosting and stray-light performance assessment of the Landsat Data Continuity Mission’s (LDCM) Operational Land Imager (OLI),” in *Proc. SPIE*, vol. 8866, p. 88661E, 2013.
- [19] R. Pfisterer, “Optical system optimization: Analyzing the effects of stray light,” *Photonics Spectra*, vol. 51, no. 3, pp. 60–68, 2017.
- [20] “Resiliency and disaggregated space architectures.” Air Force Space Command, 2013. <https://fas.org/spp/military/resiliency.pdf>. (Accessed: 24 June 2018).
- [21] P. Wegner, T. Adang, and M. Rhemann, “How to make disaggregation work,” *Air & Space Power Journal*, vol. 29, no. 6, pp. 49–55, 2015.

- [22] P. A. Lightsey, Z. Wei, D. L. Skelton, C. W. Bowers, K. I. Mehalick, S. R. Thomson, P. Knollenberg, and J. W. Arenberg, “Stray light performance for the James Webb Space Telescope,” in *Proc. SPIE*, vol. 9143, p. 91433P, 2014.
- [23] S. O. Rohrbach, R. G. Irvin, L. T. Seals, and D. L. Skelton, “Stray light modeling of the James Webb Space Telescope (JWST) Integrated Science Instrument Module (ISIM),” in *Proc. SPIE*, vol. 9947, p. 99470K, 2016.
- [24] K. S. Ellis, “Stray light characteristics of the Large Synoptic Survey Telescope (LSST),” in *Proc. SPIE*, vol. 7427, p. 742708, 2009.
- [25] A. E. Lowman and J. L. Stauder, “Stray light lessons learned from the Mars Reconnaissance Orbiter’s Optical Navigation Camera,” in *Proc. SPIE*, vol. 5526, pp. 240–248, 2004.
- [26] M. Asadnezhad, A. Eslamimajd, and H. Hajghassem, “Stray light analysis, baffle, and optical design of a high-resolution satellite camera,” *Journal of Applied Remote Sensing*, vol. 12, no. 2, 2018.
- [27] D. Liu, L. Wang, W. Yang, S. Wu, B. Fan, and F. Wu, “Stray light characteristics of the diffractive telescope system,” *Optical Engineering*, vol. 57, no. 2, 2018.
- [28] R. P. Breault and D. Milsom, “Stray-light analysis of the Cassini telescope,” in *Proc. SPIE*, vol. 1753, 1992.
- [29] J. A. Mendenhall and D. E. Lencioni, “EO-1 Advanced Land Imager stray light analysis and impact on flight data,” in *IEEE International Geoscience and Remote Sensing Symposium*, vol. 6, pp. 3114–3117 vol.6, June 2002.

- [30] S. Mills, S. Weiss, and C. Liang, "VIIRS Day/Night Band (DNB) stray light characterization and correction," in *Proc. SPIE*, vol. 8866, p. 88661P, 2013.
- [31] X. Xiong, W. Barnes, B. Guenther, and R. Murphy, "Lessons learned from MODIS," *Adv. Space Res.*, vol. 32, no. 11, pp. 2107–2112, 2003.
- [32] A. Gerace and M. Montanaro, "Derivation and validation of the stray light correction algorithm for the Thermal Infrared Sensor onboard Landsat 8," *Remote Sensing of Environment*, vol. 191, pp. 246–257, 2017.
- [33] M. Talone, G. Zibordi, I. Ansko, A. C. Banks, and J. Kuusk, "Stray light effects in above-water remote-sensing reflectance from hyperspectral radiometers," *Applied Optics*, vol. 55, no. 15, pp. 3966–3977, 2016.
- [34] M. E. Feinholz, S. J. Flora, S. W. Brown, Y. Zong, K. R. Lykke, M. A. Yarbrough, B. C. Johnson, and D. K. Clark, "Stray light correction algorithm for multichannel hyperspectral spectrographs," *Applied Optics*, vol. 51, no. 16, pp. 3631–3641, 2012.
- [35] Y. Zong, S. W. Brown, B. C. Johnson, K. R. Lykke, and Y. Ohno, "Simple spectral stray light correction method for array spectroradiometers," *Applied Optics*, vol. 45, no. 6, pp. 1111–1119, 2006.
- [36] B. Bitlis, P. A. Jansson, and J. P. Allebach, "Parametric point spread function modeling and reduction of stray light effects in digital still cameras," in *Proc. SPIE*, vol. 6498, p. 64980V, 2007.
- [37] H. Chen, X. Xiong, X. Geng, and K. Twedt, "Stray-light correction and prediction for Suomi National Polar-orbiting Partnership visible infrared imaging radiometer suite day-night band," *Journal of Applied Remote Sensing*, vol. 13, no. 2, p. 024521, 2019.

- [38] R. N. Pfisterer, K. S. Ellis, and S. M. Pompea, "The role of stray light modeling and analysis in telescope system engineering, performance assessment, and risk abatement," in *Proc. SPIE*, vol. 7738, p. 773811, 2010.
- [39] D. Léger, J. Duffaut, and F. Robinet, "MTF measurements using spotlight," in *Proc. of the 1994 International Geoscience and Remote Sensing Symposium*, 1994.
- [40] D. Helder, T. Choi, and M. Rangaswamy, "In-flight characterization of spatial quality using point spread functions," in *Proc. of the 2004 International Workshop on Radiometric and Geometric Calibration*, 2004.
- [41] J. Achatzi, G. Fischer, V. Zimmer, D. Paulus, and G. Bonnet, "Measurement and analysis of the point spread function with regard to straylight correction," in *Proc. SPIE*, vol. 9404, p. 940406, 2015.
- [42] C. D. McGillem, P. E. Anuta, E. Malaret, and K. B. Yu, "Estimation of a remote sensing system point-spread function from measured imagery," in *Machine Processing of Remotely Sensed Data Symposium*, pp. 62–68, 1983.
- [43] B. L. Markham, "The Landsat sensors' spatial responses," *IEEE Transactions on Geoscience and Remote Sensing*, vol. GE-23, no. 6, pp. 864–875, 1985.
- [44] M. Pagnutti, S. Blonski, M. Cramer, D. Helder, K. Holekamp, E. Honkavaara, and R. Ryan, "Targets, methods, and sites for assessing the in-flight spatial resolution of electro-optical data products," *Canadian Journal of Remote Sensing*, vol. 36, no. 5, pp. 583–601, 2010.

- [45] B. N. Wenny, D. Helder, J. Hong, L. Leigh, K. J. Thome, and D. Reuter, “Pre- and post-launch spatial quality of the Landsat 8 Thermal Infrared Sensor,” *Remote Sensing*, vol. 7, no. 2, pp. 1962–1980, 2015.
- [46] K. L. Yeo, A. Feller, S. K. Solanki, S. Couvidat, S. Danilovic, and N. A. Krivova, “Point spread function of SDO / HMI and the effects of stray light correction on the apparent properties of solar surface phenomena,” *Astronomy & Astrophysics*, vol. 561, p. A22, 2014.
- [47] S. Mathew, V. Zakharov, and S. K. Solanki, “Stray light correction and contrast analysis of Hinode broad-band images,” *Astronomy & Astrophysics*, vol. 501, no. 3, pp. L19–L22, 2009.
- [48] L. Yang and J. Ren, “Remote sensing image restoration using estimated point spread function,” in *2010 International Conference on Information, Networking and Automation (ICINA)*, pp. V1–48–V1–52, 2010.
- [49] J. Harvey, N. Choi, A. Krywonos, G. Peterson, and M. Bruner, “Image degradation due to scattering effects in two-mirror telescopes,” *Optical Engineering*, vol. 49, no. 6, p. 063202, 2010.
- [50] Z. Cui, M. Montanaro, A. Gerace, J. R. Schott, and B. L. Markham, “Requirement sensitivity studies for a future Landsat sensor,” *Proc. SPIE*, vol. 9607, p. 96070S, 2015.
- [51] N. Choi and J. E. Harvey, “Image degradation due to surface scatter in the presence of aberrations,” *Applied Optics*, vol. 51, no. 5, pp. 535–546, 2012.

- [52] J. Wei, G. Cao, C. Bouman, and J. Allebach, “Fast space-varying convolution and its application in stray light reduction,” in *Proc. SPIE*, vol. 7246, p. 72460B, 2009.
- [53] P. A. Lightsey and Z. Wei, “James Webb Space Telescope observatory stray light performance,” in *Proc. SPIE*, vol. 6265, p. 62650S, 2006.
- [54] P. A. Lightsey, “Stray light field dependence for the James Webb Space Telescope,” in *Proc. SPIE*, vol. 9904, p. 99040A, 2016.
- [55] T. Kuntzer, A. Fortier, and W. Benz, “SALSA: A tool to estimate the stray light contamination for low-Earth orbit observatories,” in *Proc. SPIE*, vol. 9149, p. 91490W, 2014.
- [56] T. N. Miller, M. Lampton, R. W. Besuner, M. J. Sholl, M. Liang, and S. Ellis, “Stray light assessment and mitigation for the DESI front-end optical system,” in *Proc. SPIE*, vol. 9908, p. 99088O, 2016.
- [57] M. Montanaro, A. Gerace, A. Lunsford, and D. Reuter, “Stray light artifacts in imagery from the Landsat 8 Thermal Infrared Sensor,” *Remote Sensing*, vol. 6, no. 11, pp. 10435–10456, 2014.
- [58] M. Montanaro, A. Gerace, and S. Rohrbach, “Toward an operational stray light correction for the Landsat 8 Thermal Infrared Sensor,” *Applied Optics*, vol. 54, no. 13, pp. 3963–3978, 2015.
- [59] J. R. Schott, *Remote Sensing: The Image Chain Approach*. New York: Oxford University Press, 2nd ed., 2007.

- [60] K. S. McCoy, J. P. Kerekes, S. D. Brown, A. A. Goodenough, R. V. Raqueño, J. D. Van Cor, and R. G. Irvin, “Integration of optomechanical system models with DIRSIG,” in *Proc. SPIE*, vol. 10743, p. 1074304, 2018.
- [61] “FRED Optical Engineering Software.” Photon Engineering, <https://photonengr.com>.
- [62] “DIRSIG.” Digital Imaging and Remote Sensing Laboratory, Rochester Institute of Technology, <http://www.dirsig.org/>.
- [63] Commission Internationale de l’Eclairage (CIE), “International Lighting Vocabulary. Technical Report 17 (E-1.1),” 1970.
- [64] M. Breault, Robert P., Turner, “Optical design and stray light concepts and principles,” in *Springer Handbook of Lasers and Optics* (F. Träger, ed.), pp. 427–445, Berlin: Springer-Verlag, 2nd ed., 2012.
- [65] D. R. Hearn, “Spatial calibration and imaging performance assessment of the Advanced Land Imager,” *Lincoln Laboratory Journal*, vol. 15, no. 2, pp. 225–250, 2005.
- [66] D. C. Reuter, C. M. Richardson, F. A. Pellerano, J. R. Irons, R. G. Allen, M. Anderson, M. D. Jhabvala, A. W. Lunsford, M. Montanaro, R. L. Smith, Z. Tesfaye, and K. J. Thome, “The Thermal Infrared Sensor (TIRS) on Landsat 8: Design overview and pre-launch characterization,” *Remote Sensing*, vol. 7, no. 1, pp. 1135–1153, 2015.
- [67] P. Bely, ed., *The Design and Construction of Large Optical Telescopes*. New York: Springer-Verlag, 2003.

- [68] R. P. Breault, "Control of stray light," in *Handbook of Optics. Volume II Design, Fabrication, and Testing; Sources and Detectors; Radiometry and Photometry*. (M. Bass, ed.), ch. 7, McGraw-Hill, 2010.
- [69] J. L. Stauder and R. W. Esplin, "Stray light design and analysis of the Sounding of the Atmosphere using Broadband Emission Radiometry (SABER) telescope," in *Proc. SPIE*, vol. 3437, pp. 52–59, 1998.
- [70] F. E. Nicodemus, "Directional reflectance and emissivity of an opaque surface," *Applied Optics*, vol. 4, no. 7, pp. 767–773, 1965.
- [71] F. E. Nicodemus, "Reflectance nomenclature and directional reflectance and emissivity," *Applied Optics*, vol. 9, no. 6, pp. 1474–1475, 1970.
- [72] F. O. Bartell, E. L. Dereniak, and W. L. Wolfe, "The theory and measurement of Bidirectional Reflectance Distribution Function (BRDF) and Bidirectional Transmittance Distribution Function (BTDF)," in *Proc. SPIE*, vol. 0257, pp. 154–160, 1981.
- [73] J. C. Stover, *Optical Scattering: Measurement and Analysis*. Bellingham: SPIE Press, 3rd ed., 2012.
- [74] F. Reininger, "Stray light performance optimization through system design," in *Proc. SPIE*, vol. 2260, pp. 17–28, 1994.
- [75] S. Kleiner, "Stray light and ghost images ... analyzed and reduced using simulation software," *Laser+Photonik*, pp. 46–49, 2007.

- [76] B. Ma, Z. Shen, F. Sha, C. Wang, B. Wang, Y. Ji, H. Liu, W. Li, and Z. Wang, “Evaluation and analysis of polished fused silica subsurface quality by the nanoindenter technique,” *Applied Optics*, vol. 50, no. 9, pp. C279–285, 2011.
- [77] J. Bennett and L. Mattsson, *Introduction to Surface Roughness and Scattering*. Optical Society of America, 1989.
- [78] J. Harvey, *Light Scattering Characteristics of Optical Surfaces*. PhD dissertation, University of Arizona, 1976.
- [79] J. E. Harvey, “Surface scatter phenomena: A linear, shift-invariant process,” in *Proc. SPIE*, vol. 1165, pp. 87–99, 1990.
- [80] Jacobsen, Dave, “An introduction to scattering and the surface property in TracePro.” Lambda Research Corporation, 2010. https://www.lambdares.com/wp-content/uploads/support/tracepro/tracepro_webinars/December%202010%20Webinar.pdf. (Accessed: 8 October 2018).
- [81] FRED Optical Engineering Software Help, “Scatters - Harvey-Shack.” PhotonEngineering, <https://photonengr.com>.
- [82] D. Goodman, “Stray light,” *Optics & Photonics News*, vol. 3, no. 1, pp. 52–53, 1992.
- [83] W. L. Spyak, Paul R., Wolfe, “Scatter from particulate-contaminated mirrors. part 4: properties of scatter from dust for visible to far-infrared wavelengths,” vol. 31, no. 8, pp. 1775–1784, 1992.
- [84] M. G. Dittman, “Contamination scatter functions for stray-light analysis,” in *Proc. SPIE*, vol. 4774, pp. 99–110, 2002.

- [85] R. Young, “Low-scatter mirror degradation by particle contamination,” *Optical Engineering*, vol. 15, no. 6, 1976.
- [86] IEST-STD-CC1246D: Product cleanliness levels and contamination control program, “Institute of Environmental Sciences and Technology,” 2002.
- [87] Product cleanliness levels and contamination control program, “Military Standard (MIL STD) 1246C,” 1994.
- [88] “AEROGLAZE Z306 Polyurethane Coating.” SOCOMORE The Surface Company, 2018. <https://www.socomore.com/shop/coatings/anti-erosion-coating/aeroglaze-z306/>. (Accessed: 24 June 2018).
- [89] J. Goodman, *Introduction to Fourier Optics*. Englewood: Roberts & Company, 3rd ed., 2005.
- [90] R. N. Pfisterer, “Clever tricks in optical engineering,” in *Proc. SPIE*, vol. 5524, pp. 230–239, 2004.
- [91] International Standards Organization (ISO), “ISO 9358: Optics and optical instruments - veiling glare of image forming systems - definitions and methods of measurements,” 1994.
- [92] F. Grochocki and J. Fleming, “Stray light testing of the OLI telescope,” in *Proc. SPIE*, vol. 7794, p. 77940W, 2010.
- [93] P. J. Peters, “Stray light control: An integral part of optical design,” in *Proc. SPIE*, vol. 0399, pp. 50–59, 1983.
- [94] “Zemax OpticStudio.” Zemax, <https://www.zemax.com>.

- [95] “Code V Optical Engineering Software.” Synopsys, <https://www.synopsys.com>.
- [96] “OSLO.” Lambda Research Corporation, <https://www.lambdaresearch.com>.
- [97] “ASAP.” Breault Research Corporation, <http://www.breault.com/>.
- [98] “TracePro.” Lambda Research Corporation, <https://www.lambdaresearch.com>.
- [99] R. L. Easton, *Fourier Methods in Imaging*. Chichester: Wiley, 2010.
- [100] S. Han and J. P. Kerekes, “Overview of passive optical multispectral and hyperspectral image simulation techniques,” *IEEE J. Sel. Topics Appl. Earth Observ. and Remote Sens.*, vol. 10, no. 11, pp. 4794–4804, 2017.
- [101] National Aeronautics and Space Administration (NASA), 2016, “NASA Systems Engineering Handbook, NASA/SP-2016-6105 Rev 2.” https://www.nasa.gov/sites/default/files/atoms/files/nasa_systems_engineering_handbook_0.pdf. (Accessed: 14 March 2019).
- [102] European Cooperation for Space Standardization (ECSS), 2017, “Space Engineering, ECSS-E-ST-10C, 15 February 2017.” <http://www.ecss.nl/>. (Accessed: 14 March 2019).
- [103] M. M. Verstraete, D. J. Diner, and J.-L. Bezy, “Planning for a spaceborne Earth Observation mission: From user expectations to measurement requirements,” *Environmental Science & Policy*, vol. 54, pp. 419–427, 2015.
- [104] C. d. Negueruela, M. Scagliola, D. Giudici, J. Moreno, and J. Vicent, “ARCHEO-E2E: A reference architecture for earth observation end-to-end mission performance

- simulators,” in *Proc. SESP, Simulation EGSE facilities for Space Programmes*, pp. 1–9, 2012.
- [105] K. Segl, L. Guanter, C. Rogass, T. Kuester, S. Roessner, H. Kaufmann, B. Sang, V. Mogulsky, and S. Hofer, “EeteS – The EnMAP End-to-End Simulation Tool,” *IEEE J. Sel. Topics Appl. Earth Observ. and Remote Sens.*, vol. 5, no. 2, pp. 522–530, 2012.
- [106] K. Segl, L. Guanter, F. Gascon, T. Kuester, C. Rogass, and C. Mielke, “S2eteS - An end-to-end modeling tool for the simulation of Sentinel-2 image products,” *IEEE Transactions on Geoscience and Remote Sensing*, vol. 53, no. 10, pp. 5560–5571, 2015.
- [107] J. Vicent, N. Sabater, C. Tenjo, J. R. Acarreta, M. Manzano, J. P. Rivera, P. Jurado, R. Franco, L. Alonso, J. Verrelst, and J. Moreno, “FLEX end-to-end mission performance simulator,” *IEEE Transactions on Geoscience and Remote Sensing*, vol. 54, no. 7, pp. 4215–4223, 2016.
- [108] P. Coppo, L. Chiarantini, and L. Alparone, “Design and validation of an end-to-end simulator for imaging spectrometers,” *Optical Engineering*, vol. 51, no. 11, p. 111721, 2012.
- [109] A. A. Goodenough and S. D. Brown, “DIRSIG5 : Next-generation remote sensing data and image simulation framework,” *IEEE J. Sel. Topics Appl. Earth Observ. Remote Sens.*, vol. 10, no. 11, pp. 4818–4833, 2017.
- [110] A. Gerace, J. Schott, M. Gartley, and M. Montanaro, “An analysis of the side slither on-orbit calibration technique using the DIRSIG model,” *Remote Sensing*, vol. 6, pp. 10523–10545, 2014.

- [111] R. Rengarajan and J. R. Schott, "Modeling and simulation of deciduous forest canopy and its anisotropic reflectance properties using the Digital Imaging and Remote Sensing Image Generation Tool (DIRSIG) tool," *IEEE J. Sel. Topics Appl. Earth Observ. and Remote Sens.*, vol. 10, no. 11, pp. 4805–4817, 2017.
- [112] R. S. Eon, A. D. Gerace, M. Montanaro, B. L. Ambeau, and J. T. McCorkel, "Development of a simulation environment to support intercalibration studies over the Algodones Dunes system," *Journal of Applied Remote Sensing*, vol. 12, no. 1, p. 012008, 2017.
- [113] "The DART model." Centre d'Etudes Spatiales de la Biosphère (CESBIO), <http://www.cesbio.ups-tlse.fr/us/dart.html>.
- [114] J. P. Gastellu-Etchegorry, E. Martin, and F. Gascon, "DART: A 3D model for simulating satellite images and studying surface radiation budget," *Int. J. Remote Sensing*, vol. 25, no. 1, pp. 73–96, 2004.
- [115] J.-P. Gastellu-Etchegorry, T. Yin, N. Lauret, T. Cajgfinger, T. Gregoire, E. Grau, J.-B. Feret, M. Lopes, J. Guilleux, G. Dedieu, and Z. Malenovsky, "Discrete Anisotropic Radiative Transfer (DART 5) for modeling airborne and satellite spectroradiometer and LIDAR acquisitions of natural and urban landscapes," *Remote Sensing*, vol. 7, no. 2, pp. 1667–1701, 2017.
- [116] J. d. Castro Oliveira, J.-B. Féret, F. J. Ponzoni, Y. Nouvellon, J.-P. Gastellu-Etchegorry, O. C. Campoe, J. L. Stape, L. C. E. Rodriguez, and G. Le Marie, "Simulating the canopy reflectance of different eucalypt genotypes with the DART RTM,"

- IEEE J. Sel. Topics Appl. Earth Observ. and Remote Sens.*, vol. 10, no. 11, pp. 4844–4852, 2017.
- [117] S. B. Hmida, A. Kallel, J.-P. Gastellu-Etchegorry, and J.-L. Roujean, “Crop biophysical properties estimation based on LiDAR full-waveform inversion using the DART RTM,” *IEEE J. Sel. Topics Appl. Earth Observ. and Remote Sens.*, vol. 10, no. 11, pp. 4853–4868, 2017.
- [118] A. Börner, L. Wiest, P. Keller, R. Reulke, R. Richter, M. Schaepman, and D. Schläpfer, “FLEX end-to-end mission performance simulator,” *ISPRS Journal of Photogrammetry & Remote Sensing*, vol. 55, pp. 299–312, 2001.
- [119] S. A. Cota, J. T. Bell, R. H. Boucher, T. E. Dutton, C. J. Florio, A. Franz, Geoffrey, T. J. Grycewicz, L. S. Kalman, R. A. Keller, T. S. Lomheim, D. B. Paulson, and T. S. Wilkinson, “PICASSO: an end-to-end image simulation tool for space and airborne imaging systems,” *Journal of Applied Remote Sensing*, vol. 4, p. 043535, 2010.
- [120] S. M. Adler-Golden, S. C. Richtsmeier, A. Berk, and J. W. Duff, “Fast Monte Carlo-assisted simulation of cloudy Earth backgrounds,” in *Proc. SPIE*, vol. 8534, p. 85340F, 2012.
- [121] C. Schweitzer, K. Stein, N. Wendelstein, L. Labarre, K. Caillault, S. Fauquex, C. Malherbe, A. Roblin, B. Rosier, and P. Simoneau, “Validation of the background simulation model MATISSE: Comparing results with MODIS satellite images,” in *Proc. SPIE*, vol. 8178, p. 817805, 2011.

- [122] C. Huang, J. R. G. Townshend, S. Liang, S. N. V. Kalluri, and R. S. DeFries, “Impact of sensor’s point spread function on land cover characterization: Assessment and deconvolution,” *Remote Sens. Environ.*, vol. 80, pp. 203–212, 2002.
- [123] P. Lightsey and C. Bowers, “Stray light field dependence for large astronomical space telescopes,” in *Proc. SPIE*, vol. 10398, p. 103980L, 2017.
- [124] R. Gonzalez and R. Woods, *Digital Image Processing*. Upper Saddle River: Pearson Prentice Hall, 3rd ed., 2008.
- [125] A. P. Cracknell, “Synergy in remote sensing - what’s in a pixel?,” *International Journal of Remote Sensing*, vol. 19, no. 11, pp. 2025–2047, 1998.
- [126] H. H. Barrett and W. Swindell, *Radiological Imaging: The Theory of Image Formation, Detection, and Processing*. New York: Academic Press, 1st ed., 1981.
- [127] Ž. Špiclin, M. Bürmen, F. Pernuš, and B. Likar, “Characterization and modelling of the spatially- and spectrally-varying point-spread function in hyperspectral imaging systems for computational correction of axial optical aberrations,” in *Proc. SPIE*, vol. 8215, p. 82150R, 2012.
- [128] C. DeForest, P. C. H. Martens, and M. J. Wills-Davey, “Solar coronal structures and stray light in TRACE,” *Astrophysical Journal*, vol. 690, pp. 1264–1271, 2009.
- [129] S. Wedemeyer-Böhm, “Point spread functions for the solar optical telescope onboard Hinode,” *Astronomy & Astrophysics*, vol. 487, pp. 399–412, 2008.
- [130] J. J. McCann and A. Rizzi, “Veiling glare: The dynamic range limit of HDR images,” in *Proc. SPIE*, vol. 6492, 2007.

- [131] T. Lauer, “Deconvolution with a spatially-variant PSF,” in *Proc. SPIE*, vol. 4847, p. 167, 2002.
- [132] L. B. Lucy, “An iterative technique for the rectification of observed distributions,” *Astronomical Journal*, vol. 79, no. 6, pp. 745–754, 1974.
- [133] W. H. Richardson, “Bayesian-based iterative method of image restoration,” *Journal of the Optical Society of America*, vol. 62, no. 1, pp. 55–59, 1972.
- [134] G. Meister, Y. Zong, and C. R. McClain, “Derivation of the MODIS Aqua point-spread function for ocean color bands,” *Proc. SPIE*, vol. 7081, p. 70811F, 2008.
- [135] G. Meister and C. R. McClain, “Point-spread function of the ocean color bands of the Moderate Resolution Imaging Spectroradiometer on Aqua,” *Applied Optics*, vol. 49, no. 32, pp. 6276–6285, 2010.
- [136] J. A. Esposito, X. Xiong, A. Wu, J. Sun, and W. L. Barnes, “MODIS reflective solar bands uncertainty analysis,” in *Proc. SPIE*, vol. 5542, pp. 448–458, 2004.
- [137] H. Du and K. J. Voss, “Effects of point-spread function on calibration and radiometric accuracy of CCD camera,” *Applied Optics*, vol. 43, no. 3, pp. 665–670, 2004.
- [138] M. A. Goforth, “General algorithm for stray light measurements of remote sensing imagery,” in *Proc. SPIE*, vol. 6291, p. 62910Y, 2006.
- [139] D. R. Thompson, J. W. Boardman, M. L. Eastwood, R. O. Green, J. M. Haag, P. Mouroulis, and B. Van Gorp, “Imaging spectrometer stray spectral response: In-flight characterization, correction, and validation,” *Remote Sensing of Environment*, vol. 204, pp. 850–860, 2018.

- [140] P. Mouroulis, R. O. Green, B. Van Gorp, L. B. Moore, D. W. Wilson, and H. A. Bender, “Landsat swath imaging spectrometer design,” *Optical Engineering*, vol. 55, no. 1, p. 015104, 2016.
- [141] Y. Zong, S. W. Brown, G. Meister, R. A. Barnes, and K. R. Lykke, “Characterization and correction of stray light in spectroradiometers and imaging instruments,” in *Proc. SPIE*, vol. 6744, p. 67441L, 2007.
- [142] V. Cessa, T. Beck, W. Benz, C. Broeg, D. Ehrenreich, A. Fortier, G. Peter, D. Margrin, I. Pagano, J. Y. Plessier, M. Steller, J. Szoke, N. Thomas, R. Ragazzoni, and F. Wildi, “CHEOPS: a space telescope for ultra-high precision photometry of exoplanet transits,” in *Proc. SPIE*, vol. 10563, p. 105631L, 2017.
- [143] T. Kuntzer, *Simulation of Stray Light Contamination on CHEOPS Detector*. PhD dissertation, University of Bern, 2013.
- [144] Z. Wei and P. A. Lightsey, “Stray light from galactic sky and zodiacal light for JWST,” in *Proc. SPIE*, vol. 6265, p. 62653C, 2006.
- [145] J. E. Mason, J. R. Schott, C. Salvaggio, and J. D. Sirianni, “Validation of contrast and phenomenology in the Digital Imaging and Remote Sensing (DIRS) lab’s Image Generation (DIRSIG) model,” in *Proc. SPIE*, vol. 2269, pp. 622–633, 1994.
- [146] K. Bloechl, C. De Angelis, M. Gartley, J. Kerekes, and C. E. Nance, “A comparison of real and simulated airborne multisensor imagery,” in *Proc. SPIE*, vol. 9088, p. 90880G, 2014.
- [147] “MODTRAN.” Spectral Sciences, Inc., <http://modtran.spectral.com/>.

- [148] J. R. Schott, R. V. Raqueño, N. G. Raqueño, and S. D. Brown, “A synthetic sensor/image simulation tool to support the Landsat Data Continuity Mission (LDCM),” in *ASPRS 2010 Annual Conference*, 2010.
- [149] S. Brown and A. Goodenough, “Plugin-driven sensor modeling of remote sensing imaging systems,” in *IGARSS 2017 – IEEE International Geoscience and Remote Sensing Symposium*, pp. 1445–1448, 2017.
- [150] J. R. Schott, A. D. Gerace, S. D. Brown, and M. G. Gartley, “Modeling the image performance of the Landsat Data Continuity Mission sensors,” in *Proc. SPIE*, vol. 8153, p. 81530F, 2011.
- [151] J. Schott, A. Gerace, S. Brown, M. Gartley, M. Montanaro, and D. C. Reuter, “Simulation of image performance characteristics of the Landsat Data Continuity Mission (LDCM) Thermal Infrared Sensor (TIRS),” *Remote Sensing*, vol. 4, no. 8, pp. 2477–2491, 2012.
- [152] A. Gerace, M. Gartley, J. Schott, N. Raqueño, and R. Raqueño, “Data-driven simulations of the Landsat Data Continuity Mission (LDCM) platform,” in *Proc. SPIE*, vol. 8048, p. 804815, 2011.
- [153] S. D. Brown, N. J. Sanders, A. A. Goodenough, and M. Gartley, “Modeling space-based multispectral imaging systems with DIRSIG,” in *Proc. SPIE*, vol. 8048, p. 804814, 2011.
- [154] A. D. Gerace, A. A. Goodenough, M. Montanaro, J. Yang, and J. T. McCorkel, “The development of a DIRSIG simulation environment to support instrument trade studies for the SOLARIS sensor,” in *Proc. SPIE*, vol. 9472, p. 947214, 2015.

- [155] B. R. Frieden, *Probability, Statistical Optics, and Data Testing: A Problem Solving Approach*. Berlin: Springer-Verlag, 3rd ed., 2001.
- [156] “MATLAB.” MathWorks, https://www.mathworks.com/products/matlab.html?s_tid=hp_products_matlab.
- [157] L. Wen, “An analytic technique to prove Borel’s Strong Law of Large Numbers,” *The American Mathematical Monthly*, vol. 98, no. 2, pp. 146–148, 1991.
- [158] G. L. Peterson, “Analytic expressions for in-field scattered light distributions,” in *Proc. SPIE*, vol. 5178, pp. 184–193, 2004.
- [159] S. Fray, M. Goepel, and M. Kroneberger, “Application of Peterson’s stray light model to complex optical instruments,” in *Proc. SPIE*, vol. 9904, p. 99044W, 2016.
- [160] W. J. Smith, *Modern Optical Engineering*. New York: McGraw-Hill, 4th ed., 2008.
- [161] S. Jennings, R. Pinnick, and H. Aubermann, “Effects of particulate complex refractive and particle size distribution variations on atmospheric extinction and absorption for visible through middle IR wavelengths,” *Applied Optics*, vol. 17, no. 24, pp. 3922–3929, 1978.
- [162] J. Van Cor, “Characterizing Resident Space Object Earthshine Signature Variability,” Master’s thesis, Rochester Institute of Technology, 2017.
- [163] W. Wanner, X. Li, and A. H. Strahler, “On the derivation of kernels for kernel-driven methods of bidirectional reflectance,” *Journal of Geophysical Research: Atmospheres*, vol. 100, no. D10, pp. 21077–21089, 1995.

- [164] J. Ross, *Radiation Regime and Architecture of Plant Stands*. The Hague, Netherlands: Dr. W. Junk Publishers, 1981.
- [165] X. Li and A. H. Strahler, “Geometric-optical bidirectional reflectance modeling of the discrete crown vegetation canopy: effect of crown shape and mutual shadowing,” *IEEE Transactions on Geoscience and Remote Sensing*, vol. 30, no. 2, pp. 276–292, 1992.
- [166] C. Cox and W. Munk, “Measurement of the roughness of the sea surface from photographs of the sun’s glitter,” *Journal of the Optical Society of America*, vol. 44, no. 11, pp. 838–850, 1954.
- [167] G. J. Ward, “Measuring and modeling anisotropic reflection,” *Computer Graphics*, vol. 26, no. 2, pp. 265–272, 1992.
- [168] “California Offshore 90-Meter Wind Map and Wind Resource Potential.” WindExchange, U.S. Department of Energy, <https://windexchange.energy.gov/maps-data/146>. (Accessed: 15 May 2019).
- [169] R. E. Fischer, B. Tadic-Galeb, and P. R. Yoder, Jr, *Optical System Design*. New York: SPIE Press, 2nd ed., 2008.
- [170] E. J. Knight and G. Kvaran, “Landsat-8 operational land imager design, characterization and performance,” *Remote Sensing*, vol. 6, no. 11, pp. 10286–10305, 2014.